Is the pressure difference between the oval and round windows the effective acoustic stimulus for the inner ear?

by

Susan E. Voss

Submitted to the Department of Electrical Engineering and Computer Science
in partial fulfillment of the requirements for the degree of

Master of Science in Electrical Engineering and Computer Science

at the

MASSACHUSETTS INSTITUTE OF TECHNOLOGY

February 1995

Author .....
Department of Electrical Engineering and Computer Science
January 20, 1995

Certified by .....
John J. Rosowski
Associate Professor of Otology and Laryngology, Harvard Medical School
Thesis Supervisor

Certified by .....
William T. Peake
Professor of Electrical and Bio-engineering, M.I.T.
Thesis Supervisor

Accepted by .....
F. R. Morgenthaler
Chairman, Departmental Committee on Graduate Students

Is the pressure difference between the oval and round windows the effective acoustic stimulus for the inner ear?

by

Susan E. Voss

Submitted to the Department of Electrical Engineering and Computer Science
on January 20, 1995, in partial fulfillment of the
requirements for the degree of
Master of Science in Electrical Engineering and Computer Science

Abstract

This thesis experimentally tests the common assumption that the pressure difference between the oval and round windows of the inner ear (cochlea) is the only acoustic stimulus for cochlear response. The cochlear potential, recorded at the round windows of anesthetized cats, is used as a measure of cochlear response. The sound pressures at the oval and round windows are individually controlled. A linear model of the response to the two input pressures estimates a complex common-mode gain $\underline{C}$ and a complex difference-mode gain $\underline{D}$. The magnitude of the difference-mode gain $|\underline{D}|$ is found to be at least 20 dB, and in some cases 40 to 60 dB, greater than $|\underline{C}|$; to a first approximation the pressure difference between the oval and round windows is the effective acoustic stimulus for the inner ear. This result is relevant both to models of the inner and middle ear and to clinical approaches to the improvement of hearing in ears with no ossicles.

Thesis Supervisor: John J. Rosowski
Title: Associate Professor of Otology and Laryngology, Harvard Medical School

Thesis Supervisor: William T. Peake
Title: Professor of Electrical and Bio-engineering, M.I.T.

Acknowledgments

I would like to thank my advisors Dr. John J. Rosowski and Professor William T. Peake for their constant guidance and support through all phases of this project. The three of us had numerous discussions concerning the experiments and data interpretations presented here. I learned a lot about science and the auditory system through these meetings, and I appreciate all the time spent to meet with me. I also thank John for teaching me to work with experimental animals. John spent several nights working at EPL so that he would be available when I needed help.

Many members of the Eaton-Peabody Lab helped with this project - I thank you all! Animal surgeries were performed by Leslie Dodds, Debbie Flandermeyer, Kerstin Jacob, and Tracy Liu. Debbie also assisted with several of the figures in chapters one and two. Discussions with Bertrand Delgutte, Nelson Y.S. Kiang, Sunil Puria, and Bill Sewell were particularly helpful. I thank Mike Ravicz for his assistance in teaching me to use the chamber 2 equipment.

This work was supported by NIH grants T32 DC 00038 and R01 DC 00194.

Contents

Chapter 1

Introduction

1.1 Ossicular versus non-ossicular coupling

The auditory portion of the fluid-filled inner ear (the cochlea) is enclosed by a bony capsule with two membrane-covered holes that face the middle-ear air space: the oval and round windows. In a normal ear sound is transmitted from the tympanic membrane (ear drum) to the oval window of the cochlea by the ossicles (malleus, incus, and stapes) (Fig. 1-1A). The tympanic membrane and ossicular system act to increase the sound-pressure level between the ear canal and the cochlea. This increase is generally presumed to be a result of the large area ratio between the tympanic membrane and the stapes footplate (Pickles, 1988). The round window acts as an outlet that releases the pressure transferred to the oval window by the ossicular motion. In pathological human ears with the ossicles missing hearing sensitivity is greatly reduced but hearing is still possible. In this case the sound pressure in the ear canal is neither magnified nor transmitted selectively to the oval window of the cochlea; instead the ear canal sound-pressure wave acts approximately equally on both the oval and round windows (Fig. 1-1B).

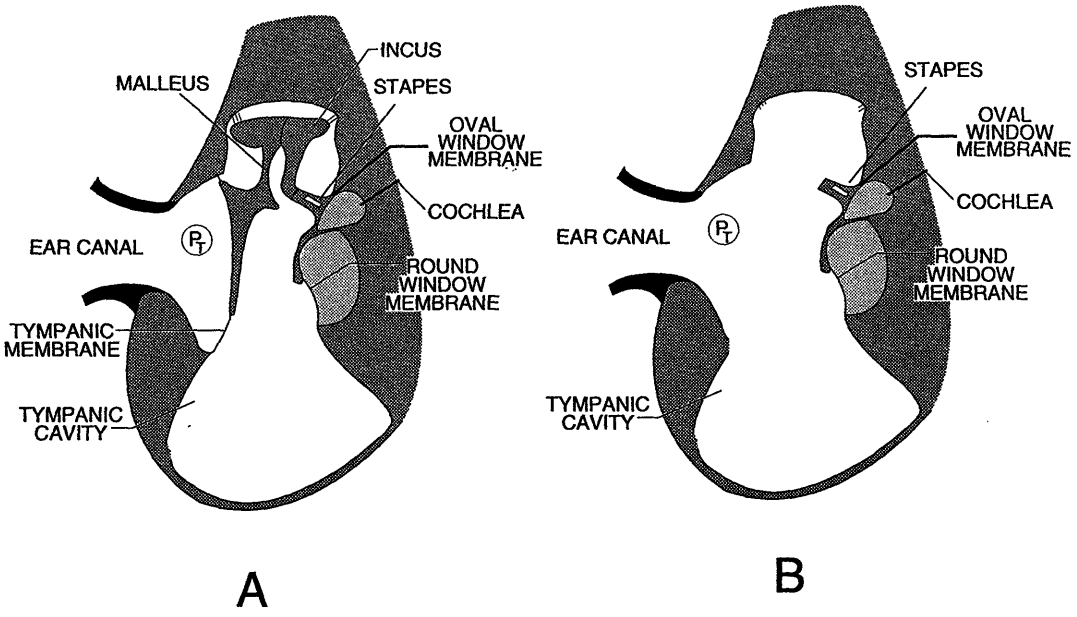

Figure 1-1: A: Schematic of a normal human ear. A sound pressure at the tympanic membrane, P_T, is magnified and transmitted to the oval window of the cochlea through the ossicular system (malleus, incus, and stapes). B: Schematic of a human ear missing the tympanic membrane, malleus, and incus. P_T is not magnified and acts approximately equally on both the oval and round windows.

Peake et al. (1992) developed a model that predicts hearing levels in both cat and human when the tympanic membrane, malleus, and incus are missing. They suggest that an important mechanism for hearing in such pathological cases is direct coupling of sound to the cochlear windows and that the cochlea responds to the pressure difference between the oval and round windows. Approximate agreement between model predictions and hearing levels in pathological ears supports the conclusion "For ears in which the tympanic membrane-ossicular chain mechanism has been disrupted available evidence for cat and human is consistent with the hypothesis that the sound-pressure difference at the cochlear windows is the dominant stimulus mechanism, at least for the higher frequencies (i.e. above 0.8 kHz)" (Peake et al. p. 258). It is difficult to come to a conclusion about the Peake et al. model fit to experimental data at lower frequencies because there are few experimental data. The existing data are discussed in Chapter 1.3.

1.2 The pressure-difference assumption

The pressure difference between the oval and round windows is often assumed to be the only acoustic stimulus to the cochlea. This assumption is prevalent in both basic science and clinical explanations of cochlear function. Models of the inner and middle ear usually assume that the cochlear fluid is incompressible and that the response of the cochlea is proportional only to the pressure difference between the oval and round windows (e.g. Zwislocki, 1965; Allen, 1985; Peake et al., 1992). Surgical approaches to hearing improvement in ears without tympanic membrane, malleus and incus attempt to maximize the window pressure difference (e.g. Wullstein, 1956; Peake et al., 1992; Merchant et al., 1995; Rosowski et al., 1995). For example, in the type IV tympanoplasty procedure the surgeon places a facia or cartilage graft across the middle-ear air space to act as a shield that isolates the round window from sound pressure in the ear canal; it is assumed that the graft functions to increase the pressure difference between the oval and round windows and thus improve hearing. The best surgical results yield hearing losses of about 20 dB. However, the surgical results are extremely variable; only 50% of the surgeries yield hearing losses of 30 dB or smaller, and post-surgical hearing losses of $40 - 50$ dB are not uncommon (Wullstein, 1956; Lee and Schuknecht, 1971; Gotay-Rodriquez and Schuknecht, 1977).

If the cochlea is assumed to be a linear system the pressure-difference assumption can be expressed as

$$\underline{Cochlear\ Response} = \underline{D}(\underline{P_{OW}} - \underline{P_{RW}}) \tag{1.1}$$

where $\underline{D}$ is a complex constant and $\underline{P_{OW}}$ and $\underline{P_{RW}}$ are the complex amplitudes of the sinusoidal sound pressures at the oval and round windows (Fig.1-2). If Equation 1.1 holds

and the cochlear system is also reciprocal then a volume velocity at the oval window, $\underline{U_{OW}}$, produces a volume velocity at the round window, $\underline{U_{RW}}$, such that $\underline{U_{OW}} = -\underline{U_{RW}}$.[1]

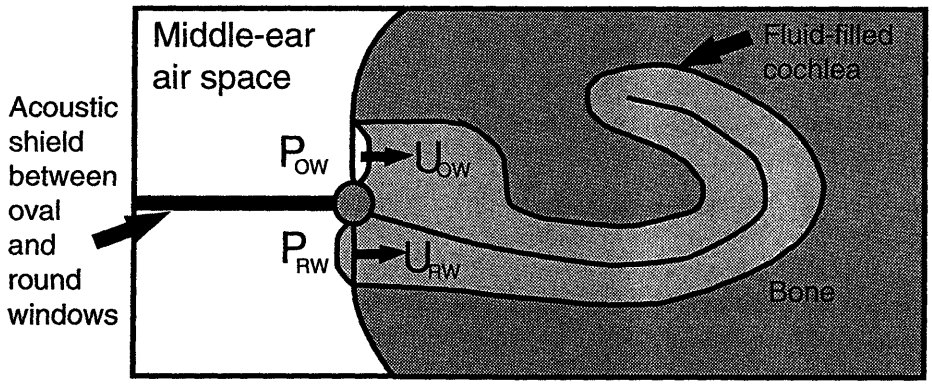

Figure 1-2: A schematic showing $\underline{P_{OW}}$ and $\underline{P_{RW}}$, the pressures at the oval and round windows, respectively. $\underline{U_{OW}}$ and $\underline{U_{RW}}$ refer to the volume velocities at the oval and round windows. It is commonly assumed that $\underline{U_{OW}} = -\underline{U_{RW}}$.

1.3 Experimental results relevant to the pressure-difference assumption

There is little experimental support for the pressure-difference assumption expressed by Equation 1.1. In fact, it has been suggested that the cochlea responds even when the

[1] If the cochlea is a linear, reciprocal system and if the response for all $\underline{P_{OW}}$ and $\underline{P_{RW}}$ is proportional to $(\underline{P_{OW}} - \underline{P_{RW}})$, then $\underline{U_{OW}} = -\underline{U_{RW}}$. Proof: Use a linear two-port network to represent the pressures and volume velocities at the oval and round windows.

$$\underline{U_{OW}} = \underline{Y_{11}}\,\underline{P_{OW}} + \underline{Y_{12}}\,\underline{P_{RW}} \tag{1.2}$$

$$\underline{U_{RW}} = \underline{Y_{21}}\,\underline{P_{OW}} + \underline{Y_{22}}\,\underline{P_{RW}} \tag{1.3}$$

It is assumed that the response of the system, here the volume velocity, is proportional to the difference in pressure between the two windows.

$$\underline{U_{OW}} = \underline{Y_{11}}\,\underline{P_{OW}} + \underline{Y_{12}}\,\underline{P_{RW}} = \underline{a}\,(\underline{P_{OW}} - \underline{P_{RW}}) \tag{1.4}$$

$$\underline{U_{RW}} = \underline{Y_{21}}\,\underline{P_{OW}} + \underline{Y_{22}}\,\underline{P_{RW}} = \underline{b}\,(\underline{P_{OW}} - \underline{P_{RW}}) \tag{1.5}$$

Equation 1.4 shows that $\underline{Y_{11}} = -\underline{Y_{12}} = \underline{a}$, and Equation 1.5 shows that $\underline{Y_{21}} = -\underline{Y_{22}} = \underline{b}$. Reciprocity requires that $\underline{Y_{21}} = \underline{Y_{12}}$ which sets $\underline{a} = -\underline{b}$. Since $\underline{a} = -\underline{b}$, Equations 1.4 and 1.5 show that $\underline{U_{OW}} = -\underline{U_{RW}}$.

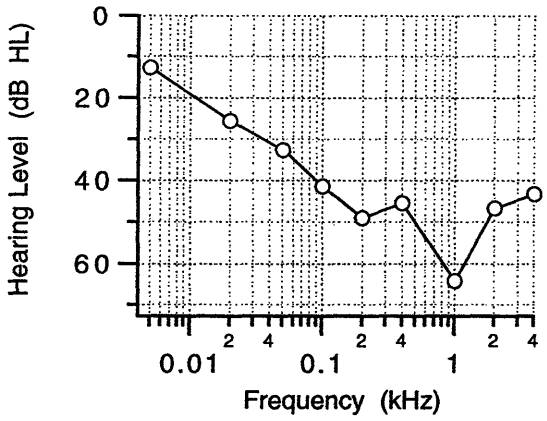

Figure 1-3: Result taken from Békésy (1936a; 1960, Fig. 5-10). Mean hearing thresholds from five cases with "unilateral loss of the eardrum, malleus, and incus" (Békésy, 1960). Hearing levels indicate hearing thresholds in dB relative to the mean hearing threshold on the normal side on which an "otological examination had shown that the inner ear was normal" (Békésy, 1960); a hearing level of 40 dB corresponds to a hearing loss of 40 dB. The results shown here suggest that hearing improves as frequency decreases for ears missing the tympanic membrane, malleus, and incus.

pressure difference between the oval and round window is zero. Békésy (1936a) reported average hearing levels from five patients with unilateral missing tympanic membranes and ossicles. He assumed that their cochleas were normal since the patients had normal hearing on the nonpathological side. Békésy concluded that the results shown in Fig. 1-3 appear to be inconsistent with Equation 1.1 through the following argument. At low frequencies the wavelength of sound is much greater than the distance between the oval and round windows (and the dimensions of the middle-ear cavity). Thus, at low frequencies the spatial variation in pressure between the oval and round windows is expected to be small and the pressure difference between the oval and round windows should decrease as frequency decreases. As a result the pressure-difference assumption expressed by Equation 1.1 predicts that hearing sensitivity in ears with no tympanic membrane, malleus, and incus should decrease as the frequency lowers. Instead Fig. 1-3 reports an improvement in hearing as frequency (and presumably pressure difference)

decreases.

Based on the results shown in Fig. 1-3 Békésy hypothesized that the cochlea may appear to be compressible due to fluid flow through the endolymphatic and perilymphatic ducts or compressibility of cochlear blood vessels. Shera and Zweig (1992) developed a model in which the scala media is assumed to be compressible; they conclude that such a model matches the Békésy result shown in Fig. 1-3.

Other evidence has some consistencies with the pressure-difference assumption expressed by Equation 1.1. Wever, Lawrence and Smith (1948) showed in cat that sound applied to the cochlea at the round window produces a cochlear-potential magnitude similar to that produced by the same sound applied to the oval window (the angle of the cochlear potential was not reported). Wever and Lawrence (1950) applied tonal stimuli to the oval and round windows simultaneously and measured the cochlear-potential response. (The oval-window stimulus was applied at the tympanic membrane through the ossicular chain while the round-window stimulus was applied through a tube coupled directly to the round-window membrane.) The stimuli were balanced such that each of them produced the same cochlear-potential magnitude when applied alone. Wever and Lawrence (1950, p. 462) described the response when the two stimuli were presented simultaneously and the angle between them was varied over one cycle: "the cochlear potentials vary in magnitude according to the phase relation between the sound waves entering by the two pathways. Under usual conditions a phase relation can always be found at which this response is just double what it would be for either pathway alone. This is a maximum value for these stimuli; the response falls off if the phase is altered in either direction from this setting. As the phase is further altered the response falls rapidly, and it approaches a value of zero as the phase is changed 180 degrees from the

maximum setting". Fig. 1-4 shows the only example of such a measurement that was published by Wever and Lawrence (1950).

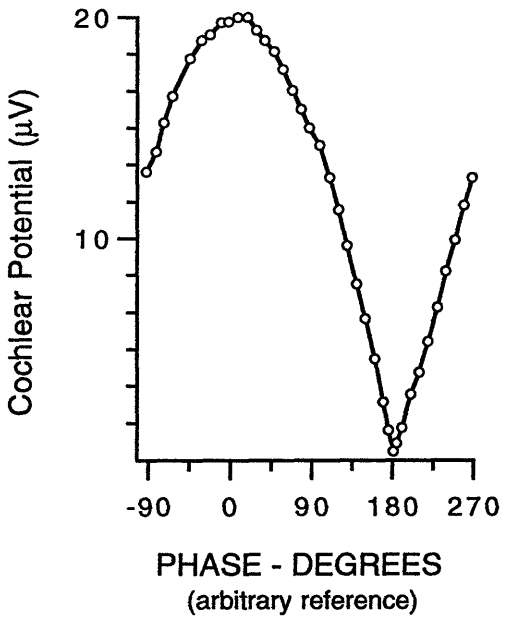

Figure 1-4: Result taken from Wever and Lawrence (1950). The cochlear-potential magnitude was measured as the oval and round windows were simultaneously stimulated. The phase of one of the stimuli was varied. This plot shows the cochlear-potential magnitude as a function of the phase of the varied stimulus. The value 0 degrees was arbitrarily chosen and does not mean that the two stimuli had a phase difference of 0 degrees at that point on the axis.

In another set of experiments, stimuli balanced as described above were delivered directly to the oval and round windows and the angle between the stimuli required for a minimal magnitude response, ψ_{MIN}, was plotted as a function of frequency. The result is shown in Fig. 1-5. At frequencies below 1000 Hz and above 4000 Hz the data in Fig. 1-5 are clearly inconsistent with Equation 1.1. Even though $|\underline{P_{OW}}|$ and $|\underline{P_{RW}}|$ are not known, Equation 1.1 requires the difference in angle between $\underline{P_{OW}}$ and $\underline{P_{RW}}$ to be zero when the cochlear-response magnitude is a minimum. The angle differences reported in Fig. 1-5 range from 0.03 to 0.09 cycles (11 to 34 degrees) for frequencies below 1000 Hz while at frequencies above 4000 Hz the angle differences range from 0 to 0.5 cycles (0 to

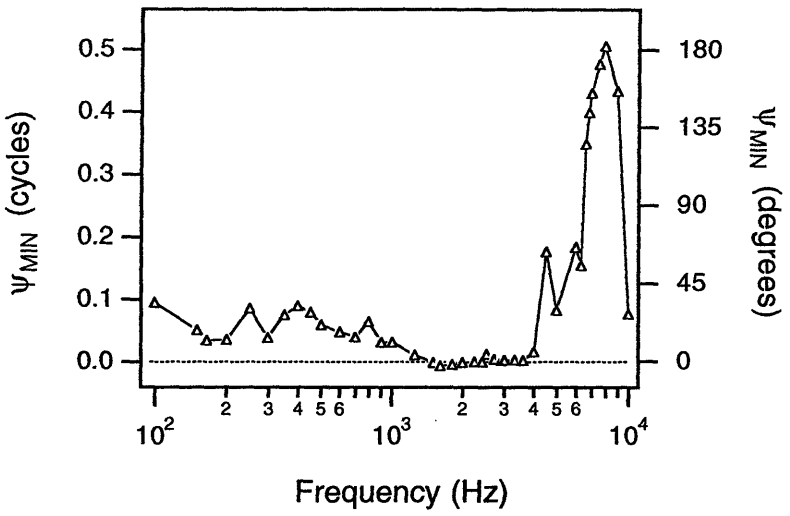

Figure 1-5: Result taken from Wever and Lawrence (1950). The oval and round windows were stimulated simultaneously and the phase relation between the stimuli was varied until a minimum cochlear-potential response was obtained. The phase difference between the oval and round-window stimuli required for this minimal cochlear-potential response, ψ_{MIN}, is plotted here as a function of frequency.

180 degrees). At frequencies between 1000 Hz and 4000 Hz the data shown in Fig. 1-5 are consistent with Equation 1.1 because the differences in angle between $\underline{P_{OW}}$ and $\underline{P_{RW}}$ are nearly zero. However, it is impossible to relate directly the data in either Fig. 1-4 or Fig. 1-5 to Equation 1.1 because $|\underline{P_{OW}}|$ and $|\underline{P_{RW}}|$ were not measured.

1.4 Common-mode and difference-mode responses

A general linear system description of the cochlear response includes a "common-mode" term. In the cochlea common-mode mechanisms might include effects of cochlear fluid or blood vessel compressibility and flow through cochlear ducts. However, compressibility of cochlear contents need not produce a common-mode response; a symmetrically compressible cochlea may have no common-mode response.

Common-mode mechanisms can be included in Equation 1.1 by adding a common-

mode term to the difference-mode term.

$$\underline{Cochlear\ Response} = \underbrace{\underline{D}(\underline{P_{OW}} - \underline{P_{RW}})}_{difference-mode\ response} + \underbrace{\frac{1}{2}\underline{C}(\underline{P_{OW}} + \underline{P_{RW}})}_{common-mode\ response} \tag{1.6}$$

The gain constants $\underline{D}$ and $\underline{C}$ are the difference-mode gain and the common-mode gain, respectively. Equation 1.6 reduces to Equation 1.1 when $\underline{C} = 0$.

The aim of this thesis is to determine the relative importance of the difference-mode and common-mode terms to the cochlear response. The cochlear response to direct simultaneous stimulation of the oval and round windows is examined in a manner similar to that of Wever and Lawrence (1950). The cochlear-potential response is measured in cat ears while the magnitudes and angles of the sound-pressure amplitudes at the oval and round windows are controlled; these cochlear-potential measurements are used to estimate the difference-mode gain $\underline{D}$ and the common-mode gain $\underline{C}$. Comparison of $\underline{D}$ and $\underline{C}$ determines the importance of the pressure difference at the two windows relative to the summation of pressure at the two windows. $\underline{D}$ and $\underline{C}$ are compared using the common-mode rejection ratio (CMRR).

$$CMRR = 20log_{10}|\frac{\underline{D}}{\underline{C}}| \tag{1.7}$$

Chapter 2

Experimental methods

2.1 Subjects

Measurements were made on seven cat ears. The first three ears were used to develop the experimental methodology; the pressure measurements in these animals were not stable to within less than a few dB over long periods of time. Appendix A contains a description of the measurements on each cat.

2.2 Stimulus paradigms

Two types of stimuli were used: "single-sided" and "simultaneous". The single-sided level series are measurements of the cochlear potential, V_{CP}, made while either the oval or round window was stimulated with a tone of increasing sound-pressure level. The simultaneous-stimuli measurements refer to cochlear-potential measurements made while the oval and round windows were stimulated simultaneously; sound pressures of nearly equal magnitude (generally within 0.1 dB) were presented to the oval and round windows (P_{OW} and P_{RW}) while the angle of one of the pressures was varied over one

cycle. $\underline{V_{CP}}$ was measured as a function of ψ, the phase difference between the sound pressures at the two windows. A measurement "set" refers to the set of data points collected as ψ varied from 0 to 1 cycle.

2.3 Experimental configuration

Fig.2-1 shows a schematic of the experimental set-up. The tympanic membrane, malleus, and incus were surgically removed from a Dial and sodium pentobarbital anesthetized cat. A petroleum-jelly soaked piece of cotton was inserted into the foramen of the septum so that the tympanic and bulla air spaces were isolated from each other. A calibrated probe-tube microphone and sound-source assembly positioned in the ear canal both delivered and measured the sound pressure in the space around the oval window, $\underline{P_{OW}}$. A similar assembly positioned over a hole made in the bulla wall delivered and measured the sound pressure in the space around the round window, $\underline{P_{RW}}$. The sound sources were "Beyer dynamic " earphones and the microphones were "Larson Davis 2530" quarter inch condenser microphones.

2.4 Probe-tube microphone calibration

The experimental measurements required two calibrated microphones. OW_{mic} refers to the probe-tube microphone which measured the sound pressure in the tympanic cavity and RW_{mic} refers to the probe-tube microphone which measured the sound pressure in the bulla cavity. OW_{mic} and RW_{mic} were calibrated separately using a coupler and reference microphone, REF_{mic}.

A calibration source (Larson Davis) of 114 dB SPL at 250 Hz was coupled to REF_{mic}

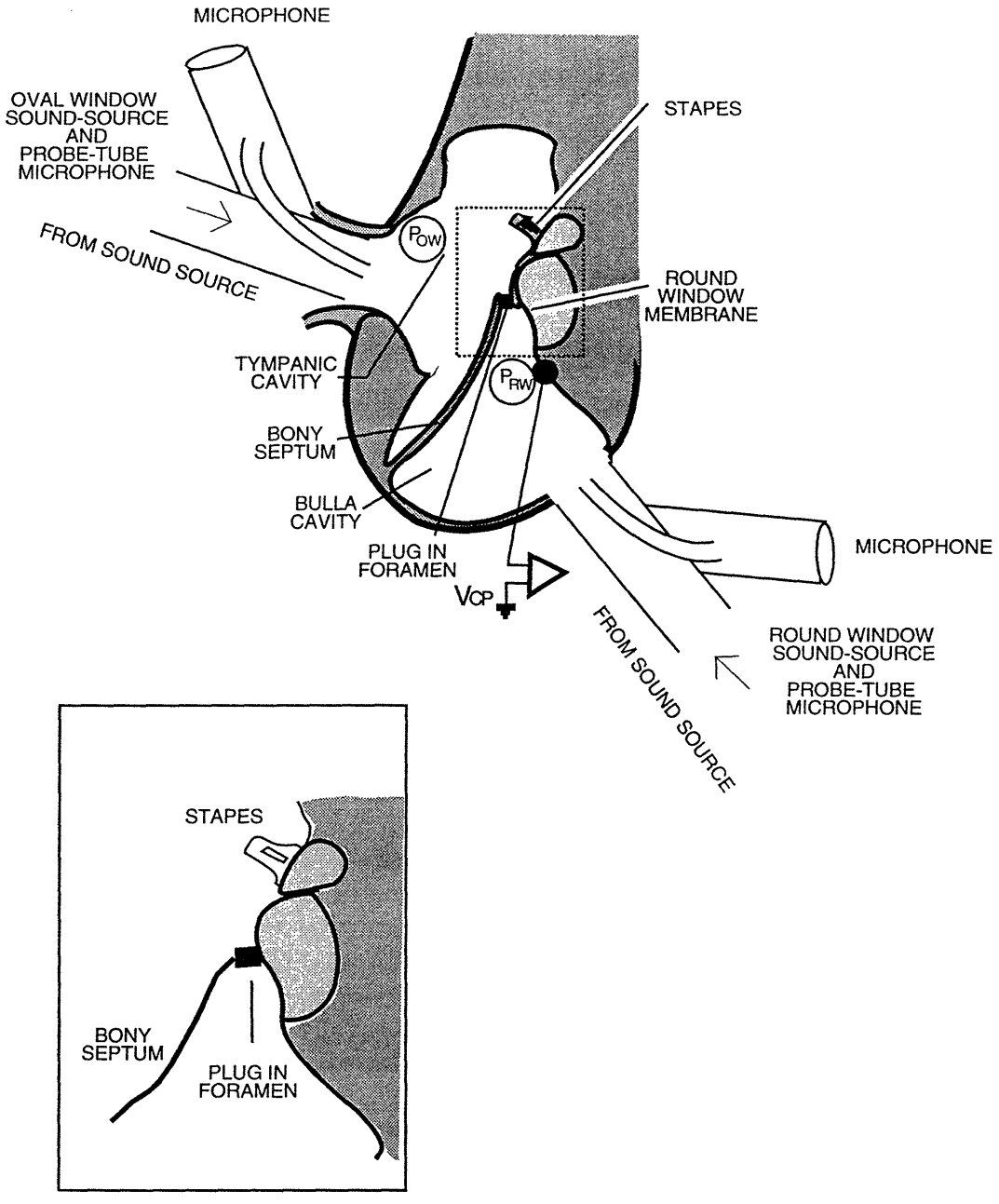

Figure 2-1: A schematic of the experimental set-up of the cat middle-ear. The inset is a blowup of the petroleum-jelly soaked cotton plug in the foramen of the septum.

to determine the relationship between sound-pressure level and the voltage output of REF_{mic}. This measurement combined with a measurement of the frequency response of REF_{mic} provided the transfer function between sound-pressure level, SPL, and the reference microphone voltage, $V_{REF_{mic}}$: $\frac{SPL}{V_{REF_{mic}}}$.

One at a time, each probe-tube microphone and sound-source assembly was coupled to REF_{mic} for the calibration procedure (Fig. 2-2). To calibrate the oval-window probe microphone, the transfer function between the voltage measured by the reference microphone, $V_{REF_{mic}}$ and the voltage into the earphone generated by channel A of the digital-to-analog converter, $V_{DAC_{OW}}$, was measured: $\frac{V_{REF_{mic}}}{V_{DAC_{OW}}}$. Next the transfer function between the voltage measured by the oval-window probe-tube microphone, $V_{OW_{mic}}$, and $V_{DAC_{OW}}$ was measured: $\frac{V_{OW_{MIC}}}{V_{DAC_{OW}}}$. These transfer functions yield the relation between sound-pressure level and the voltage of the oval-window microphone.

$$\left[\frac{SPL}{V_{REF_{mic}}}\right]\left[\frac{V_{REF_{mic}}}{V_{DAC_{OW}}}\right]\left[\frac{V_{DAC_{OW}}}{V_{OW_{mic}}}\right] = \frac{SPL}{V_{OW_{mic}}} \tag{2.1}$$

The transfer function between $\frac{SPL}{V_{RW_{mic}}}$ was found in the same manner. The round-window earphone was driven by channel B of the digital-to-analog converter $V_{DAC_{RW}}$.

The two microphones, OW_{mic} and RW_{mic}, should measure the same sound-pressure level because they were calibrated with a common reference microphone. The relative calibration between the oval and round window microphones was checked periodically during the experiments on Cats #5, #6, and #7. After each calibration a short brass tube was used to couple the two probe-tube microphone and sound-source assemblies together; the two probe-tube tips were less than 2 mm apart. A sound common to both microphones was produced and it was confirmed that the calibrations of the two

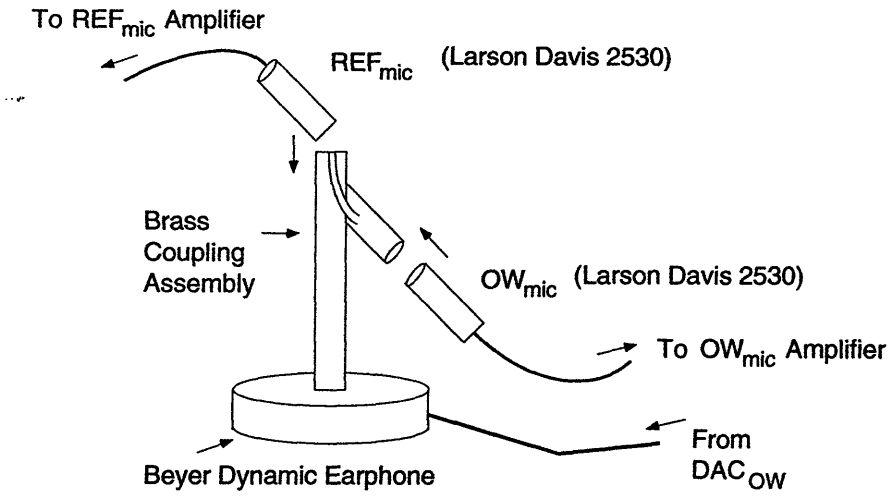

Figure 2-2: The Beyer dynamic earphone is coupled to both REF_{mic} and OW_{mic} for the calibration procedure of the oval-window probe-microphone and sound-source assembly. Experimental measurements were made with the same assembly, without REF_{mic}. The part of the assembly to which REF_{mic} coupled here is where the assembly was attached to the cat. A similar assembly is used to couple REF_{mic} and RW_{mic} for the calibration procedure of the round-window probe-microphone and sound-source assembly.

microphones were consistent. The results of this procedure are further discussed in Chapter 4.

2.5 Animal preparation

Cats weighing between 1.7 and 2.2 kg were anesthetized with Dial (between 1.25 cc and 1.65 cc) and sodium pentobarbital (between 0.83 cc and 1 cc); the doses depended on the weight of the animal. Boosters of Dial (10% of the original dose) were given throughout the experiments, as determined by a toe-pinch response or 20% increase in heart rate. Most cats received 0.1 cc penicillin to fight infections.

Removal of the ossicles required several steps. First, as much as possible of the cartilaginous ear canal was surgically removed in order to increase visibility of the middle-

ear air space. Next, an approximately circular hole with a diameter of about 5 mm was made in the dorsal-lateral-posterior part of the widely exposed bulla in order to provide visibility of both the round window and the foramen of the bony septum; this hole was later used to couple the round-window probe-tube microphone and sound-source assembly to the bulla cavity. Two methods were used to remove the ossicles; both required a dissecting microscope.

The ossicles of Cats #1, #2, #3, and #4 were removed as follows.

1. The tympanic membrane was removed with a set of small forceps.
2. The manubrium was held with the forceps and gently wiggled until the lateral process and sometimes other parts of the malleus came loose; the pieces were removed. This made the incudo-stapedial joint partially visible.
3. The incudo-stapedial joint was disarticulated with the use of a "Schuknecht hook" (Storz Instrument Co.), and the incus was either removed or left loose in the tympanic space.
4. The foramen was plugged with petroleum-jelly soaked cotton by placing the cotton in the foramen with an approach through the ear canal and tympanic cavity. This approach was difficult due to poor visibility of the foramen through the earcanal.

A different approach was used to remove the ossicles from Cats #5, #6, and #7.

1. The tympanic cavity was visualized through the 5 mm diameter hole in the bulla wall and the foramen. Either part of Spence's cartilage or the chorda tympani branch of the facial nerve was immediately in sight through the foramen. This disrupted the view of the incudo-stapedial joint. Any such "soft tissue" obstructions were moved out of the way by breaking them with the Schuknecht hook.
2. The Schuknecht hook was introduced into the tympanic cavity through the bulla cavity and the foramen; the incudo-stapedial joint was disarticulated. The visibility during this procedure varied among cats.
3. The tympanic membrane and other ossicles were removed through the ear canal.
4. The stapes and incus disarticulation was visually confirmed, by looking through the ear canal.
5. The foramen was plugged with petroleum-jelly soaked cotton through the bulla cavity approach.

After the ossicles were removed, the round-window wire-electrode tip was positioned near (Cats #1 to #4) or on (Cats #5 to #7) the round-window membrane. The electrode was advanced through a small hole in the bulla cavity with a micro-manipulator; the process was visualized through the larger $5mm$ diameter bulla wall hole with a dissecting microscope. The wire electrode was glued to the bulla wall to minimize movement and seal the hole.

2.6 Computer measurements of sound pressure and cochlear potential

The digital-to-analog converter on a computer generated a two second stimulus tone(s). The two second amplified microphone-output(s) and cochlear-potential voltage responses were measured using the computer's analog-to-digital converter that sampled each response on a different channel at 12 kHz. Each channel of the analog-to-digital converter output was divided into 50 segments, and each segment was an integer number of periods in duration. The segments were averaged and the magnitude and angle of the fundamental component of the average is reported as the cochlear-potential response. The averaged microphone voltages were converted into sound-pressure levels using the previously measured microphone calibrations.

2.7 Cochlear potentials and TTX

The AC cochlear potential is composed of two dominant components: cochlear microphonic (CM) and compound action potential (CAP). CM refers to the response of the cochlear sensory hair cells and is believed to increase linearly with sound-pressure level

over a large stimulus range (Pickles, 1988). The nonlinear CAP is generated by the auditory nerve fibers.

The cochlear-potential response is represented as a linear-system response to the two inputs $\underline{P_{OW}}$ and $\underline{P_{RW}}$ (Chapter 3). This model is not consistent with the nonlinear CAP component in the cochlear response. Tetrodotoxin (TTX) was used to eliminate the CAP in Cats #6 and #7. TTX pharmacologically blocks action potentials generated by voltage-gated sodium channels; others have used TTX to block the compound action potential of the auditory nerve (Kaplan et al. , 1983; Dolan et al. , 1989). Here 1 mg of TTX (Sigma Chem. Co.) was mixed with 1 ml of artificial perilymph; a 3.13 mM solution resulted. Eight μl of this solution was dropped on the round-window membrane from where it diffused through the round window-membrane into the cochlea over a time course of a few hours. The cochlear-potential response to clicks and tone bursts was measured pre and post TTX administration to confirm that the CAP response was eliminated; these results are included in Appendix A.

2.8 Definition of noisefloor

Noisefloors are defined as follows for measurements on Cats #5, #6, and #7: M cochlear-potential measurements were made with no stimulus. The noisefloor is defined as the mean of these M magnitude measurements plus two standard deviations (all in dB). In most cases (but not all) $M = 11$. Such noisefloor measurements were not made during the experiments on Cats #1, #2, #3, and #4. However, several measurements of $\underline{V_{CP}}$ in response to a 1000 Hz stimulus were made. The mean plus two standard deviations of the appropriate frequency component of these measurements ($M > 11$) were used as estimates of the noisefloor. For these four animals, the noisefloor at 1000 Hz is defined to

be the same as the noisefloor at 800 Hz. Tables of noisefloor measurements are included in Appendix A.

2.9 Independent control of oval and round window sound pressures

The bony septum that divides the cat middle-ear air space provides some natural acoustic isolation between the oval and round windows. The petroleum-jelly soaked cotton plug that was inserted into the foramen of the septum further isolated the sounds at the two windows. A measurement of the acoustic "crosstalk" between $\underline{P_{OW}}$ and $\underline{P_{RW}}$ from Cat #7 is shown in Fig. 2-3, and measurements from the other cats are included in Appendix A. Such measurements of sound isolation with the plug in place demonstrated that the isolation was generally greater than 40 dB between 75 Hz and 1000 Hz. This amount of isolation allows for control of $\underline{P_{OW}}$ and $\underline{P_{RW}}$ through the separate sound sources. Note that, since $\underline{P_{OW}}$ and $\underline{P_{RW}}$ are always measured, acoustic "crosstalk" between the oval and round window sound-pressure sources is accounted for in the analysis.

2.10 Frequency range

Measurements were made at frequencies between 75 and 1000 Hz. This low frequency range was chosen because low frequency results from both Békésy and Wever and Lawrence (Chapter 1) contradict the pressure-difference assumption (Equation 1.1). It was not possible to make measurements at frequencies below 75 Hz because the sound sources did not generate enough pressure to produce measurable cochlear potentials at these frequencies. The measurements were limited to low frequencies ($<$ 1000 Hz) so

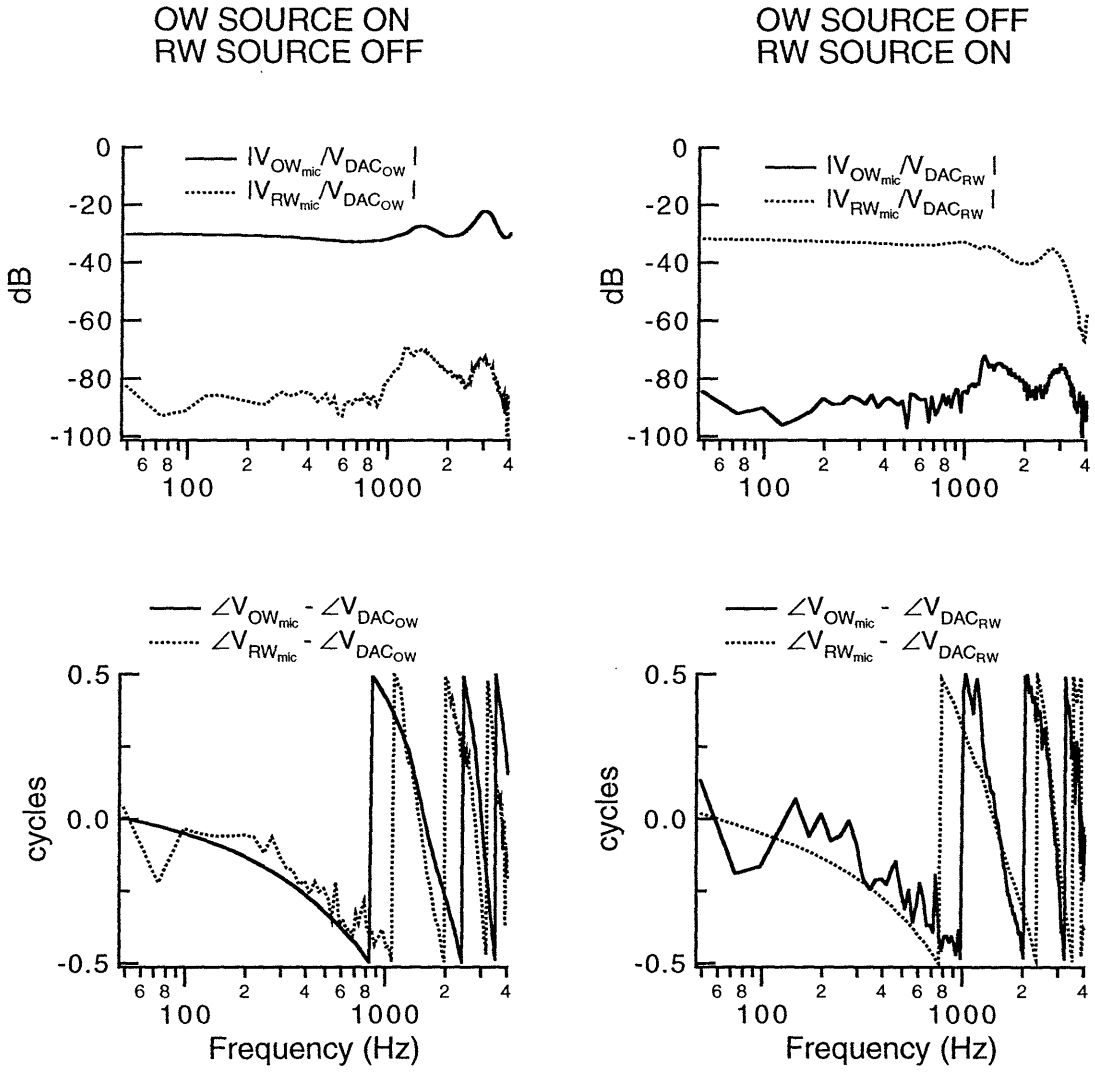

Figure 2-3: Measurements of acoustic crosstalk between the tympanic and bulla cavities from Cat #7. LEFT: Measurement of the transfer function between the oval-window microphone response $V_{OW_{mic}}$ and the oval-window sound-source input $V_{DAC_{OW}}$, and measurement of the transfer function between the round-window microphone response $V_{RW_{mic}}$ and the oval-window sound-source input $V_{DAC_{OW}}$. The round-window sound-source was off. RIGHT: Measurement of the transfer function between the oval-window microphone response $V_{OW_{mic}}$ and the round-window sound-source input $V_{DAC_{RW}}$, and measurement of the transfer function between the round-window microphone response $V_{RW_{mic}}$ and the round-window sound-source input $V_{DAC_{RW}}$. The oval-window sound-source was off.

that it is reasonable to assume that the pressure at each probe-tube-microphone input is the same as the pressure at the respective cochlear window a few millimeters away. At these frequencies the wavelengths are much greater than the distance between the probe-tube and the window; the shortest wavelengths are more than 30X the largest cavity dimensions. The validity of this assumption was tested (Chapter 4.2).

Chapter 3

Methods of estimating common and difference-mode gains, C and D

The cochlear potential measured at the round window, $\underline{V_{CP}}$, is modeled as a linear function of the sound pressures at the oval and round windows, $\underline{P_{OW}}$ and $\underline{P_{RW}}$. A linear system representation is shown in Fig. 3-1.

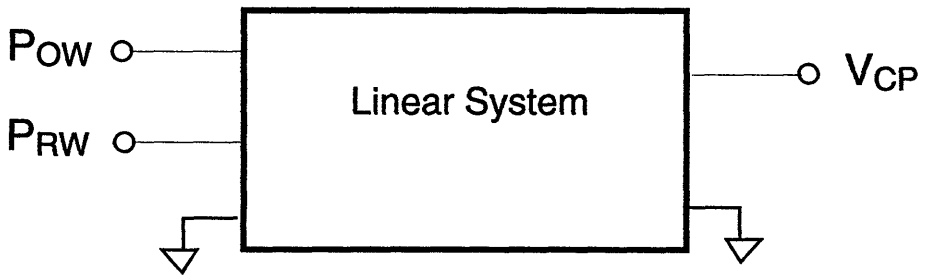

Figure 3-1: A general linear system representation of the cochlear response V_{CP} to the pressures P_{OW} and P_{RW}. The system input is describe by acoustic variables, and the system output is described by electric variables.

Since $\underline{P_{OW}}$ and $\underline{P_{RW}}$ are two independent inputs, the response $\underline{V_{CP}}$ must also be described by two independent terms, as in Equation 1.6:

$$\underline{V_{CP}} = \underbrace{\underline{D}(\underline{P_{OW}} - \underline{P_{RW}})}_{difference-mode\ response} + \underbrace{\frac{1}{2}\underline{C}(\underline{P_{OW}} + \underline{P_{RW}})}_{common-mode\ response} . \tag{3.1}$$

The two independent terms of this equation include a "difference-mode" term, the product of the difference-mode gain $\underline{D}$ and the difference-mode input $(\underline{P_{OW}} - \underline{P_{RW}})$, and a "common-mode" term, the product of the common-mode gain $\underline{C}$ and the common-mode input $\frac{1}{2}(\underline{P_{OW}} + \underline{P_{RW}})$.

The simultaneous-stimuli measurements of $\underline{V_{CP}}$, $\underline{P_{OW}}$, and $\underline{P_{RW}}$ (Chapter 2) are used to estimate the difference and common-mode gains, $\underline{\hat{D}}$ and $\underline{\hat{C}}$, using two separate fitting procedures of Equation 3.1 to the measured data (Chapter 3.1 and Chapter 3.2). All data points such that $|\underline{V_{CP}}| > Noisefloor$ are weighted equally in the fitting procedures; data points below the noisefloor are not used.

A model prediction for each data point, $\underline{\hat{V}_{CP}}$, is calculated from the estimates $\underline{\hat{D}}$ and $\underline{\hat{C}}$ and the measured $\underline{P_{OW}}$ and $\underline{P_{RW}}$ for each measurement set.

$$\underline{\hat{V}_{CP}} = \underline{\hat{D}}(\underline{P_{OW}} - \underline{P_{RW}}) + \frac{1}{2}\underline{\hat{C}}(\underline{P_{OW}} + \underline{P_{RW}}) \tag{3.2}$$

The relative sizes of $|\underline{\hat{D}}|$ and $|\underline{\hat{C}}|$ are described by the common-mode rejection-ratio (CMRR).

$$\hat{CMRR} = 20log_{10}|\frac{\hat{D}}{\hat{C}}| \tag{3.3}$$

Correlation coefficients that describe the fit of $\underline{\hat{V}_{CP}}$ to the measured $\underline{V_{CP}}$ are calculated for each measurement set (Chapter 3.3). Experimental and model parameters are

Experimental and Model Parameters	
Symbol	Description
$\underline{P_{OW}}$	Complex pressure at the oval window (N/m^2)
$\underline{P_{RW}}$	Complex pressure at the round window (N/m^2)
$\underline{V_{CP}}$	Complex voltage at the round window (cochlear potential)
$\underline{P_{DIFF}} = \underline{P_{OW}} - \underline{P_{RW}}$	Difference-mode pressure
$\underline{P_{SUM}} = \frac{1}{2}(\underline{P_{OW}} + \underline{P_{RW}})$	Common-mode pressure
$\underline{\hat{V}_{CP}}$	Model prediction of cochlear potential
$\underline{\hat{D}}$	Estimate of the difference-mode gain ($Volts\ \frac{m^2}{N}$)
$\underline{\hat{C}}$	Estimate of the common-mode gain ($Volts\ \frac{m^2}{N}$)
$\underline{\hat{CMRR}}$	Estimate of the common-mode rejection ratio

Table 3.1: Experimental and model parameters.

summarized in Table 3.1.

3.1 Linear fit to the data

A linear-least-squares fit of Equation 3.1 is made to the data points of each measurement set in the following manner. The notation in Equation 3.1 is simplified to express the model as

$$\underline{V_{CP}} = \underline{D}\,\underline{P_{DIFF}} + \underline{C}\,\underline{P_{SUM}} \tag{3.4}$$

where $\underline{P_{DIFF}} = \underline{P_{OW}} - \underline{P_{RW}}$ and $\underline{P_{SUM}} = \frac{1}{2}(\underline{P_{OW}} + \underline{P_{RW}})$. Equation 3.4 can be expressed as

$$\underline{V_{CP_i}} = \underline{D}\,\underline{P_{DIFF_i}} + \underline{C}\,\underline{P_{SUM_i}} \tag{3.5}$$

where the subscript i refers to a specific data point. Each measurement set consists of a series of N such data points and can be expressed in matrix format as

$$\boldsymbol{V_{CP}} = \boldsymbol{P} \cdot \boldsymbol{\beta} \tag{3.6}$$

where

$$\boldsymbol{V_{CP}} = \begin{pmatrix} \underline{V_{CP_1}} \\ \underline{V_{CP_2}} \\ \vdots \\ \underline{V_{CP_N}} \end{pmatrix} \tag{3.7}$$

$$\boldsymbol{P} = \begin{pmatrix} \underline{P_{DIFF_1}} & \underline{P_{SUM_1}} \\ \underline{P_{DIFF_2}} & \underline{P_{SUM_2}} \\ \vdots & \\ \underline{P_{DIFF_N}} & \underline{P_{SUM_N}} \end{pmatrix} \tag{3.8}$$

$$\boldsymbol{\beta} = \begin{pmatrix} \underline{D} \\ \underline{C} \end{pmatrix}. \tag{3.9}$$

The estimate of β, $\hat{\beta}$, that minimizes the expression

$$\chi^2 = \sum_{i=1}^{N} \left| (\underline{\hat{D}}\, \underline{P_{DIFF_i}} + \underline{\hat{C}}\, \underline{P_{SUM_i}}) - \underline{V_{CP_i}} \right|^2 = |\boldsymbol{P} \cdot \hat{\beta} - \boldsymbol{V_{CP}}|^2 \tag{3.10}$$

is found using singular value decomposition (SVD) techniques to solve Equation 3.6 for β (Press et al. , 1992). This method is used to eliminate undesirable effects of singular or nearly singular matrices. The $NX2$ matrix $\boldsymbol{P}$ defined by Equation 3.8 can be expressed in terms of the product of three new matrices:

$$\boldsymbol{P} = \boldsymbol{U} \cdot \boldsymbol{W} \cdot \boldsymbol{V}^T \tag{3.11}$$

where $\boldsymbol{U}$ is an $NX2$ orthogonal matrix ($\boldsymbol{U}^T \cdot \boldsymbol{U} = 1$), $\boldsymbol{W}$ is a $2X2$ diagonal matrix, and $\boldsymbol{V}$ is a $2X2$ orthogonal matrix ($\boldsymbol{V}^T \cdot \boldsymbol{V} = 1$). The $\hat{\beta}$ that minimizes χ^2 from Equation 3.10 can be expressed as

$$\hat{\beta} = \begin{pmatrix} \underline{\hat{D}} \\ \underline{\hat{C}} \end{pmatrix} = \boldsymbol{P}^{-1} \boldsymbol{V_{CP}} = \boldsymbol{V} \cdot [\boldsymbol{diag}(\tfrac{1}{w_j})] \cdot \boldsymbol{U}^T \cdot \boldsymbol{V_{CP}} \tag{3.12}$$

where $[\boldsymbol{diag}(\frac{1}{w_j})]$ refers to the diagonal matrix comprised of the reciprocal of each element of the diagonal matrix $\boldsymbol{W}$ defined by Equation 3.11. The solution of Equation 3.12 can be equivalently written as

$$\hat{\beta} = \begin{pmatrix} \hat{\underline{D}} \\ \hat{\underline{C}} \end{pmatrix} = \sum_{i=1}^{2} (\frac{U_{(i)} \cdot V_{CP}}{w_i}) V_{(i)} \tag{3.13}$$

where the subscript (i) refers to the vector which comprises the i^{th} column of $\boldsymbol{U}$ and $\boldsymbol{V}$ and w_i refers to the diagonal element $\boldsymbol{W}(i,i)$ (Press et al. , 1992).

3.2 Logarithmic fit to the data

All data points are equally weighted in the linear-least-squares fit described above (Chapter 3.1). However, the measurements of $\underline{V_{CP}}$ made while the oval and round windows were simultaneously stimulated with variations in the relative phases of the stimuli have a dynamic range of about 40 dB; equal weighting of data points puts an emphasis on the regions where $|\underline{V_{CP}}|$ is largest. To increase sensitivity to the points where $|\underline{V_{CP}}|$ is small, estimates of $\underline{D}$ and $\underline{C}$ are found with a least-squares fit to

$$log(\underline{V_{CP}}) = log(\underline{D}\underline{P_{DIFF}} + \underline{C}\underline{P_{SUM}}), \tag{3.14}$$

which requires the minimization of

$$\chi^2 = \sum_{i=1}^{N} \left| log(\hat{\underline{D}}\,\underline{P_{DIFF_i}} + \hat{\underline{C}}\,\underline{P_{SUM_i}}) - log(\underline{V_{CP_i}}) \right|^2 . \tag{3.15}$$

Since Equation 3.15 is nonlinear it is not possible to use the method of Chapter 3.1. Instead, a four dimensional space is searched to find values of $|\underline{D}|$, $\angle\underline{D}$, $|\underline{C}|$, and $\angle\underline{C}$ that minimize χ^2.

The search procedure employs the "fmins" function in Matlab (Macintosh version 4.1, The Mathworks, Inc.) to find a local minimizer of Equation 3.15. The "fmins" function

uses a "simplex" method (Nash, 1979; Press et al. , 1992) to search the four dimensional space. In this case the "simplex" is a four dimensional geometric shape which must contain the desired values of $|\underline{D}|$, $\angle\underline{D}$, $|\underline{C}|$, and $\angle\underline{C}$. The values of $|\underline{D}|$, $\angle\underline{D}$, $|\underline{C}|$, and $\angle\underline{C}$ that were found using the least-squares fit of Equation 3.4 are used as an initial guess to center the simplex. The four dimensional simplex is defined by five vertices which are determined using the nonzero initial guess; each element of each vertex is between 0.9 and 1.1 times the initial guess. Next, Equation 3.15 is evaluated at each vertex of the simplex. The vertex that produces the largest value when Equation 3.15 is evaluated is replaced; it is reflected about the centroid of the other three vertices and through steps of reflection, expansion, reduction, and contraction (Nash, 1979) the vertex with a maximum function value (Equation 3.15) is replaced. This process is repeated until the simplex has shrunk to a size such that the evaluation of Equation 3.15 at all vertices differs by less than 0.0001. The estimates of $|\underline{D}|$, $\angle\underline{D}$, $|\underline{C}|$, and $\angle\underline{C}$ at this local minimum of Equation 3.15 are used as the "logarithmic" model fit.

3.3 Correlation coefficients

Two correlation coefficients are computed for each measurement set; ρ_{MAG} describes the model fit $|\underline{\hat{V}_{CP}}|$ to $|\underline{V_{CP}}|$, and $\rho_{\angle}$ describes the model fit $\angle\underline{\hat{V}_{CP}}$ to $\angle\underline{V_{CP}}$. The difference between the variance of the measured magnitude and angle data,

$$\sigma^2_{MAG} = \frac{1}{N-1}\sum_{i=1}^{N}[|log(\underline{\bar{V}_{CP}})| - |log(\underline{V_{CP_i}})|]^2 \tag{3.16}$$

$$\sigma^2_{\angle} = \frac{1}{N-1}\sum_{i=1}^{N}[\angle\underline{\bar{V}_{CP}} - \angle\underline{V_{CP_i}}]^2, \tag{3.17}$$

and the variance of the mean squared error between the data and model prediction,

$$\sigma^2_{MAG-ERROR} = \frac{1}{N-2}\sum_{i=1}^{N}[|log(\underline{V_{CP_i}})| - |log(\underline{\hat{V}_{CP_i}})|]^2 \tag{3.18}$$

$$\sigma^2_{\angle-ERROR} = \frac{1}{N-2}\sum_{i=1}^{N}[\angle\underline{V_{CP}} - \angle\underline{\hat{V}_{CP_i}}]^2, \tag{3.19}$$

is used to calculate the correlation coefficients

$$\rho_{MAG} = \sqrt{\frac{\sigma^2_{MAG} - \sigma^2_{MAG-ERROR}}{\sigma^2_{MAG}}} \tag{3.20}$$

and

$$\rho_{\angle} = \sqrt{\frac{\sigma^2_{\angle} - \sigma^2_{\angle-ERROR}}{\sigma^2_{\angle}}}. \tag{3.21}$$

In order to compare the two model fits, linear (Chapter 3.1) and logarithmic (Chapter 3.2), the correlation coefficients for both models are based on Equation 3.14; additionally all data and model fits are plotted on logarithmic scales. $|\underline{\bar{V}_{CP}}|$ and $\angle\underline{\bar{V}_{CP}}$ refer to the mean value of the measurement set and N is the total number of data points in the measurement set. $|\underline{\hat{V}_{CP_i}}|$ and $\angle\underline{\hat{V}_{CP_i}}$ refer to the model prediction at the i^{th} data point.

Chapter 4

Pressure measurement errors

Categories of potential errors in the measurements of $\underline{P_{OW}}$ and $\underline{P_{RW}}$ include: errors in the calibration of the microphone systems and pressure variations within the tympanic and bulla cavities, which make the measured pressures differ from the pressures at the oval and round windows. This chapter discusses these errors and estimates their sizes.

4.1 Calibration errors

4.1.1 Stability of absolute and relative calibrations

The exact calibration of each microphone is not critical for the experiments presented in this thesis. However, the relative calibrations of the two microphones used to measure $\underline{P_{OW}}$ and $\underline{P_{RW}}$ must be determined precisely. For example, if a common tone is presented identically to both microphones it is critical that the calibrated sound-pressure response be the same in magnitude and angle for both microphones.

Changes in temperature and humidity may affect each absolute microphone calibration. However, such changes are likely to be correlated between the two microphones

and probably do not introduce significant errors.

The calibration procedure (discussed in Chapter 2.4) determines the ratio between the sound pressure at the microphone input and the voltage generated at the microphone output, $\frac{P_{mic}}{V_{mic}}$. The calibration procedure was repeated several times during the experiments on Cats #4, #5 , #6, and #7 and the changes in $\frac{P_{mic}}{V_{mic}}$ as a function of time are used as one measure of error that exists in the measurements of $\underline{P_{OW}}$ and $\underline{P_{RW}}$. The changes in $\frac{P_{mic}}{V_{mic}}$ for all the cats are included in Appendix A. The largest variations in $\frac{P_{mic}}{V_{mic}}$ for Cats #4 to #7 occurred in Cat #7; these variations are presented here as an example.

Changes in the magnitude and angle of $\frac{P_{mic}(initial\ calibration)}{V_{mic}(initial\ calibration)}$ as a function of time are shown in Fig. 4-1 for the measurements made on Cat #7. The maximum change in calibration during the experiments is used as a "worst-case" estimate of the error that exists in any given calibration. This estimate is plotted as a function of frequency in Fig. 4-2. The error estimates are not constant with frequency and they are not the same for the four cats. The oval-window microphone was consistently more variable than the round-window microphone. The maximum change in calibration during the experiment on Cat #7 was nearly 0.8 dB in magnitude at 100 Hz and nearly 0.015 *cycles* in angle at 1000 Hz. The maximum calibration changes seen in Fig. 4-1 probably over-estimate errors in $\underline{P_{OW}}$ and $\underline{P_{RW}}$.

The relative calibration between the oval and round window microphones was further checked periodically during the experiments on Cats #5, #6, and #7. After each calibration a short brass tube was used to couple the two probe-tube microphone and sound-source assemblies together; the two probe-tube microphone tips were less than 2 mm apart so the inputs to the microphones would be identical. When the calibrated

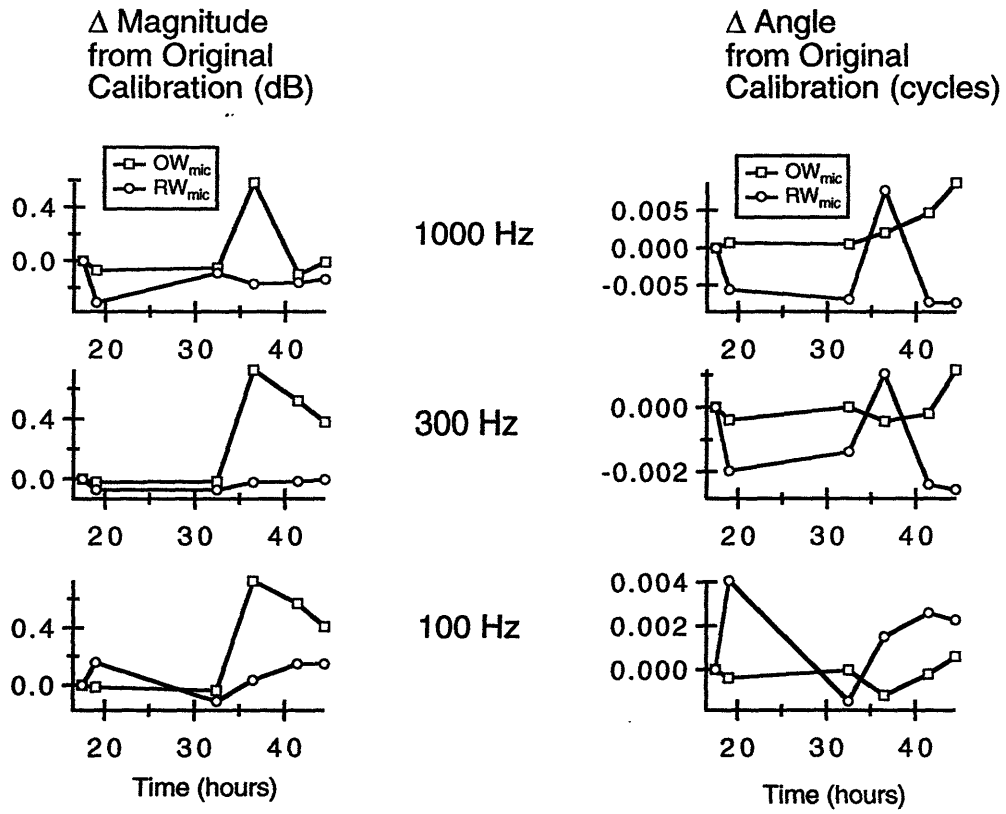

Figure 4-1: The differences in $\frac{P_{mic}}{V_{mic}}$ between the initial calibration and subsequent calibrations during the experiment on Cat #7. Note expanded vertical scales. The first measurement of $\frac{P_{mic}}{V_{mic}}$ is used to normalize all succeeding measurements of $\frac{P_{mic}}{V_{mic}}$; magnitudes (in dB) and angles (in cycles) of the ratios are plotted. Time of day = 17 hours is the time of initial calibration.

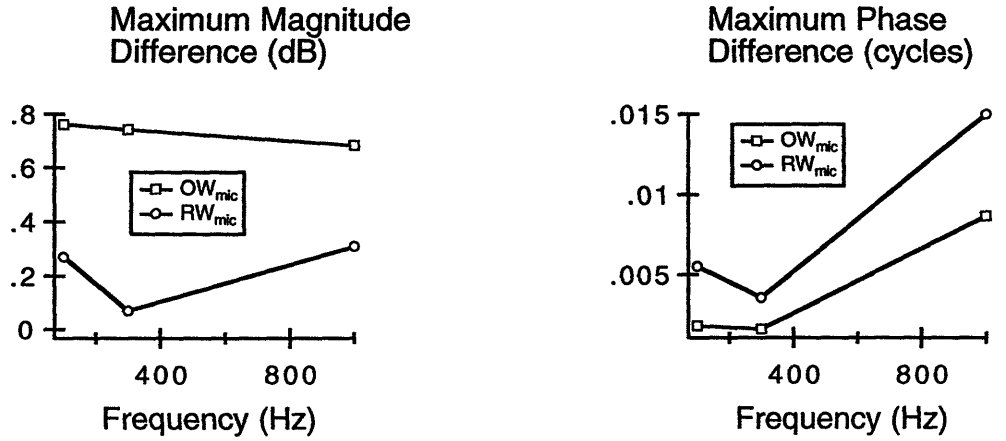

Figure 4-2: The maximum changes in $\frac{P_{mic}}{V_{mic}}$ as a function of frequency during the experiment on Cat #7.

microphone outputs differed by more than 0.1 dB in magnitude or 0.002 *cycles* in phase the microphones were re-calibrated and any measurements that relied on the faulty calibration were discarded.

4.1.2 Movement of acoustic assembly

Additional measurements were made in a brass tube to understand better the microphone variations that occur over time and that occur as a result of coupling and decoupling to and from the cat head. In the tube, as in the cat head, the response of each microphone contains two sources of variability: variation in the microphone response and variation in the sound-source output. The variability in the two microphone responses was quantified by making repeated measurements in the brass tube assembly. Changes in the source output should cause correlated changes in the output of both microphones. Changes in microphone sensitivity could also be correlated if they result from changes in temperature or absolute pressure.

50 consecutive measurements were made with a 1000 Hz tone stimulus while the two sound-source and microphone assemblies were coupled together; the time between the first and 50^{th} measurement was about 5 minutes. The sound pressure measured by the two microphones and the differences between the two microphone measurements are shown in Fig. 4-3A and C, respectively. Fig. 4-3A illustrates that the outputs of both microphones changed with time by about 0.15 dB in magnitude and 0.003 *cycles* in angle. The difference between the microphone outputs changed less with time; the variation was only 0.04 dB in magnitude and 0.0003 *cycles* in phase (Fig. 4-3C). These data can be interpreted to show that small changes occur in both sound-source output and microphone sensitivity over time, and the larger change is apparently in sound-source

output.

Next, 50 consecutive measurements were made in which the two sound-source and microphone assemblies were uncoupled from and then recoupled to the brass tube between each measurement; the time between the first and 50^{th} measurement was about 10 minutes. Such a procedure mimics the uncoupling and recoupling of the sound-source and microphone assemblies to the cat. The sound pressure measured by the two microphones and the differences between the two microphone measurements for this case are shown in Fig. 4-3B and C. The uncoupling-recoupling results (Fig. 4-3B) show changes in microphone output that have a range of about 0.3 dB in magnitude and 0.005 *cycles* in angle. The variation in the difference between the microphone outputs is about 0.1 dB in magnitude and 0.003 *cycles* in angle (Fig. 4-3C).

The measurements in Fig. 4-3 indicate that the system is less stable when movements of the sound-source and microphone assemblies are made. The large correlation between the two microphone outputs clearly demonstrates that most of the observed variation is the sound-source output. The variations observed in the microphone outputs when movements of the brass-tube assembly are made are appreciably smaller than the total calibration variations in the cat ear observed when the system was recalibrated during the experiments (Fig. 4-1); the changes caused by movement of the system are likely to be a part of the total calibration changes (Fig. 4-1).

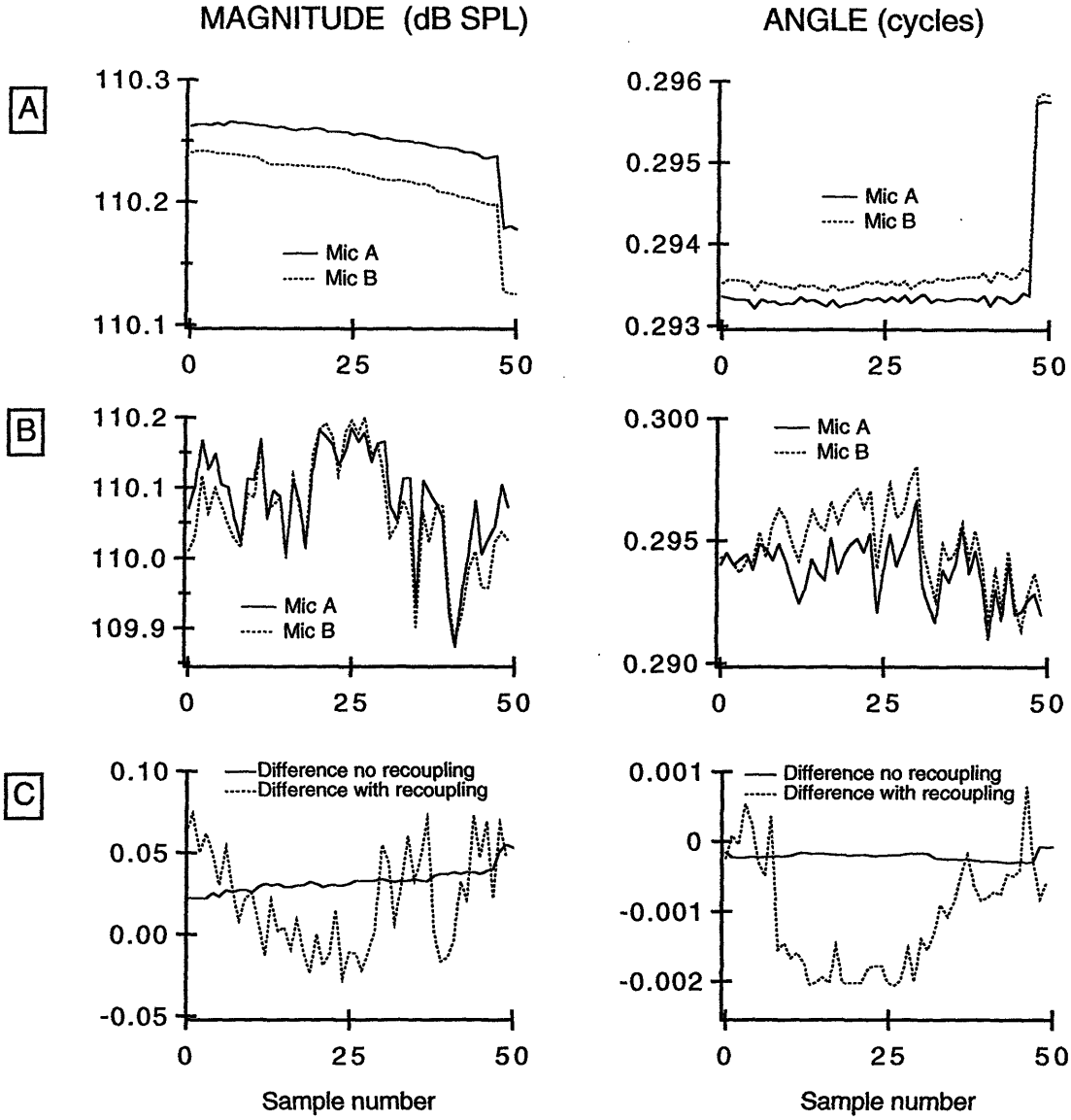

Figure 4-3: (A) 50 consecutive measurements by both microphones of a common $1000 Hz$ tone within a tube. Here the system was not touched between measurements. The time between the first and 50^{th} measurement was about 5 minutes. (B) 50 consecutive measurements by both microphones of a common $1000\ Hz$ tone within a tube. Here the system was decoupled and recoupled between each measurement. The time between the first and 50^{th} measurement was about 10 minutes. (C) The difference between the measurements shown in (A) and the difference between the measurements shown in (B). This difference is a measure of the variation of the microphone responses.

4.2 Spatial variations in pressure in the tympanic and bulla cavities

$\underline{P_{OW}}$ and $\underline{P_{RW}}$ are the measured pressures at the medial end of the ear canal and at the bulla wall. Differences may exist between these measured pressures and the pressures at the oval and round windows. To estimate these differences, pressure measurements were made at different locations in the bulla cavity (of a dead cat). The round-window sound-source and probe-tube microphone assembly was coupled to the bulla cavity as shown in Fig. 2-1. A second probe-tube microphone, mounted on a manipulator, was introduced into the bulla cavity near this assembly. This second probe-tube microphone was systematically moved across the bulla cavity from the bulla wall toward the round window, and the responses of both microphones to tonal stimuli were recorded. The calibration for the moving microphone was defined by assuming that the pressures measured by both microphones were the same when the moving microphone was positioned at the bulla wall.

Fig. 4-4 shows the ratio of the two pressure measurements, as a function of distance from the movable probe tube entrance at the bulla wall, for measurements at 1000 Hz. The $0\,mm$ position defined the bulla wall position, and the opening of the round window niche was at the 4.6 mm position. A total of five measurements was made at each position during three trials; a trial consisted of calibrating the moving microphone by making a measurement while the probe tube was at the bulla wall and then making one to three pressure measurements at each location as the probe tube was advanced systematically toward the round window. These measurements and their averages are shown in Fig.4-4. The probe moving toward the round window measured slight variations

in the pressure magnitude relative to the round-window microphone; these variations were on average less than 0.05 dB different from the pressure magnitude at the bulla wall. There were also variations in the pressure angle relative to the round-window microphone output; advancing the moving microphone led to a lag or decrease in angle relative to the pressure at the bulla wall. On average, the angle at the round window niche lagged the angle at the bulla wall by about 0.0008 *cycles*; this lag is only 6% of the phase lag of 0.013 *cycles* predicted theoretically for unidirectional uniform plane wave propagation. [1] The presence of the probe-tube microphone in the bulla cavity had little or no effect on the pressure magnitude measured by the round-window microphone; while the measurements shown in Fig. 4-4 were made, the largest magnitude changes in the pressure at the bulla wall were less than $0.02 dB$ in magnitude. The presence of the probe tube may have affected the pressure angle measured by the round-window microphone; the maximum change in these angle measurements was 0.001 *cycles*. However, such variations in angle measurement are smaller than the variations that result in movement of the acoustic system (Fig. 4-3B). The measurements of Fig. 4-4 support the assumption that there is little spatial variation in the pressure in the bulla cavity; therefore the pressure measured at the bulla cavity wall is an accurate representation of the pressure at the round window (Chapter 2.10).

Pressure variations in the bulla cavity at 100 Hz were also measured; these variations were smaller than those shown in Fig. 4-4 at 1000 Hz. The differences between the pressure at the round window and the estimated $\underline{P_{RW}}$ should be largest at 1000 Hz since the shortest wavelength involved in all experiments is at 1000 Hz. Additionally

[1] If the speed of sound is $345 \frac{m}{sec}$ and the distance traveled is 4.6 mm then the phase lag for a uniform plane wave would be $\frac{0.0046\ m}{\frac{345\ m\ sec^{-1}}{1000\ sec^{-1}}} = 0.013$ *cycles*.

the differences between the measured pressure and the actual pressure at the oval or round window should be greatest in the bulla cavity since this cavity is larger than the tympanic cavity.

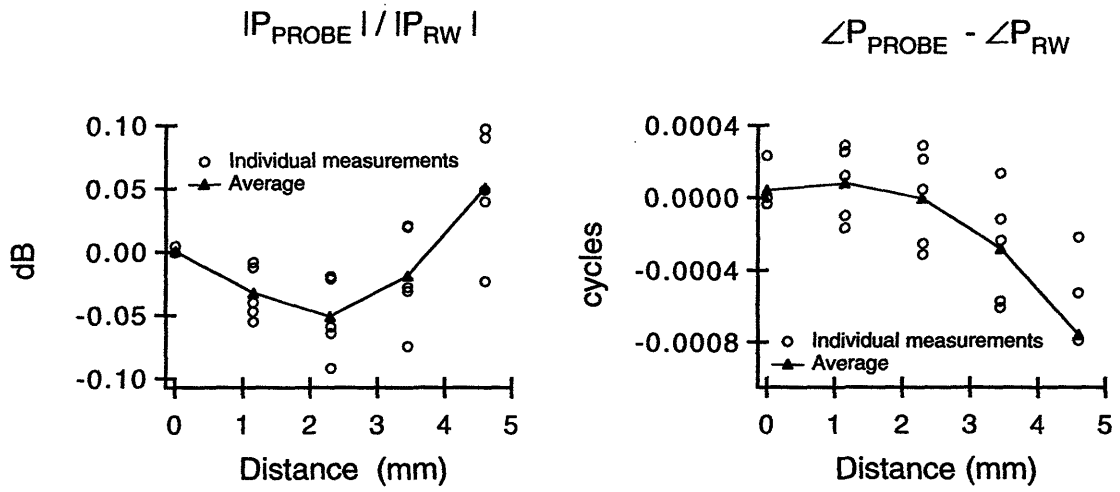

Figure 4-4: The reported pressures are measured as a function of distance from the bulla wall and are relative to the pressures measured simultaneously at the bulla wall. A probe tube microphone was advanced from the bulla wall (Distance=0 mm) to the round window niche (Distance=4.6 mm) .

4.3 Summary of pressure error estimates

Changes in the calibrations of the acoustic systems over the course of an experiment are the largest errors discussed here (Fig. 4-1). The contribution to these errors caused by movements of the system are clearly smaller than the total errors (Fig. 4-3). Errors due to spatial variation in pressure within the cavities are negligible compared to the total errors.

The total errors observed for the measurements on Cats #1, #2, #3 were much greater than those observed for the measurements on Cats #4, #5, #6, and #7 (Appendix A). The measurement system was improved by altering the components of the sound-source and microphone assemblies to have tighter fits. For this reason the results

and discussion presented in the body of this thesis emphasize results from Cats #4 to #7; results from Cats #1 to #3 are similar and can be found in the appendices.

Chapter 5

Results: Stimulus to one window

5.1 Experimental results

Single-sided cochlear-potential measurements were made as a function of increasing sound-pressure level while either the oval or round window was stimulated. The pressure at the unstimulated window was effectively zero because the foramen plug was in place. Examples of such measurements made on Cat #6 at 100 Hz, 300 Hz, and 1000 Hz are shown in Fig. 5-1, 5-2, and 5-3. These results are characteristic of results from all other cats (Appendix B).

The cochlear-potential response is described by its magnitude and angle. A linear dependence requires:

1. The cochlear-potential magnitude must increase with stimulus level with a slope of 1 with dB scales.
2. The cochlear-potential angle must be independent of stimulus level.

Nonlinear features can be seen in the pre-TTX measurements shown in Fig. 5-1, 5-2, and 5-3. The cochlear-potential magnitude does not always increase linearly with a slope of 1, even at levels well above the noisefloor; Fig. 5-3 provides the clearest example of

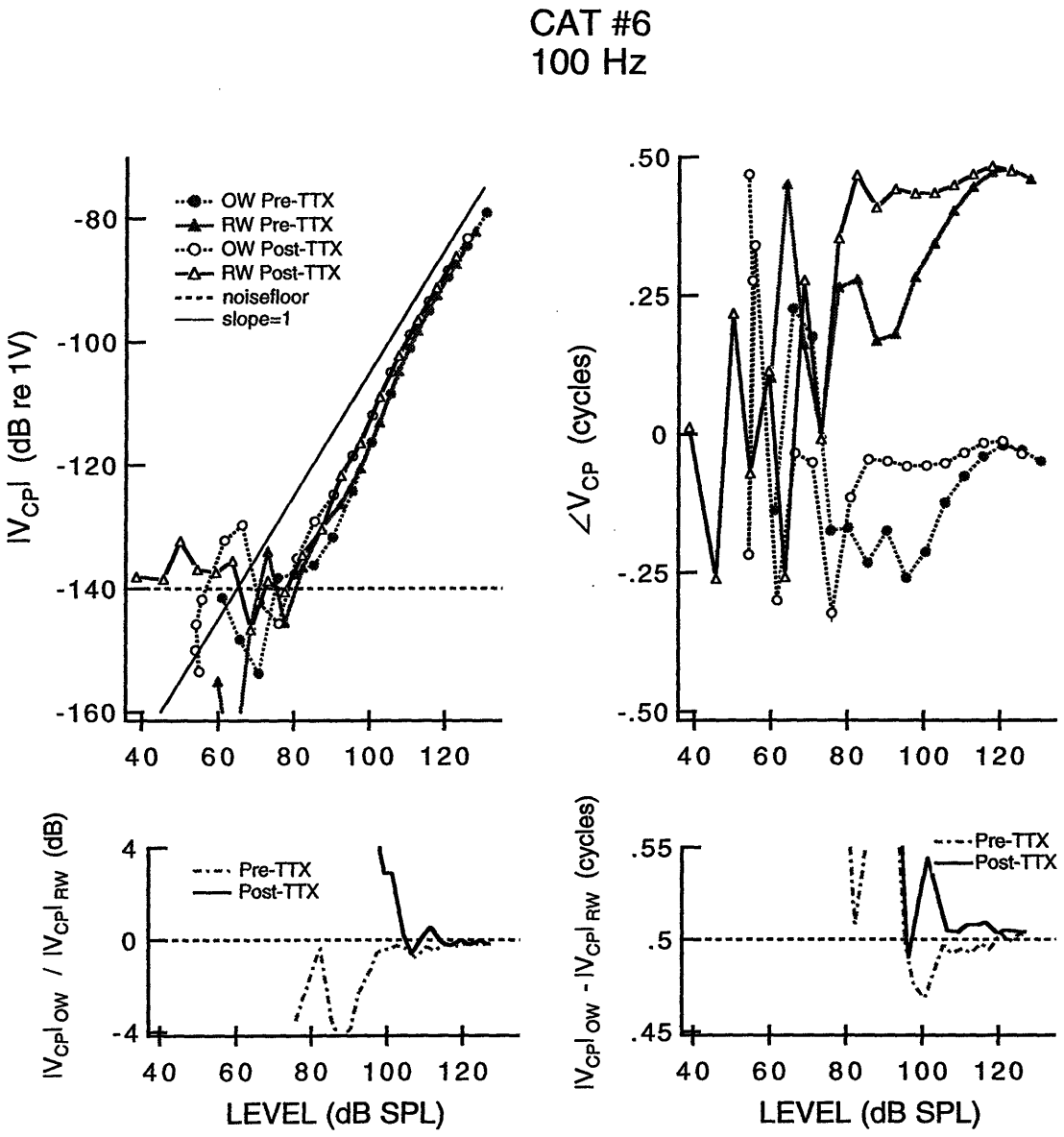

Figure 5-1: CAT #6: 100 Hz. TOP: Magnitude and angle of V_{CP} as a function of sound-pressure level both before and after the application of TTX. Either the oval or round window was stimulated. BOTTOM: Ratio between the oval-window response and the round-window response from the plots shown at the top.

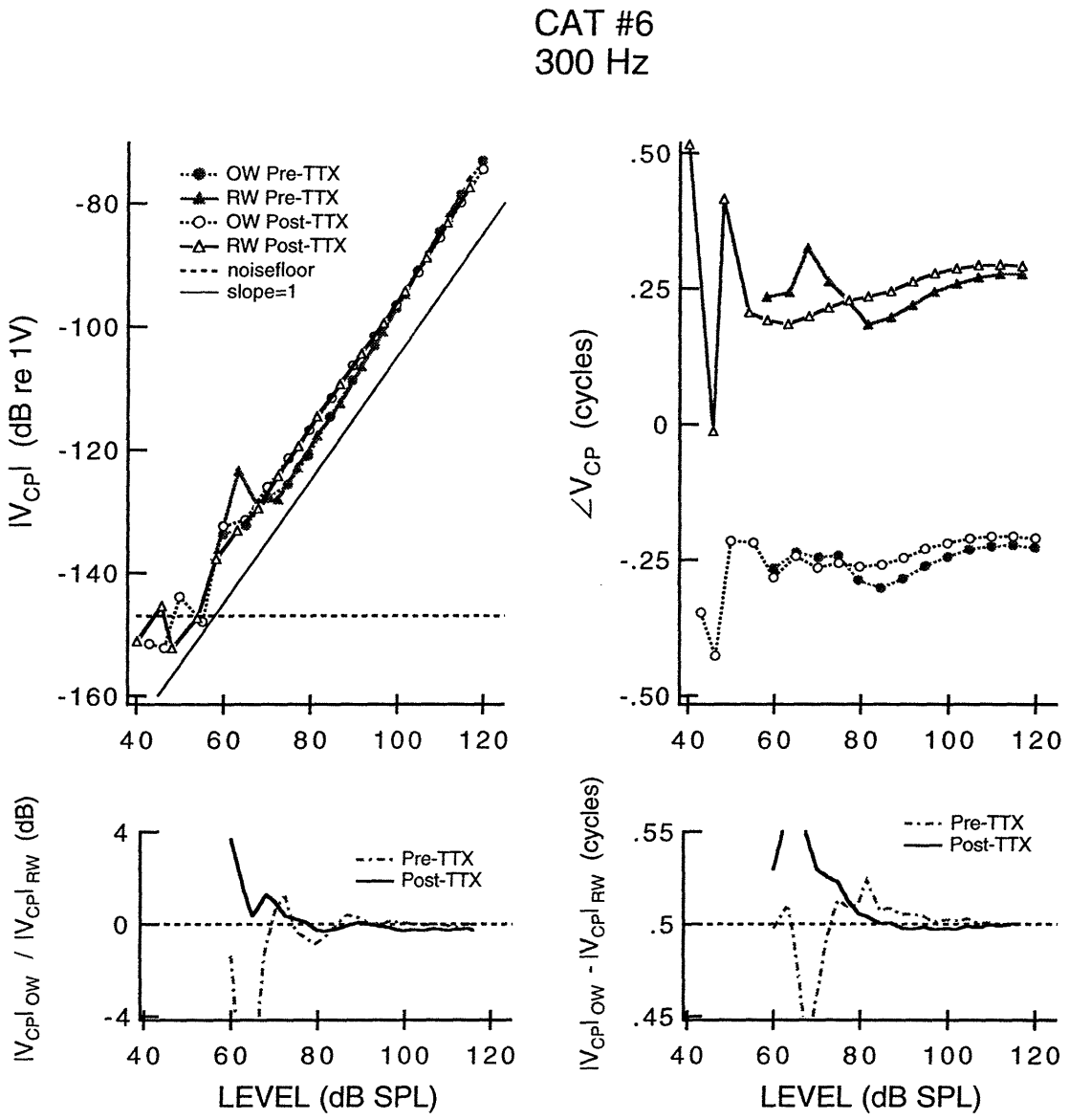

Figure 5-2: CAT #6: 300 Hz. TOP: Magnitude and angle of V_{CP} as a function of sound-pressure level both before and after the application of TTX. Either the oval or round window was stimulated. BOTTOM: Ratio between the oval-window response and the round-window response from the plots shown at the top.

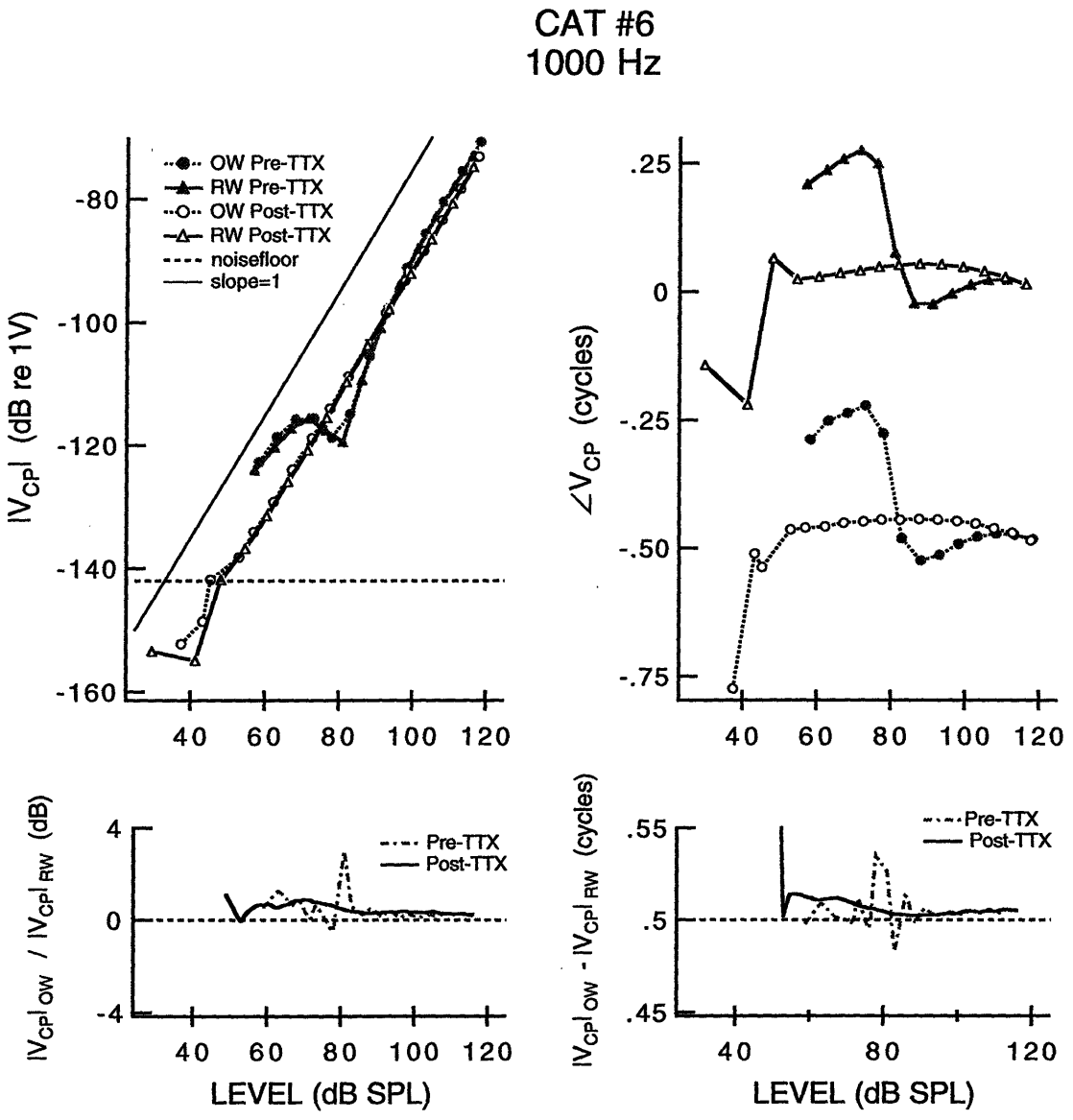

Figure 5-3: CAT #6: 1000 Hz. TOP: Magnitude and angle of V_{CP} as a function of sound-pressure level both before and after the application of TTX. Either the oval or round window was stimulated. BOTTOM: Ratio between the oval-window response and the round-window response from the plots shown at the top.

this nonlinear feature. At the stimulus levels between 60 and 80 $dB\ SPL$ the cochlear-potential magnitude both increases and decreases with increasing stimulus level. The cochlear-potential angle varies over the entire stimulus range; pre-TTX 100 and 300 Hz measurements (Fig. 5-1 and Fig. 5-2, pre-TTX) have cochlear-potential angles that increase with stimulus level over much of the stimulus dynamic range. (Many of the other 100 and 300 Hz measurements included in Appendix B have cochlear-potential angles that decrease with increasing stimulus level.) The cochlear-potential angle at 1000 Hz (Fig. 5-3) increases with increasing stimulus level except for a sudden quarter-cycle decrease at a mid-stimulus level. This type of transition is evident in all of the 1000 Hz measurements on the other six animals (Appendix B).

TTX was added to the cochleas of Cat #6 and Cat #7 (Chapter 2.7) to reduce the nonlinear component of the cochlear-potential response. The effect of TTX on Cat #6 is shown in Fig. 5-1, 5-2, and 5-3, and the effect of TTX on Cat #7 is shown in Fig. B-7, B-16, and B-34. TTX had larger effects on the Cat #6 results compared to the Cat #7 results. The 1000 Hz cochlear-potential magnitude nonlinearity described above (Fig. 5-3) is essentially eliminated after the application of TTX. TTX also appears to reduce nonlinearities present in the cochlear-potential magnitude response at 100 and 300 Hz (Fig. 5-1 and 5-2).

The ratio between the response to the oval-window stimulus and the round-window stimulus is also plotted in Fig. 5-1, 5-2, and 5-3 and in the Appendix B figures. In general, the cochlear-potential response magnitude is nearly independent of the stimulated window while the angle is nearly 0.5 cycles different for the two windows. The difference in magnitude (in dB) between the cochlear-potential response to the oval-window stimulus and the round-window stimulus is often greater at lower stimulus levels than at higher

stimulus levels; however, the difference rarely exceeds 2 dB and is often less than 1 dB (Appendix B). The difference in angle between the cochlear-potential response to the oval-window stimulus and the round-window stimulus is usually 0.5 ± 0.05 *cycles*; the largest deviations from 0.5 *cycles* occur most at the lower stimulus levels (Appendix B).

Cochlear-potential magnitude sensitivities from all seven cats are compared in Fig. 5-4. These results are interpolated from the plots in Appendix B. The top plot shows the sound pressure required to produce a cochlear-potential magnitude of $10\mu V$ when the stimulus is delivered to the oval window, and the middle plot shows the sound pressure required to produce a cochlear-potential magnitude of $10\mu V$ when the stimulus is delivered to the round window. The bottom plot is the dB difference between the sound pressure required with an oval-window stimulus and the sound pressure required with a round-window stimulus to produce a $10\mu V$ cochlear-potential magnitude response; the difference is never more than 2.5 dB SPL.

Cochlear-potential angle measurements from all seven cats are compared in Fig. 5-5. These results are also interpolated from the plots in Appendix B. The top plot shows the cochlear-potential angle, relative to $\underline{P_{OW}}$, which corresponds to a cochlear-potential magnitude of $10\mu V$ when the stimulus is delivered to the oval window. The middle plot shows the cochlear-potential angle, relative to $\underline{P_{RW}}$, which corresponds to a cochlear-potential magnitude of $10\mu V$ when the stimulus is delivered to the round window. The bottom plot is the difference between the two cochlear-potential angles. The difference is near 0.5 *cycles* in most cases and is always 0.5 ± 0.07 *cycles*.

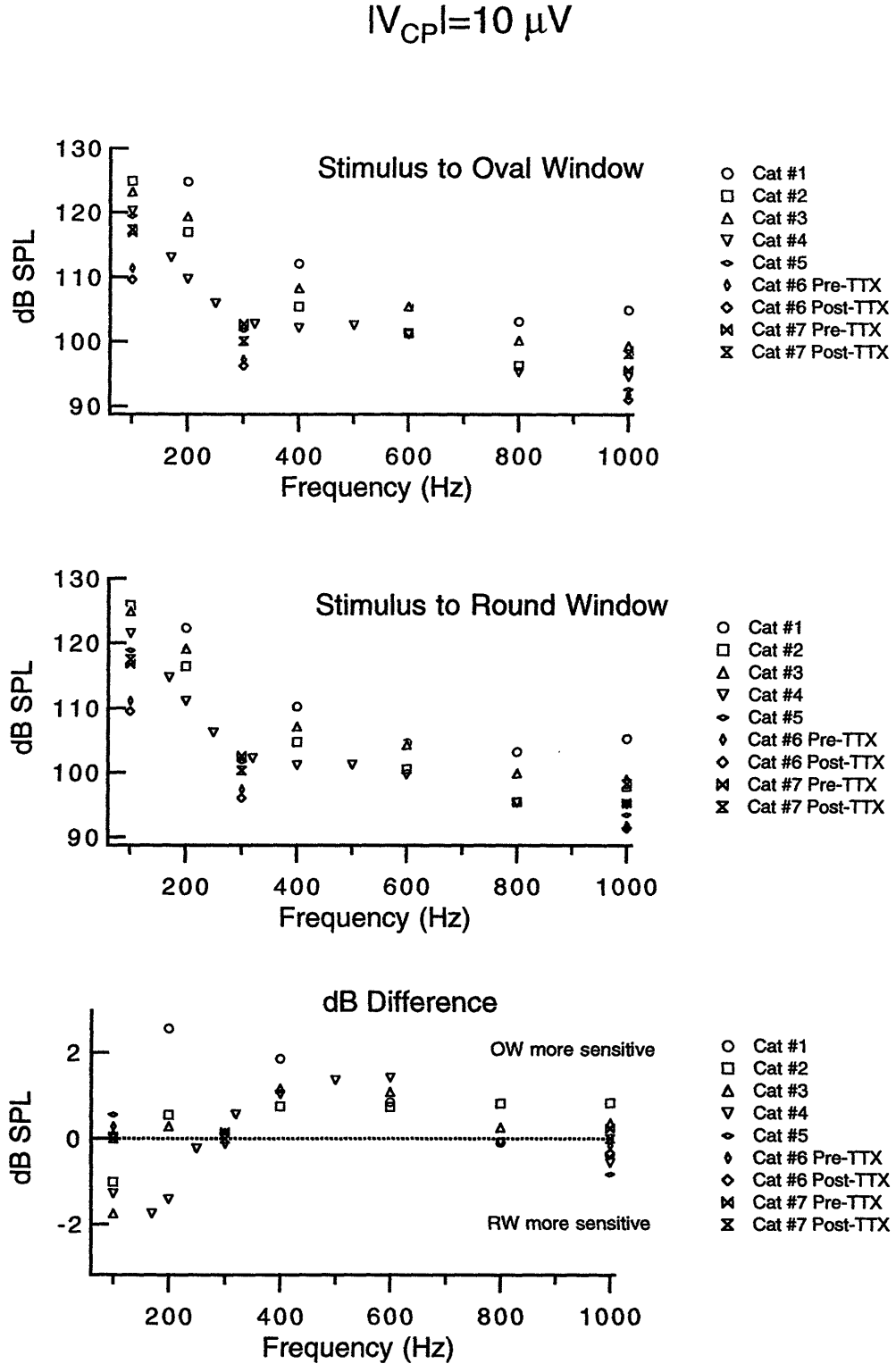

Figure 5-4: TOP: Sound-pressure levels required for a $10\mu V$ cochlear-potential magnitude response when the oval window was stimulated. MIDDLE: Sound-pressure levels required for a $10\mu V$ cochlear-potential magnitude response when the round window was stimulated. BOTTOM: The dB difference between the top and middle plots.

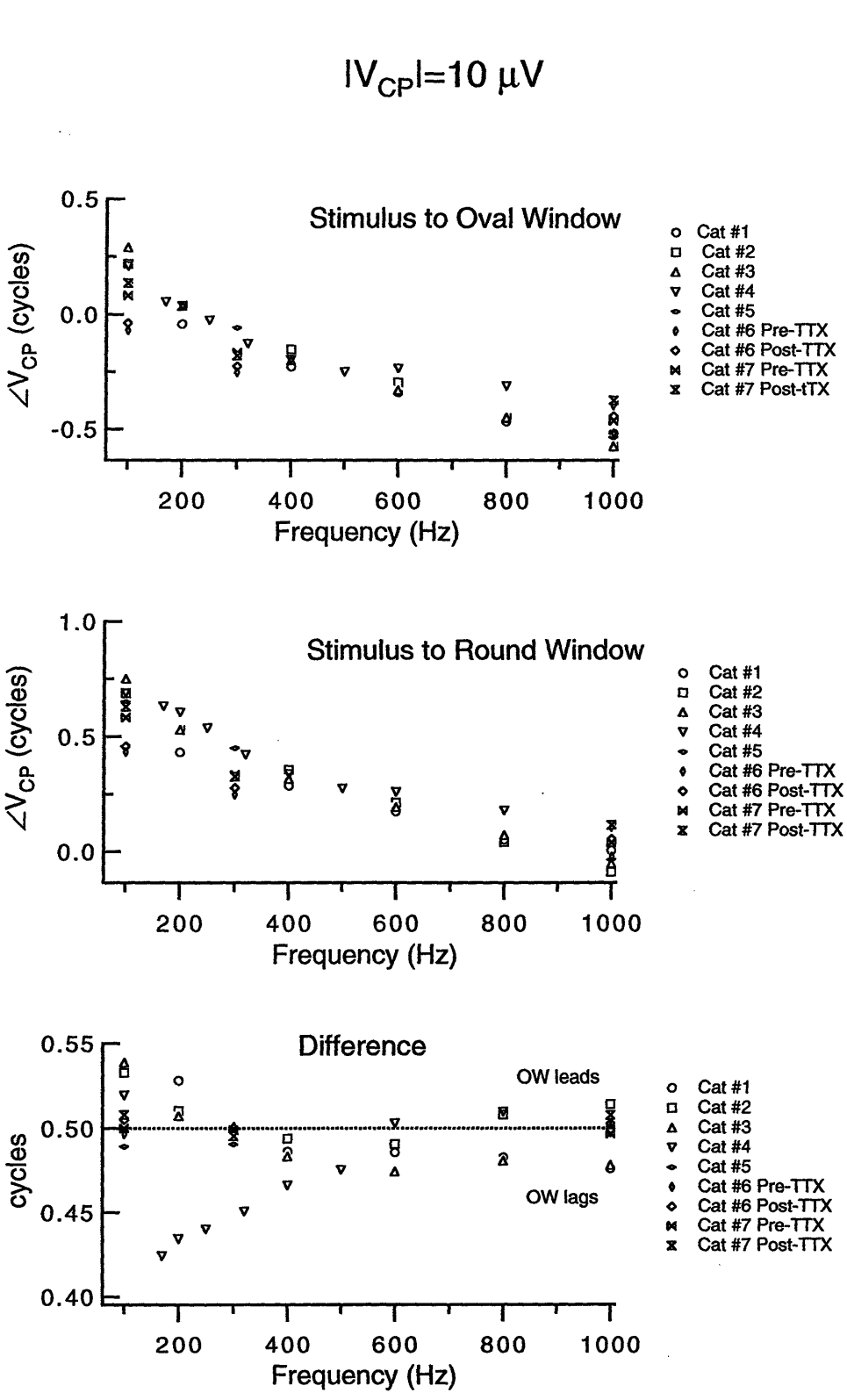

Figure 5-5: TOP: Cochlear-potential angle when the cochlear-potential magnitude response was $10\mu V$ and the oval window was stimulated (relative to angle of P_{OW}). MIDDLE: Cochlear-potential angle when the cochlear-potential magnitude response was $10\mu V$ and the round window was stimulated (relative to angle of P_{RW}). BOTTOM: The difference between the top and middle plots

5.2 Discussion

If the common-mode gain $\underline{C}$ is negligibly small in magnitude (pressure-difference assumption), when only the oval window is stimulated

$$\underline{V_{CP}} = \underline{D}\,\underline{P_{OW}}, \tag{5.1}$$

since $\underline{P_{RW}} \approx 0$. Likewise, when only the round window is stimulated the pressure-difference assumption can be expressed as

$$\underline{V_{CP}} = -\underline{D}\,\underline{P_{RW}}, \tag{5.2}$$

since $\underline{P_{OW}} \approx 0$. Equations 5.1 and 5.2 show that the pressure-difference assumption requires the cochlear-potential magnitude to be independent of the stimulated window and the cochlear-potential angle to be dependent on the stimulated window such that the difference between the cochlear-potential angles when the oval and round windows are stimulated is 0.5 *cycles*.

$$\textit{Stimulus to oval window}: \quad |\underline{V_{CP}}| = |\underline{D}|\,|\underline{P_{OW}}| \tag{5.3}$$

$$\textit{Stimulus to round window}: \quad |\underline{V_{CP}}| = |\underline{D}|\,|\underline{P_{RW}}| \tag{5.4}$$

and

$$\textit{Stimulus to oval window}: \quad \angle\underline{V_{CP}} = \angle\underline{D} + \angle\underline{P_{OW}} \tag{5.5}$$

$$\textit{Stimulus to round window}: \quad \angle\underline{V_{CP}} = \angle\underline{D} + \angle\underline{P_{RW}} + 0.5\,\textit{cycles} \tag{5.6}$$

Fig. 5-4 and 5-5 show that these requirements of the pressure-difference assumption are approximated when $|\underline{V_{CP}}| = 10\mu V$. Fig. 5-4 shows that the ratio between the oval-window and round-window sound pressures, when $|\underline{V_{CP}}| = 10\mu V$, is never greater than 2.5 dB and this ratio is often ± 0.2 dB. Fig. 5-5 shows that the difference in cochlear-potential angle between the responses obtained from an oval-window and round-window stimulus is nearly 0.5 *cycles*.

Differences between the results shown in Fig. 5-4 and 5-5 and the pressure-difference assumption can be interpreted as a combination of measurements errors and contributions of the common-mode response. A general representation of the single-sided stimuli responses uses Equation 3.1 when the oval and round windows are stimulated, respectively.

$$\textit{Stimulus to oval window}: \quad \underline{V_{CP}} = \underline{D}\,\underline{P_{OW}} + \frac{1}{2}\underline{C}\,\underline{P_{OW}} \tag{5.7}$$

$$\textit{Stimulus to round window}: \quad \underline{V_{CP}} = -\underline{D}\,\underline{P_{RW}} + \frac{1}{2}\underline{C}\,\underline{P_{RW}} \tag{5.8}$$

Equations 5.7 and 5.8 could be solved simultaneously to give estimates of $\underline{D}$ and $\underline{C}$. However, the methods of the next chapter are more robust in the estimates of $\underline{C}$. The single-sided measurements presented here do not control for small amounts of acoustic crosstalk through the foramen plug; instead the unstimulated window pressure is assumed zero. Additionally, the cochlear-potential measurements are taken at different times, not simultaneously, and small changes in cochlear sensitivity can occur and cause small changes in the measured cochlear-potential response.

If $|\underline{C}| << |\underline{D}|$ we can ignore the common-mode component and estimate $\underline{D}$ based on the pressure-difference assumption and the single-sided stimuli measurements discussed in this chapter.

$$\textit{Stimulus to oval window}: \quad \hat{\underline{D}} = \frac{\underline{V_{CP}}}{\underline{P_{OW}}} \tag{5.9}$$

$$\textit{Stimulus to round window}: \quad \hat{\underline{D}} = -\frac{\underline{V_{CP}}}{\underline{P_{RW}}} \tag{5.10}$$

Estimates of $\underline{D}$ as a function of stimulus level are shown in Fig.5-6 for the single-sided measurements of Fig. 5-1, 5-2, and 5-3. Estimates of $\underline{D}$ as a function of stimulus level for all other single-sided measurements are included in Appendix B. These estimates of $\underline{D}$ can be used as a measure of the linearity of a single-sided cochlear-potential measurement; if the cochlear response is linear then both $|\underline{D}|$ and $\angle\underline{D}$ are independent of stimulus level.

Fig.5-6 shows that the estimates of $\underline{D}$ are dependent on sound-pressure level; therefore $\underline{V_{CP}}$ is not linear. The variations in $\underline{D}$ are largest at the lower sound-pressure levels. The dependence of $\underline{D}$ on level at 1000 Hz is prominent in both magnitude and angle; this dependence is much reduced after the application of TTX. The level dependency at 300 Hz is small compared to those at 1000 Hz and 100 Hz and it too is reduced after the application of TTX. At 100 Hz, nonlinearities in $\underline{V_{CP}}$ are present both before and after the application of TTX; the level dependence of $\angle\underline{V_{CP}}$ seems to be reduced after the application of TTX.

Level dependencies in $\hat{\underline{D}}$ shown in Appendix B are not consistent for one frequency across cats or for one cat at all frequencies. In several cases the estimate of $|\underline{D}|$ varies by one to two orders of magnitude and the estimate of $\angle\underline{D}$ varies by nearly 0.5 *cycles* as a function of sound-pressure level (Fig. B-3, B-4, B-6, B-9, B-10, B-29 and B-33, pre-TTX). In other cases the estimates of $|\underline{D}|$ and $\angle\underline{D}$ are nearly constant as a function of sound-pressure level (Fig. B-7, B-18, B-19, B-27, B-31 and B-33, post-TTX).

The difference-mode gain $\underline{D}$ appears to be level dependent, at least in some cases. At 1000 Hz the nonlinearities may be a result of the CAP contribution to the cochlear potential since $\underline{D}$ becomes nearly independent of level after the application of TTX. But the source of nonlinearity at 100 Hz is not clear. It could be argued that the TTX was not as effective for the lower frequencies because the TTX did not permeate the entire cochlea; neurons with the ability to phase-lock to a 100 Hz tone extend further toward the apex of the cochlea than neurons with the ability to phase-lock to a 1000 Hz stimulus. It is possible that the lower frequency stimuli evoked responses from apical neurons whose CAP's were unaffected by the TTX. It is also possible that the more apical hair cells have a nonlinear response.

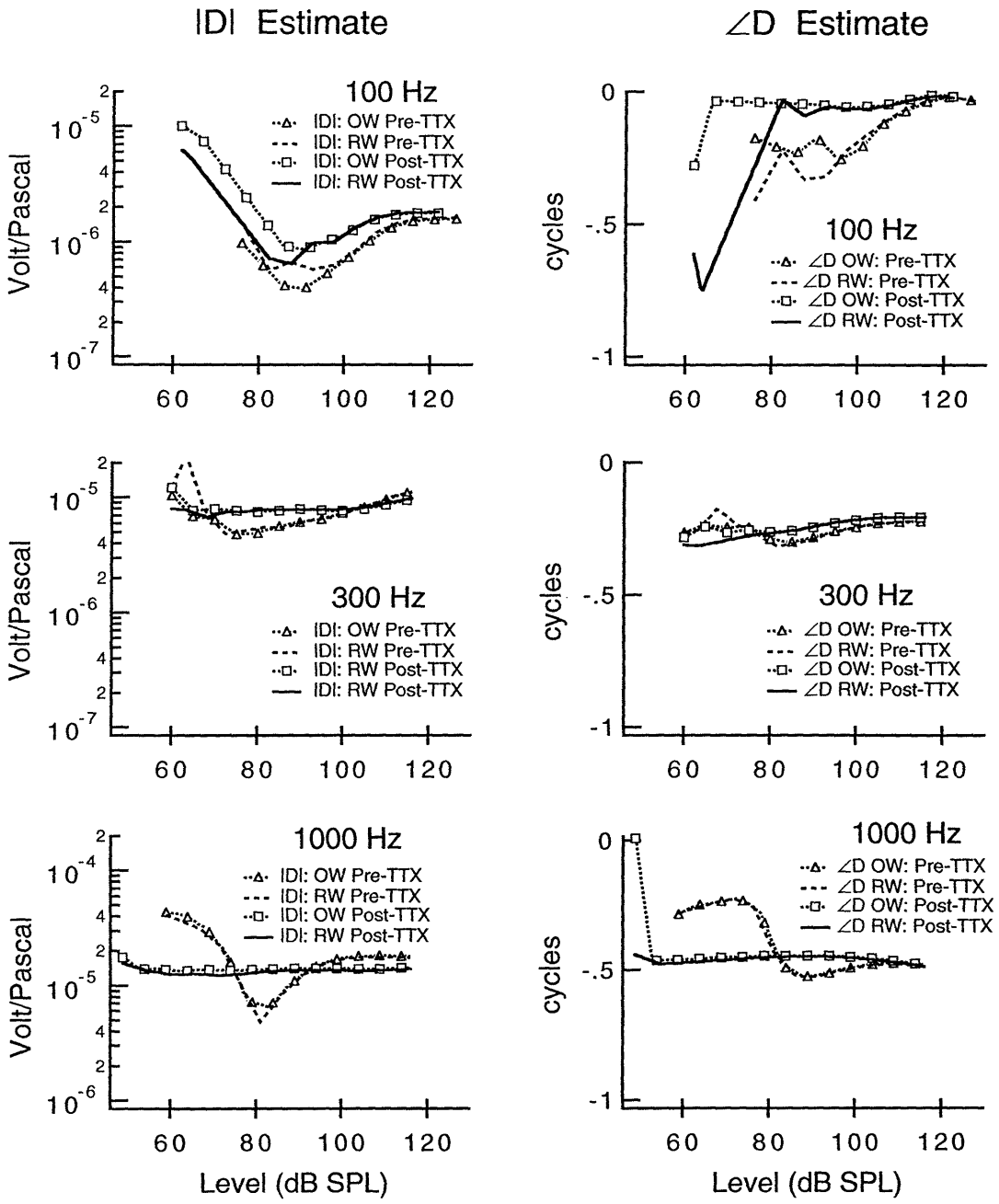

Figure 5-6: Estimates of D from the single-sided cochlear-potential measurements on Cat #6 both before and after the application of TTX. TOP: 100 Hz. MIDDLE: 300 Hz. BOTTOM: 1000 Hz.

Fig. 5-7 and 5-8 summarize the estimates of $\underline{D}$ found from measurements on all seven cats. The estimate of $\underline{D}$ is reported for the level at which the interpolated cochlear-potential magnitude was $10\mu V$. There are not large differences between the estimates of $\underline{D}$ found from the stimulus to the oval window and stimulus to the round window cases. Inter-frequency variations for one cat are larger than inter-cat variations for one frequency. In general, $|\underline{D}|$ increases with frequency and $\angle\underline{D}$ decreases with frequency. This result is further discussed in Chapter 6.

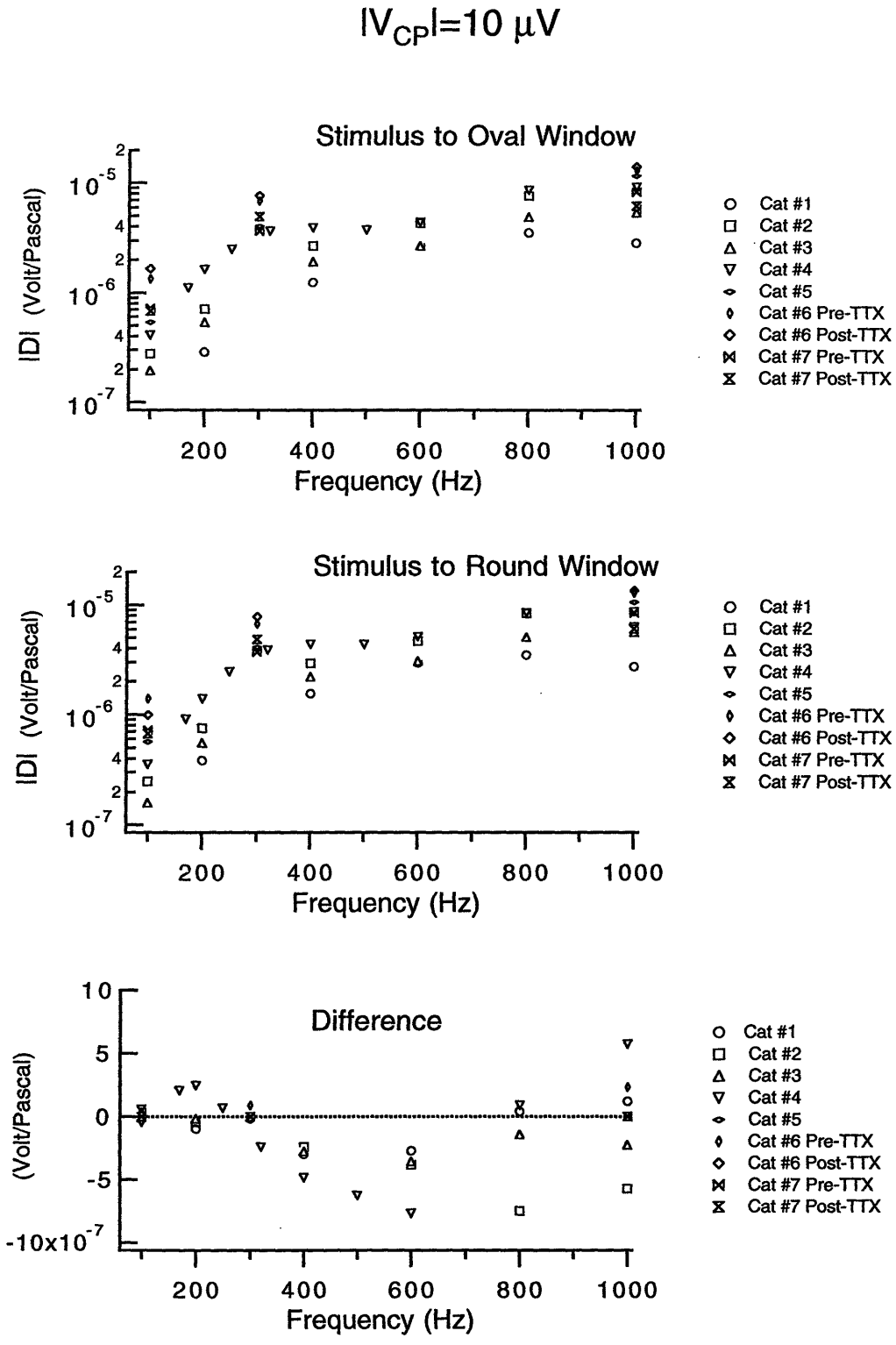

Figure 5-7: Estimates of $|\underline{D}|$ found from Equations 5.9 and 5.10 at a sound-pressure level such that $|\underline{V_{CP}}| = 10\mu V$.

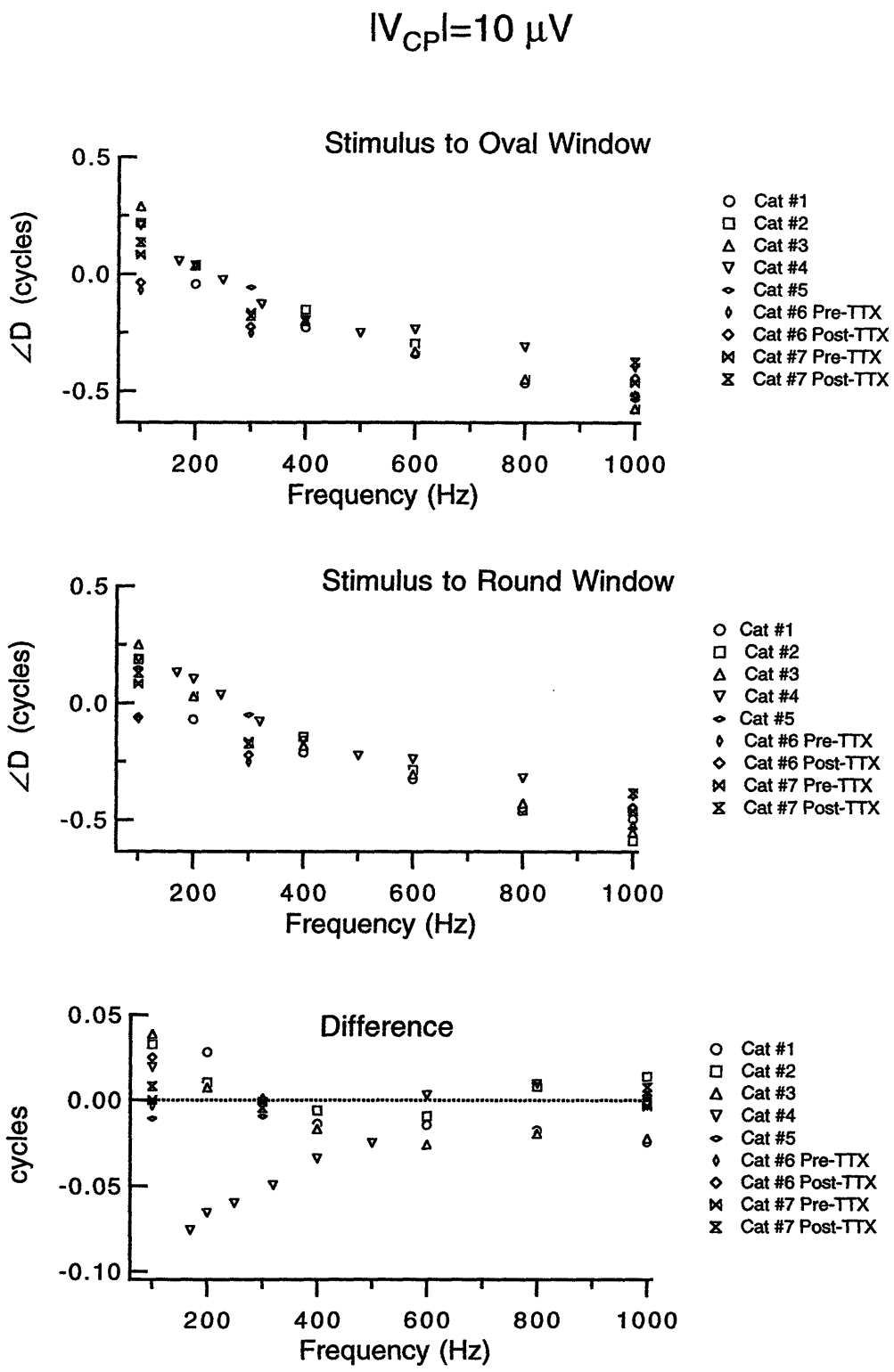

Figure 5-8: Estimates of the angle of $\underline{D}$ found from Equations 5.9 and 5.10 at a sound-pressure level such that $|\underline{V_{CP}}| = 10\mu V$.

Chapter 6

Results: Stimuli to both windows

6.1 Experimental results

Simultaneous-stimuli measurement sets were made by stimulating both the oval and round windows and varying the phase difference ψ between the two stimuli over one cycle. All such measurement sets are shown in Appendix C. The discussion in this chapter emphasizes measurements from Cats #4, #5, #6, and #7 because errors in the pressure measurements of $\underline{P_{OW}}$ and $\underline{P_{RW}}$ were smaller during these later experiments.

Fig. 6-1 and 6-2 show simultaneous-stimuli measurement sets made at 1000 Hz on Cat #7 with sound-pressure level as a parameter; the data in Fig. 6-1 were taken before the application of TTX and the data in Fig. 6-2 were taken after the application of TTX. The cochlear-potential magnitude and angle measurements are plotted as a function of ψ, the phase difference between the oval and round-window sound pressures. The left-hand plot is the cochlear-potential magnitude, the middle plot is the cochlear-potential magnitude in the region around $\psi \approx 0$, and the right-hand plot is the cochlear-potential angle. Data points where $|\underline{V_{CP}}| > Noisefloor$ are represented by open circles and data

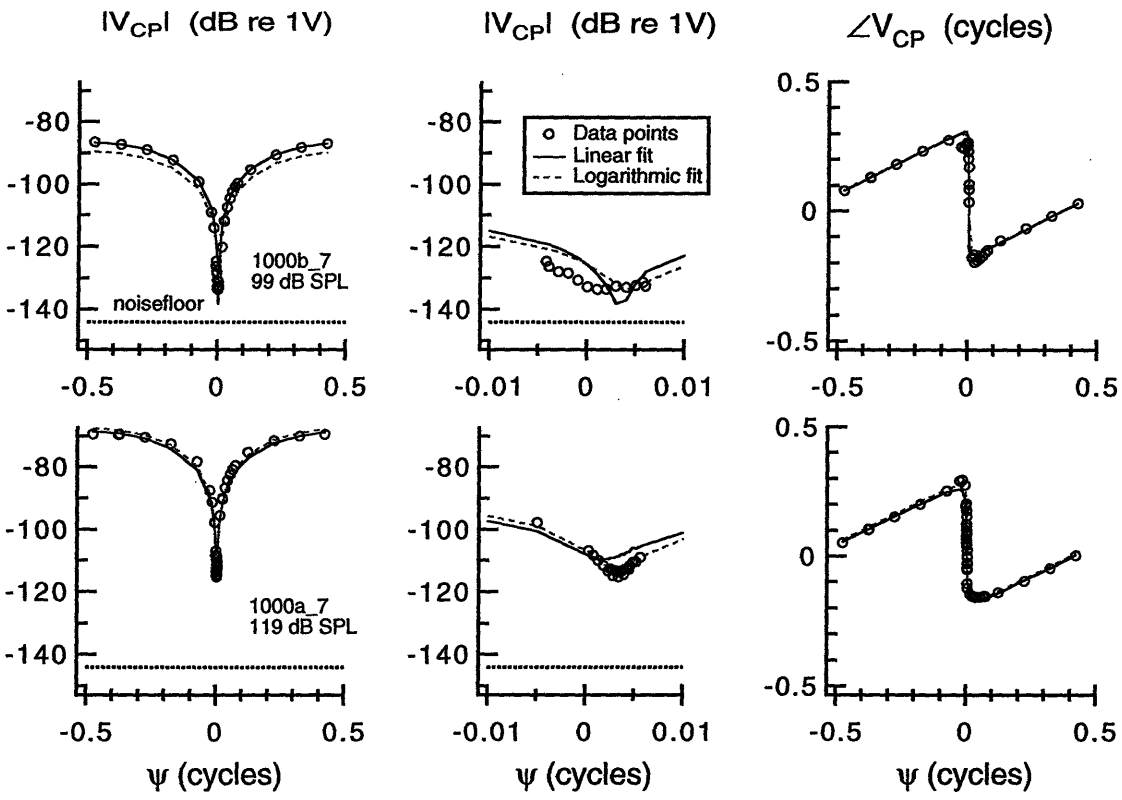

Figure 6-1: Simultaneous-stimuli measurement sets and model fits at 1000 Hz on Cat #7 before the application of TTX.

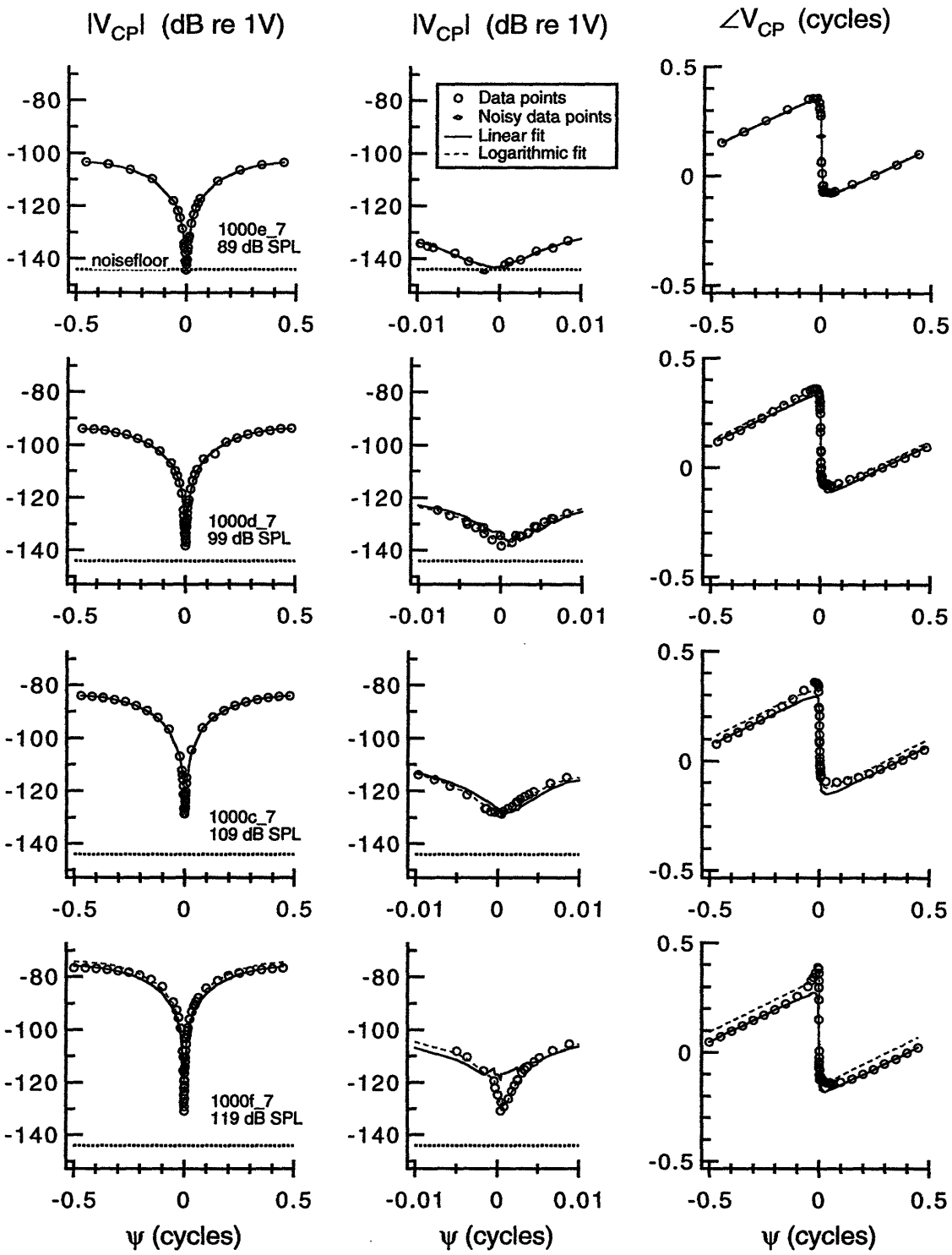

Figure 6-2: Simultaneous-stimuli measurement sets and model fits at 1000 Hz on Cat #7 after the application of TTX.

points where $|\underline{V_{CP}}| < Noisefloor$ are represented by open ovals. Each plot has a label associated with it to identify the measurement order; for example the label "1000e_7" refers to the fifth measurement made on Cat #7 at 1000 Hz. The measurement sets are plotted in order of increasing stimulus level and not chronological order, and the sound-pressure level printed on the magnitude plot is the measured sound-pressure level of both $|\underline{P_{OW}}|$ and $|\underline{P_{RW}}|$.

Several features of the measurement sets shown in Fig.6-1 and 6-2 are seen in all of the measurements shown in Appendix C. The cochlear-potential magnitude plots are roughly symmetric about $\psi = 0$. A magnitude minimum occurs at an inter-window stimulus phase difference $\psi_{MIN} \approx 0 cycles$. A magnitude maximum occurs near $\psi = 0.5 cycles$ and is always close to the sum of the two cochlear-potential response magnitudes recorded when the oval and round windows are individually stimulated. The dynamic range of a given measurement set, the dB difference between the maximum and minimum cochlear-potential magnitude, is roughly 40 dB when $|\underline{P_{OW}}| \approx |\underline{P_{RW}}|$. The dynamic range is sometimes limited by the noisefloor, especially when $|\underline{P_{OW}}|$ and $|\underline{P_{RW}}|$ are at lower values.

In general, the cochlear-potential angle data points increase with increasing values of ψ except for a sudden 0.5 *cycle* shift at $\psi \approx 0$. However, for some of the ears deviations from this pattern occur, especially at the lower frequencies, as illustrated in Fig. 6-3 with examples from five of the seven experimental animals. Between $\psi = -0.5$ and $\psi = 0$ the cochlear-potential angle increases with increasing ψ and shifts by about $0.5 cycles$ at $\psi = 0$. But between $\psi = 0$ and $\psi = 0.5$ the cochlear-potential angle does not increase at the same rate as it increased between $\psi = -0.5$ and $\psi = 0$. In fact, the cochlear-potential angle remains roughly constant between $\psi = 0$ and $\psi = 0.1$ for the examples

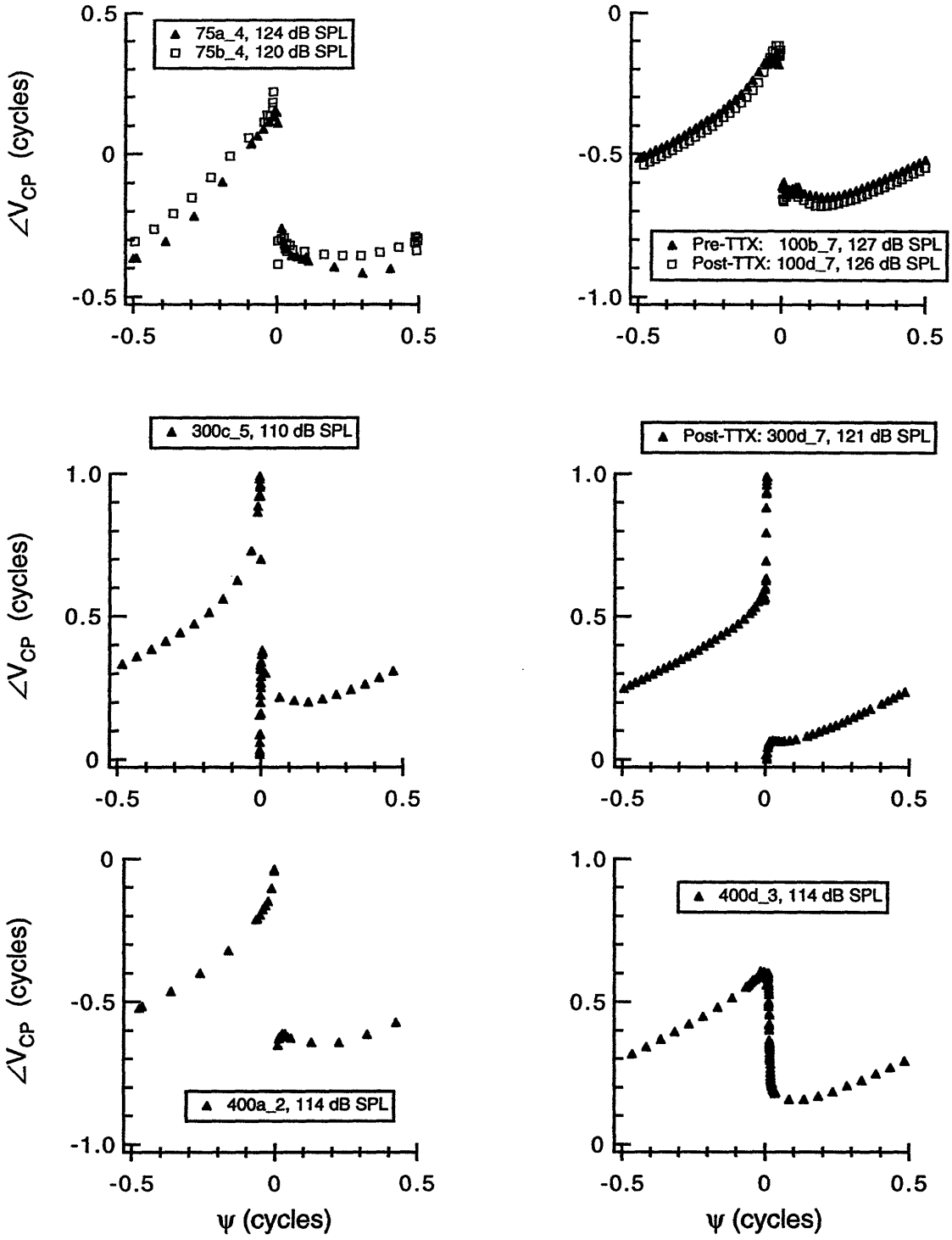

Figure 6-3: Cochlear-potential angle measurements as a function of ψ, the phase difference between the pressure at the oval and round windows. These measurements were selected to demonstrate an asymmetry around $\psi = 0$. The legends identify the frequency of the measurement, the measurement order on a given cat, and the cat on which the measurement was made.

shown in Fig. 6-3. To test if this asymmetry about $\psi = 0$ is a result of the order in which the data points were collected, data points from Cat #5 were collected both in order of increasing ψ and in a random order; there was no appreciable difference in the shape of the curve. The asymmetry could also be a result of nonlinear behavior of the neural component of the cochlear potential. The example from Cat #7 at 100 Hz in Fig. 6-3 shows that TTX did not affect the asymmetry, but TTX did not have large effects on the single-sided cochlear potential measurements at 100 Hz on Cat #7 either (Fig. B-7). The cause or mechanism of the angle asymmetry is not known.

There are not large differences between the pre-TTX measurement sets and the post-TTX measurement sets on either Cat #6 or Cat #7. The biggest differences occur at 1000 Hz; 1000 Hz pre and post-TTX measurement sets are compared in Fig. 6-4. Differences between the pre and post-TTX measurement sets were expected to be most obvious around $\psi = 0$ because single-sided level series measurements showed that TTX had the biggest influence on $\underline{V_{CP}}$ at the lower stimulus levels or when $|\underline{V_{CP}}| < -120\, dB\ re\ 1V$ (Fig. B-33 and B-34). The only pre-TTX simultaneous-stimuli measurement set at 1000 Hz on Cat #7 which includes data points such that $|\underline{V_{CP}}| < -120\, dB\ re\ 1V$ is shown in Fig. 6-1 and is labeled "1000b_7". Comparison of this pre-TTX measurement with the post-TTX measurement set in Fig. 6-2 labeled "1000d_7" shows nearly equivalent results in the region around $\psi = 0$, the region where the TTX was expected to have the biggest effect on the result (Fig. 6-4). Instead, the biggest difference between the pre and post-TTX measurements is an approximate $5\, dB$ decrease in cochlear-potential magnitude after the application of TTX; this decrease is most easily seen in regions where $\psi \approx 0.5$ and in the single-sided measurements of Fig. B-34. Fig. 6-4 also compares the pre and post-TTX simultaneous-stimuli measurements from Cat #6 at 1000 Hz;

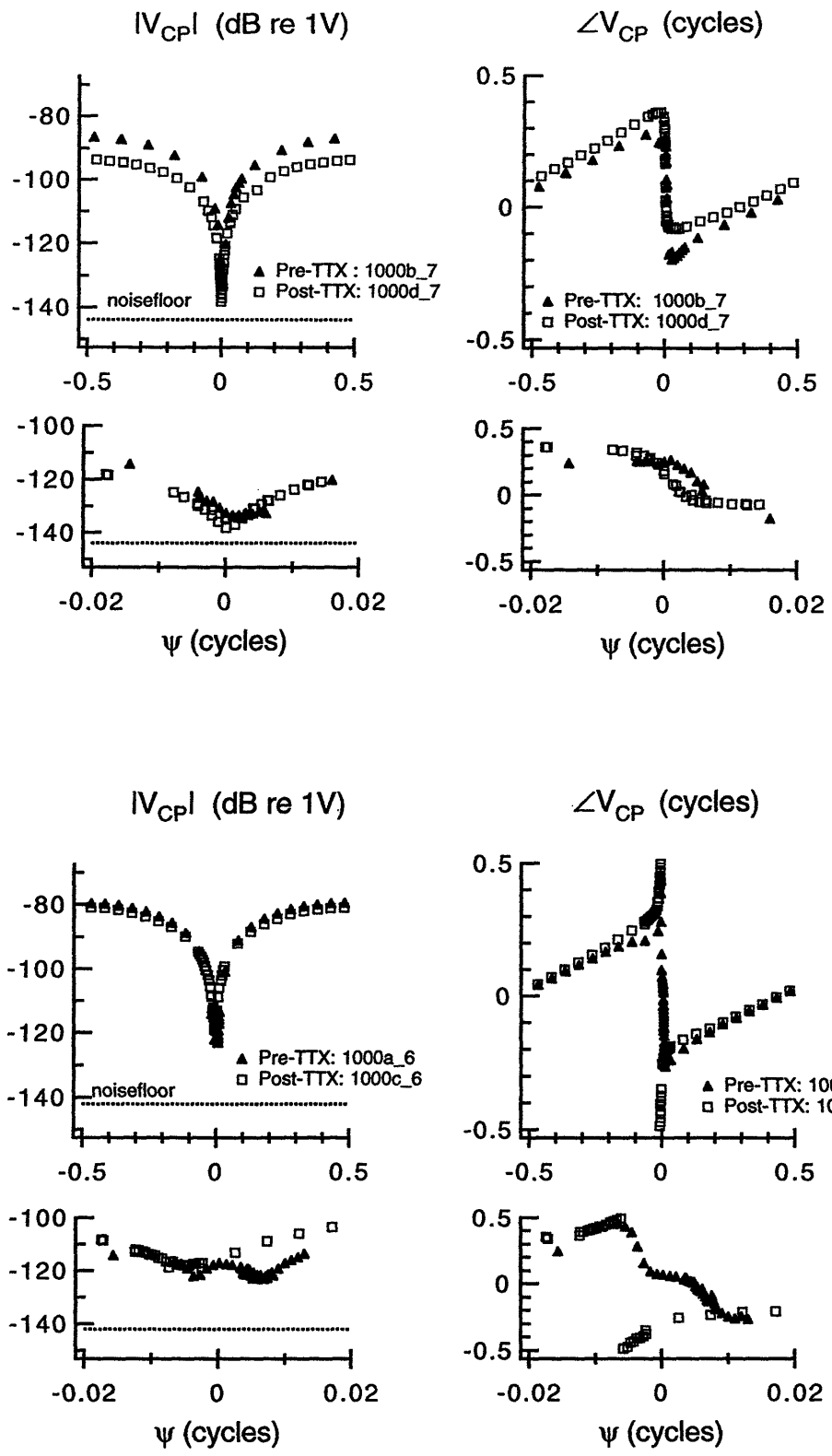

Figure 6-4: Comparison of pre and post-TTX cochlear-potential measurements as a function of ψ, the phase difference between the pressure at the oval and round windows, when the oval and round windows were stimulated with nearly equal sound-pressure levels. TOP: Cat #7 measurements at 99 dB SPL. BOTTOM: Cat #6 measurements at 104 dB SPL.

there are slight differences in the cochlear-potential magnitude and angle around $\psi = 0$. These differences could be a result of the TTX, or differences between pre and post-TTX measurements could also be caused by slight changes or imbalances in $|\underline{P_{OW}}|$ and $|\underline{P_{RW}}|$.

6.2 Model fits to the data: Estimation of C and D

We estimate the difference-mode and common-mode gains using the methods described in Chapter 3. The measured values of $\underline{V_{CP}}$, $\underline{P_{OW}}$, and $\underline{P_{RW}}$ at each and every data point are used to determine the estimates $\underline{\hat{D}}$ and $\underline{\hat{C}}$ that produce the least-squares difference to Equation 3.4 ("linear fit") or Equation 3.14 ("logarithmic fit") for each measurement set. The model fits to the cochlear-potential data, $\underline{\hat{V}_{CP}}$, obtained from Equation 3.4 and Equation 3.14 are included on the plots of the simultaneous-stimuli measurement sets in Appendix C and Fig. 6-1 and 6-2. There are not large differences between the results of the two fitting procedures; the discussion here will concentrate on the linear fit of Equation 3.4.

Many general aspects of the model fits are consistent with the data: the magnitude maxima from both the fits and the data are nearly the same and both occur at $\psi \approx 0.5$, the magnitude minimum from both the fits and the cochlear-potential data all occur at $\psi \approx 0$, and the angles of both the models and the cochlear-potential data change rapidly by about 0.5 *cycles* at $\psi \approx 0$. Differences between the linear and logarithmic fits are so small that in most cases the two plots are nearly indistinguishable. The major difference is illustrated in Fig. 6-1 (measurement "1000a_7") and Fig. 6-2 (measurement "1000f_7"). The largest deviation between the linear model fit and the cochlear-potential data occurs near $\psi = 0$ because the magnitude of the cochlear potential is small in this region and large fractional differences are not weighted strongly in the linear-least-squares fit of

Equation 3.4. The logarithmic fit does a better job fitting $\hat{V_{CP}}$ to the data points near $\psi = 0$ but the fit near $\psi = 0.5$ is not as good as the linear model fit.

The linear model predictions of $\hat{D}$ and $\hat{C}$ from Equation 3.4 are summarized in Fig.6-5 for all measurement sets on Cats #4 to #7. The estimates of $|\underline{D}|$ are more than an order of magnitude greater than the estimates of $|\underline{C}|$, and the magnitudes of both gains increase by approximately an order of magnitude as frequency increases from 75 to 1000 Hz. The estimates of $|\underline{D}|$ have a smaller standard deviation than the estimates of $|\underline{C}|$ on a logarithmic scale, and the estimates of $\angle\underline{D}$ have a much smaller standard deviation than the estimates of $\angle\underline{C}$.

The common-mode rejection-ratio (CMRR) is calculated for all measurement sets using Equation 3.3: $\hat{CMRR} = 20log_{10}|\frac{\hat{D}}{\hat{C}}|$. $\hat{CMRR}$ values are shown in Fig. 6-6 and do not appear to be a function of frequency. The mean values of $\hat{CMRR}$ range from 27.5 dB (75 Hz) to 34.5 dB (800 Hz). The lowest $\hat{CMRR}$ is 18.6 dB at 300 Hz and the highest $\hat{CMRR}$ is 53.8 dB at 100 Hz. The variation in $\hat{CMRR}$ is not surprising since the standard deviation of $\hat{C}$ is large and $\hat{CMRR}$ is calculated from $\hat{C}$.

The correlation coefficients calculated for the model fit to each measurement set using Equations 3.20 and 3.21 are shown in Fig. 6-7. In general, the magnitude correlation coefficients are higher than the angle correlation coefficients. With the exception of the two measurement sets at 75 Hz, the mean magnitude correlation coefficients are all greater than 0.95, and the mean minus the standard deviation of all magnitude correlation coefficients is greater than 0.9. The mean angle correlation coefficients are all greater than 0.85, and the mean minus the standard deviation of all angle correlation coefficients is greater than 0.7 (with the exception of the two measurement sets at 75 Hz). The angle correlation coefficients are more difficult to describe and less meaningful

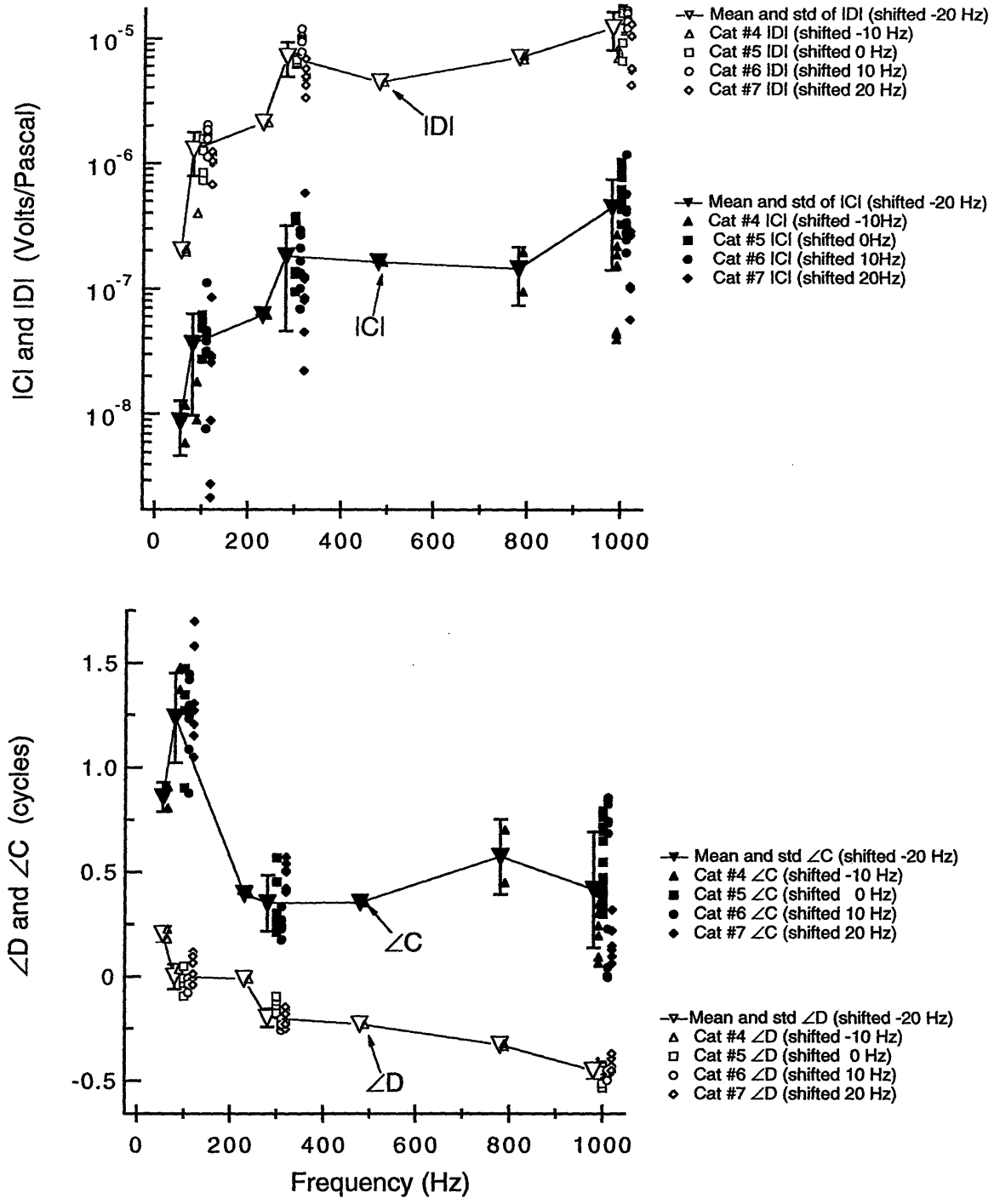

Figure 6-5: Estimate of D and C for each measurement set from Cats #4 to #7. D estimates are represented by open symbols and C estimates are represented by closed symbols. Because most of the measurements were at 100, 300, or 1000 Hz the plotted points tend to overlap. To increase legibility, points for a given cat are shifted right or left by a small amount, as indicated in the keys. TOP: Magnitudes of D and C. BOTTOM: Angles of D and C.

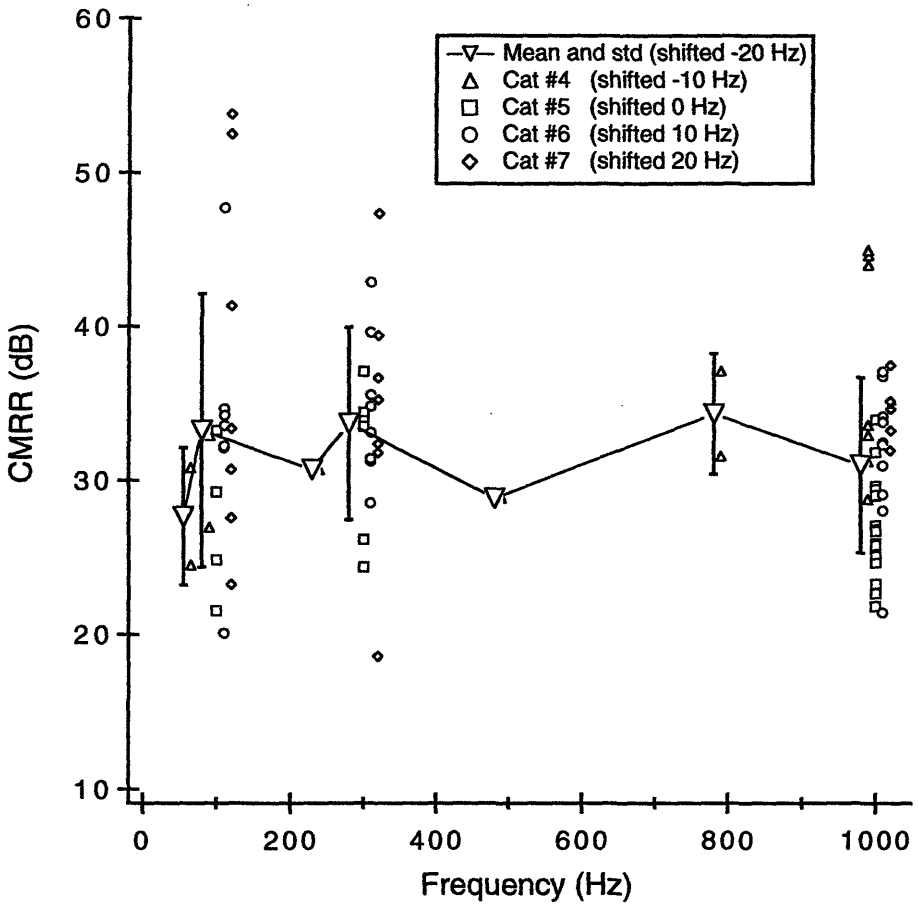

Figure 6-6: Calculation of the common-mode rejection-ratio (CMRR) from the estimates of D and C for each measurement set from Cats #4 to #7. Because most of the measurements were at 100, 300, or 1000 Hz the plotted points tend to overlap. To increase legibility, points for a given cat are shifted right or left by a small amount, as indicated in the keys.

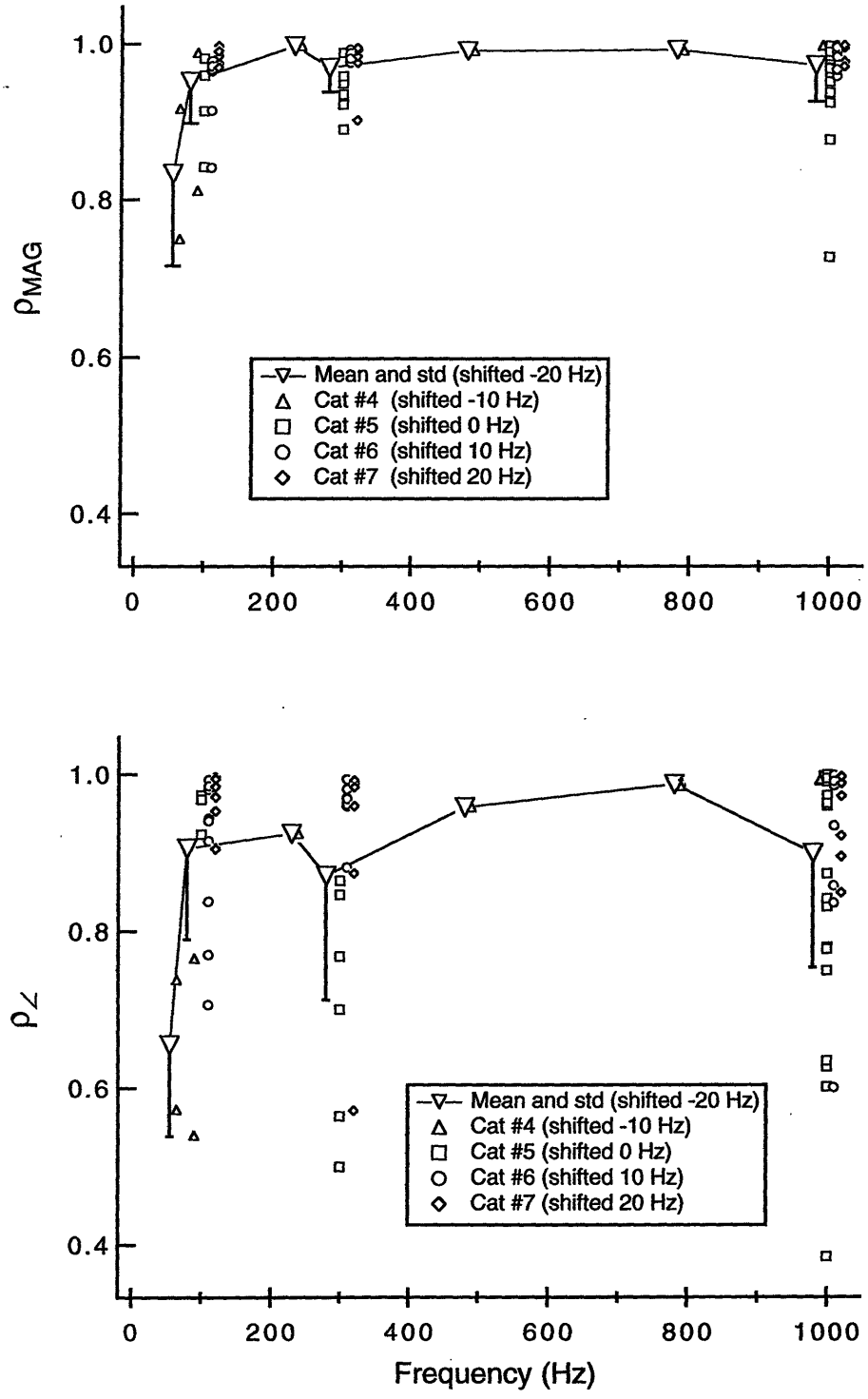

Figure 6-7: Correlation coefficients calculated for each model fit from Cats #4 to #7. Because most of the measurements were at 100, 300, or 1000 Hz the plotted points tend to overlap. To increase legibility, points for a given cat are shifted right or left by a small amount, as indicated in the keys.

than the magnitude correlation coefficients because the angle data is periodic with a period of 1 *cycle* and the computed angle correlation coefficients can change when the angle data takes different values, or is "unwrapped" around different points.

Fig. 6-8 compares the estimates of $\underline{D}$ found in Chapter 5 to those found here. The analysis in Chapter 5 assumes $\underline{C} = 0$ and $\underline{D}$ is estimated as a function of level from the single-sided level-series measurements. The estimates plotted in Fig. 6-8 are the means computed from Cats #4 to #7 using the results of Fig. 5-7 and 5-8. Pre and post-TTX measurements for Cat #6 and #7 were made; only pre-TTX measurements are included in the mean estimates shown in Fig. 6-8 so that the results from these cats don't dominate the results. Standard deviations are not included because each mean estimate from Chapter 5 is computed from only one to four data points. The simultaneous-stimuli measurement points in Fig. 6-8 are the mean values previously shown in Fig. 6-5. There do not appear to be large differences between the two methods of estimating the difference-mode gain $\underline{D}$.

6.3 Discussion

6.3.1 General model behavior

In the model described by Equation 3.1 $\underline{V_{CP}}$ depends on both the magnitudes and angles of the two complex constants $\underline{D}$ and $\underline{C}$. This section illustrates how the model's behavior depends on these quantities; the magnitudes and angles of $\underline{D}$ and $\underline{C}$ are specifically chosen and *Response* defined by Equation 6.1 is computed. The signals "*waveA*" and "*waveB*" are sinusoids of the same frequency and the variable ψ describes the phase difference

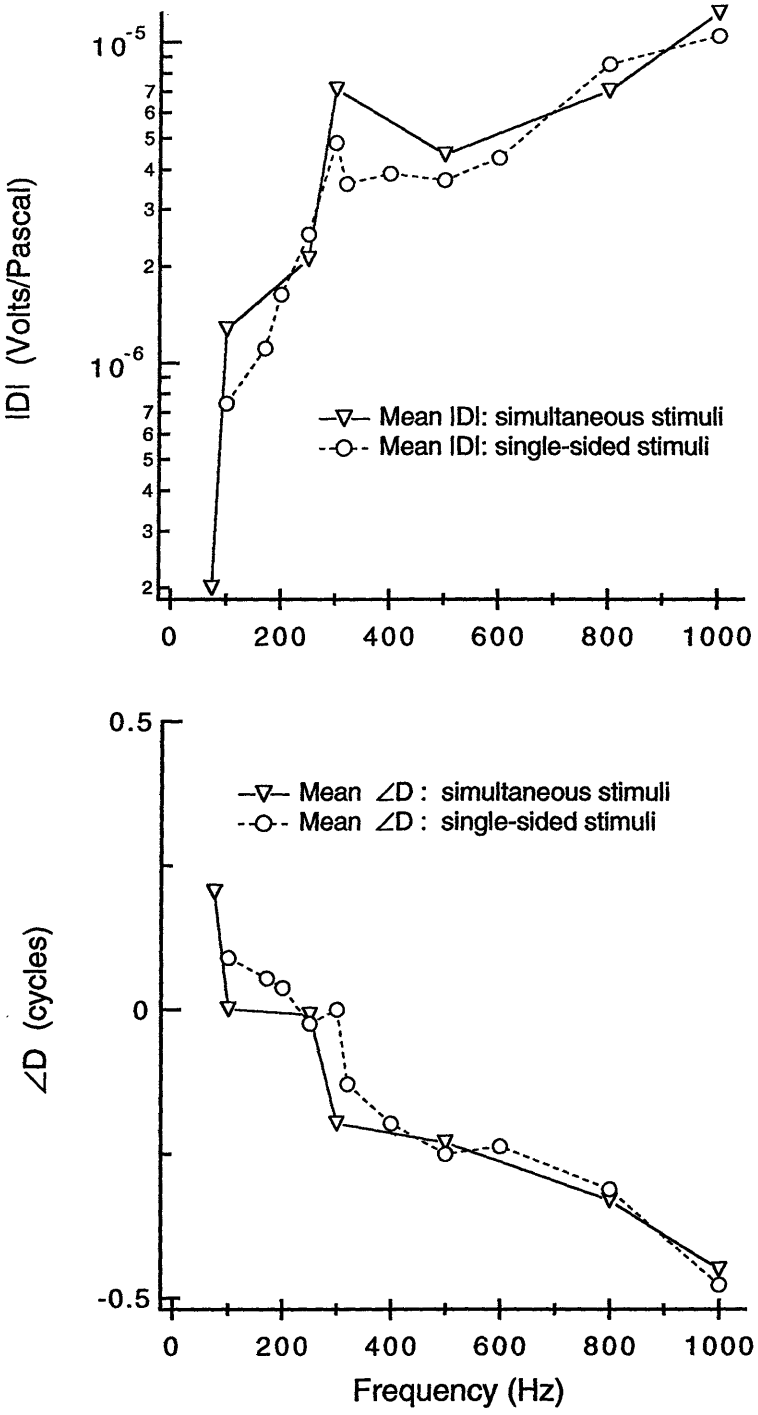

Figure 6-8: Mean estimates of D using single-sided stimuli (Chapter 5) and simultaneous stimuli (Chapter 6). The single-sided mean values of D are computed from the data shown in Figures 5-7 and 5-8; only data from Cats #4 to #7 are used, and for Cats #6 and #7 only the pre-TTX single-sided stimuli measurements are used. The simultaneous stimuli mean values of D were previously shown in Figure 6-5.

between them.

$$Response = \underline{D}(waveA - waveB) + \frac{1}{2}\underline{C}(waveA + waveB) \tag{6.1}$$

Common-mode gain of zero

A simple form of Equation 6.1 is to assume $\underline{C} = 0$.

$$Response = \underline{D}(waveA - waveB) \tag{6.2}$$

Equation 6.2 is the pressure-difference assumption of Equation 1.1; three interesting cases of Equation 6.2 are illustrated in Fig. 6-9.

1. Fig. 6-9A shows the case of $|waveA| = |waveB|$ and $\underline{D} = 1$. $|Response|$ goes to zero at $\psi = 0$ and $\angle Response$ shifts from -0.25 *cycles* at $\psi = 0^-$ to -0.75 *cycles* at $\psi = 0^+$.
2. Fig. 6-9B shows the case of $|waveA| = |waveB|$ and $\underline{D} = j$. $|Response|$ goes to zero at $\psi = 0$ and $\angle Response$ shifts from 0 *cycles* at $\psi = 0^-$ to -0.5 *cycles* at $\psi = 0^+$.
3. Fig. 6-9C shows the case of $|waveA| = 2|waveB|$ and $\underline{D} = 1$. $|Response|$ goes to a nonzero minimum of $|Response| = |waveA - waveB|$ at $\psi = 0$ and $\angle Response$ shifts from -0.25 *cycles* to 0.25 *cycles* near $\psi = 0$, but the phase shift is more gradual than the cases where $|waveA| = |waveB|$.

To summarize, $\underline{C} = 0$ requires $|Response|$ to be a minimum at $\psi = 0$. This minimum is zero only when $|waveA| = |waveB|$. When $|waveA| = |waveB|$, $\angle Response$ is undefined at $\psi = 0$ because $|Response| = 0$. In general, $|\underline{D}|$ affects $|Response|$, and $\angle\underline{D}$ affects $\angle Response$. Differences between the magnitudes of the two input waves, $|waveA|$ and $|waveB|$, can have big effects on $|Response|$ at values of ψ near zero; when these magnitudes are not equal it is impossible for $|Response|$ to reach zero.

To connect these examples to the experiments of this thesis, suppose that $\underline{P_{OW}} = waveA$, $\underline{P_{RW}} = waveB$, $\underline{V_{CP}} = Response$, and the common-mode gain is zero. This

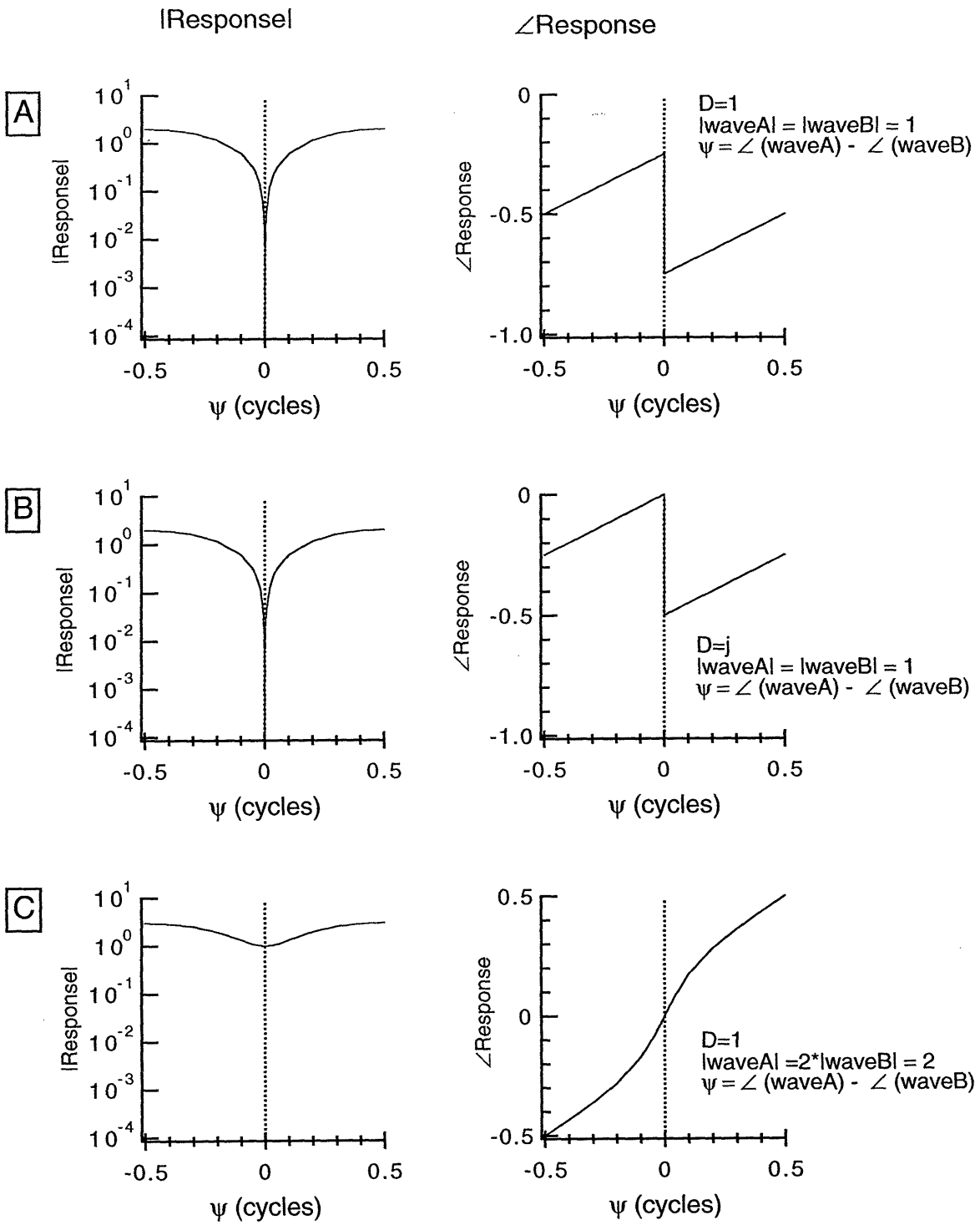

Figure 6-9: Model behavior when C=0 and (A) D=1, $|waveA| = |waveB|$; (B) D=j, $|waveA| = |waveB|$; (C) D=1, $|waveA| = 2|waveB|$.

situation is described by the pressure-difference assumption (Equation 1.1). Under these conditions $|\underline{V_{CP}}|$ should be limited by the noisefloor at $\psi = 0$ whenever $|\underline{P_{OW}}| = |\underline{P_{RW}}|$. During most of the measurements, attempts were made to keep $|\underline{P_{OW}}| = |\underline{P_{RW}}|$, but it was not uncommon for $|\underline{P_{OW}}|$ to differ from $|\underline{P_{RW}}|$ by about 0.05 to 0.1 $dB\ SPL$ (the resolution of the attenuators which set $|\underline{P_{OW}}|$ and $|\underline{P_{RW}}|$ was 0.1 dB). If $|\underline{P_{OW}}| \neq |\underline{P_{RW}}|$, the dynamic range of the magnitude response is limited

$$Dynamic\ Range = \frac{Maximum\ Response}{Minimum\ Response} = \frac{|\underline{V_{CP}}|_{\psi=0.5}}{|\underline{V_{CP}}|_{\psi=0}} = \frac{|\underline{P_{OW}} + \underline{P_{RW}}|}{|\underline{P_{OW}} - \underline{P_{RW}}|}. \tag{6.3}$$

The following example illustrates the effect of a small difference between $|\underline{P_{OW}}|$ and $|\underline{P_{RW}}|$ on the total dynamic range of the response. Suppose

$$|\underline{P_{OW}}| = 2\ Pa = 100\ dB\ SPL \tag{6.4}$$

and

$$|\underline{P_{RW}}| = 2.01\ Pa = 100.05\ dB\ SPL. \tag{6.5}$$

The maximum response is proportional to the maximum effective input stimulus

$$|(\underline{P_{OW}} - \underline{P_{RW}})|_{\psi=0.5} = 4.01\ Pa \approx 106\ dB\ SPL \tag{6.6}$$

and the minimum response is proportional to the minimum effective input stimulus

$$|(\underline{P_{OW}} - \underline{P_{RW}})|_{\psi=0} = -0.01\ Pa \approx 55\ dB\ SPL. \tag{6.7}$$

The total dynamic range is the ratio of these two values.

$$Dynamic\ Range = 51\ dB \tag{6.8}$$

$|\underline{P_{OW}}|$ and $|\underline{P_{RW}}|$ differ by only 0.05 $dB\ SPL$ in this example, but the dynamic range is 51 dB. Most of the measurement sets shown in Appendix C have dynamic ranges between 40 and 50 dB.

The observed dynamic range is limited not only by our ability to set $|\underline{P_{OW}}| = |\underline{P_{RW}}|$, but also by our ability to measure a response at exactly $\psi = 0$. If $|\underline{P_{OW}}| = |\underline{P_{RW}}|$ but the measurement made closest to $\angle\underline{P_{OW}} = \angle\underline{P_{RW}}$ is really $\angle\underline{P_{OW}} = \angle\underline{P_{RW}} \pm 0.01\ cycles$

such that $\psi = \pm 0.01\ cycles$, the maximum dynamic range of $|\underline{V_{CP}}|$ is limited to 26 dB. Here is an example to illustrate this limitation. Suppose

$$|\underline{P_{OW}}| = 2\ Pa = 100\ dB\ SPL \tag{6.9}$$

and

$$|\underline{P_{RW}}| = 2\ Pa = 100\ dB\ SPL. \tag{6.10}$$

The maximum response is proportional to the maximum effective input stimulus

$$|(\underline{P_{OW}} - \underline{P_{RW}})|_{\psi=0.5} = 4\ Pa \approx 106\ dB\ SPL \tag{6.11}$$

and the minimum response is proportional to the minimum effective input stimulus

$$|(P_{OW} - P_{RW})|_{\psi=0.01} = |2 - 2e^{0.01j}|\ Pa \approx 0.13\ Pa \approx 80\ dB\ SPL \tag{6.12}$$

The total dynamic range is the ratio of these two values.

$$Dynamic\ Range = 26\ dB \tag{6.13}$$

In the same way, a measurement made such that $\psi = \pm 0.001\ cycles$ is the closest measurement made to $\psi = 0$ gives a maximum dynamic range of about 55 dB.

It is clear that mismatches in magnitude as small as $0.05\ dB$ in magnitude and $0.001 cycles$ in angle can have severe effects on the minimum $|\underline{V_{CP}}|$ value that is measured in a given measurement set, if $\underline{C} = 0$.

Non-zero common-mode gain

This section presents examples constructed to examine the behavior of Equation 6.1 when both $|\underline{D}|$ and $|\underline{C}|$ are nonzero. Only cases where $|\underline{D}| >> |\underline{C}|$ are presented because the experimental results and model predictions shown earlier in this chapter suggest that $|\underline{D}| >> |\underline{C}|$ for the cat cochlear system. The examples here use $|\underline{D}| = 1$ and $|\underline{C}| = 0.1$ which corresponds to $CMRR = 20 dB$. Smaller values of $|\underline{C}|$ are not used because as the difference between $|\underline{D}|$ and $|\underline{C}|$ increases (as $CMRR$ increases) it becomes more difficult to observe visually the effects of $\underline{C}$ on *Response* in Equation 6.1. Three interesting cases are illustrated in Fig. 6-10.

1. Fig. 6-10A shows that when $\underline{D}$ and $\underline{C}$ have the same angle, and $|\underline{D}| >> |\underline{C}|$, $|Response|$ is a minimum at $\psi = 0$ and $\angle Response$ makes a 0.5 *cycle* transition near $\psi = 0$. The difference between this case and the one shown in Fig.6-9A, where $\underline{C} = 0$, is that at $\psi = 0$ the minimum in magnitude is limited by the common-mode component to be $\frac{1}{2}\underline{C}(waveA + waveB)$ and can never be zero, and the angle changes more slowly around $\psi = 0$.

2. Fig. 6-10B shows that when $\underline{D}$ and $\underline{C}$ differ in angle by 0.25 *cycles* the minimum value of $|Response|$ does not occur at $\psi = 0$, the 0.5 *cycle* transition in angle is not centered at $\psi = 0$, and the minimum of $|Response|$ is zero. For this special case $|Response| = 0$ at $\psi = 0.016$ *cycles* (see discussion below). Additionally, the dynamic range of $|Response|$ is infinite (only 70 dB shows due to finite sampling resolution), but $CMRR$ is still 20 dB.

3. Fig. 6-10C shows that when $\underline{D}$ and $\underline{C}$ have angles that differ by amounts other than $\pm j$, the minimum value of $|Response|$ does not generally occur at $\psi = 0$, the 0.5 *cycle* transition in angle does not generally occur at $\psi = 0$, and the minimum of $|Response|$ is not generally zero. For this case the minimum value of $|Response|$ occurs at $\psi = 0.01$ and the minimum of $|Response|$ is 0.07.

To summarize, when $|\underline{D}| >> |\underline{C}|$ and $\angle\underline{D} = \angle\underline{C}$, $|Response|$ goes to a minimum at $\psi = 0$ and this magnitude minimum is determined by $|\underline{C}|$. When $\angle\underline{D}$ and $\angle\underline{C}$ are not equal the magnitude minimum does not occur at $\psi = 0$ and $|Response|$ can have a larger dynamic range than when $\angle\underline{D} = \angle\underline{C}$. For the special case of $\angle\underline{D}$ differing from $\angle\underline{C}$ by ± 0.25 *cycles* there exists a value of ψ, ψ_0, such that $|Response|$ goes to zero. If

$$Response = 0 = \underline{D}(waveA - waveB) + \frac{1}{2}\underline{C}(waveA + waveB) \tag{6.14}$$

the ratio $\frac{\underline{D}}{\underline{C}}$ can be determined as

$$\frac{D}{C} = \frac{1}{2}\left(\frac{1 + \frac{waveA}{waveB}}{1 - \frac{waveA}{waveB}}\right) = \frac{1}{2}\left(\frac{1 + Xe^{j\psi_0}}{1 - Xe^{j\psi_0}}\right) \tag{6.15}$$

where $\frac{waveA}{waveB} = Xe^{j\psi_0}$, X is the ratio between $|waveA|$ and $|waveB|$, and ψ_0 is the phase difference between $waveA$ and $waveB$ when $|Response| = 0$. When $X = 1$, as in Fig. 6-10B, the solution of Equation 6.15 can be approximated as

$$\frac{D}{C} = \frac{-1}{jsin(\psi_0)} \tag{6.16}$$

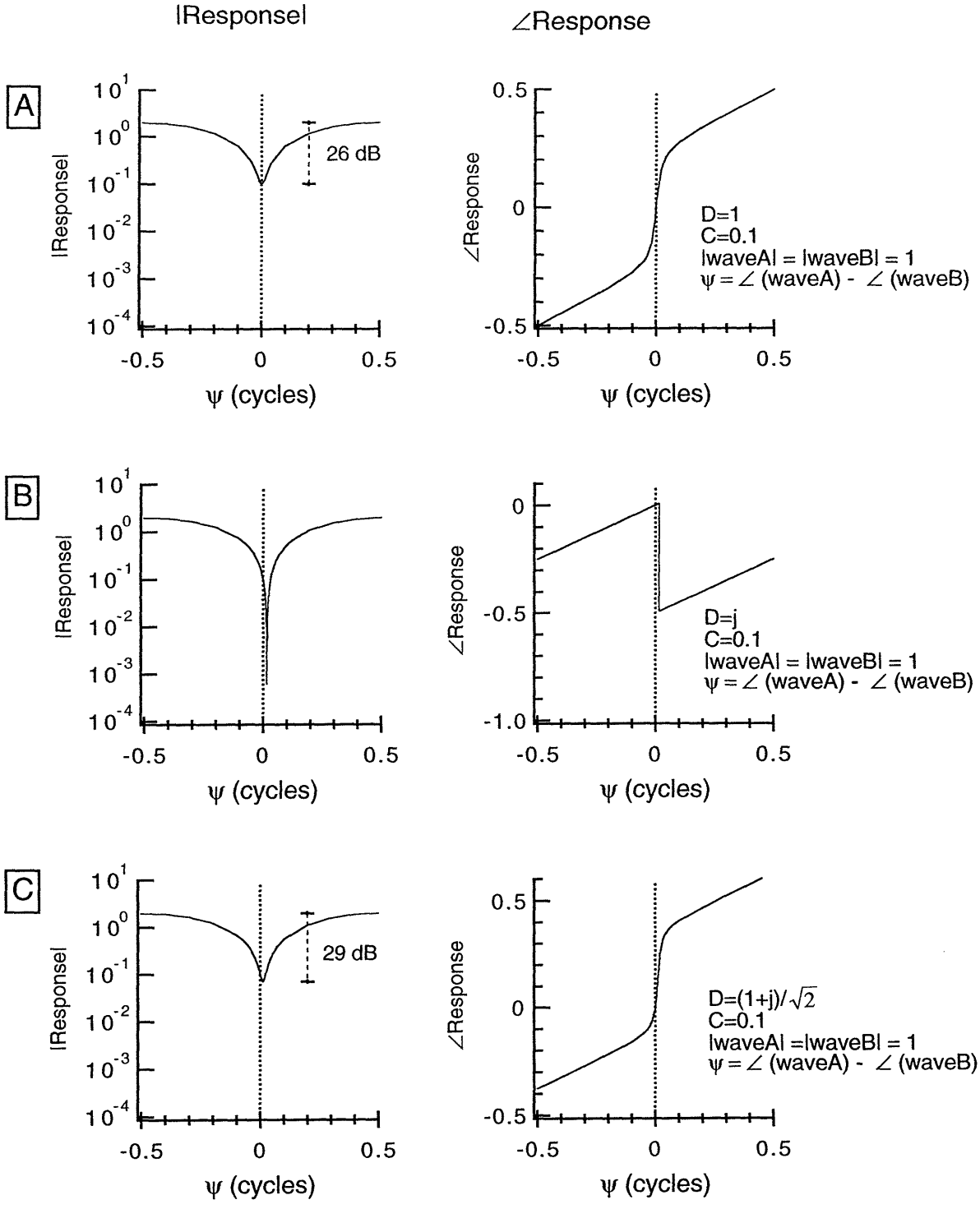

Figure 6-10: Model behavior when $|waveA| = |waveB|$ and (A) D=1, C=0.1; (B) D=j, C=0.1; (C) $D = \frac{(1+j)}{\sqrt{2}}$, C=0.1. In all three cases CMRR=20 dB.

or

$$\psi_0 = sin^{-1}(j\frac{\underline{C}}{\underline{D}}) \tag{6.17}$$

Equation 6.17 has solutions only when $\angle\underline{D}$ differs from $\angle\underline{C}$ by $\pm 0.25 cycles$; thus $|Response|$ can go to zero only under this special condition.

6.3.2 Why is it difficult to estimate C?

We have seen that the dynamic ranges of the experimental measurement sets can be limited by several factors.

1. Small deviations from $|\underline{P_{OW}}| = |\underline{P_{RW}}|$
2. The inability to make measurements at exactly ψ_{MIN}
3. Noisefloors
4. Contributions of a common-mode component to the response

It is difficult to separate the effects of these factors from each other and from measurement errors in $\underline{P_{OW}}$ and $\underline{P_{RW}}$.

To better understand the contribution of the difference-mode and common-mode components to the total cochlear response, as a function of ψ, Equation 3.1 is decomposed. If $|\underline{P_{OW}}|$ and $|\underline{P_{RW}}|$ are exactly equal then $\underline{D}$ can be found directly when $\psi = 0.5$ and $\underline{C}$ can be found directly when $\psi = 0$.

$$\underline{D} = \frac{\underline{V_{CP}}}{\underline{P_{OW}} - \underline{P_{RW}}} - \frac{1}{2}\frac{\underline{C}(\underline{P_{OW}} + \underline{P_{RW}})}{\underline{P_{OW}} - \underline{P_{RW}}} = \frac{\underline{V_{CP}}}{\underline{P_{OW}} - \underline{P_{RW}}}\,|_{\psi=0.5} = \frac{\underline{V_{CP}}}{2\underline{P_{OW}}}\,|_{\psi=0.5} \tag{6.18}$$

$$\underline{C} = 2\left[\frac{\underline{V_{CP}}}{\underline{P_{OW}} + \underline{P_{RW}}} - \frac{\underline{D}(\underline{P_{OW}} - \underline{P_{RW}})}{\underline{P_{OW}} + \underline{P_{RW}}}\right] = 2\frac{\underline{V_{CP}}}{\underline{P_{OW}} + \underline{P_{RW}}}\,|_{\psi=0} = \frac{\underline{V_{CP}}}{\underline{P_{OW}}}\,|_{\psi=0} \tag{6.19}$$

Equation 6.18 can yield a robust estimate of $\underline{D}$ even when ψ only approximates $0.5 cycles$ because $|\underline{V_{CP}}|$ is large and does not change rapidly when $\psi \approx 0.5$, and the term $\frac{\underline{V_{CP}}}{\underline{P_{OW}} - \underline{P_{RW}}}$ is much larger than the term $\frac{1}{2}\frac{\underline{C}(\underline{P_{OW}} + \underline{P_{RW}})}{\underline{P_{OW}} - \underline{P_{RW}}}$. However, when $|\underline{C}| << |\underline{D}|$ and there are

just slight deviations from $\underline{P_{OW}} = \underline{P_{RW}}$ in either magnitude or angle, Equation 6.19 can make large errors in the estimates of $\underline{C}$ because $|\underline{V_{CP}}|$ changes rapidly when $\psi \approx 0$, and the term $2\frac{\underline{V_{CP}}}{\underline{P_{OW}}+\underline{P_{RW}}}$ is on the same order as the term $\frac{\underline{D}(\underline{P_{OW}}-\underline{P_{RW}})}{\underline{P_{OW}}+\underline{P_{RW}}}$. Therefore, when $|\underline{C}| << |\underline{D}|$, the common-mode response only dominates $\underline{V_{CP}}$ when $\underline{P_{OW}} = \underline{P_{RW}}$ and the difference-mode response is much less than the common-mode response. It is difficult to make the difference-mode component of the response go to zero, or at least become smaller than the common-mode component of the response, because ψ is never exactly zero and $|\underline{P_{OW}}|$ is never exactly equal to $|\underline{P_{RW}}|$. As a result, the estimate of $\underline{C}$ is highly dependent on both the resolution of the measurement system and errors in a single measurement, while the estimate of $\underline{D}$ is not significantly affected by such factors.

6.3.3 How much is the estimate of C affected by small errors in pressure measurements?

The discussion in Chapter 4 suggests that errors in the measurements of $\underline{P_{OW}}$ and $\underline{P_{RW}}$ are probably less than 0.5 dB in magnitude and 0.01 *cycles* in angle; here we examine the effects of such errors on the estimates $\hat{\underline{D}}$, $\hat{\underline{C}}$, and $\hat{CMRR}$. To examine the effects of the errors in $|\underline{P_{OW}}|$, $|\underline{P_{RW}}|$, $\angle\underline{P_{OW}}$, and $\angle\underline{P_{RW}}$, the measured $\underline{V_{CP}}$ and $\underline{P_{RW}}$ values from the measurement set labeled "1000f_7" shown in Fig. 6-2 are held constant while errors that range from -0.5 to $0.5\,dB$ in magnitude and -0.01 to $0.01\,cycles$ in angle are added to the measured value of $\underline{P_{OW}}$. New estimates of $\underline{D}$, $\underline{C}$, and $CMRR$ are computed from Equation 3.1 for each combination of magnitude and angle error.

Fig. 6-11 shows effects on $\hat{\underline{D}}$ and $\hat{\underline{C}}$ of small errors in the measurement of $\underline{P_{OW}}$. The errors have little effect on $|\underline{D}|$ or $\angle\underline{D}$ but there are large changes in $|\underline{C}|$ and $\angle\underline{C}$. The ratio between the maximum and minimum values of $|\underline{D}|$ is nearly 1 (1.07), and the difference

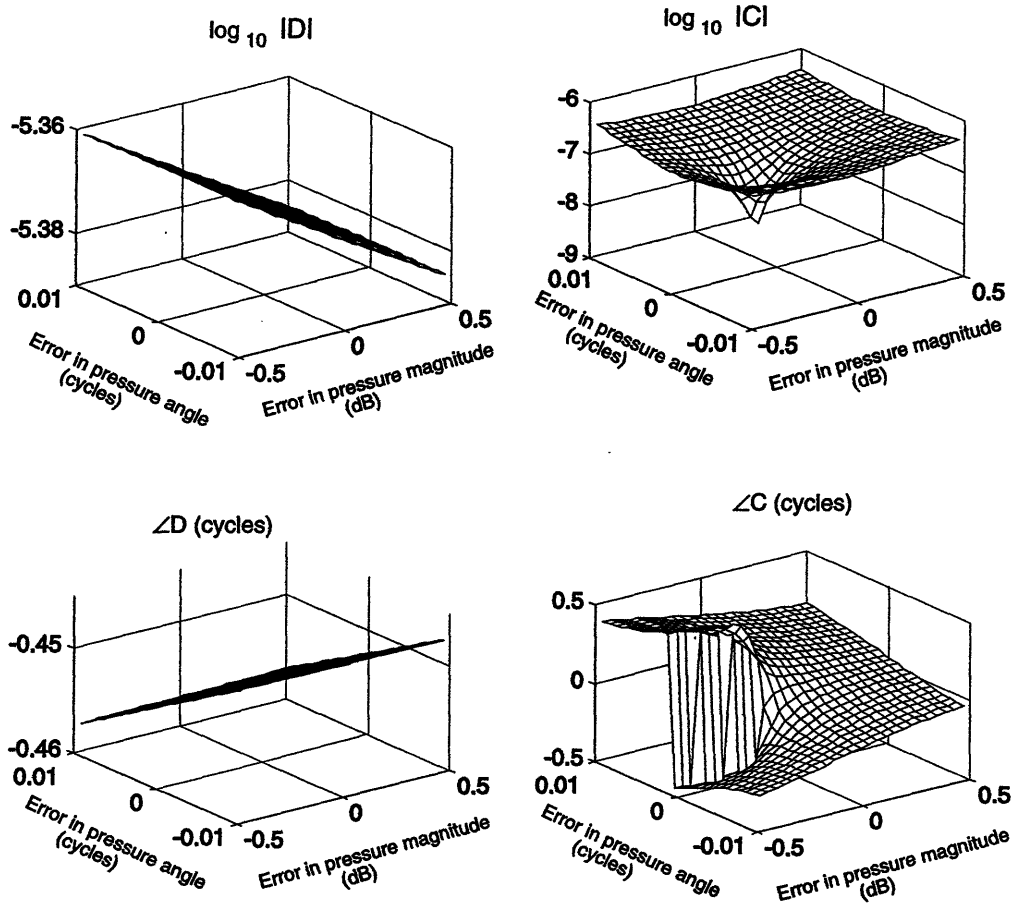

Figure 6-11: Estimates of D and C made for combinations of small errors in the magnitude and angle of P_{OW}. The errors in pressure magnitude range from -0.5 to 0.5 dB and the errors in pressure angle range from -0.01 to 0.01 cycles.

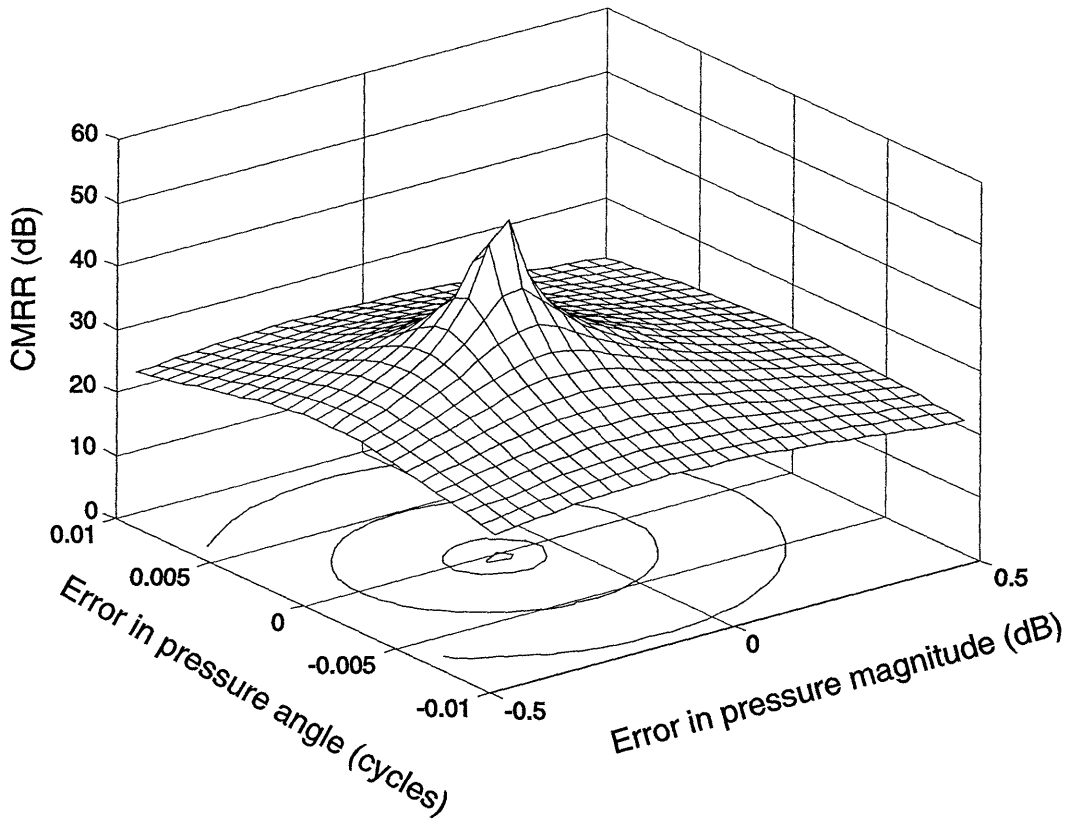

Figure 6-12: Estimates of $CMRR$ made for combinations of small errors in the magnitude and angle of P_{OW}. The errors in pressure magnitude range from -0.5 to 0.5 dB and the errors in pressure angle range from -0.01 to 0.01 cycles. Contour lines for $CMRR = 50, 40, 30, 25$ are drawn in the $CMRR = 0$ plane.

between the maximum and minimum values of $\angle\underline{D}$ is less than 0.01 *cycles*. However, the ratio between the maximum and minimum values of $|\underline{C}|$ is infinite; if the plotted points had been sampled more densely this would be visible from Fig. 6-11. The angle $\angle\underline{C}$ takes values from -0.5 to 0.5 *cycles*. Since $C\hat{M}RR$ is computed directly from $\underline{\hat{D}}$ and $\underline{\hat{C}}$, it is not surprising that $C\hat{M}RR$ shows the same type of variation as $|\underline{\hat{C}}|$; at the magnitude and angle error where $|\underline{\hat{C}}|$ goes to zero, $C\hat{M}RR$ goes to infinity (Fig. 6-12).

The procedure illustrated here, introducing errors in the measured values of $|\underline{P_{OW}}|$ and $\angle\underline{P_{OW}}$ and calculating $\underline{\hat{D}}$, $\underline{\hat{C}}$, and $C\hat{M}RR$ from each synthesized value of $|\underline{P_{OW}}|$ and $\angle\underline{P_{OW}}$, was performed on all measurement sets from Cats #4 to #7. A plot of $C\hat{M}RR$ such as the one shown in Fig. 6-12 was formed with ranges of ± 0.5 *dB* in magnitude and ± 0.01 *cycles* in angle from the original measurement. In most cases a large peak occurred at some point on the plot (the location varied) while the minimum $C\hat{M}RR$ value was never less than about 20 dB. In a few cases the maximum peak of the mesh was not contained within ± 0.5 *dB* in magnitude and ± 0.01 *cycles* in angle from the original measurement, but part of the peaked area always existed within this range.

The position of the peak in the $C\hat{M}RR$ vs. $\underline{P_{OW}}$ error analyses did not stay constant among measurement sets. In some cases consecutive measurement sets made at the same frequency and level, and with no movement of the microphone and sound-source assemblies, predict peaks in the $C\hat{M}RR$ plots that are in different quadrants. This suggests that something about the cochlear-potential response changed with time; based on the result shown in Fig. 4-3 it does not seem possible that the microphone responses could change by up to 0.2 dB in magnitude and 0.005 *cycles* in angle in a small amount of time when the microphone and sound-source assemblies were not touched.

To summarize, small errors in $\underline{P_{OW}}$ and $\underline{P_{RW}}$, and possibly small changes in the

cochlear-potential sensitivity, can cause large variations in the estimate $\hat{\underline{C}}$ and thus $\hat{CMRR}$. The upper-bound of $\underline{C}$, or the lower bound of $CMRR$, remains approximately constant for the error range examined here; $CMRR$ is rarely less than 20 dB at any frequency for any combination of magnitude and angle error introduced here. On the other hand, the lower-bound of $\underline{C}$, or the upper bound of $CMRR$, is more difficult to define. $CMRR$ has a peak value of infinity (or $|\underline{C}|$ has a minimum value of 0) for some combination of magnitude and angle error introduced here in almost all of the measurement sets. These large dependencies of $\hat{CMRR}$ and $\hat{\underline{C}}$ on the precision of the pressure measurements coupled with a possible change in cochlear sensitivity over time makes it impossible to determine an upper bound for $CMRR$ other than infinity from our measurements.

6.3.4 Comparison to Wever and Lawrence

The experimentally measured minimum of $|\underline{V_{CP}}|$ occurs at a difference in phase between the oval and round-window sound pressures $\psi = \psi_{MIN_{data}}$. $\psi_{MIN_{data}}$ is an interesting quantity because it helps describe $\underline{D}$ and $\underline{C}$. If $\underline{C} = 0$, $\psi_{MIN_{data}}$ must equal zero, but more generally $\psi_{MIN_{data}}$ is also equal to zero when $\angle\underline{D} = \angle\underline{C}$ (Chapter 6.3.1). In some of the measurements $\psi_{MIN_{data}}$ occurs when $|\underline{V_{CP}}|$ is below the noisefloor, and the precise value of $\psi_{MIN_{data}}$ is not known. However, the minimum magnitude of the model prediction, $\hat{\underline{V_{CP}}}$, which occurs at $\psi_{MIN_{model}}$, is always known. A t-test of the null hypothesis "the mean value of $\psi_{MIN_{data}}$ and the mean value of $\psi_{MIN_{model}}$ are the same", shows that there are not statistically significant differences between these two mean values at 100, 300, and 1000 Hz ($p = 0.01$). Additionally, t-tests of the null hypotheses "the mean value of $\psi_{MIN_{data}}$ is equal to zero" and "the mean value of $\psi_{MIN_{model}}$ is equal to zero", show

that there are not statistically significant differences between the mean value of $\psi_{MIN_{data}}$ and $\psi_{MIN_{data}} = 0$ and the mean value of $\psi_{MIN_{data}}$ and $\psi_{MIN_{model}} = 0$ at 100, 300, and 1000 Hz ($p = 0.01$). Since the minimum magnitude of the model prediction, $\underline{\hat{V}_{CP}}$, occurs at $\psi = \psi_{MIN_{model}} \approx \psi_{MIN_{data}} \approx 0$, we use $\psi_{MIN_{model}}$ to represent the experimental $\psi_{MIN_{data}}$ results.

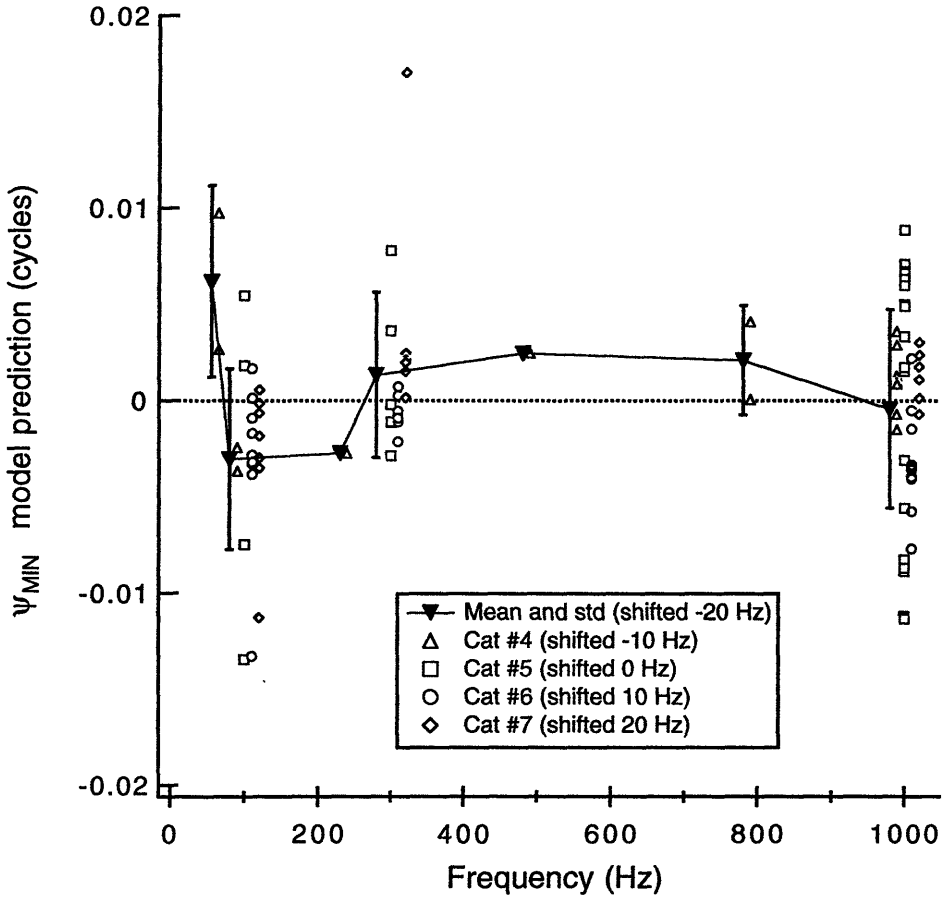

Figure 6-13: $\psi_{MIN_{model}}$, the difference in phase between the oval and round-window pressures at which the minimum magnitude of the model prediction $\hat{V}_{CP}$ occurs, for each measurement set from Cats #4 to #7. To increase legibility, points for a given cat are shifted right or left by a small amount, as indicated in the keys.

Fig.6-13 plots $\psi_{MIN_{model}}$ as a function of frequency; $\psi_{MIN_{model}}$ is within $0.02 cycles$ of

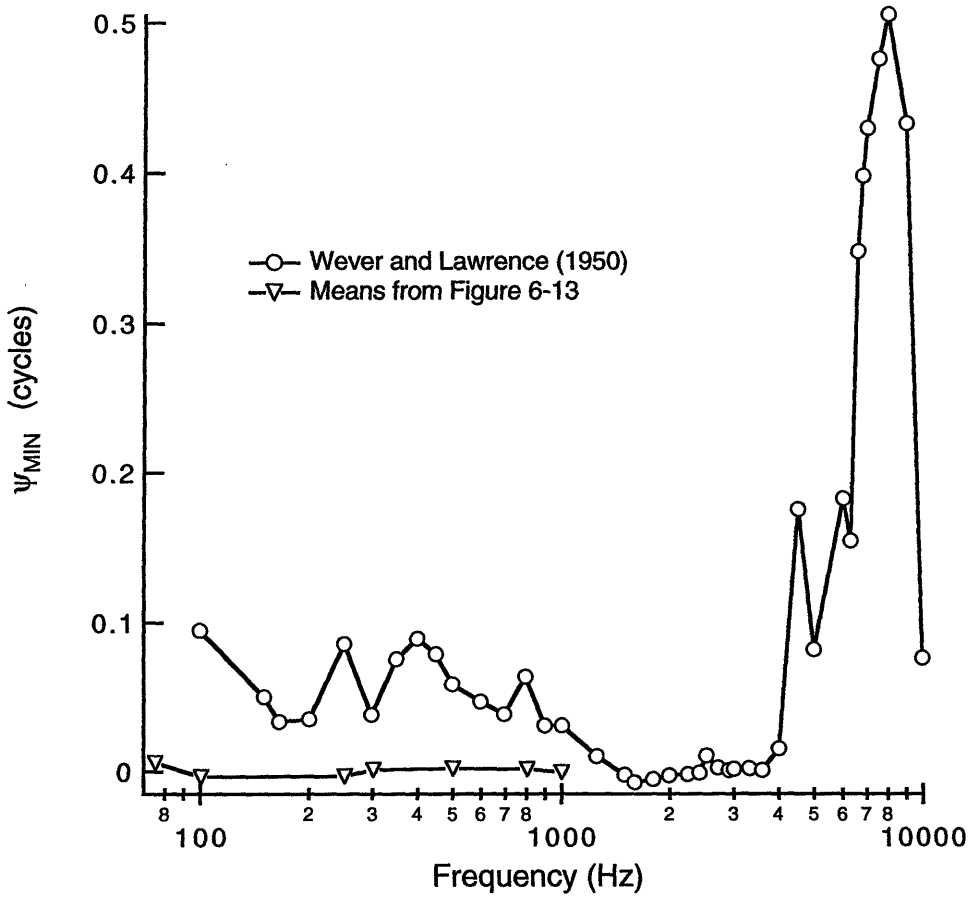

Figure 6-14: Comparison of $\psi_{MIN_{data}}$ from Wever and Lawrence (1950) with the model prediction $\psi_{MIN_{model}}$ from the data presented here. There are minor differences in $\psi_{MIN_{model}}$ and $\psi_{MIN_{data}}$ found in this thesis; see text for details.

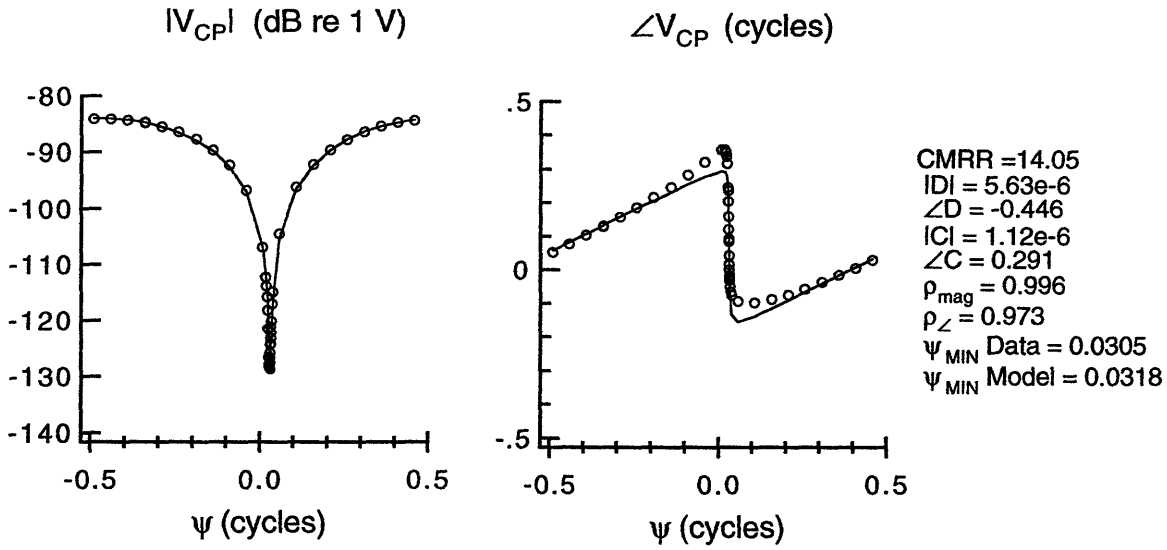

Figure 6-15: Data from measurement "1000c_7" of this thesis shifted such that $\psi_{MIN_{data}} = 0.03\,cycles$ in order to correspond to the result of Wever and Lawrence (1950). The linear fit to this shifted data results in $\hat{CMRR} = 14\,dB$, a decrease of $21\,dB$ from the result found in this thesis.

$\psi = 0$ for all measurement sets from Cats #4 to #7. Fig.6-14 compares the means values of $\psi_{MIN_{model}}$ found here to the values of $\psi_{MIN_{data}}$ measured by Wever and Lawrence (1950). The Wever and Lawrence values appear significantly different from $\psi_{MIN_{data}} \approx 0$ for frequencies between 100 and 1000 Hz, but the measurements reported in this thesis suggest that $\psi_{MIN_{data}}$ and $\psi_{MIN_{model}}$ occur at $\psi \approx 0$.

Differences between the results found in this thesis and those found by Wever and Lawrence are illustrated as follows. The ψ values from the data of measurement set "1000c_7", shown in Fig. 6-2, are shifted by $0.03\,cycles$ (the $\psi_{MIN_{data}}$ reported by Wever and Lawrence, 1950) and the least-squares fit is again applied to the data. This result is shown in Fig. 6-15; the shifted data is barely distinguishable from the result in Fig. 6-2. However the shift of only $0.03\,cycles$ in $\psi_{MIN_{data}}$ has a significant affect on the estimates of $\underline{C}$ and $CMRR$; this shift increases $|\hat{\underline{C}}|$ from $1.04 * 10^{-7}$ to $1.12 * 10^{-6}$ and reduces

$\hat{CMRR}$ from $35dB$ to $14dB$. Thus the results of Wever and Lawrence suggest much lower $\hat{CMRR}$ values than those found here. The nonzero values of ψ_{MIN} reported by Wever and Lawrence between 100 and 1000 Hz are suggestive of a significant common-mode component of the cochlear-potential response.

6.3.5 Comments on the Békésy result

Audiometric results from Békésy (1936a; 1960, Fig. 5-10) suggestive of a nonzero common-mode gain were discussed in Chapter 1.3. Briefly, using ears with no ossicles Békésy measured an increase in hearing sensitivity as frequency decreased; it is presumed that this increased sensitivity was correlated with a decrease in the pressure difference between the oval and round windows. If this is true, such a result is not consistent with the experimental results of this thesis. However, several factors can possibly explain the Békésy result.

The threshold measurements performed on the ears with no ossicles do not necessarily measure the threshold of hearing of the ossicle-less ear. Instead, the thresholds are determined by the most sensitive sensation to an acoustic stimulus presented to the ear with a head phone. One possibility is that a tactile sensation had a lower threshold than the hearing sensation for the subjects tested. Between 5 and 20 Hz the average threshold measured on these subjects is within one order of magnitude of one measure of tactile thresholds to intense sound stimuli (Békésy 1936b; 1960, Fig. 7-48). Another possibility is that "acoustic crosstalk" occurred between the earphone and the contralateral "normal" ear. It does not appear that potential responses from the normal ear were masked.

Chapter 7

Summary

Experimental results which directly support the common assumption that the cochlea responds to the difference in pressure between the oval and round windows were presented. The cochlear response was represented as two components: the difference-mode response results from the difference in pressure between the oval and round windows and the common-mode response results from the summation in the pressures at the oval and round windows. The common-mode response was difficult to measure because it was small compared to the total cochlear response. A conservative summary of our data is that the common-mode gain is at least one order of magnitude smaller than the difference-mode gain. However, most of our data is also consistent with a common-mode gain of zero. Thus the ratio between the difference-mode gain and the common-mode gain, CMRR, is between 20 dB and infinity.

It is not trivial to put a tighter bound on this large CMRR range. To decrease the current range, the uncertainties in pressure measurements of less than 0.5 dB in magnitude and 0.01 cycles in angle must be reduced. Also, further study of how the cochlear-potential response changes with time is needed.

The importance of the difference-mode response to hearing suggests that procedures such as the type IV tympanoplasty should improve hearing in ears with no ossicles. Surgeons should continue attempts to maximize the pressure difference between the oval and round windows.

Appendix A

Summary of experimental animals and calibrations

Appendix A summarizes all experiments used to develop the methodology and to obtain results for this thesis. Information specific to each cat is briefly discussed. Measurements of the acoustic isolation between $\underline{P_{OW}}$ and $\underline{P_{RW}}$, as shown in Fig. 2-3, are presented for each experimental animal. Also, changes in the calibrations of the sound-source and microphone assemblies, as depicted in Fig. 4-1 and 4-2, are shown for each experiment. Measurements used to define all noisefloors are displayed in tables. Responses from Cats #6 and #7 to clicks and tone bursts are shown for both pre and post-TTX measurements.

A.1 Brief description of each experiment

Cat#1: July 14, 1993

Both single-sided and simultaneous-stimuli measurements were made on the left ear. The sound sources were not re-calibrated during the experiment. At the end of the

experiment a calibration was performed and the result was significantly different from the calibration at the beginning of the experiment; the sound-pressure measurements of magnitude and angle by the oval and round-window microphones are questionable to within several dB in magnitude and several degrees in angle. At the end of the experiment the earcanal was found to be full of fluid a few minutes after the removal of the oval-window sound source and microphone. It is not known how much of this fluid was in the earcanal and middle-ear space during the experiment or how much of the fluid seeped into the earcanal from the tissue surrounding the meatus after the removal of the microphone. Additionally, condensation was present on the diaphragm of the earcanal microphone. There was no fluid in the bulla cavity and no condensation on the round-window microphone. The round window looked opaque and vascular; it is possible that an infection existed. In subsequent experiments the sound systems were recalibrated several times over the course of the experiment, the middle-ear air spaces were monitored and the cats were given penicillin to fight infections.

Cat#2: July 27, 1993

Severe bleeding occurred during the first attempt to plug the foramen of the left middle-ear space. The right ear was surgically prepared and more severe bleeding occurred when the external carotid was cut. The cat survived and single-sided and simultaneous-stimuli measurements were made but responses were not repeatable during the simultaneous stimuli measurements. Additionally muscular activity superimposed on the cochlear-potential response was observed.

Cat#3: August 5, 1993

There were no physiologic problems with the cat. Numerous single-sided and simultaneous-stimuli measurements were made on the left ear. In several cases the pressures at the two windows were not equal in magnitude; instead the pressures were chosen such that the resultant single-sided cochlear-potential magnitudes were equal. The system was re-calibrated several times during the experiment. Variations in calibrations occurred which were significantly greater than those in the final four experiments.

The stability of the acoustic systems was increased substantially after this experiment. Parts of the couplers between the sound-sources and microphones were modified to have tighter fits. This alteration allowed the acoustic assemblies to be moved without large changes in calibration (Chapter 4).

Cat#4: September 22, 1993

There were no physiologic problems with the cat. The acoustic systems were re-calibrated several times during the experiment and the changes in calibration were much smaller than previous experiments; these changes were on the order of a few tenths of a dB in magnitude and a hundredth of a cycle in angle (Fig. A-12 and A-13). Measurements were made at 75 Hz, 100 Hz, 250 Hz, 500 Hz, 800 Hz, and 1000 Hz. Prior to this experiment the cochlear-potential electrode was coupled through a 1000 Ω resistor to ground. Radiation from the sound sources at maximum input levels did not produce an electrical artifact that could be recorded by the resistor - electrode system.

Cat#5: March 21, 1994

There were no physiologic problems with the cat. The acoustic systems were re-calibrated several times during the experiment and the changes in calibration were less than 0.2 dB in magnitude and less than 0.003 cycles in angle (Fig. A-14 and A-15). After each calibration a small brass tube was used to couple the two sound-source and microphone assemblies together. A sound common to both microphones was produced and it was confirmed that the two microphone calibrations were consistent. This procedure was repeated after the assemblies were decoupled from the cat. Measurements were made at 100 Hz, 300 Hz, and 1000 Hz on the right ear. The effect of artifactual coupling from the earphones to the cochlear-potential electrode was not checked. The distance from the oval window to the position of the probe tube in the earcanal was measured to be 4.9 mm, and the distance from the round window to the position of the probe tube on the bulla cavity was measured to be 7.6 mm; the difference is 2.7 mm.

Cat#6: August 11, 1994

There were no physiologic problems with the cat. The system was re-calibrated several times during the experiment and the changes were less than 0.2 dB in magnitude and less than 0.004 cycles in angle (Fig. A-16 and A-17). The calibrations were checked with the small brass tube described above. Measurements were made at 100 Hz, 300 Hz, and 1000 Hz on the right ear. TTX was applied to reduce the neural component of the cochlear-potential response (CAP). A significant electrical artifact from the sound source was found at the end of the experiment. When the sound sources were plugged with cotton and then recoupled to the cat the round-window-electrode response increased linearly with input voltage. The highest levels were comparable to and possibly greater than

the lowest cochlear-potential measurements made during the experiment; it is likely that the simultaneous-stimuli cochlear-potential measurements were contaminated by this electrical artifact when $|\underline{V_{CP}}|$ was near a minimum.

Cat#7: September 8, 1994

There were no physiologic problems with the cat. The system was re-calibrated several times during the experiment and the changes were less than 0.8 dB in magnitude and less than 0.015 cycles in angle (Fig. A-18 and A-19). Measurements were made at 100 Hz, 300 Hz, and 1000 Hz on the right ear. The calibrations were checked with the small brass tube described above. TTX was applied to eliminate the neural component of the cochlear-potential response. All cables used in the experiments were shielded and no electrical artifact was detectable.

A.2 Acoustic crosstalk for each animal

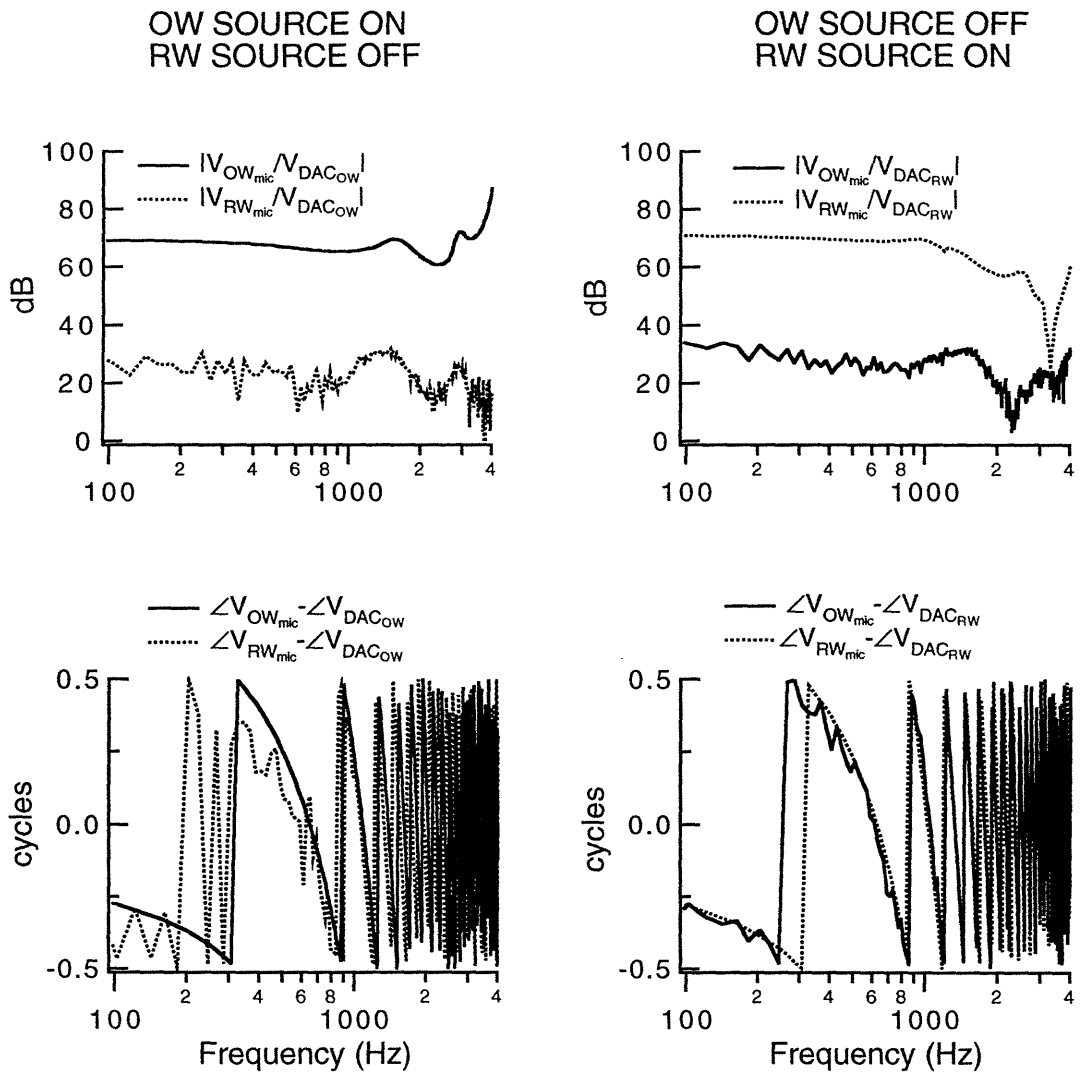

Figure A-1: Measurements of acoustic crosstalk between the tympanic and bulla cavities from Cat #1. LEFT: Measurement of the transfer function between the oval-window microphone response $V_{OW_{mic}}$ and the oval-window sound-source input $V_{DAC_{OW}}$, and measurement of the transfer function between the round-window microphone response $V_{RW_{mic}}$ and the oval-window sound-source input $V_{DAC_{OW}}$. The round-window sound-source was off. RIGHT: Measurement of the transfer function between the oval-window microphone response $V_{OW_{mic}}$ and the round-window sound-source input $V_{DAC_{RW}}$, and measurement of the transfer function between the round-window microphone response $V_{RW_{mic}}$ and the round-window sound-source input $V_{DAC_{RW}}$. The oval-window sound-source was off.

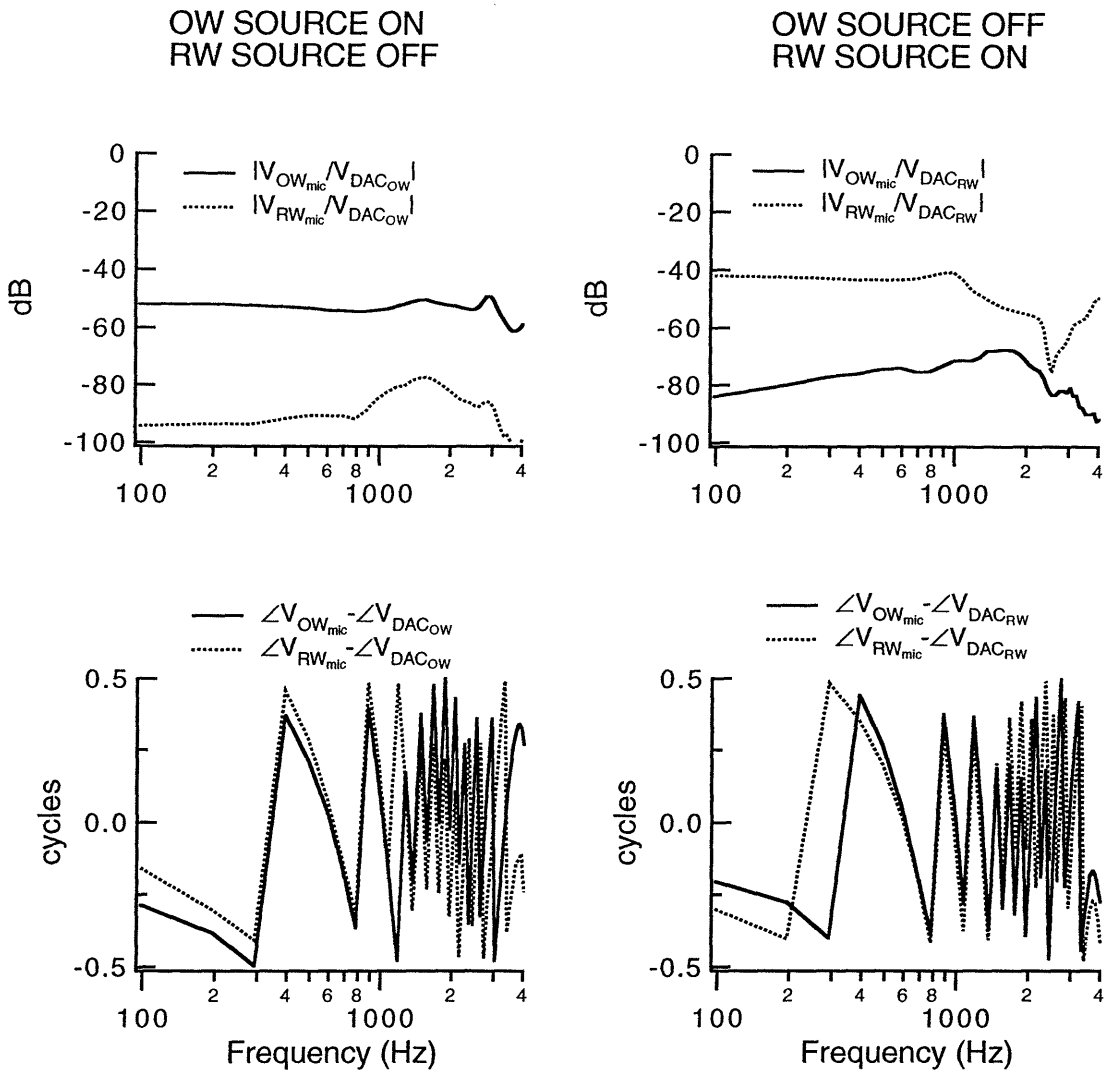

Figure A-2: Measurements of acoustic crosstalk between the tympanic and bulla cavities from Cat #2. LEFT: Measurement of the transfer function between the oval-window microphone response $V_{OW_{mic}}$ and the oval-window sound-source input $V_{DAC_{OW}}$, and measurement of the transfer function between the round-window microphone response $V_{RW_{mic}}$ and the oval-window sound-source input $V_{DAC_{OW}}$. The round-window sound-source was off. RIGHT: Measurement of the transfer function between the oval-window microphone response $V_{OW_{mic}}$ and the round-window sound-source input $V_{DAC_{RW}}$, and measurement of the transfer function between the round-window microphone response $V_{RW_{mic}}$ and the round-window sound-source input $V_{DAC_{RW}}$. The oval-window sound-source was off.

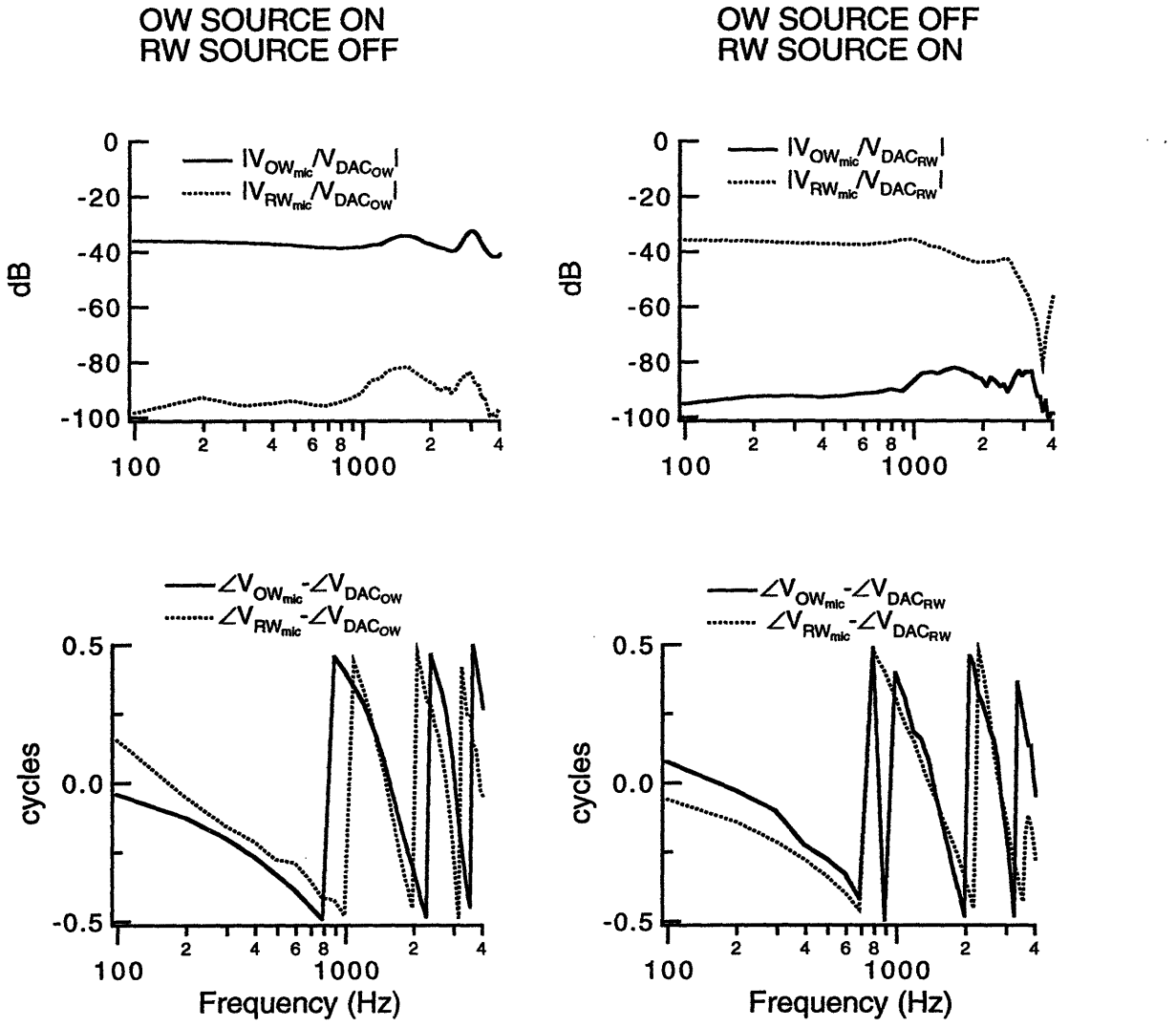

Figure A-3: Measurements of acoustic crosstalk between the tympanic and bulla cavities from Cat #3. LEFT: Measurement of the transfer function between the oval-window microphone response $V_{OW_{mic}}$ and the oval-window sound-source input $V_{DAC_{OW}}$, and measurement of the transfer function between the round-window microphone response $V_{RW_{mic}}$ and the oval-window sound-source input $V_{DAC_{OW}}$. The round-window sound-source was off. RIGHT: Measurement of the transfer function between the oval-window microphone response $V_{OW_{mic}}$ and the round-window sound-source input $V_{DAC_{RW}}$, and measurement of the transfer function between the round-window microphone response $V_{RW_{mic}}$ and the round-window sound-source input $V_{DAC_{RW}}$. The oval-window sound-source was off.

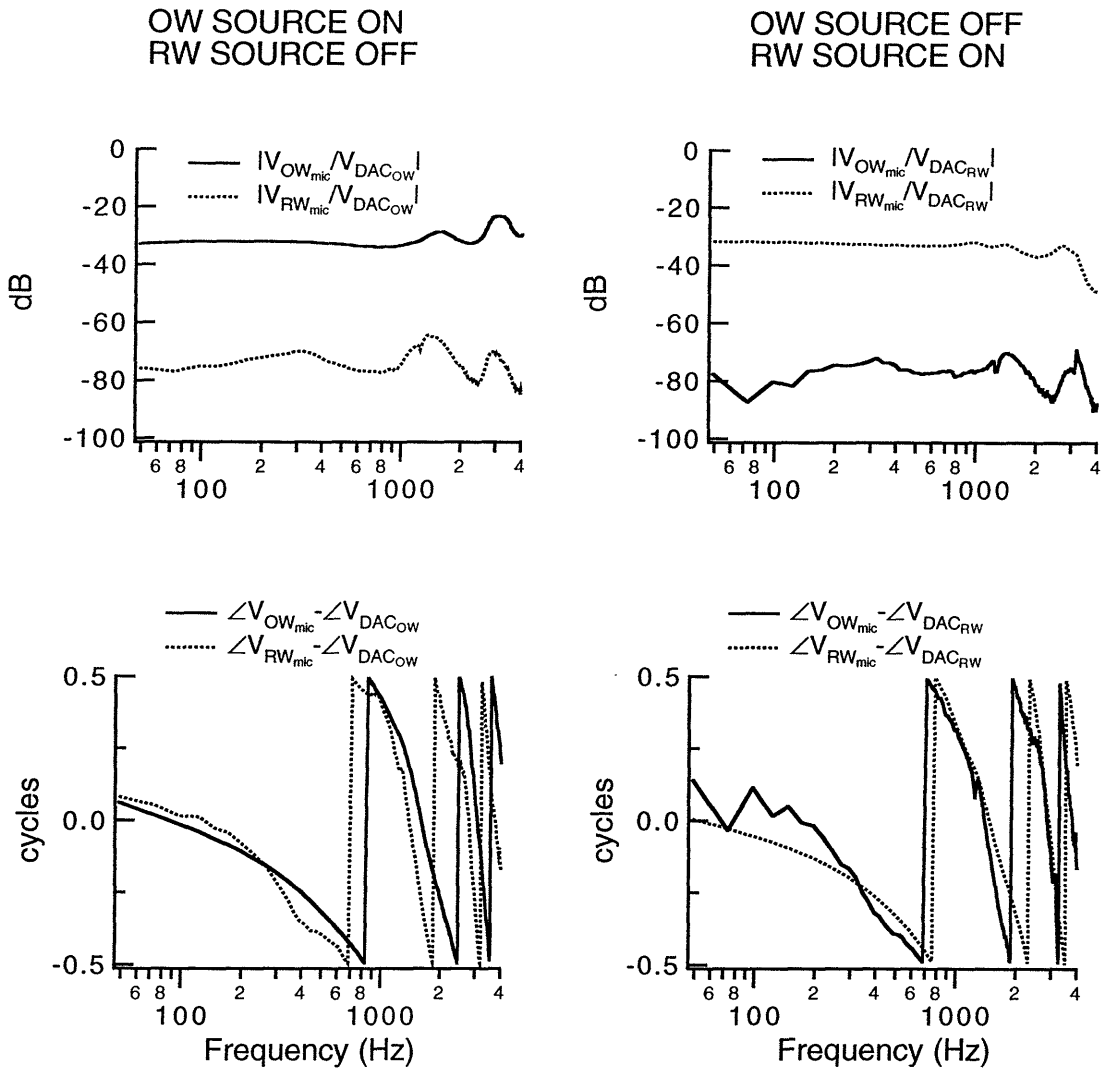

Figure A-4: Measurements of acoustic crosstalk between the tympanic and bulla cavities from Cat #4. LEFT: Measurement of the transfer function between the oval-window microphone response $V_{OW_{mic}}$ and the oval-window sound-source input $V_{DAC_{OW}}$, and measurement of the transfer function between the round-window microphone response $V_{RW_{mic}}$ and the oval-window sound-source input $V_{DAC_{OW}}$. The round-window sound-source was off. RIGHT: Measurement of the transfer function between the oval-window microphone response $V_{OW_{mic}}$ and the round-window sound-source input $V_{DAC_{RW}}$, and measurement of the transfer function between the round-window microphone response $V_{RW_{mic}}$ and the round-window sound-source input $V_{DAC_{RW}}$. The oval-window sound-source was off.

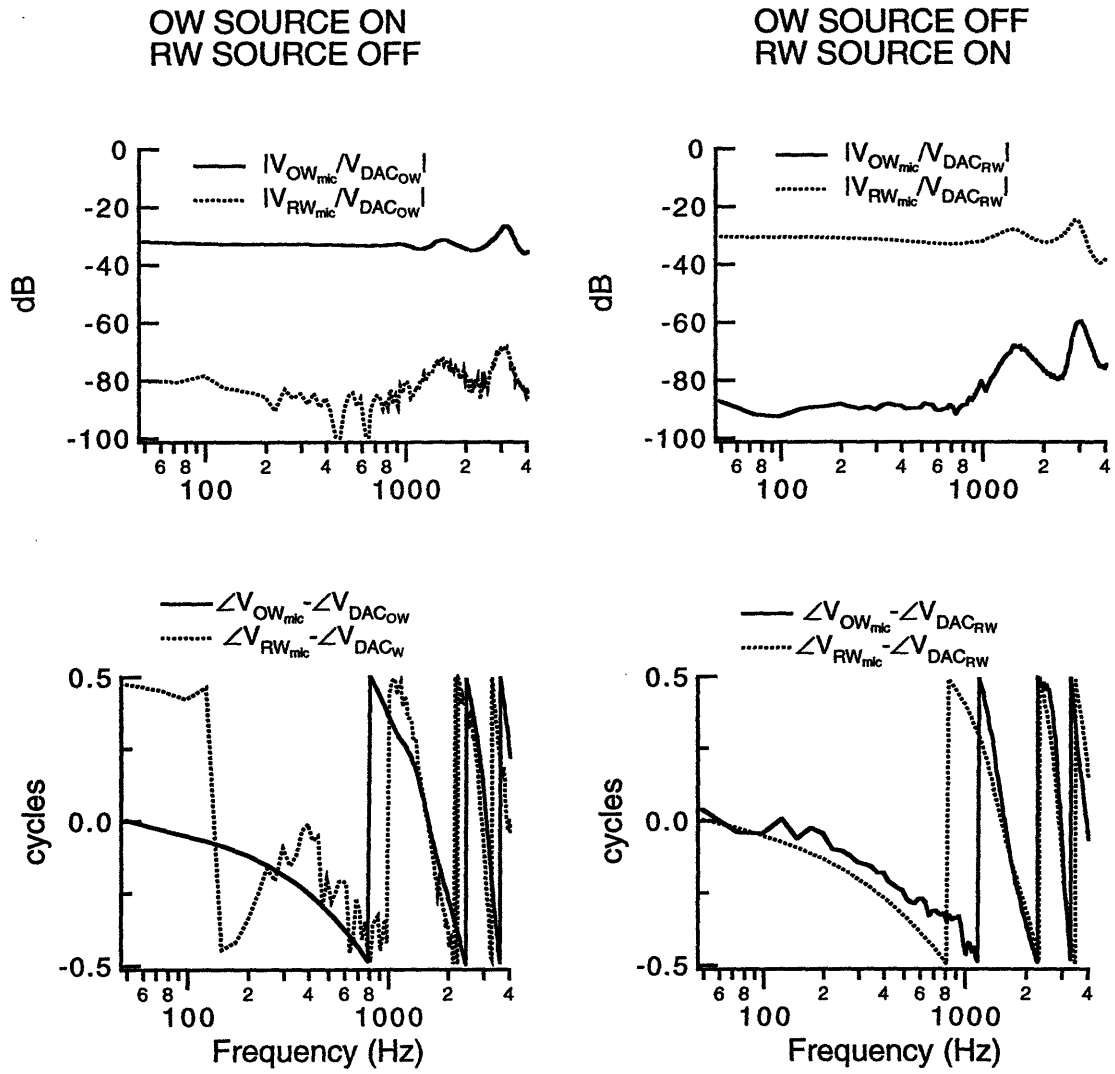

Figure A-5: Measurements of acoustic crosstalk between the tympanic and bulla cavities from Cat #5. LEFT: Measurement of the transfer function between the oval-window microphone response $V_{OW_{mic}}$ and the oval-window sound-source input $V_{DAC_{OW}}$, and measurement of the transfer function between the round-window microphone response $V_{RW_{mic}}$ and the oval-window sound-source input $V_{DAC_{OW}}$. The round-window sound-source was off. RIGHT: Measurement of the transfer function between the oval-window microphone response $V_{OW_{mic}}$ and the round-window sound-source input $V_{DAC_{RW}}$, and measurement of the transfer function between the round-window microphone response $V_{RW_{mic}}$ and the round-window sound-source input $V_{DAC_{RW}}$. The oval-window sound-source was off.

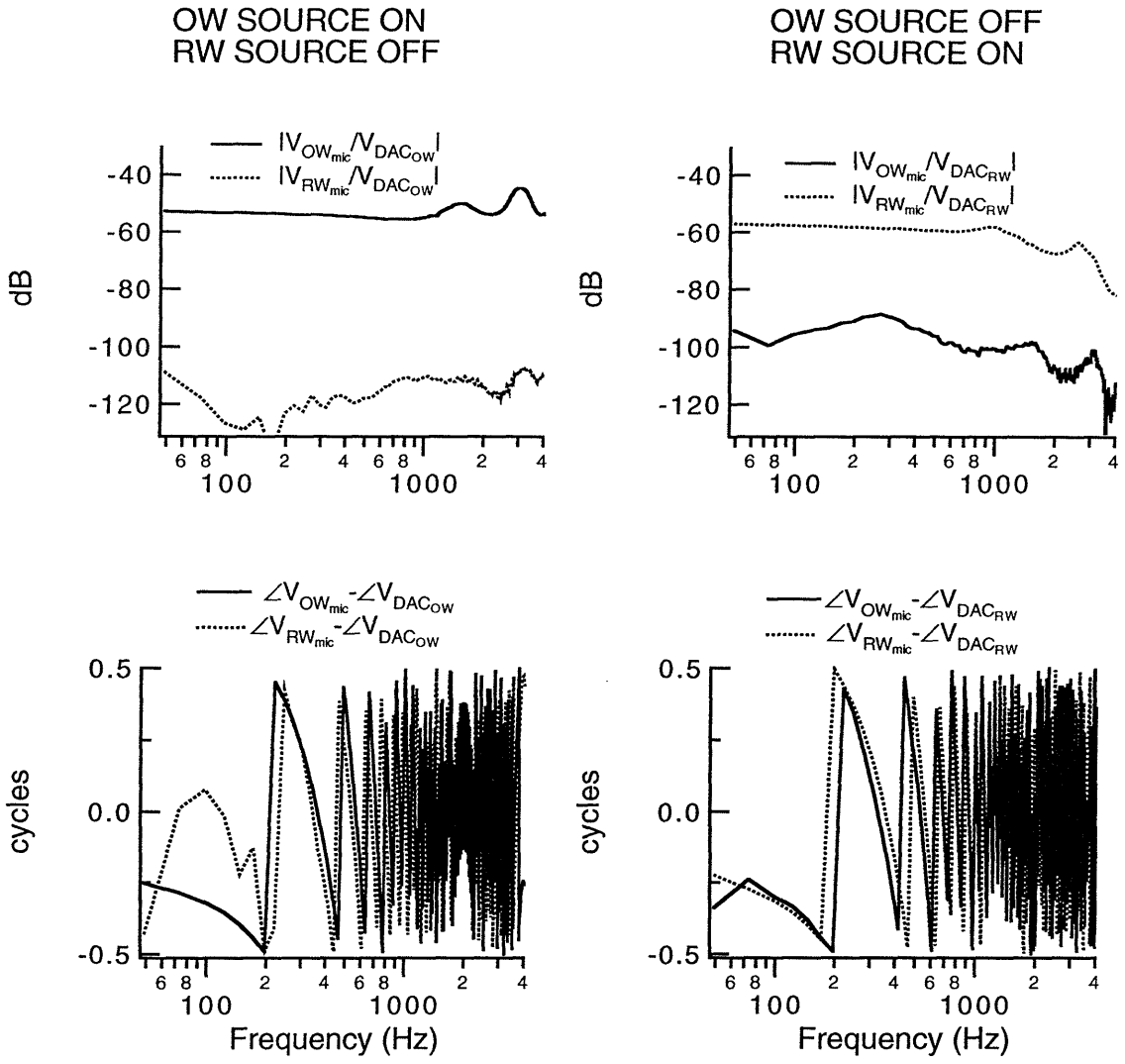

Figure A-6: Measurements of acoustic crosstalk between the tympanic and bulla cavities from Cat #6. LEFT: Measurement of the transfer function between the oval-window microphone response $V_{OW_{mic}}$ and the oval-window sound-source input $V_{DAC_{OW}}$, and measurement of the transfer function between the round-window microphone response $V_{RW_{mic}}$ and the oval-window sound-source input $V_{DAC_{OW}}$. The round-window sound-source was off. RIGHT: Measurement of the transfer function between the oval-window microphone response $V_{OW_{mic}}$ and the round-window sound-source input $V_{DAC_{RW}}$, and measurement of the transfer function between the round-window microphone response $V_{RW_{mic}}$ and the round-window sound-source input $V_{DAC_{RW}}$. The oval-window sound-source was off.

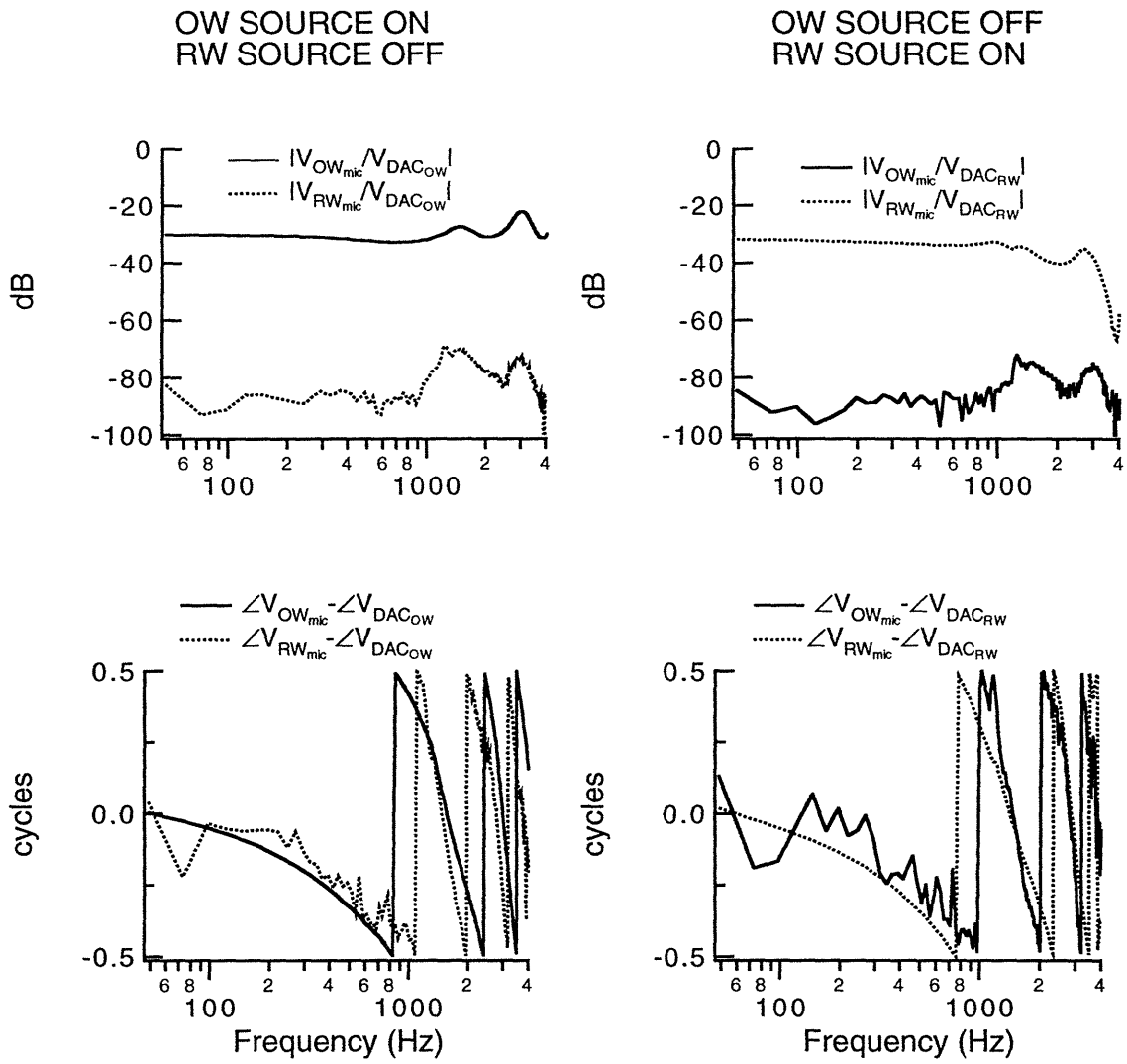

Figure A-7: Measurements of acoustic crosstalk between the tympanic and bulla cavities from Cat #7. LEFT: Measurement of the transfer function between the oval-window microphone response $V_{OW_{mic}}$ and the oval-window sound-source input $V_{DAC_{OW}}$, and measurement of the transfer function between the round-window microphone response $V_{RW_{mic}}$ and the oval-window sound-source input $V_{DAC_{OW}}$. The round-window sound-source was off. RIGHT: Measurement of the transfer function between the oval-window microphone response $V_{OW_{mic}}$ and the round-window sound-source input $V_{DAC_{RW}}$, and measurement of the transfer function between the round-window microphone response $V_{RW_{mic}}$ and the round-window sound-source input $V_{DAC_{RW}}$. The oval-window sound-source was off.

A.3 Changes in microphone calibration

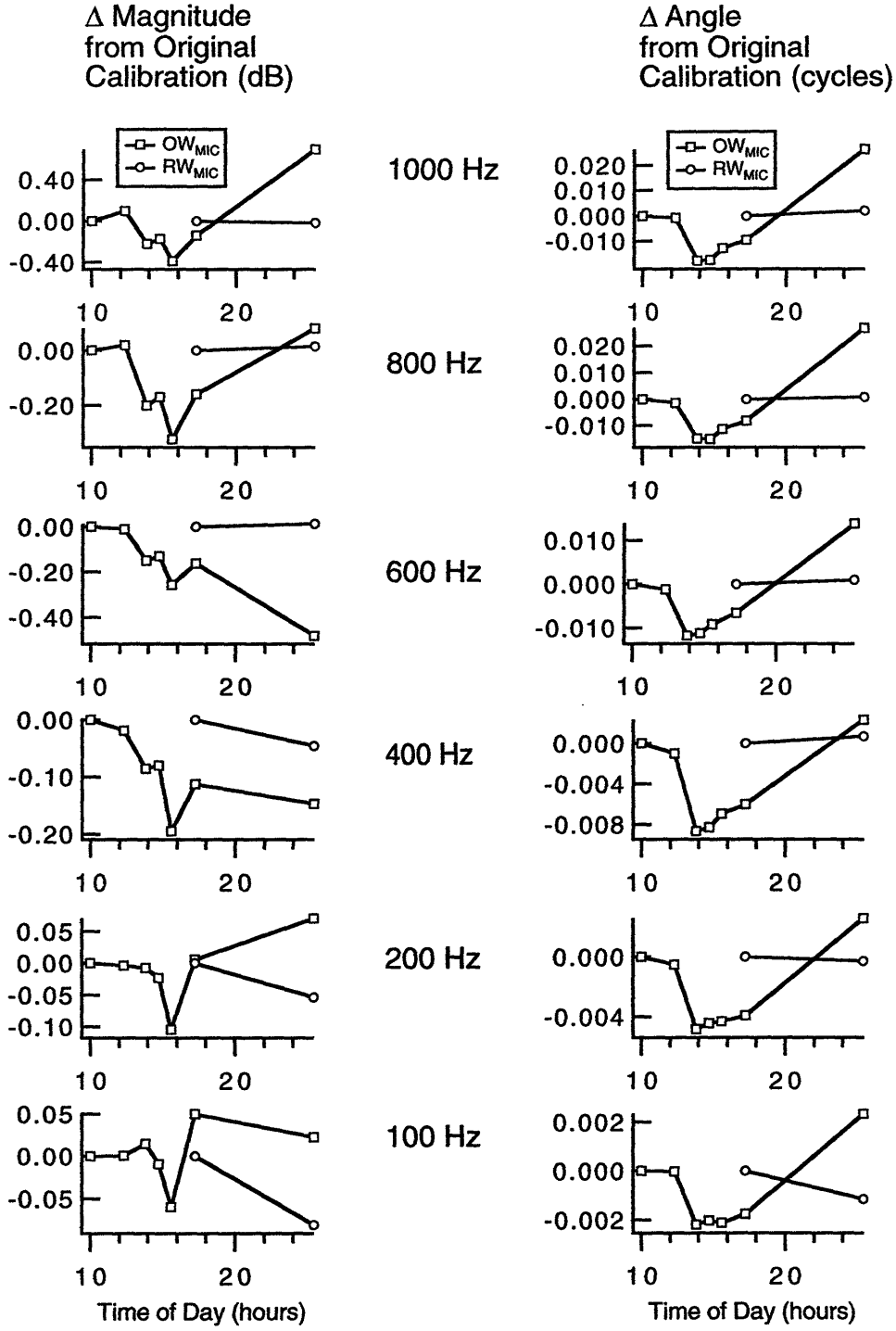

Figure A-8: The differences in $\frac{SPL}{V_{OW_{mic}}}$ and $\frac{SPL}{V_{RW_{mic}}}$ between the initial calibration and subsequent calibrations during the experiment on Cat #2. The first measurement of $\frac{SPL}{V_{OW_{mic}}}$ ($\frac{SPL}{V_{RW_{mic}}}$) was used to normalize all succeeding measurements of $\frac{SPL}{V_{OW_{mic}}}$ ($\frac{SPL}{V_{RW_{mic}}}$); magnitudes (in dB) and angles (in cycles) of the ratios are plotted. Time of day = 10 hours is the time of initial calibration.

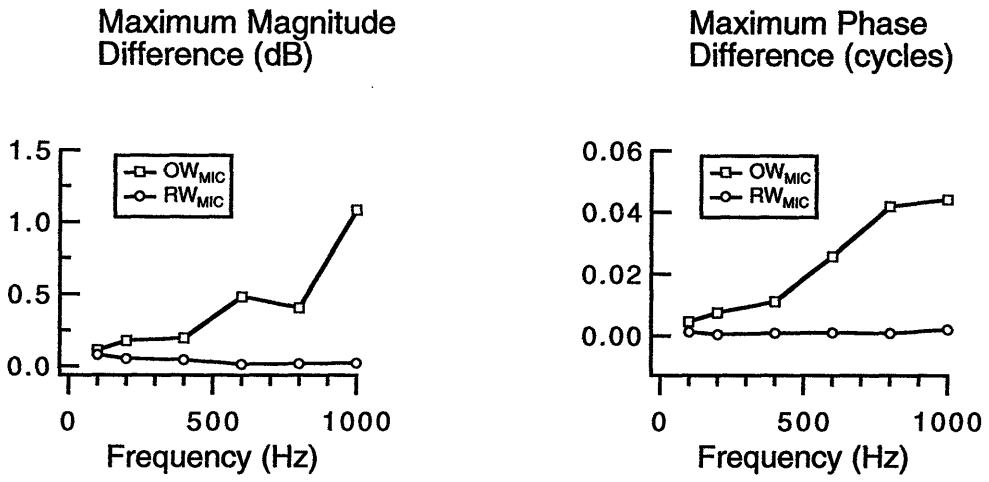

Figure A-9: The maximum changes in $\frac{SPL}{V_{OW_{mic}}}$ and $\frac{SPL}{V_{RW_{mic}}}$ as a function of frequency during the experiment on Cat #2.

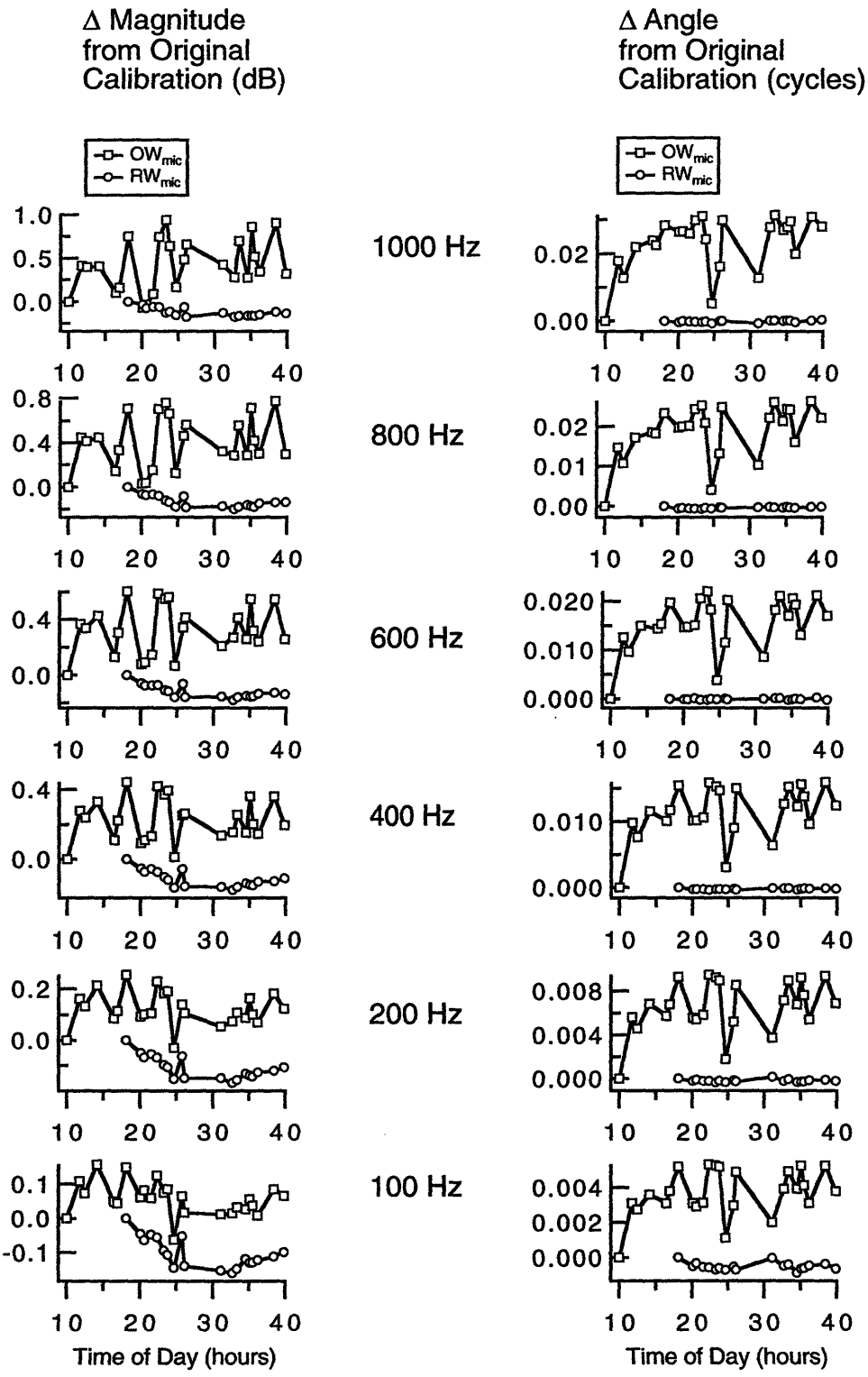

Figure A-10: The differences in $\frac{SPL}{V_{OW_{mic}}}$ and $\frac{SPL}{V_{RW_{mic}}}$ between the initial calibration and subsequent calibrations during the experiment on Cat #3. The first measurement of $\frac{SPL}{V_{OW_{mic}}}$ ($\frac{SPL}{V_{RW_{mic}}}$) was used to normalize all succeeding measurements of $\frac{SPL}{V_{OW_{mic}}}$ ($\frac{SPL}{V_{RW_{mic}}}$); magnitudes (in dB) and angles (in cycles) of the ratios are plotted. Time of day = 10 hours is the time of initial calibration.

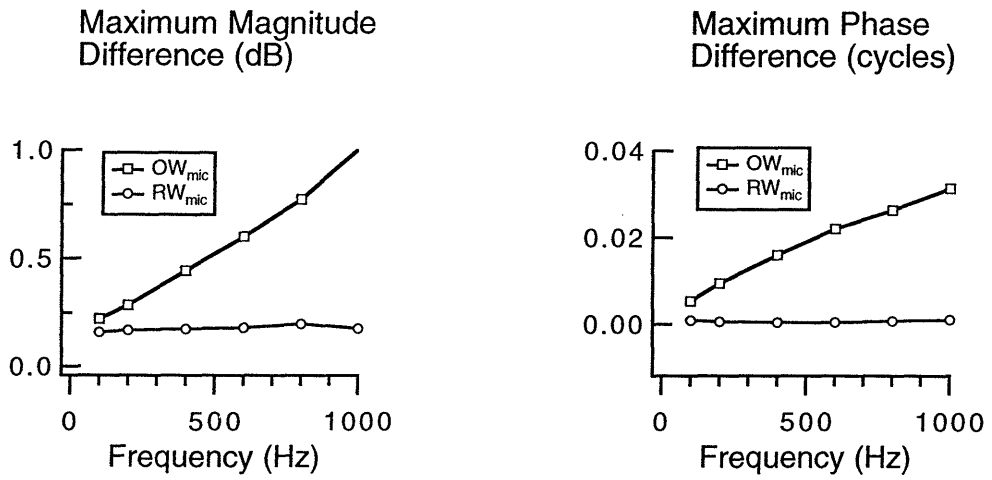

Figure A-11: The maximum changes in $\frac{SPL}{V_{OW_{mic}}}$ and $\frac{SPL}{V_{RW_{mic}}}$ as a function of frequency during the experiment on Cat #3.

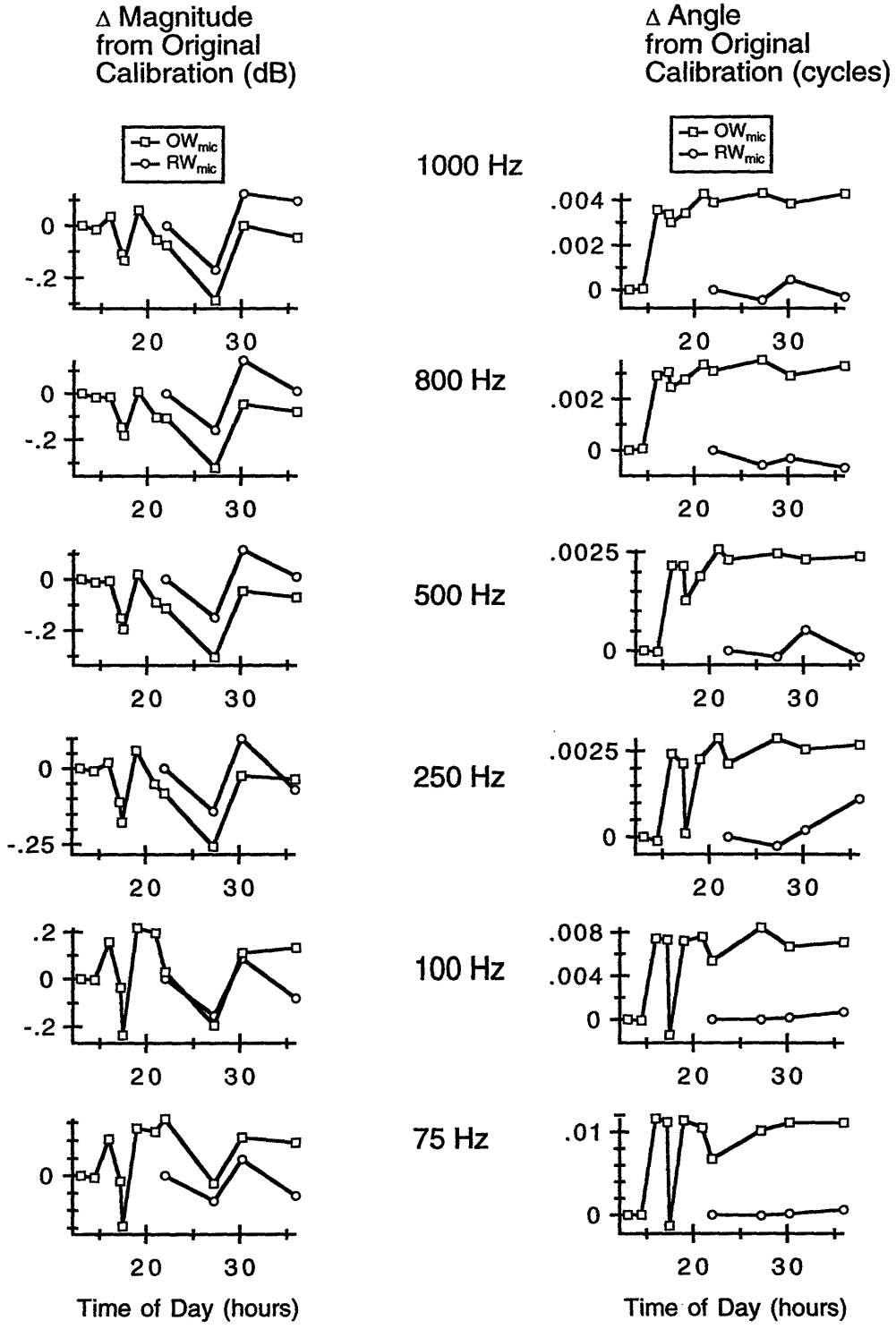

Figure A-12: The differences in $\frac{SPL}{V_{OW_{mic}}}$ and $\frac{SPL}{V_{RW_{mic}}}$ between the initial calibration and subsequent calibrations during the experiment on Cat #4. The first measurement of $\frac{SPL}{V_{OW_{mic}}}$ ($\frac{SPL}{V_{RW_{mic}}}$) was used to normalize all succeeding measurements of $\frac{SPL}{V_{OW_{mic}}}$ ($\frac{SPL}{V_{RW_{mic}}}$); magnitudes (in dB) and angles (in cycles) of the ratios are plotted. Time of day = 12 hours is the time of initial calibration.

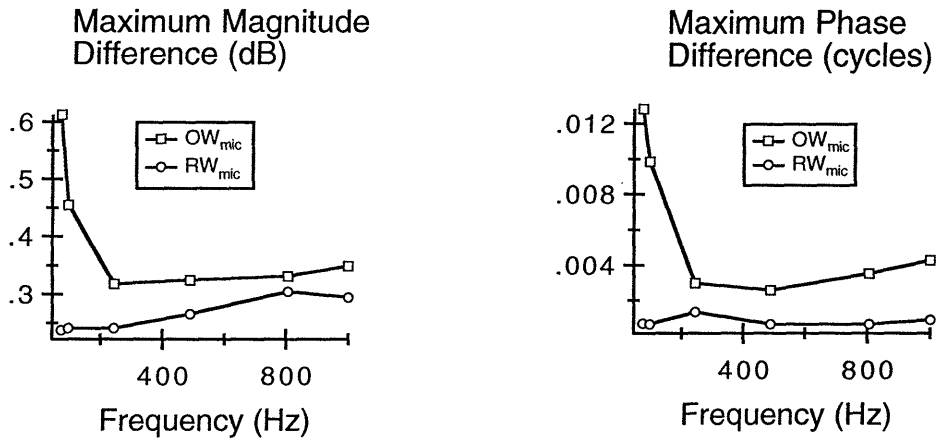

Figure A-13: The maximum changes in $\frac{SPL}{V_{OW_{mic}}}$ and $\frac{SPL}{V_{RW_{mic}}}$ as a function of frequency during the experiment on Cat #4.

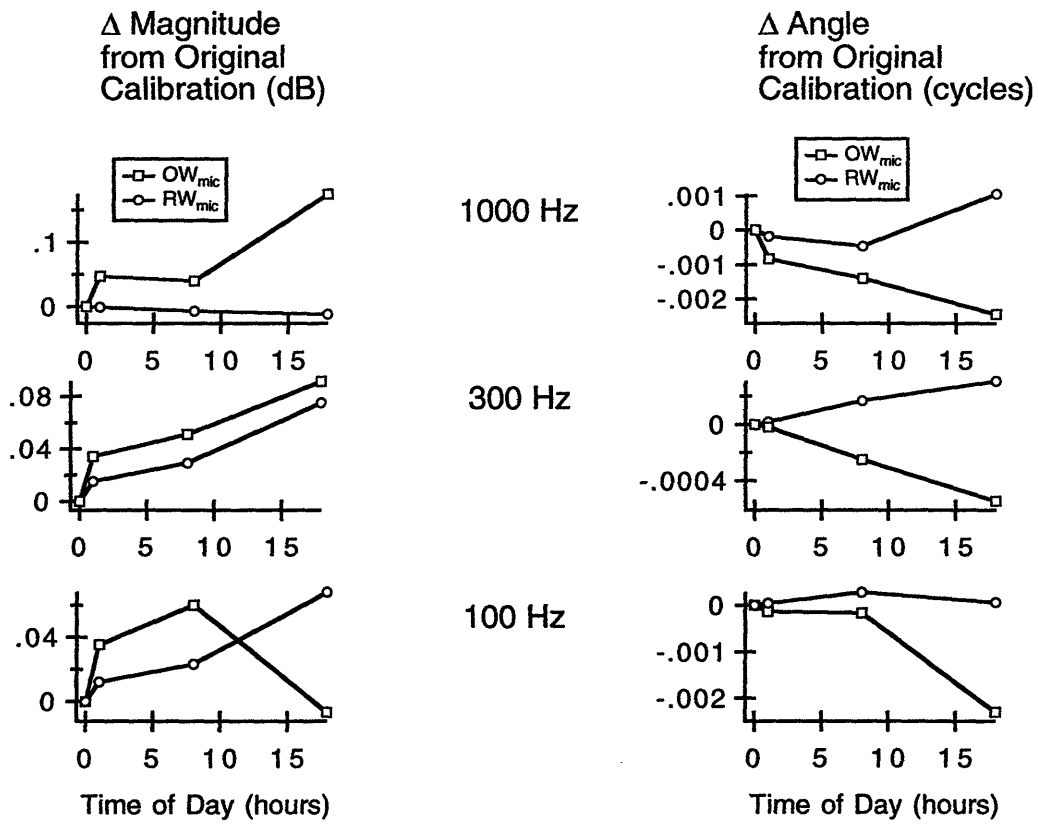

Figure A-14: The differences in $\frac{SPL}{V_{OW_{mic}}}$ and $\frac{SPL}{V_{RW_{mic}}}$ between the initial calibration and subsequent calibrations during the experiment on Cat #5. The first measurement of $\frac{SPL}{V_{OW_{mic}}}$ ($\frac{SPL}{V_{RW_{mic}}}$) was used to normalize all succeeding measurements of $\frac{SPL}{V_{OW_{mic}}}$ ($\frac{SPL}{V_{RW_{mic}}}$); magnitudes (in dB) and angles (in cycles) of the ratios are plotted. Time of day = 0 hours is the time of initial calibration.

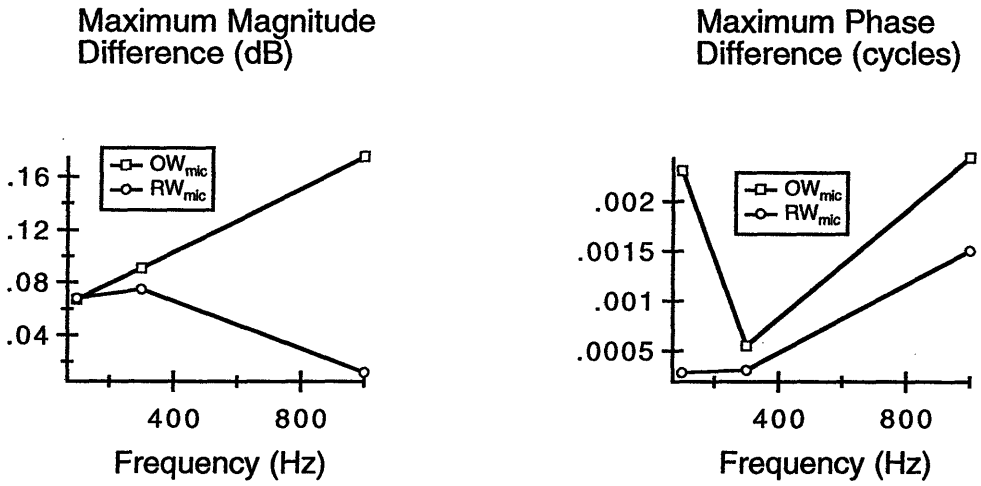

Figure A-15: The maximum changes in $\frac{SPL}{V_{OW_{mic}}}$ and $\frac{SPL}{V_{RW_{mic}}}$ as a function of frequency during the experiment on Cat #5.

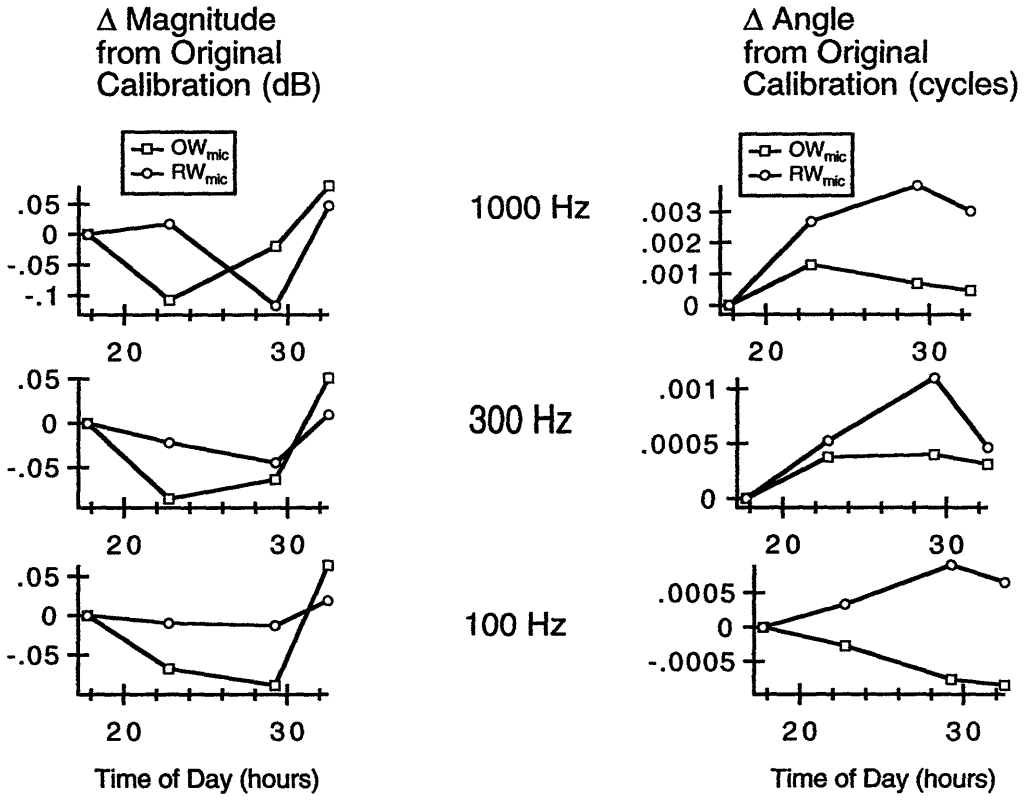

Figure A-16: The differences in $\frac{SPL}{V_{OW_{mic}}}$ and $\frac{SPL}{V_{RW_{mic}}}$ between the initial calibration and subsequent calibrations during the experiment on Cat #6. The first measurement of $\frac{SPL}{V_{OW_{mic}}}$ ($\frac{SPL}{V_{RW_{mic}}}$) was used to normalize all succeeding measurements of $\frac{SPL}{V_{OW_{mic}}}$ ($\frac{SPL}{V_{RW_{mic}}}$); magnitudes (in dB) and angles (in cycles) of the ratios are plotted. Time of day = 18 hours is the time of initial calibration.

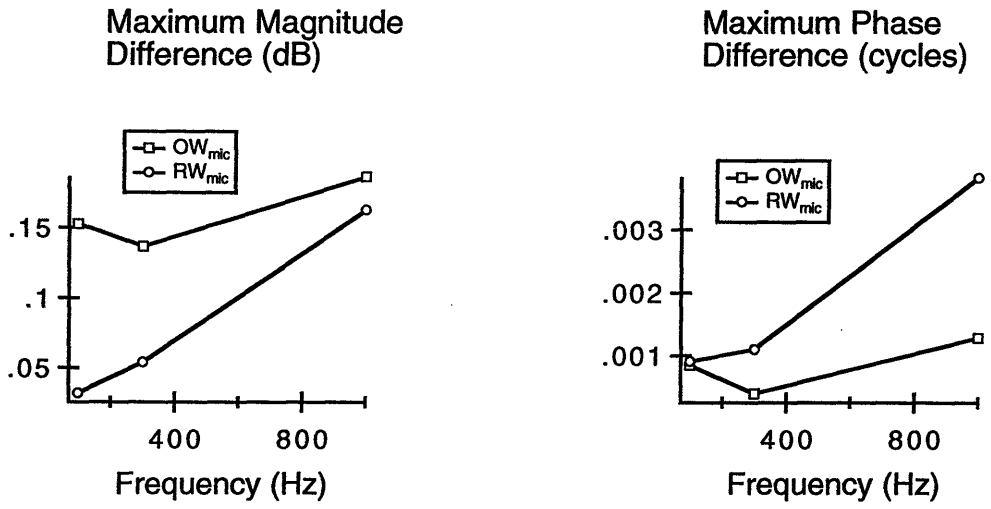

Figure A-17: The maximum changes in $\frac{SPL}{V_{OW_{mic}}}$ and $\frac{SPL}{V_{RW_{mic}}}$ as a function of frequency during the experiment on Cat #6.

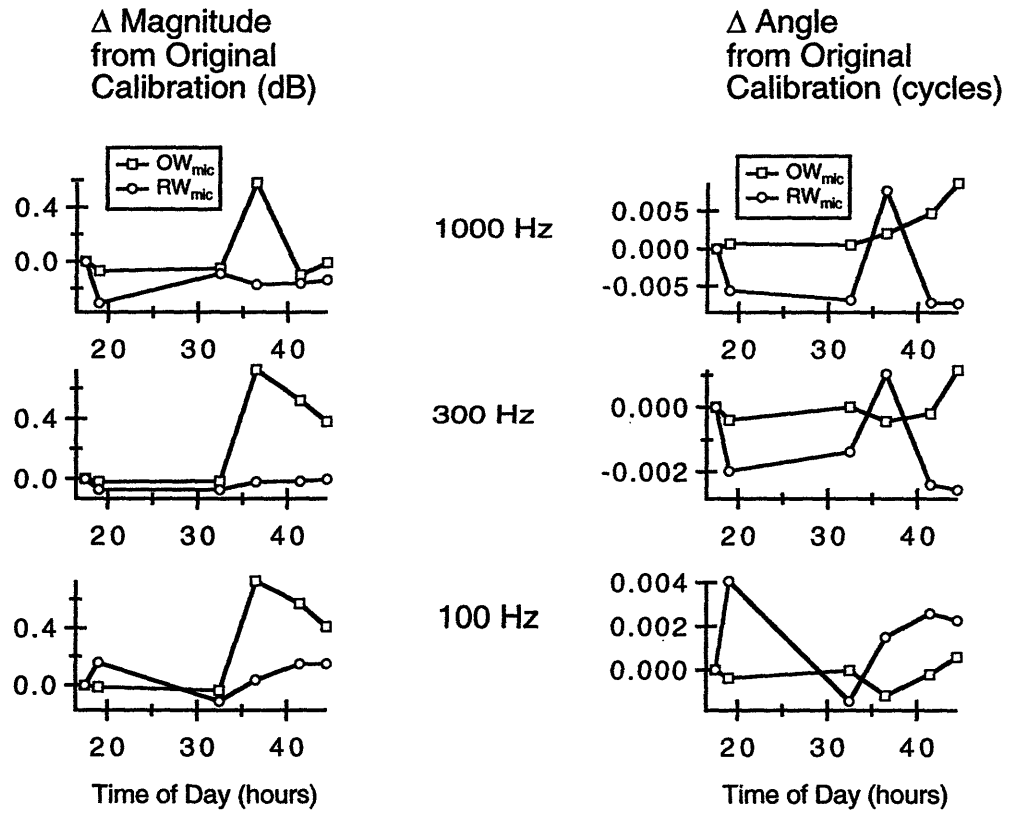

Figure A-18: The differences in $\frac{SPL}{V_{OW_{mic}}}$ and $\frac{SPL}{V_{RW_{mic}}}$ between the initial calibration and subsequent calibrations during the experiment on Cat #7. The first measurement of $\frac{SPL}{V_{OW_{mic}}}$ ($\frac{SPL}{V_{RW_{mic}}}$) was used to normalize all succeeding measurements of $\frac{SPL}{V_{OW_{mic}}}$ ($\frac{SPL}{V_{RW_{mic}}}$); magnitudes (in dB) and angles (in cycles) of the ratios are plotted. Time of day = 17 hours is the time of initial calibration.

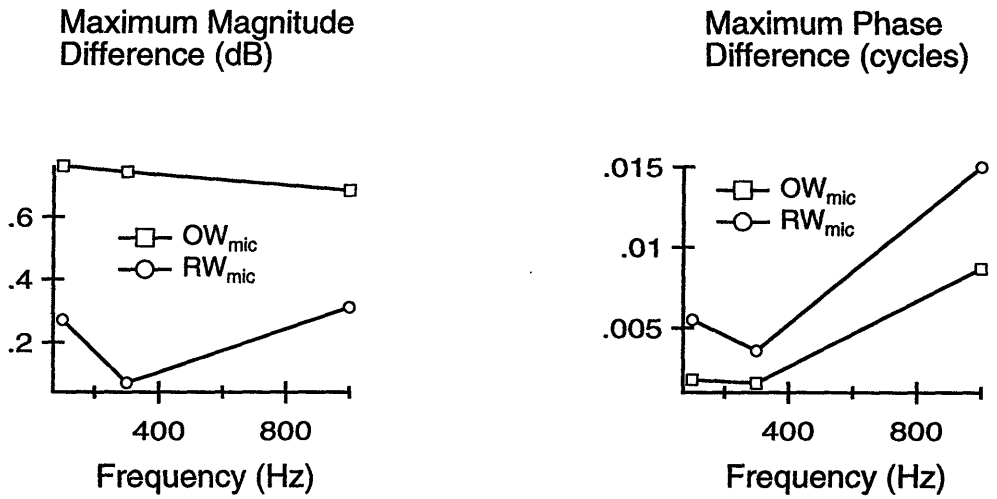

Figure A-19: The maximum changes in $\frac{SPL}{V_{OW_{mic}}}$ and $\frac{SPL}{V_{RW_{mic}}}$ as a function of frequency during the experiment on Cat #7.

A.4 Noisefloor calculations

NOISEFLOOR MEASUREMENTS: CAT #1					
	100 Hz	200 Hz	400 Hz	600 Hz	800 Hz
	-148	-160	-151	-160	-147
	-146	-148	-151	-150	-162
	-146	-150	-166	-157	-174
	-144	-153	-162	-164	-151
	-160	-148	-165	-161	-163
	-158	-162	-153	-155	-157
	-142	-164	-158	-157	-153
	-158	-150	-150	-152	-150
	-146	-159	-160	-149	-149
	-148	-150	-154	-150	-150
	-149	-147	-158	-155	-146
	-172	-159	-153	-152	-157
	-149	-148	-156	-153	-147
	-155	-170	-151	-155	-151
mean	-152	-155	-156	-155	-154
std	8	7	5	4	8
Noisefloor	-135	-140	-146	-146	-138

Table A.1: Measurements used to define the noisefloor of V_{CP} from Cat #1. The first 15 rows are the specified frequency component of the $|V_{CP}|$ response to a 1000 Hz tone, in units of dB re 1 volt. These measurements are averaged and used as an estimate of the noisefloor of V_{CP}. The noisefloor is defined as the mean plus two standard deviations (also in dB re 1 volt). For simplicity the numbers have been rounded to the nearest integer, however, the calculations used more significant digits.

NOISEFLOOR MEASUREMENTS: CAT #2					
	100 Hz	200 Hz	400 Hz	600 Hz	800 Hz
	-115	-118	-128	-129	-135
	-120	-132	-141	-146	-141
	-115	-124	-130	-133	-135
	-117	-124	-133	-132	-139
	-120	-128	-137	-131	-136
	-118	-125	-128	-138	-137
	-122	-131	-148	-136	-158
	-130	-138	-145	-136	-143
	-125	-135	-140	-137	-145
	-112	-119	-125	-132	-130
	-123	-125	-141	-146	-138
	-113	-135	-142	-141	-139
	-124	-130	-131	-139	-141
	-121	-131	-133	-141	-137
	-117	-128	-130	-140	-138
	-130	-149	-150	-148	-141
	-114	-124	-130	-131	-133
	-131	-130	-134	-137	-143
	-113	-121	-126	-132	-132
mean	-120	-129	-135	-137	-139
std	6	7	7	6	6
Noisefloor	-108	-114	-120	-126	-127

Table A.2: Measurements used to define the noisefloor from V_{CP} of Cat #2. The first 15 rows are the specified frequency component of the V_{CP} response to a 1000 Hz tone, in units of dB re 1 volt. These measurements are averaged and used as an estimate of the noisefloor of V_{CP}. The noisefloor is defined as the mean plus two standard deviations (also in dB re 1 volt). For simplicity the numbers have been rounded to the nearest integer, however, the calculations used more significant digits.

NOISEFLOOR MEASUREMENTS: CAT #3					
	100 Hz	200 Hz	400 Hz	600 Hz	800 Hz
	-131	-133	-144	-135	-146
	-156	-135	-145	-138	-149
	-137	-135	-139	-146	-145
	-133	-133	-145	-144	-147
	-133	-134	-142	-142	-140
	-131	-131	-142	-137	-143
	-136	-138	-146	-143	-148
	-140	-142	-149	-147	-141
	-151	-135	-143	-144	-147
	-143	-137	-144	-136	-145
	-140	-136	-147	-150	-147
	-144	-137	-145	-139	-143
	-139	-136	-144	-135	-149
	-147	-132	-141	-141	-154
	-143	-133	-146	-142	-147
	-130	-134	-143	-148	-138
	-136	-134	-145	-142	-148
	-138	-134	-150	-159	-150
mean	-139	-135	-144	-143	-146
std	7	3	3	6	4
Noisefloor	-125	-130	-139	-131	-139

Table A.3: Measurements used to define the noisefloor from V_{CP} of Cat #3. The first 15 rows are the specified frequency component of the V_{CP} response to a 1000 Hz tone, in units of dB re 1 volt. These measurements are averaged and used as an estimate of the noisefloor of V_{CP}. The noisefloor is defined as the mean plus two standard deviations (also in dB re 1 volt). For simplicity the numbers have been rounded to the nearest integer, however, the calculations used more significant digits.

NOISEFLOOR MEASUREMENTS: CAT #4					
	75 Hz	100 Hz	250 Hz	500 Hz	800 Hz
	-143	-142	-149	-159	-156
	-132	-135	-145	-154	-160
	-148	-131	-147	-159	-141
	-129	-140	-133	-142	-146
	-144	-134	-142	-151	-150
	-144	-143	-165	-160	-150
	-140	-141	-153	-154	-154
	-137	-140	-154	-156	-158
	-136	-148	-156	-155	-158
	-124	-127	-141	-149	-149
	-133	-131	-141	-141	-147
	-133	-137	-152	-154	-162
	-144	-144	-158	-165	-150
	-137	-142	-151	-160	-157
	-138	-132	-142	-163	-156
	-134	-141	-151	-156	-151
	-134	-151	-145	-152	-156
	-142	-150	-150	-156	-154
	-132	-142	-153	-160	-155
	-142	-134	-152	-156	-151
	-140	-141	-152	-162	-163
	-144	-139	-164	-156	-169
mean	-138	-139	-150	-155	-154
std	6	6	8	6	6
Noisefloor	-126	-127	-135	-143	-141

Table A.4: Measurements used to define the noisefloor from V_{CP} of Cat #4. The first 22 rows are the specified frequency component of the V_{CP} response to a 1000 Hz tone, in units of dB re 1 volt. These measurements are averaged and used as an estimate of the noisefloor of V_{CP}. The noisefloor is defined as the mean plus two standard deviations (also in dB re 1 volt). For simplicity the numbers have been rounded to the nearest integer, however, the calculations used more significant digits.

NOISEFLOOR MEASUREMENTS: CAT #5						
	100 Hz	300 Hz	300 Hz	300 Hz	1000 Hz	1000 Hz
	-134	-129	-139	-143	-155	-146
	-144	-128	-143	-142	-156	-147
	-127	-122	-141	-142	-145	-147
	-129	-134	-150	-144	-143	-156
	-124	-134	-129	-136	-163	-162
	-123	-125	-136	-138	-143	-153
		-128	-139		-150	-148
		-127	-139		-150	-142
		-128	-130		-146	-149
		-131	-145		-146	-145
		-125	-134		-158	-141
mean	-130	-128	-139	-141	-151	-149
std	8	4	6	3	7	6
Noisefloor	-115	-121	-126	-134	-137	-136

Table A.5: Measurements used to define the noisefloor of V_{CP} from Cat #5. Either 11 or 6 measurements of V_{CP} (dB re 1 volt) were made with no stimulus. These measurements are averaged and used as an estimate of the noisefloor of V_{CP}. The noisefloor is defined as the mean plus two standard deviations (also in dB re 1 volt). For simplicity the numbers have been rounded to the nearest integer, however, the calculations used more significant digits.

NOISEFLOOR MEASUREMENTS: CAT #6			
	100 Hz	300 Hz	1000 Hz
	-149	-149	-147
	-148	-155	-147
	-151	-158	-143
	-159	-154	-151
	-147	-150	-149
	-145	-154	-148
			-147
			-143
			-146
			-148
			-146
mean	-150	-153	-147
std	5	3	2
Noisefloor	-140	-147	-142

Table A.6: Measurements used to define the noisefloor from V_{CP} of Cat #6. Either 11 or 6 measurements of V_{CP} (dB re 1 volt) were made with no stimulus. These measurements are averaged and used as an estimate of the noisefloor of V_{CP}. The noisefloor is defined as the mean plus two standard deviations (also in dB re 1 volt). For simplicity the numbers have been rounded to the nearest integer, however, the calculations used more significant digits.

NOISEFLOOR MEASUREMENTS: CAT #7			
	100 Hz	300 Hz	1000 Hz
	-139	-155	-148
	-132	-165	-158
	-130	-154	-161
	-131	-156	-150
	-133	-143	-159
	-141	-152	-148
	-134	-155	-160
	-139	-158	-155
	-167	-164	-158
	-138	-160	-148
	-136	-160	-153
mean	-138	-156	-154
std	10	6	5
Noisefloor	-118	-144	-144

Table A.7: Measurements used to define the noisefloor from V_{CP} of Cat #7. 11 measurements of V_{CP} (dB re 1 volt) were made with no stimulus. These measurements are averaged and used as an estimate of the noisefloor of V_{CP}. The noisefloor is defined as the mean plus two standard deviations (also in dB re 1 volt). For simplicity the numbers have been rounded to the nearest integer, however, the calculations used more significant digits.

A.5 Effects of TTX

TTX was added to the cochleas of Cat #6 and Cat #7 in order to eliminate the nonlinear CAP component of the cochlear-potential response (Chapter 2.7). Cochlear-potential measurements were made in response to click and tone-burst stimuli both before and after the application of TTX.

Pre and post-TTX cochlear-potential responses to click stimuli (approximately 85 dB SPL) are shown in Fig. A-20 and A-21 for Cat #6 and Cat #7, respectively. In both cases a small cochlear-microphonic response occurs at about 1 ms; the Cat #6 cochlear microphonic is about 5 μV (Fig. A-20), and the Cat #7 cochlear microphonic is about $2\mu V$ (Fig.A-21). The cochlear-microphonic component of the cochlear-potential response is not affected by the TTX. The responses from both cats also have neural components which occur between about 2 and 4 ms; the peak at about 2 ms is often referred to as the N1 component. The N1 component from Cat #7 is about 20 μV larger than the N1 component from Cat #6. The N1 and other neural components of the cochlear-potential response are eliminated after the application of TTX; this suggests the TTX successfully blocked at least some of the nonlinear neural response in these animals.

Pre and post-TTX cochlear-potential responses to 100 Hz and 1000 Hz tone-burst stimuli (approximately 110 $dB\ SPL$) are shown in Fig. A-22, A-23, A-24, and A-25. The Cat #6 cochlear-potential response to a 100 Hz tone burst shows a change after the application of TTX; the pre-TTX response looks "noisy" and nonlinear while the post-TTX response resembles the linear 100 Hz stimulus tone. The pre and post-TTX cochlear-potential responses to a 100 Hz tone burst from Cat #7 are similar and neither response looks as nonlinear as the pre-TTX 100 Hz response from Cat #6. The application of TTX also affected the cochlear-potential response to 1000 Hz tone-burst stimuli. Both

the Cat #6 and Cat #7 pre-TTX responses show an initial increased response at about 2 ms; this increase is the neural component of the cochlear-potential response and it is eliminated after the application of TTX. Additionally, the post-TTX 1000 Hz tone-burst responses are smaller than the pre-TTX ones.

These pre and post-TTX responses suggest that the TTX successfully blocked much of the neural component of the cochlear-potential response. However, as discussed in Chapter 5, some of the post-TTX single-sided level-series measurements made at the lower frequencies exhibited nonlinearities. It is possible that the TTX was not completely effective at the lowest stimulus frequencies.

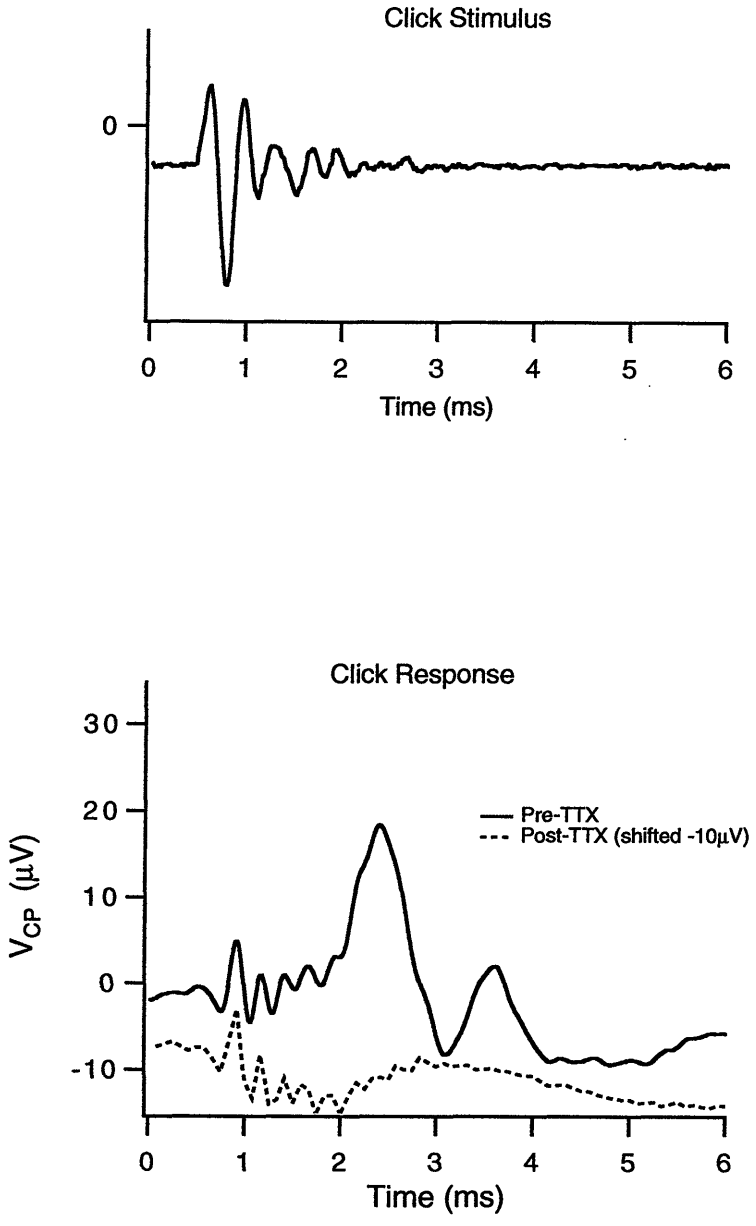

Figure A-20: Cat #6. TOP: Click stimulus at about 85 dB SPL. BOTTOM: Response to the click stimulus both before and after the application of TTX to the round window membrane. Measurements made between 3 hours and 18 hours after the application of TTX did not show large variations.

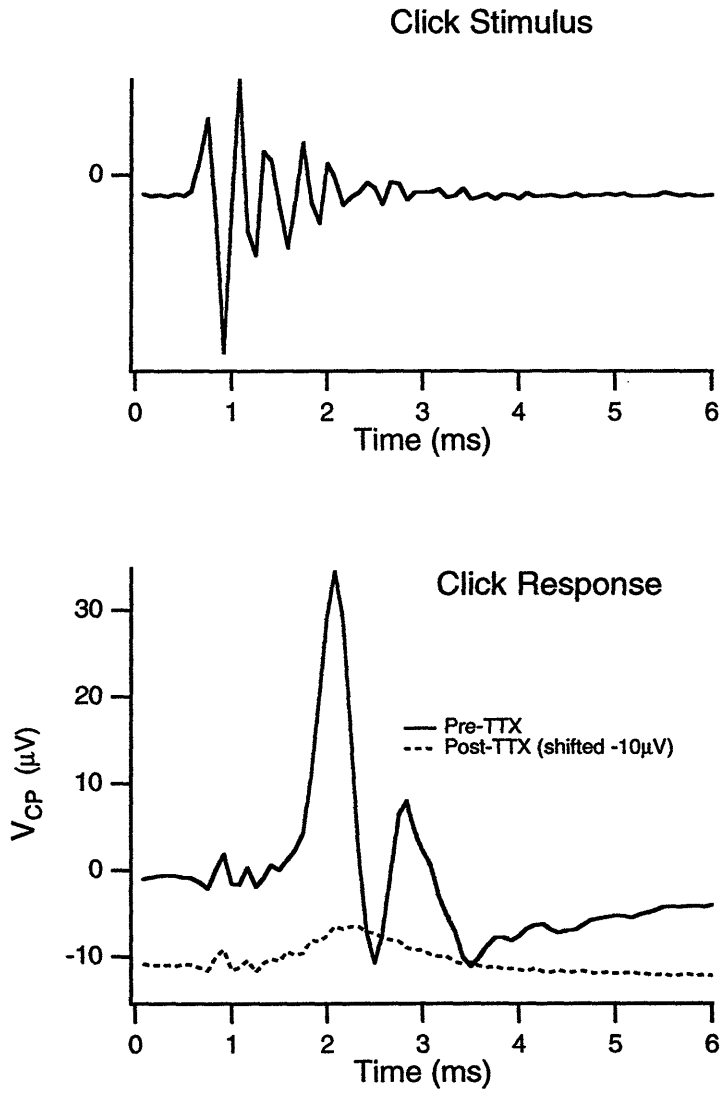

Figure A-21: Cat #7. TOP: Click stimulus at about 85 dB SPL. BOTTOM: Response to the click stimulus both before and after the application of TTX to the round window membrane. Measurements made between 3 hours and 18 hours after the application of TTX did not show large variations.

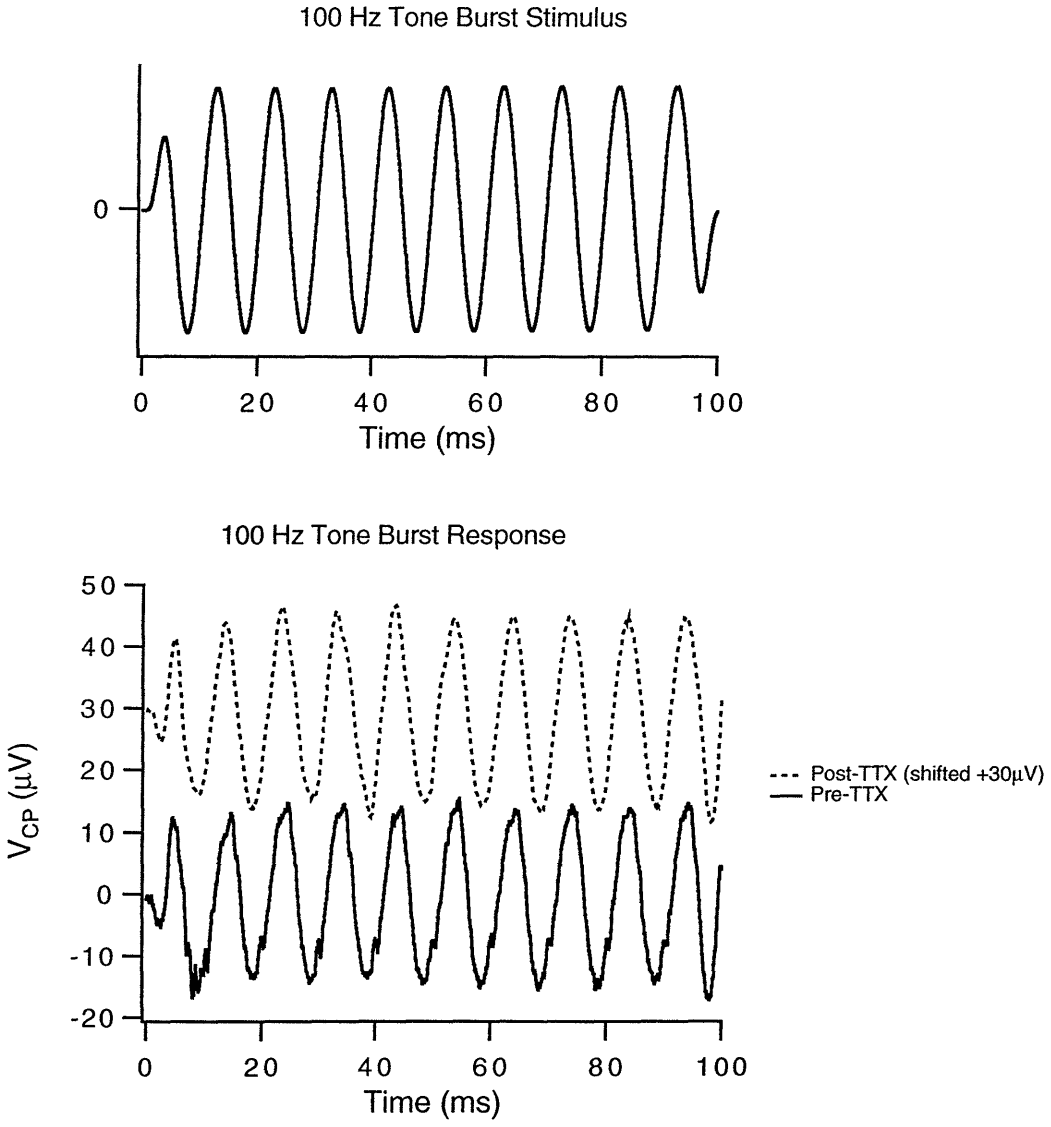

Figure A-22: Cat #6. TOP: 100 Hz tone-burst stimulus at about 110 dB SPL. BOTTOM: Response to 100 Hz tone-burst stimulus before and after application of TTX to the round window membrane. Measurements made between 3 hours and 18 hours after the application of TTX did not show large variations.

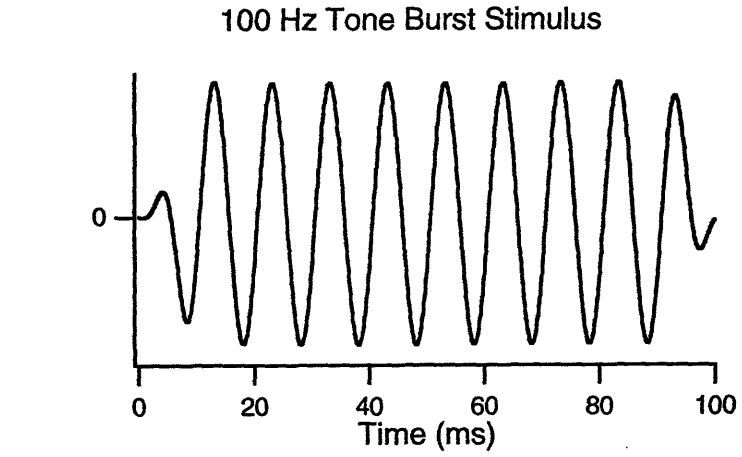

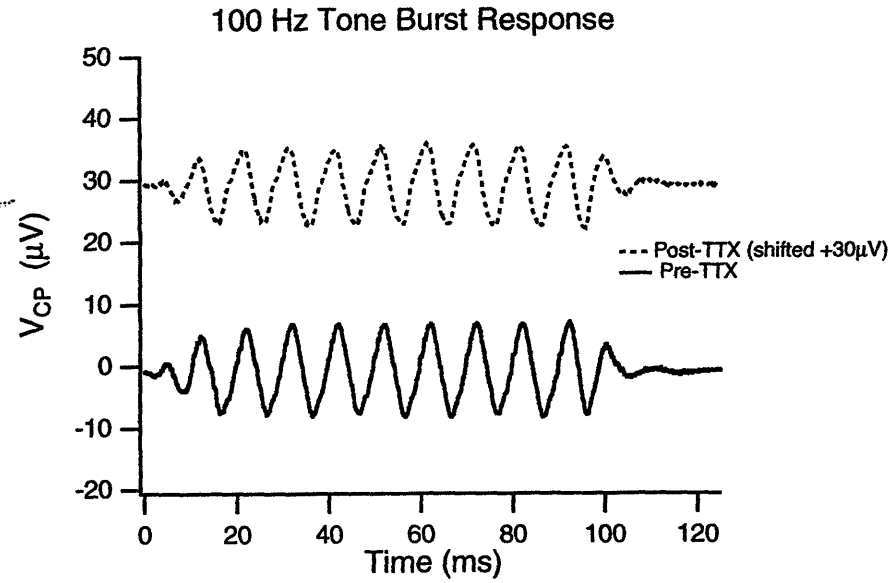

Figure A-23: Cat #7. TOP: 100 Hz tone-burst stimulus at about 110 dB SPL. BOTTOM: Response to 100 Hz tone-burst stimulus before and after application of TTX to the round window membrane. Measurements made between 3 hours and 18 hours after the application of TTX did not show large variations.

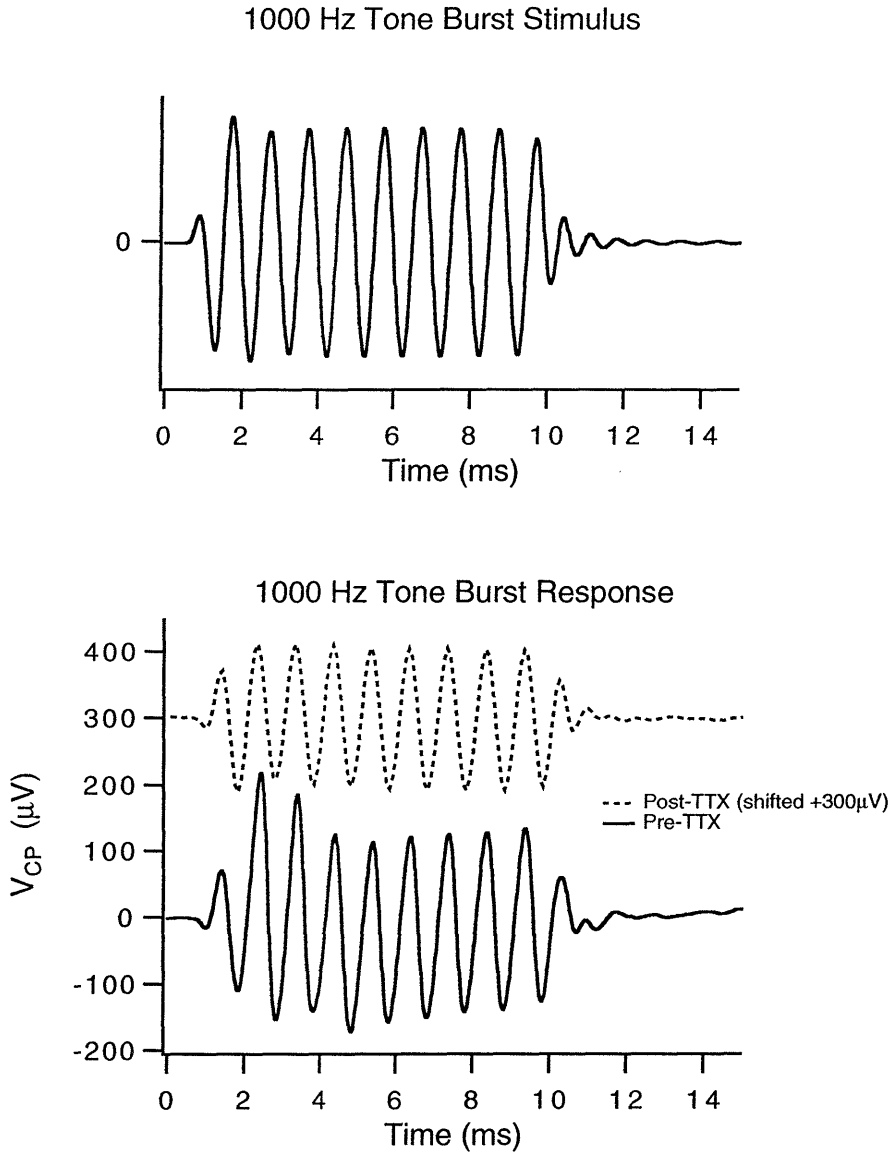

Figure A-24: Cat #6. TOP: 1000 Hz tone-burst stimulus at about 110 dB SPL. BOTTOM: Response to 100 Hz tone-burst stimulus before and after application of TTX to the round window membrane. Measurements made between 3 hours and 18 hours after the application of TTX did not show large variations.

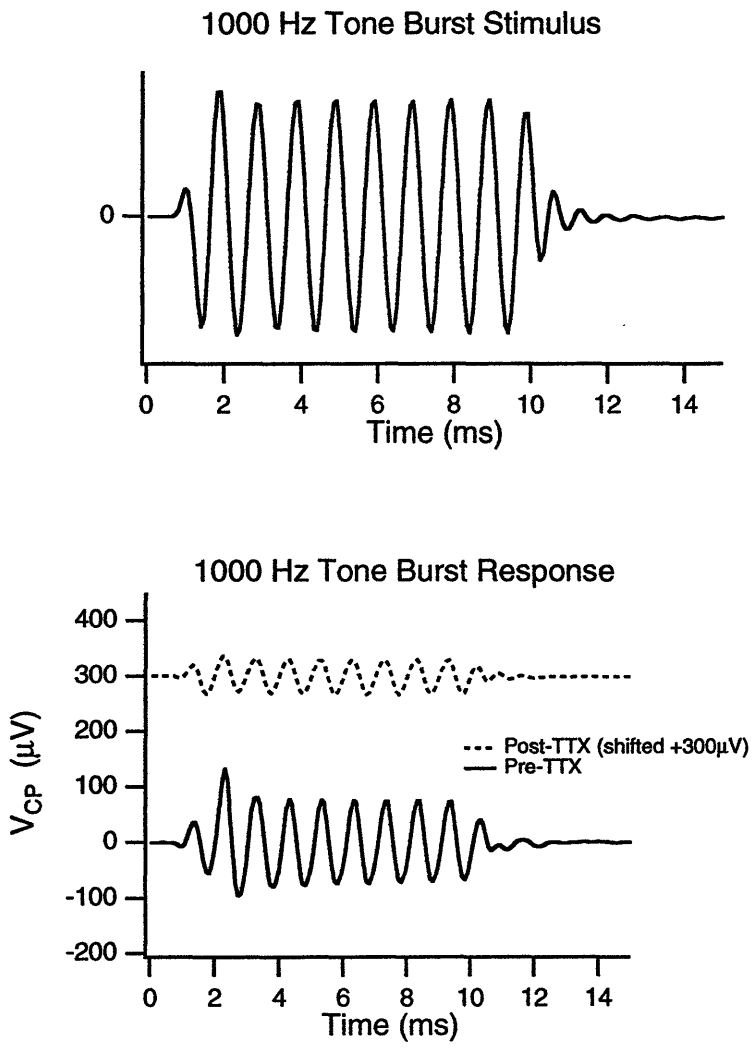

Figure A-25: Cat #7. TOP: 1000 Hz tone-burst stimulus at about 110 dB SPL. BOTTOM: Response to 100 Hz tone-burst stimulus before and after application of TTX to the round window membrane. Measurements made between 3 hours and 18 hours after the application of TTX did not show large variations.

Appendix B

Summary of results: Stimulus to one window

Data from all single-sided level series measurements are contained within this appendix. There are differences among the experiments (Cats #1 to #7) which are discussed in Appendix A.

All of the figures in this appendix have the same layout.

- The top left hand plot is the magnitude of the cochlear-potential response as a function of stimulus sound-pressure level for single-sided stimuli at both the oval and round windows.
- The top right hand plot is the angle of the cochlear-potential response as a function of stimulus sound-pressure level for stimuli at both the oval and round windows.
- The middle left hand plot is the dB difference between the cochlear-potential magnitude when the oval window is stimulated and the cochlear-potential magnitude when the round window is stimulated, as a function of stimulus sound-pressure level. This difference is the dB difference between the two responses in the top left hand plot.
- The middle right hand plot is the difference in angle between the cochlear-potential angle when the oval window is stimulated and the cochlear-potential angle when the round window is stimulated. This difference is the difference in cycles between the two responses in the top right hand plot.

- The lower left hand plot is an estimate of $|\underline{D}|$ where $\underline{D}$ is obtained from the data in the top two plots and Equation 1.1: $\underline{V_{CP}} = \underline{D}(\underline{P_{OW}} - \underline{P_{RW}})$. Here it is assumed that $\underline{C} = 0$ and the pressure at the unstimulated window is zero.
- The lower right hand plot is an estimate of $\angle\underline{D}$ described above.

The figures are arranged first in order of increasing frequency. Within each frequency the figures are arranged in chronological order of experimental cat. An attempt was made to keep all axes ranges constant for each group of measurements at a specific frequency. In a few cases this was not practical. When the phase angle plots have different absolute ranges the relative range is constant.

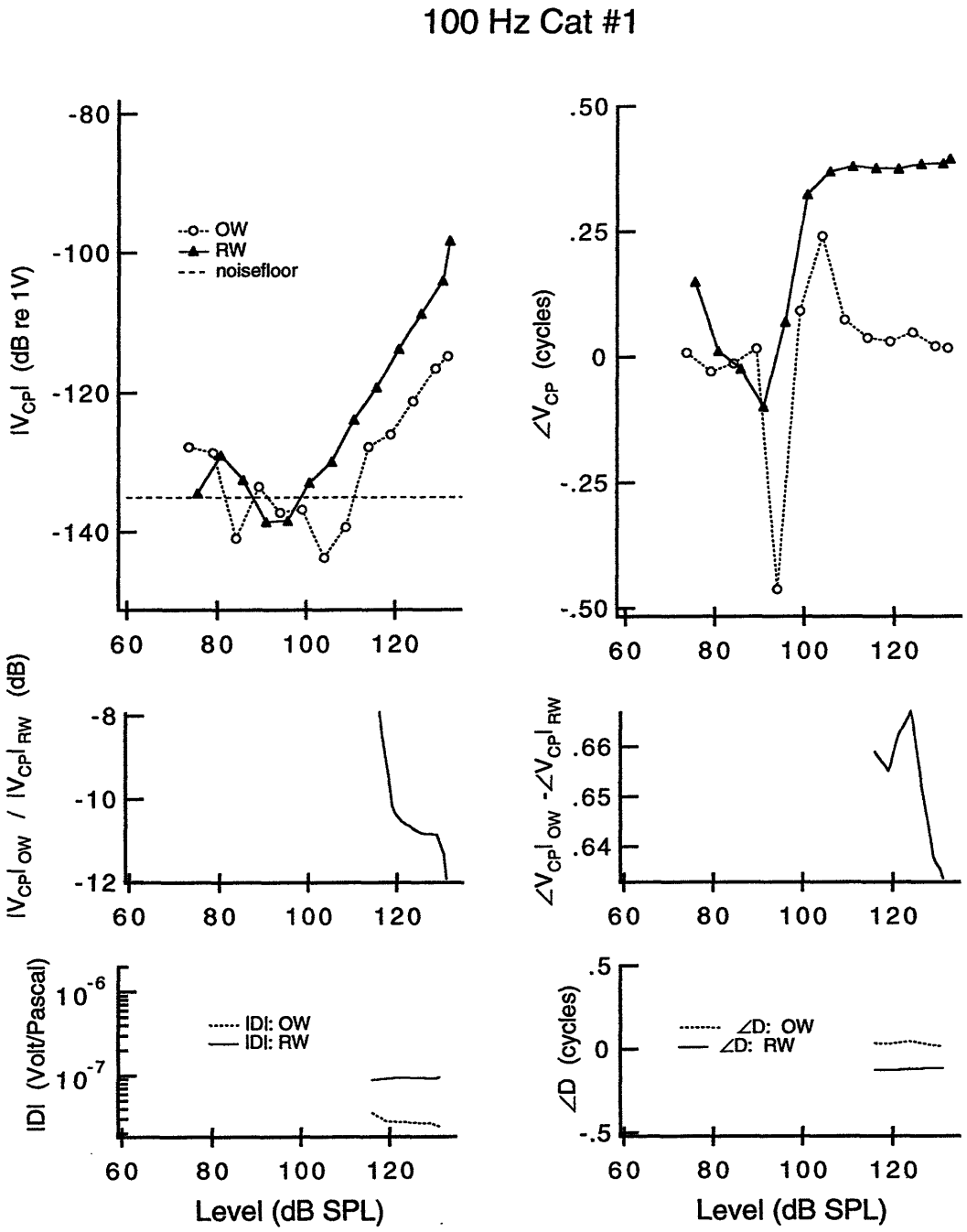

Figure B-1: TOP: Single-sided level-series measurements made on Cat #1 at 100 Hz. Either the oval or the round window was stimulated. MIDDLE: Ratio of the measurement made while the oval window was stimulated and the measurement made while the round window was stimulated. BOTTOM: Estimate of D (difference-mode gain) from the single-sided level-series measurements. In this estimation it is assumed that $|\underline{C}| << |\underline{D}|$.

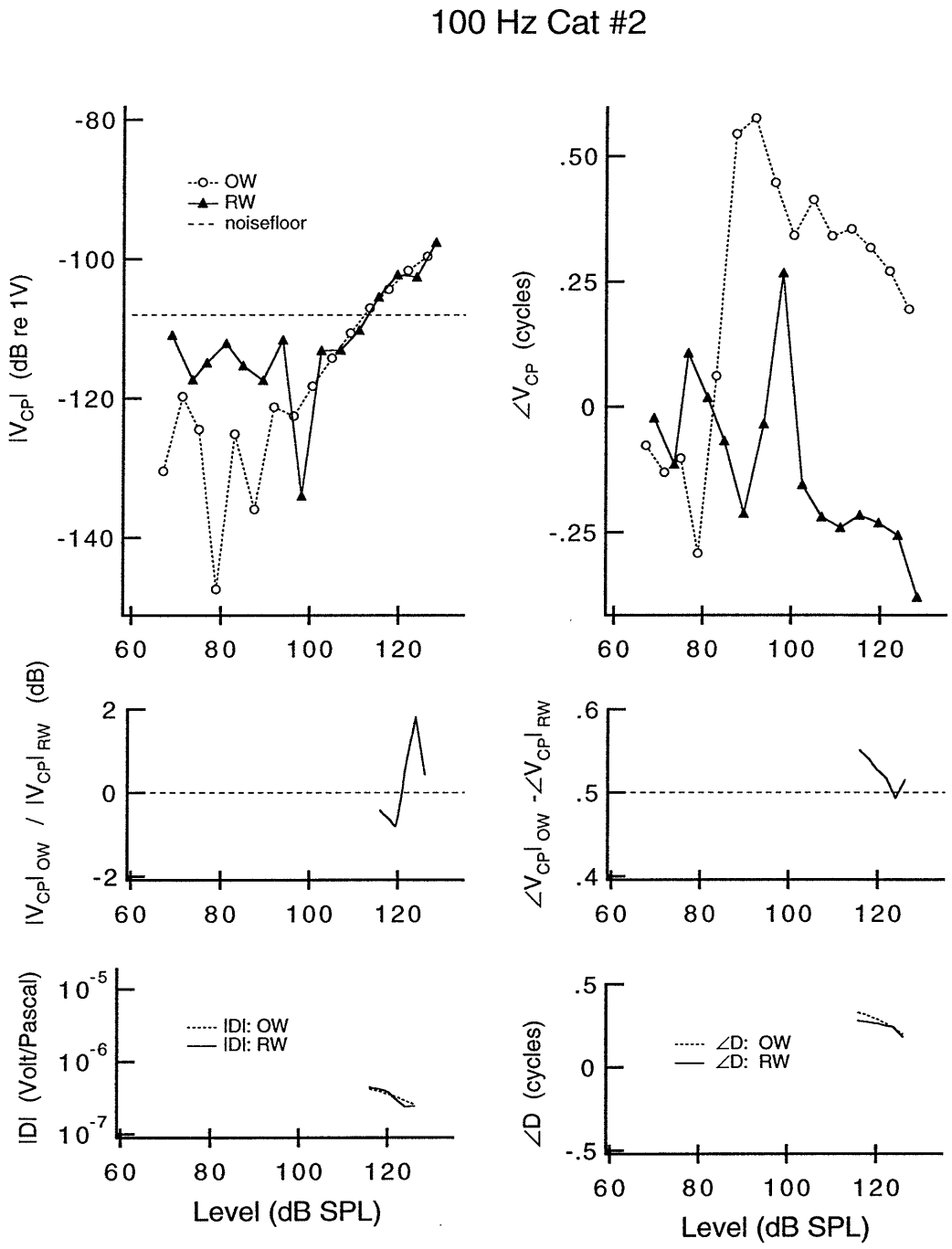

Figure B-2: TOP: Single-sided level-series measurements made on Cat #2 at 100 Hz. Either the oval or the round window was stimulated. MIDDLE: Ratio of the measurement made while the oval window was stimulated and the measurement made while the round window was stimulated. BOTTOM: Estimate of D (difference-mode gain) from the single-sided level-series measurements. In this estimation it is assumed that $|\underline{C}| << |\underline{D}|$.

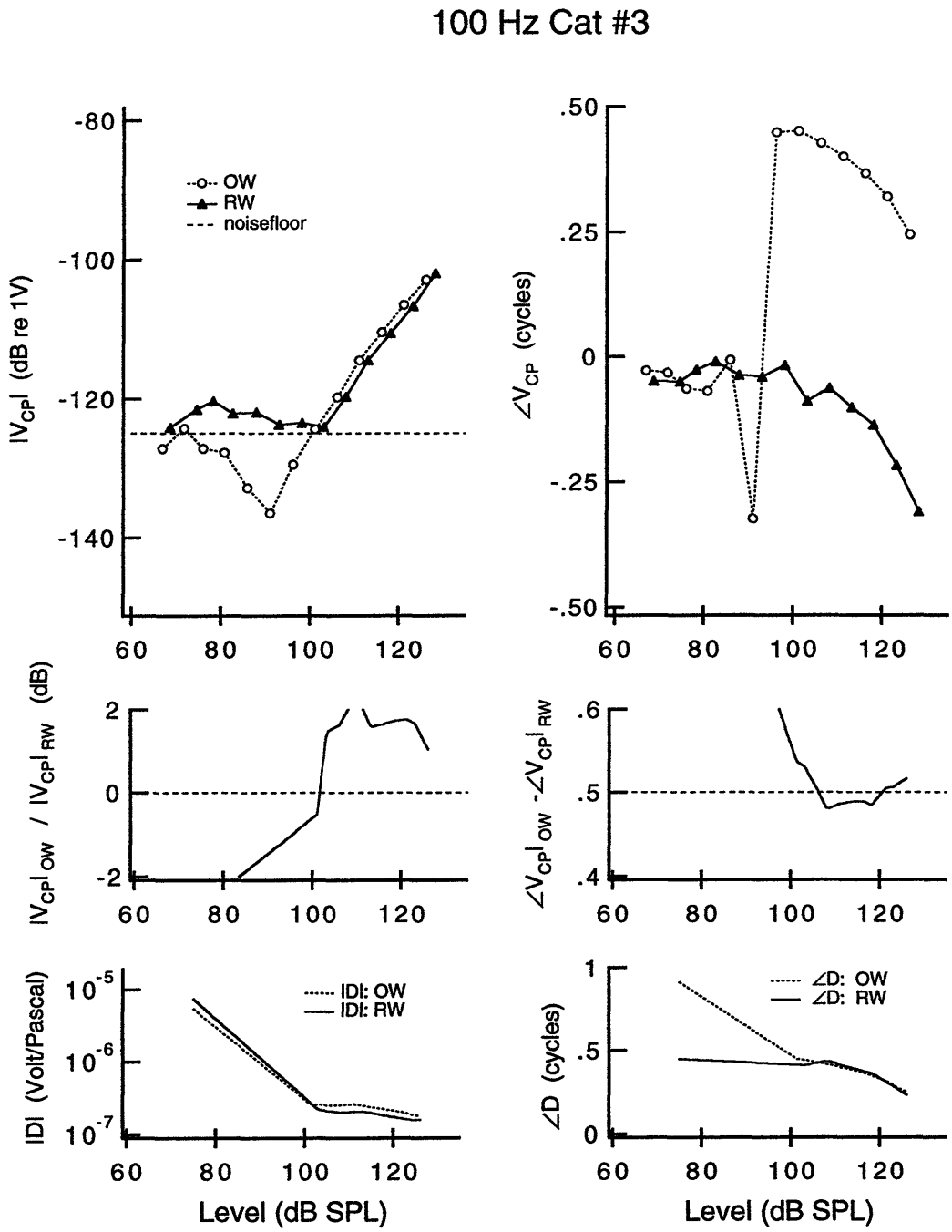

Figure B-3: TOP: Single-sided level-series measurements made on Cat #3 at 100 Hz. Either the oval or the round window was stimulated. MIDDLE: Ratio of the measurement made while the oval window was stimulated and the measurement made while the round window was stimulated. BOTTOM: Estimate of D (difference-mode gain) from the single-sided level-series measurements. In this estimation it is assumed that $|\underline{C}| << |\underline{D}|$.

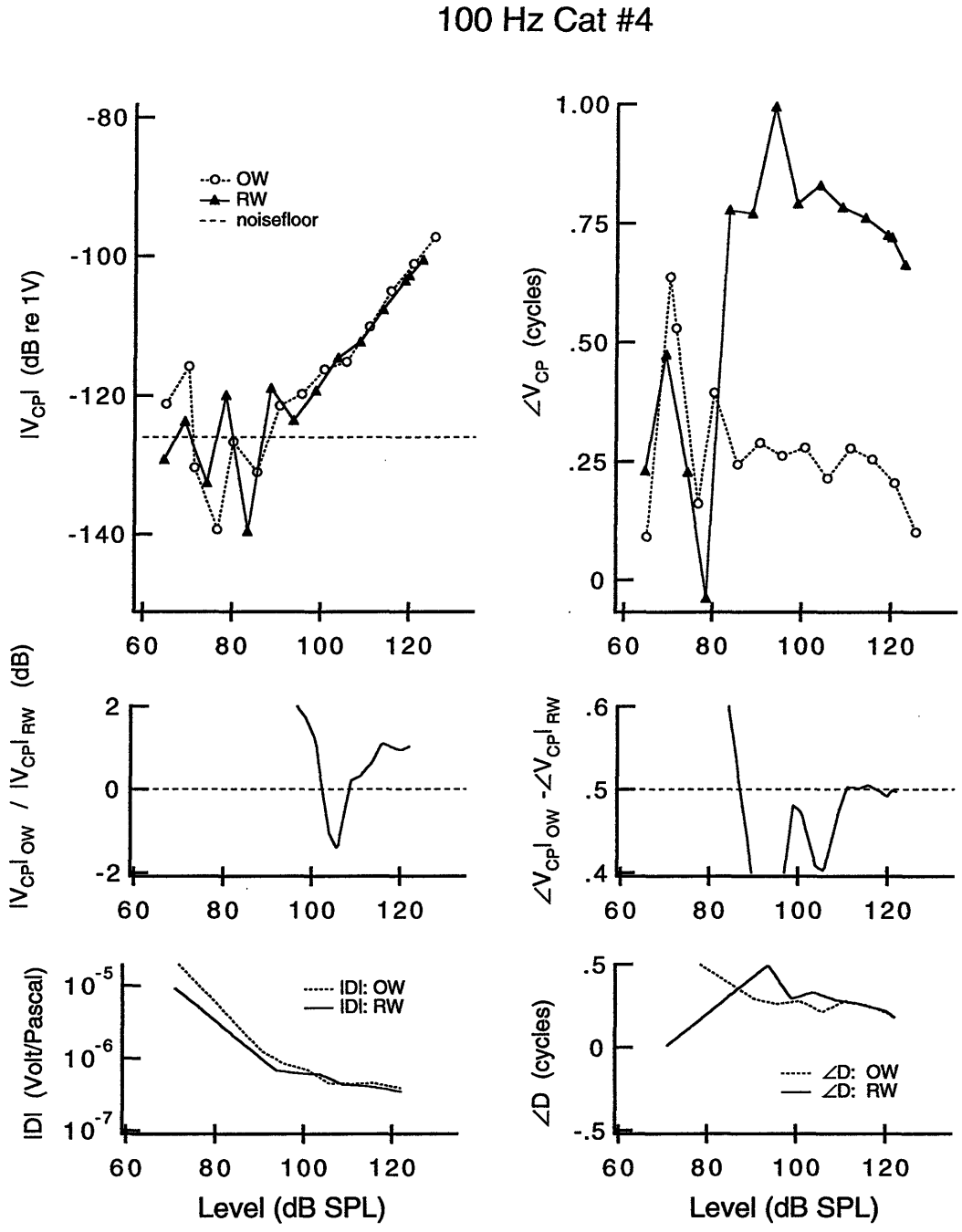

Figure B-4: TOP: Single-sided level-series measurements made on Cat #4 at 100 Hz. Either the oval or the round window was stimulated. MIDDLE: Ratio of the measurement made while the oval window was stimulated and the measurement made while the round window was stimulated. BOTTOM: Estimate of D (difference-mode gain) from the single-sided level-series measurements. In this estimation it is assumed that $|\underline{C}| << |\underline{D}|$.

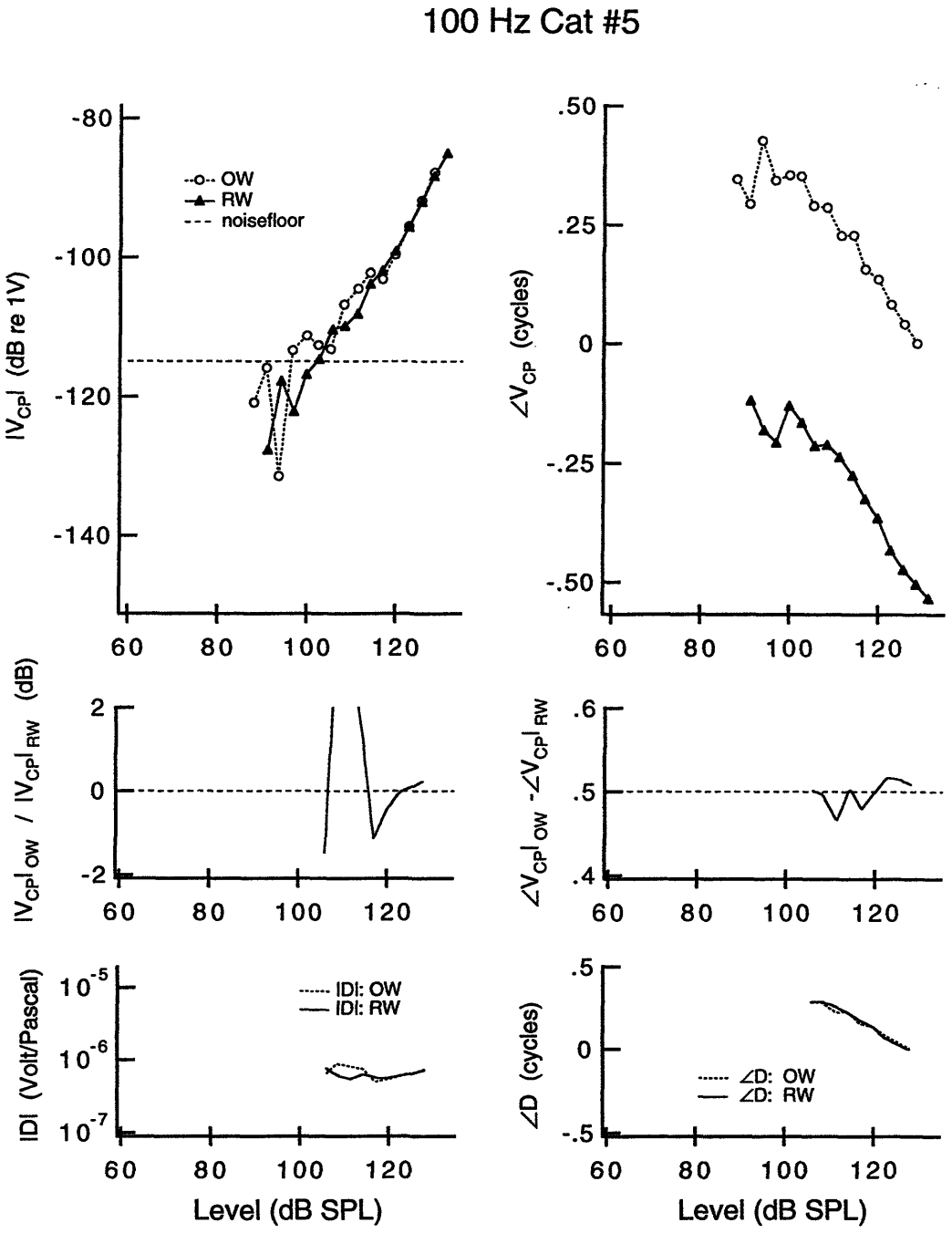

Figure B-5: TOP: Single-sided level-series measurements made on Cat #5 at 100 Hz. Either the oval or the round window was stimulated. MIDDLE: Ratio of the measurement made while the oval window was stimulated and the measurement made while the round window was stimulated. BOTTOM: Estimate of D (difference-mode gain) from the single-sided level-series measurements. In this estimation it is assumed that $|\underline{C}| << |\underline{D}|$.

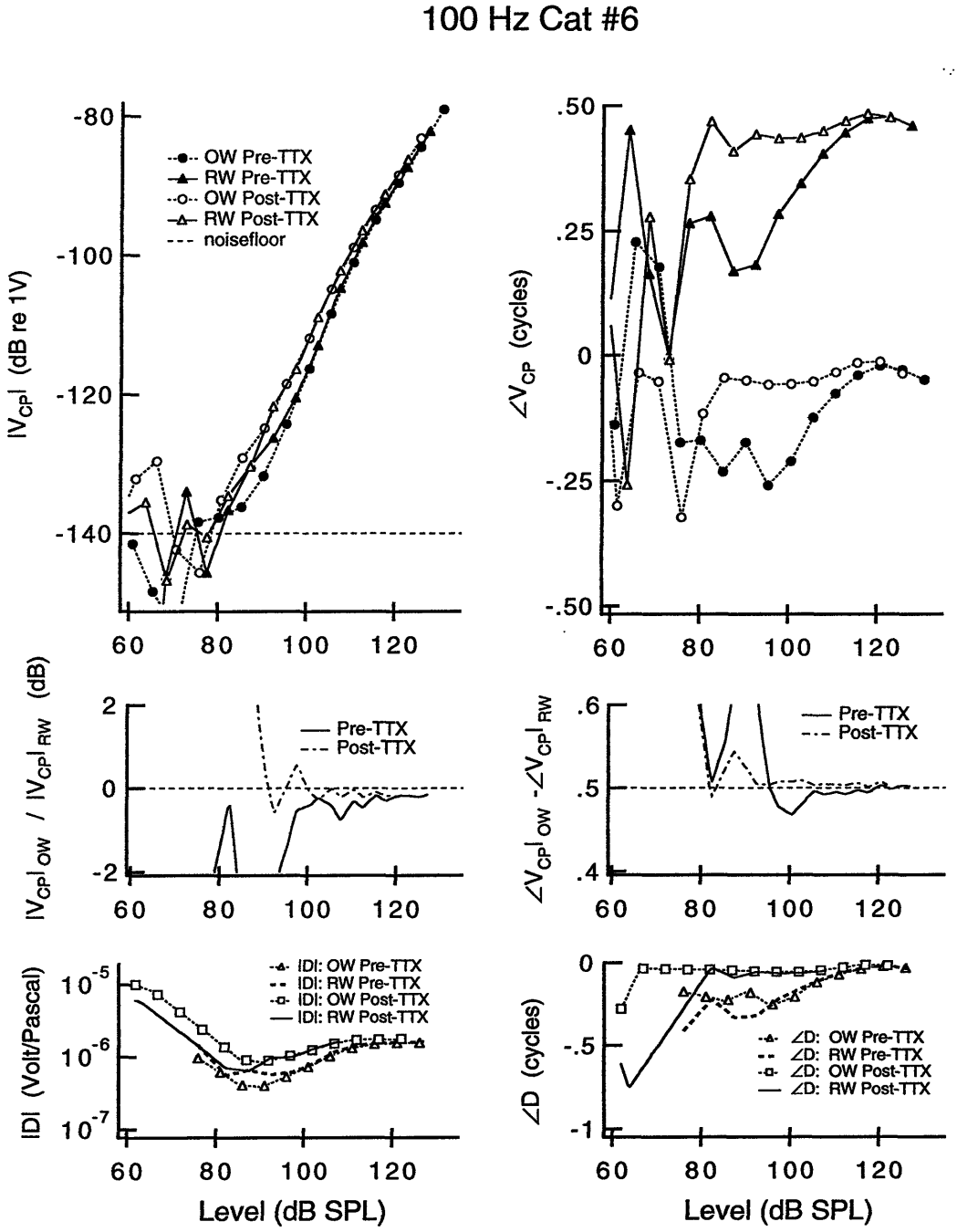

Figure B-6: TOP: Single-sided level-series measurements made on Cat #6 at 100 Hz before and after the application of TTX. Either the oval or the round window was stimulated. MIDDLE: Ratio of the measurement made while the oval window was stimulated and the measurement made while the round window was stimulated. BOTTOM: Estimate of D (difference-mode gain) from the single-sided level-series measurements. In this estimation it is assumed that $|\underline{C}| << |\underline{D}|$.

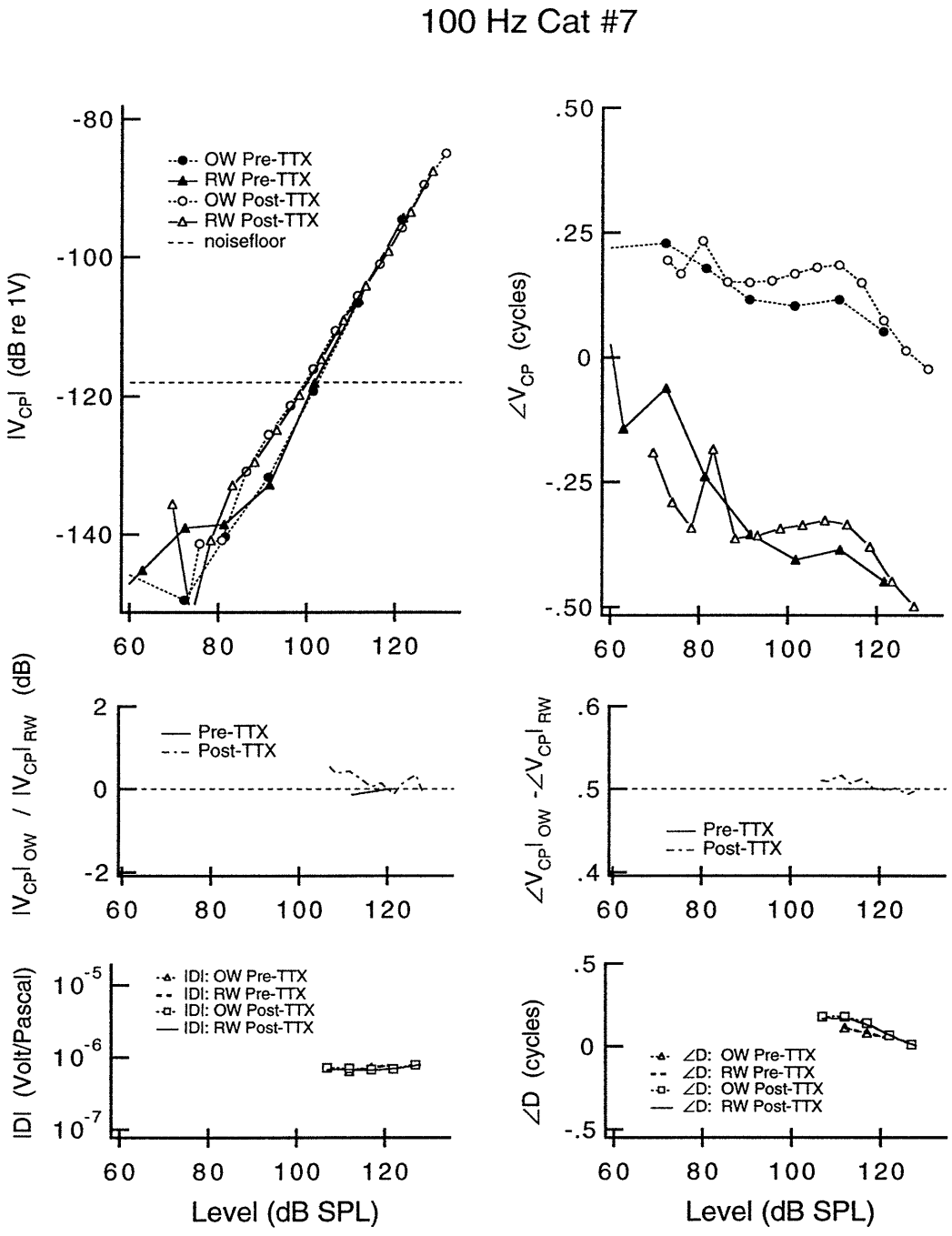

Figure B-7: TOP: Single-sided level-series measurements made on Cat #7 at 100 Hz before and after the application of TTX. Either the oval or the round window was stimulated. MIDDLE: Ratio of the measurement made while the oval window was stimulated and the measurement made while the round window was stimulated. BOTTOM: Estimate of D (difference-mode gain) from the single-sided level-series measurements. In this estimation it is assumed that $|\underline{C}| << |\underline{D}|$.

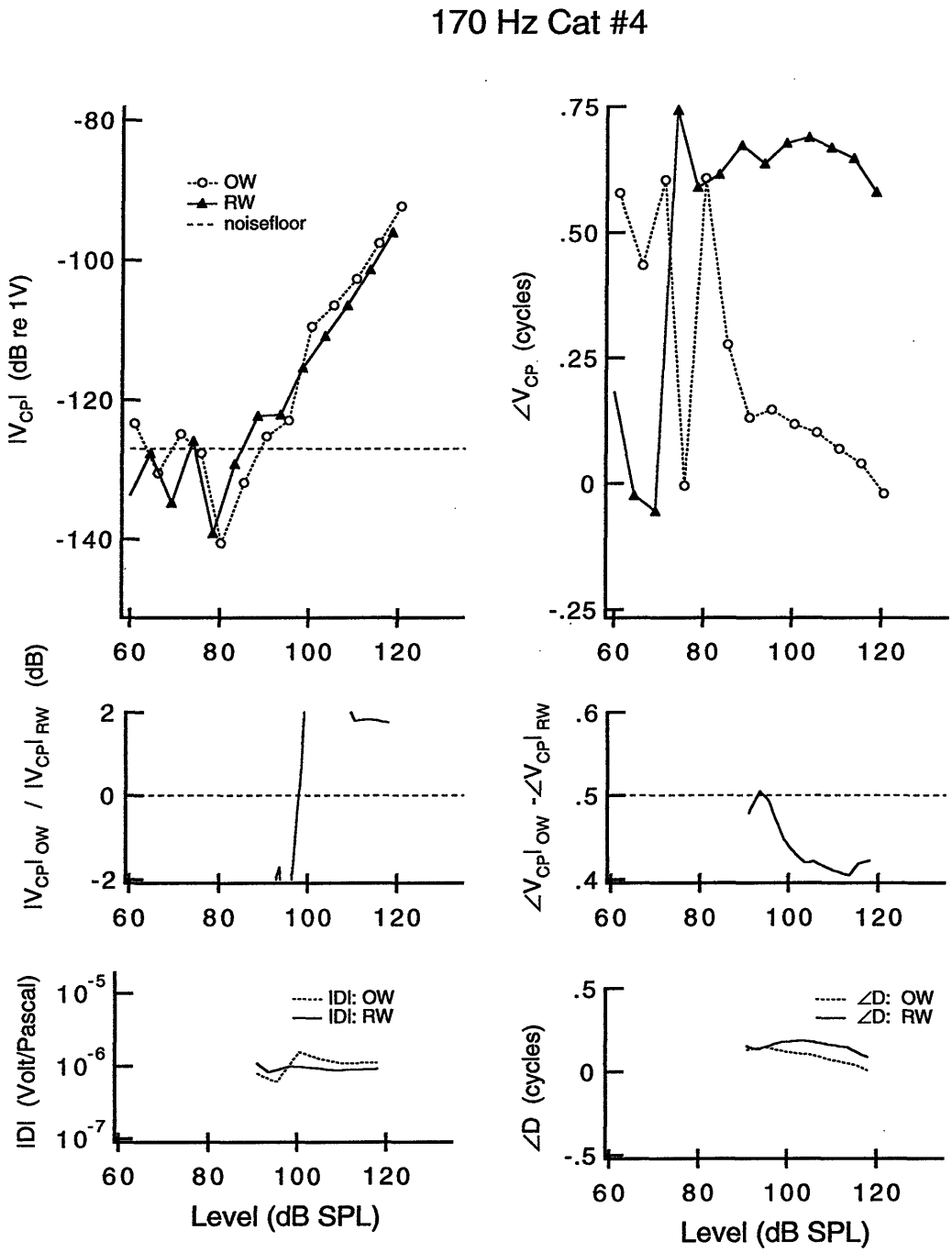

Figure B-8: TOP: Single-sided level-series measurements made on Cat #4 at 170 Hz. Either the oval or the round window was stimulated. MIDDLE: Ratio of the measurement made while the oval window was stimulated and the measurement made while the round window was stimulated. BOTTOM: Estimate of D (difference-mode gain) from the single-sided level-series measurements. In this estimation it is assumed that $|\underline{C}| << |\underline{D}|$.

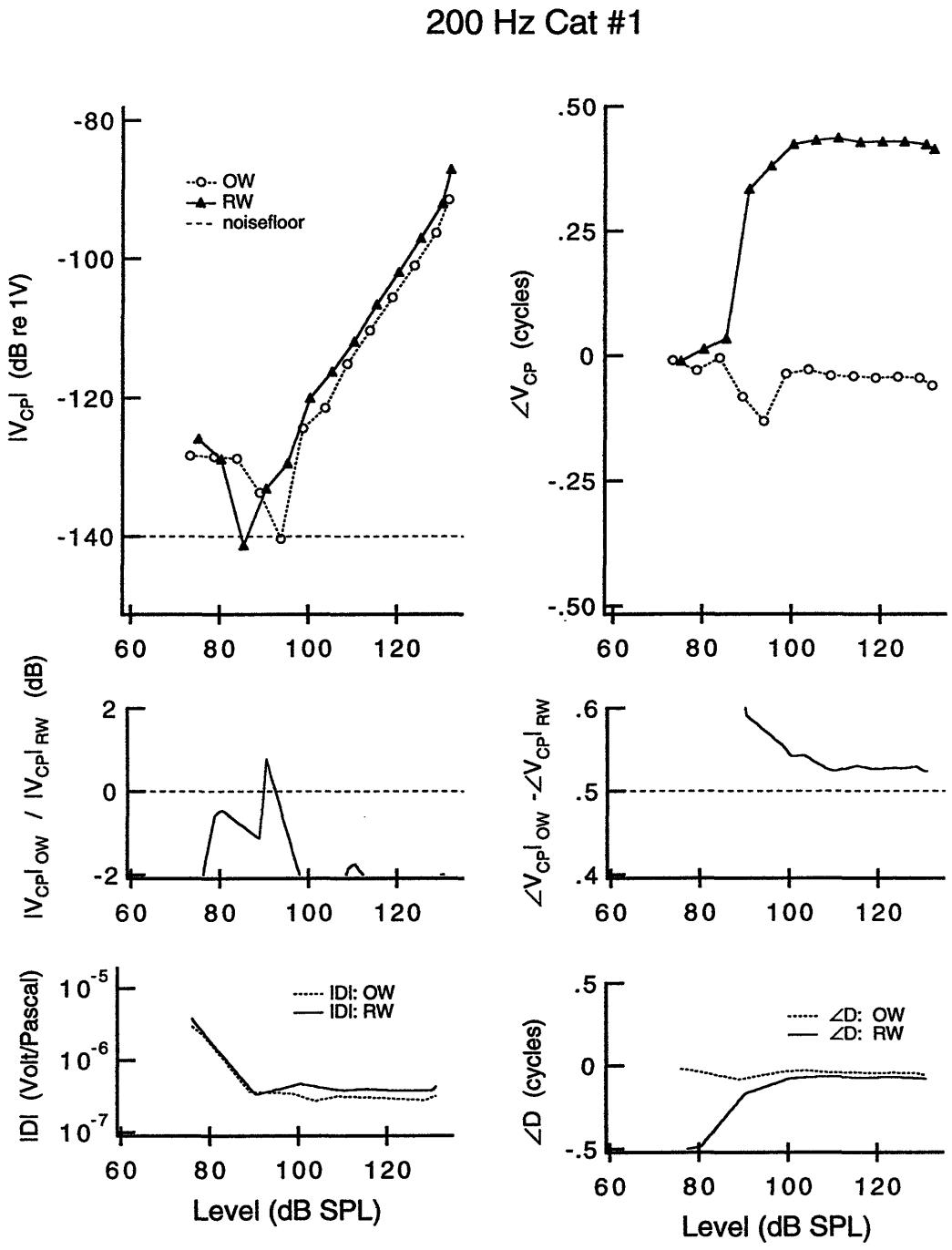

Figure B-9: TOP: Single-sided level-series measurements made on Cat #1 at 200 Hz. Either the oval or the round window was stimulated. MIDDLE: Ratio of the measurement made while the oval window was stimulated and the measurement made while the round window was stimulated. BOTTOM: Estimate of D (difference-mode gain) from the single-sided level-series measurements. In this estimation it is assumed that $|\underline{C}| << |\underline{D}|$.

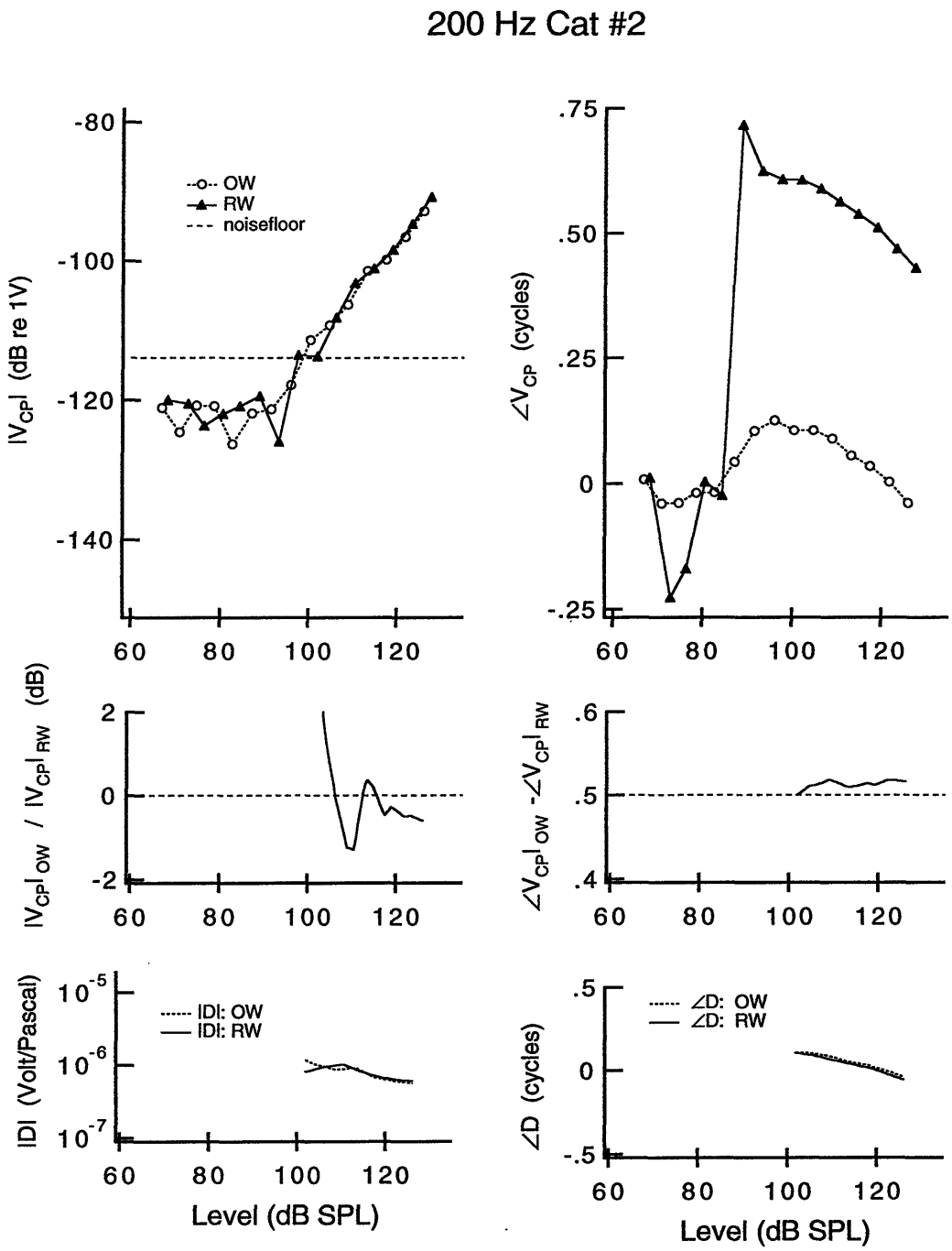

Figure B-10: TOP: Single-sided level-series measurements made on Cat #2 at 200 Hz. Either the oval or the round window was stimulated. MIDDLE: Ratio of the measurement made while the oval window was stimulated and the measurement made while the round window was stimulated. BOTTOM: Estimate of D (difference-mode gain) from the single-sided level-series measurements. In this estimation it is assumed that $|\underline{C}| << |\underline{D}|$.

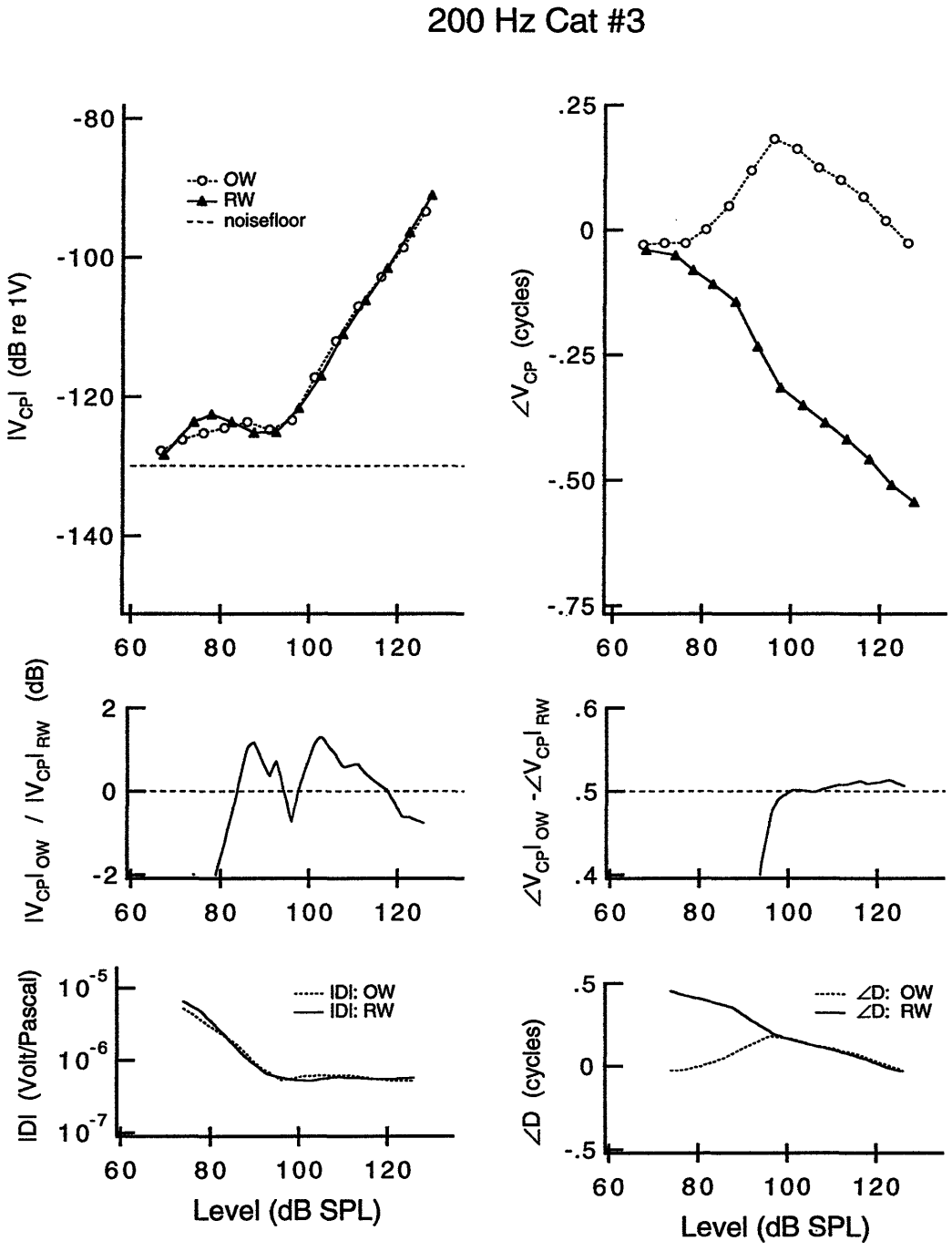

Figure B-11: TOP: Single-sided level-series measurements made on Cat #3 at 200 Hz. Either the oval or the round window was stimulated. MIDDLE: Ratio of the measurement made while the oval window was stimulated and the measurement made while the round window was stimulated. BOTTOM: Estimate of D (difference-mode gain) from the single-sided level-series measurements. In this estimation it is assumed that $|\underline{C}| << |\underline{D}|$.

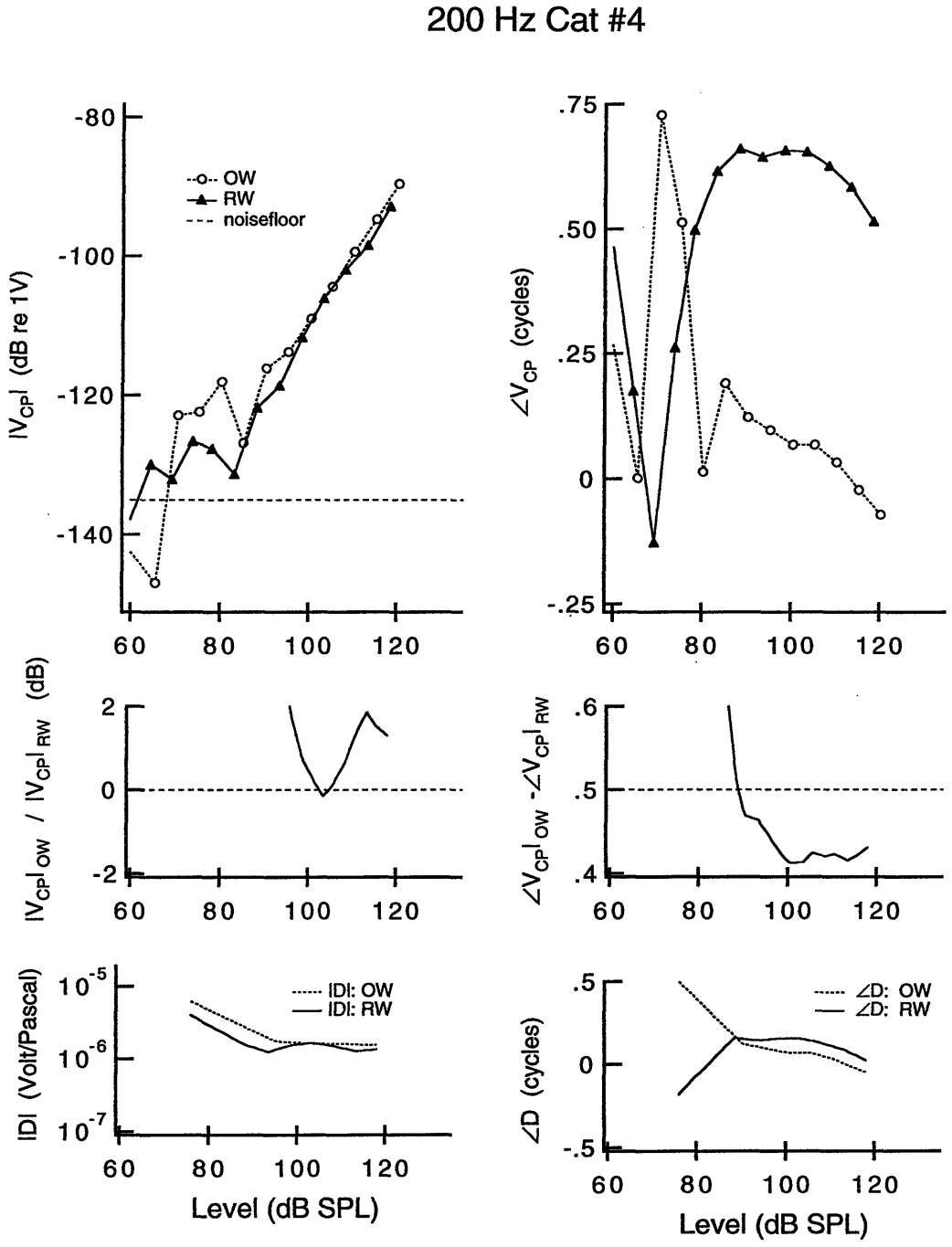

Figure B-12: TOP: Single-sided level-series measurements made on Cat #4 at 200 Hz. Either the oval or the round window was stimulated. MIDDLE: Ratio of the measurement made while the oval window was stimulated and the measurement made while the round window was stimulated. BOTTOM: Estimate of D (difference-mode gain) from the single-sided level-series measurements. In this estimation it is assumed that $|\underline{C}| << |\underline{D}|$.

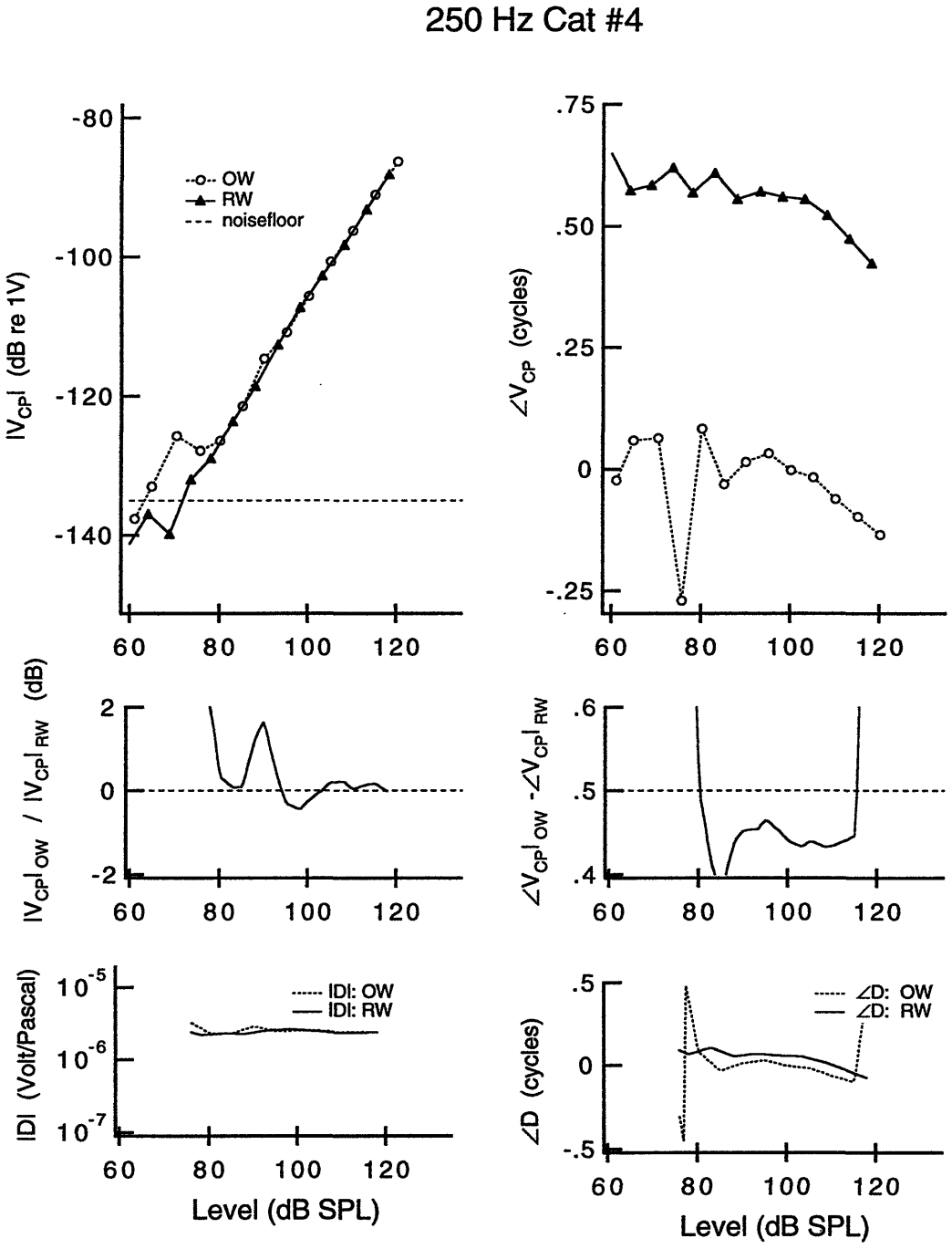

Figure B-13: TOP: Single-sided level-series measurements made on Cat #4 at 250 Hz. Either the oval or the round window was stimulated. MIDDLE: Ratio of the measurement made while the oval window was stimulated and the measurement made while the round window was stimulated. BOTTOM: Estimate of D (difference-mode gain) from the single-sided level-series measurements. In this estimation it is assumed that $|\underline{C}| << |\underline{D}|$.

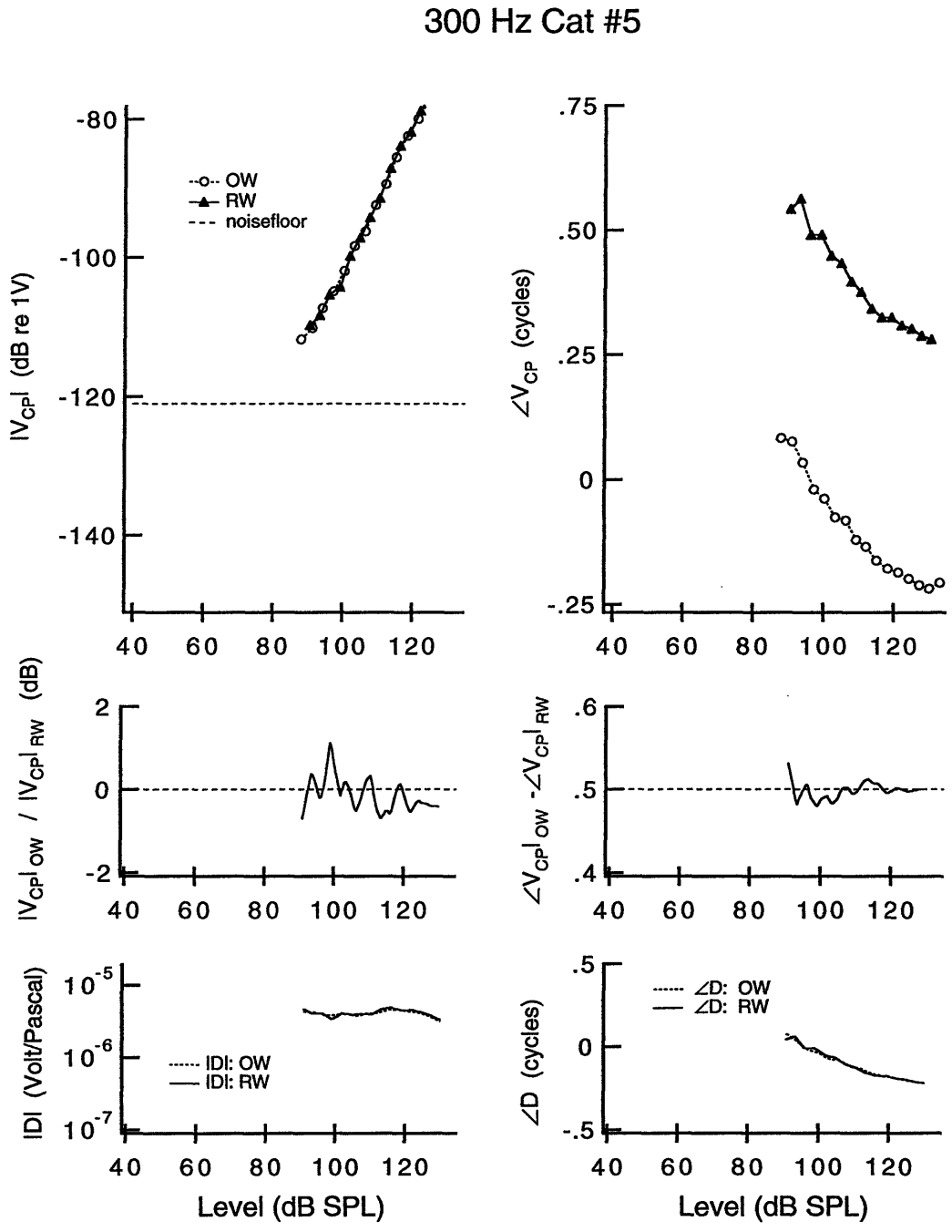

Figure B-14: TOP: Single-sided level-series measurements made on Cat #5 at 300 Hz. Either the oval or the round window was stimulated. MIDDLE: Ratio of the measurement made while the oval window was stimulated and the measurement made while the round window was stimulated. BOTTOM: Estimate of D (difference-mode gain) from the single-sided level-series measurements. In this estimation it is assumed that $|\underline{C}| << |\underline{D}|$.

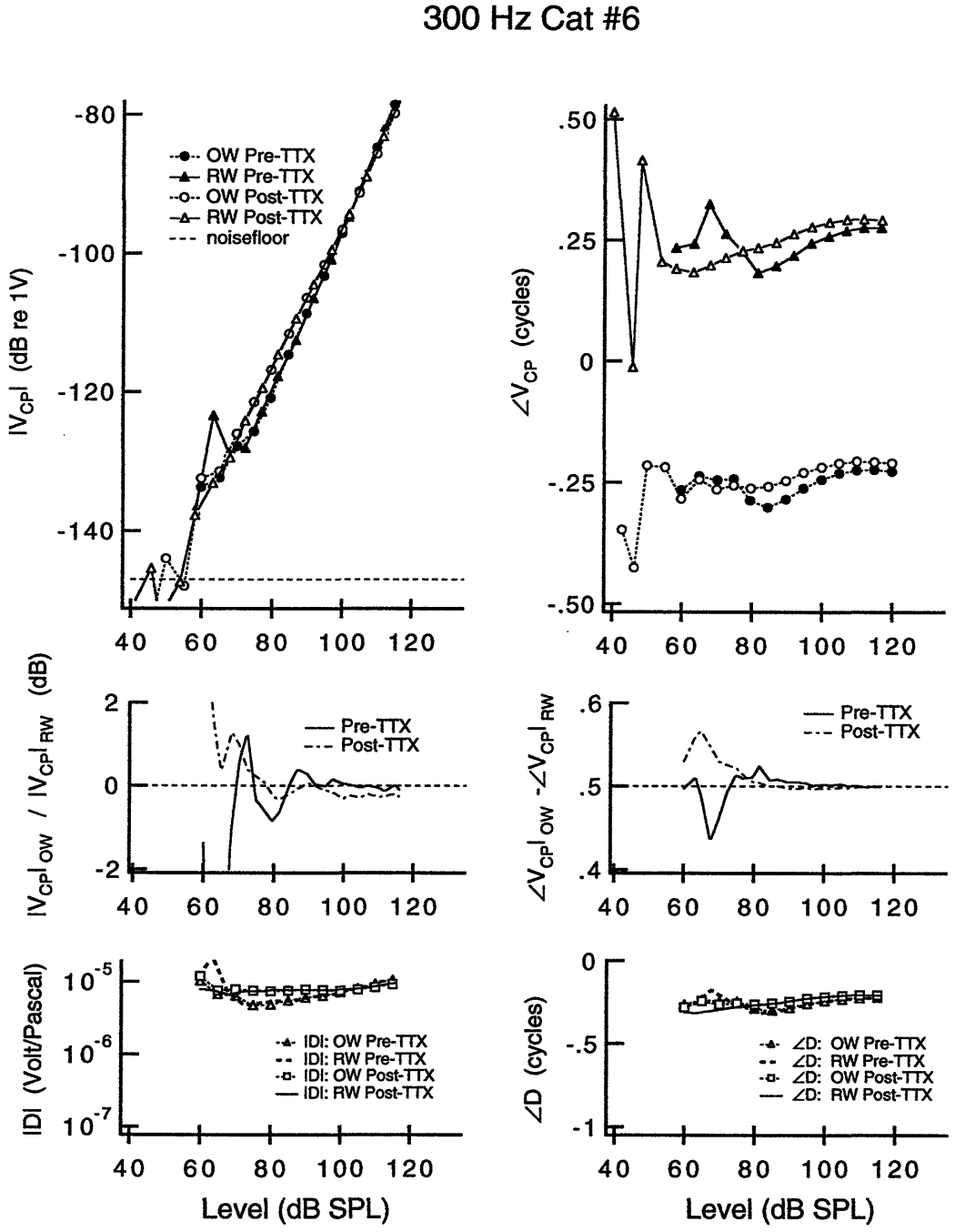

Figure B-15: TOP: Single-sided level-series measurements made on Cat #6 at 300 Hz before and after the application of TTX. Either the oval or the round window was stimulated. MIDDLE: Ratio of the measurement made while the oval window was stimulated and the measurement made while the round window was stimulated. BOTTOM: Estimate of D (difference-mode gain) from the single-sided level-series measurements. In this estimation it is assumed that $|\underline{C}| << |\underline{D}|$.

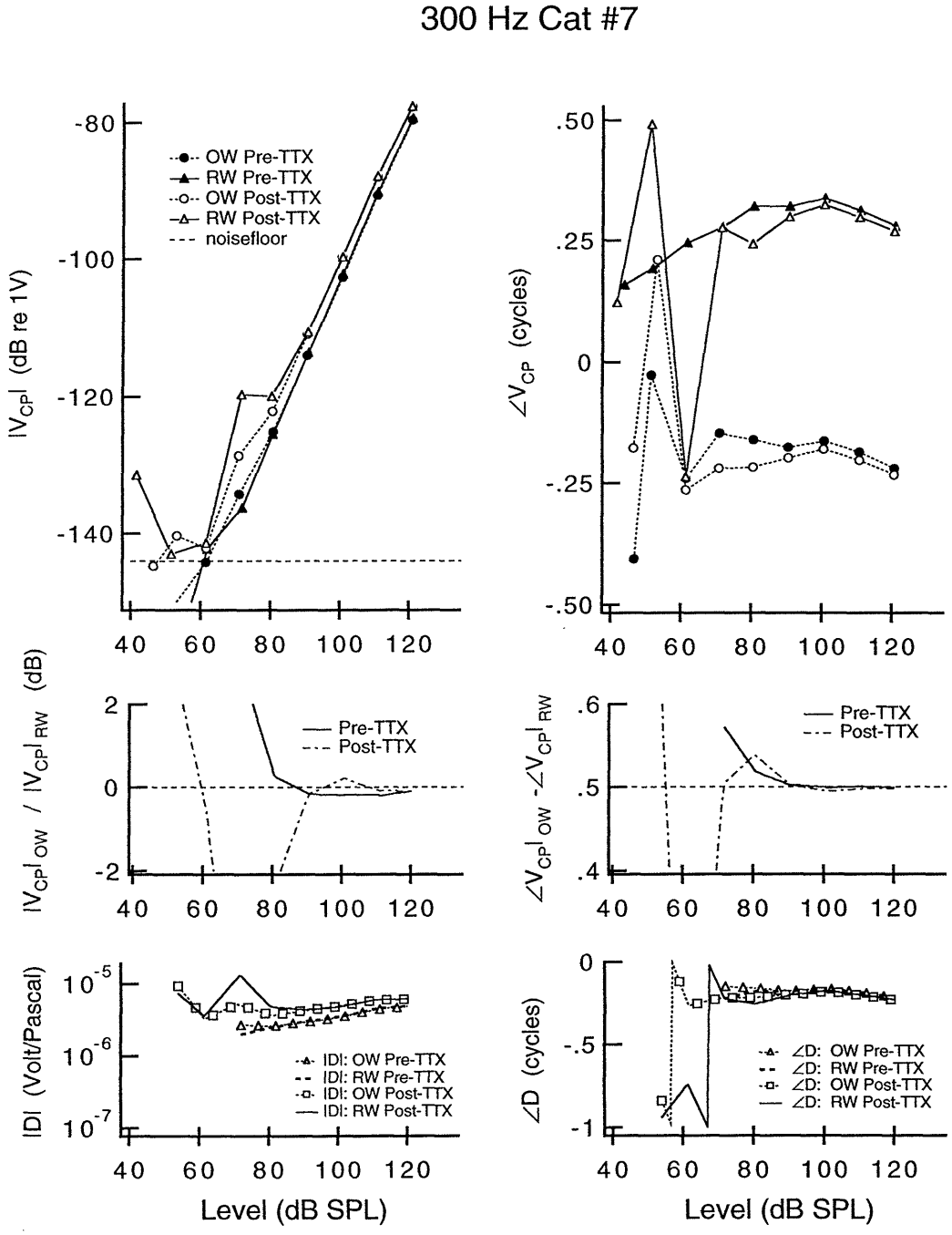

Figure B-16: TOP: Single-sided level-series measurements made on Cat #7 at 300 Hz before and after the application of TTX. Either the oval or the round window was stimulated. MIDDLE: Ratio of the measurement made while the oval window was stimulated and the measurement made while the round window was stimulated. BOTTOM: Estimate of D (difference-mode gain) from the single-sided level-series measurements. In this estimation it is assumed that $|\underline{C}| << |\underline{D}|$.

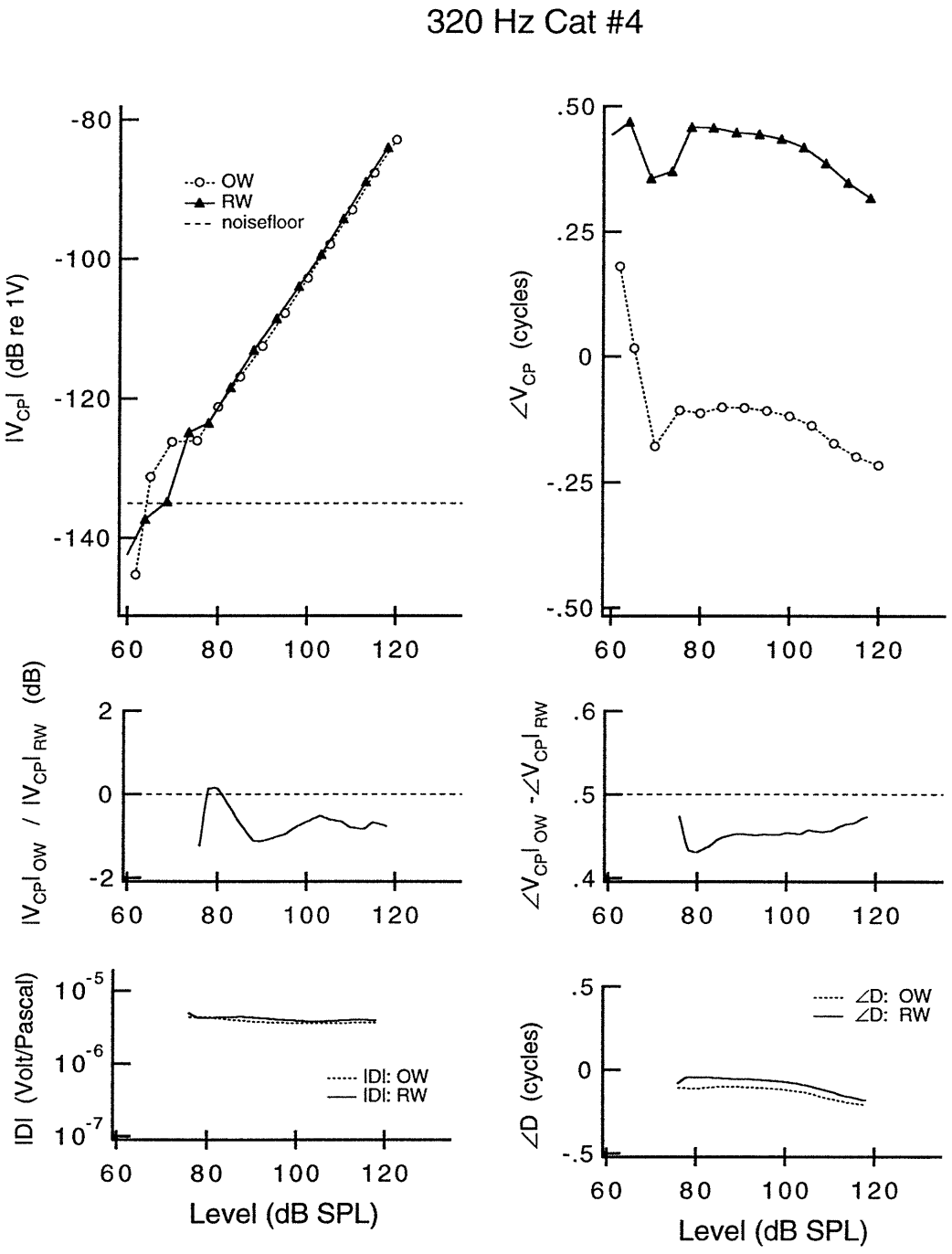

Figure B-17: TOP: Single-sided level-series measurements made on Cat #4 at 320 Hz. Either the oval or the round window was stimulated. MIDDLE: Ratio of the measurement made while the oval window was stimulated and the measurement made while the round window was stimulated. BOTTOM: Estimate of D (difference-mode gain) from the single-sided level-series measurements. In this estimation it is assumed that $|\underline{C}| << |\underline{D}|$.

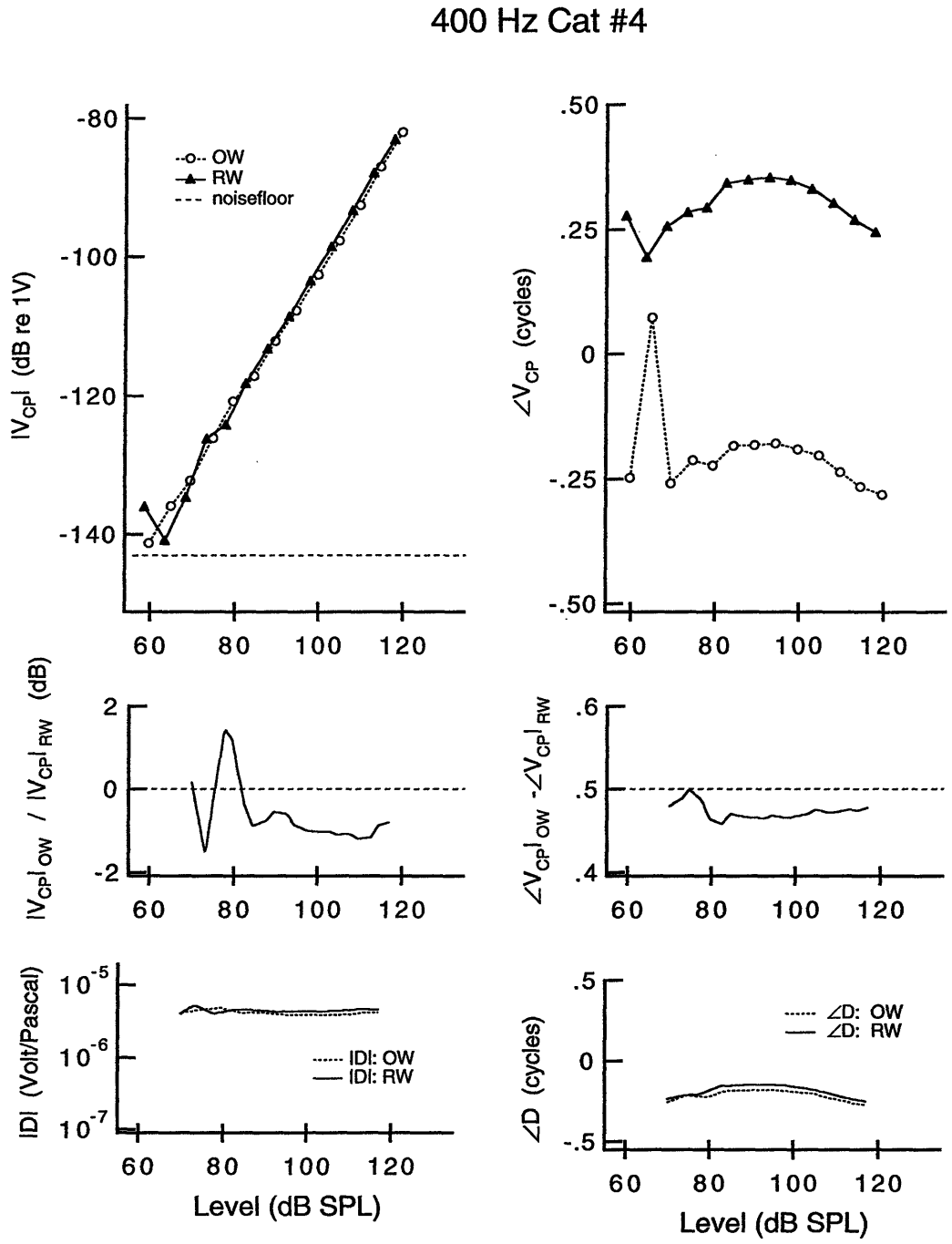

Figure B-18: TOP: Single-sided level-series measurements made on Cat #4 at 400 Hz. Either the oval or the round window was stimulated. MIDDLE: Ratio of the measurement made while the oval window was stimulated and the measurement made while the round window was stimulated. BOTTOM: Estimate of D (difference-mode gain) from the single-sided level-series measurements. In this estimation it is assumed that $|\underline{C}| << |\underline{D}|$.

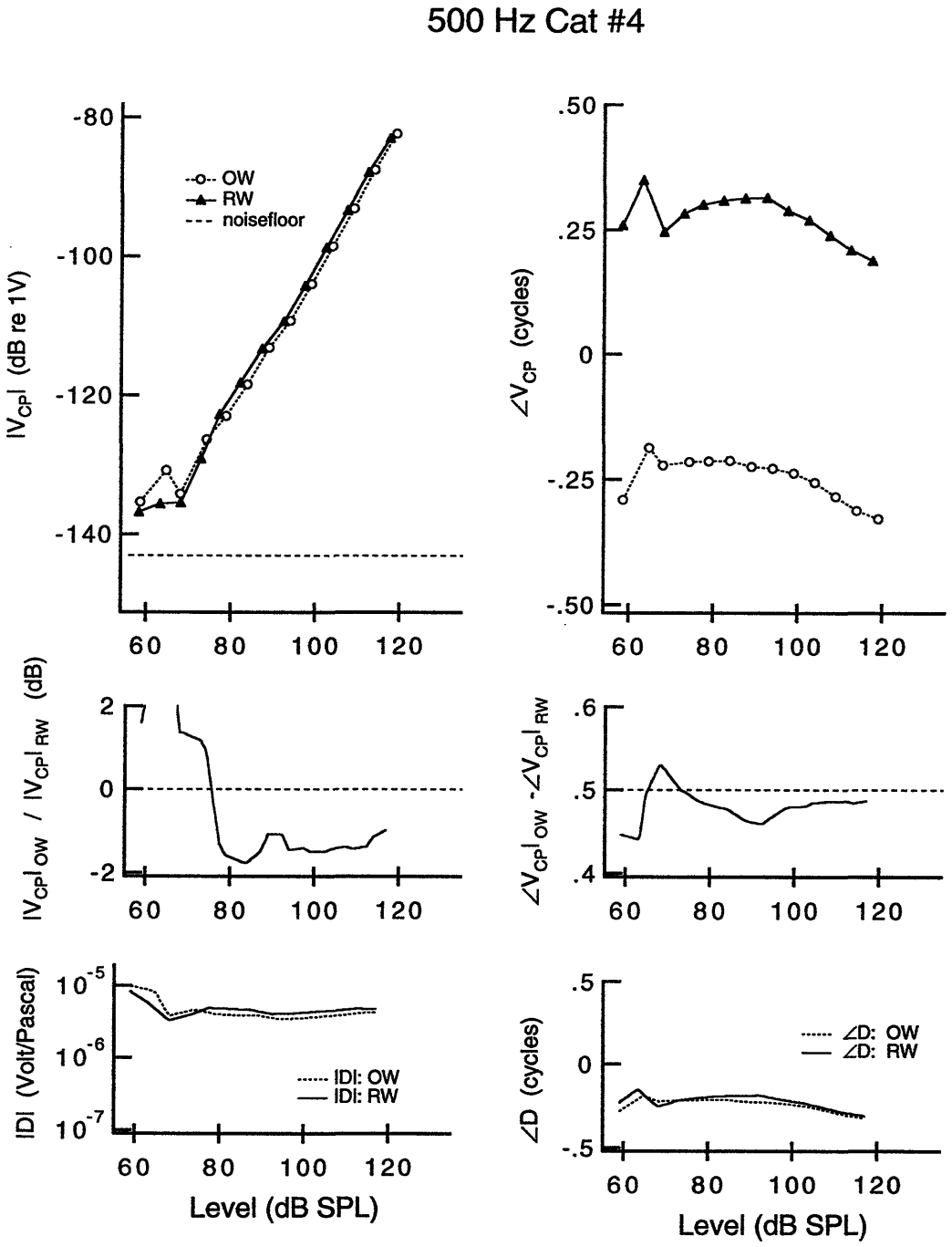

Figure B-19: TOP: Single-sided level-series measurements made on Cat #4 at 500 Hz. Either the oval or the round window was stimulated. MIDDLE: Ratio of the measurement made while the oval window was stimulated and the measurement made while the round window was stimulated. BOTTOM: Estimate of D (difference-mode gain) from the single-sided level-series measurements. In this estimation it is assumed that $|\underline{C}| << |\underline{D}|$.

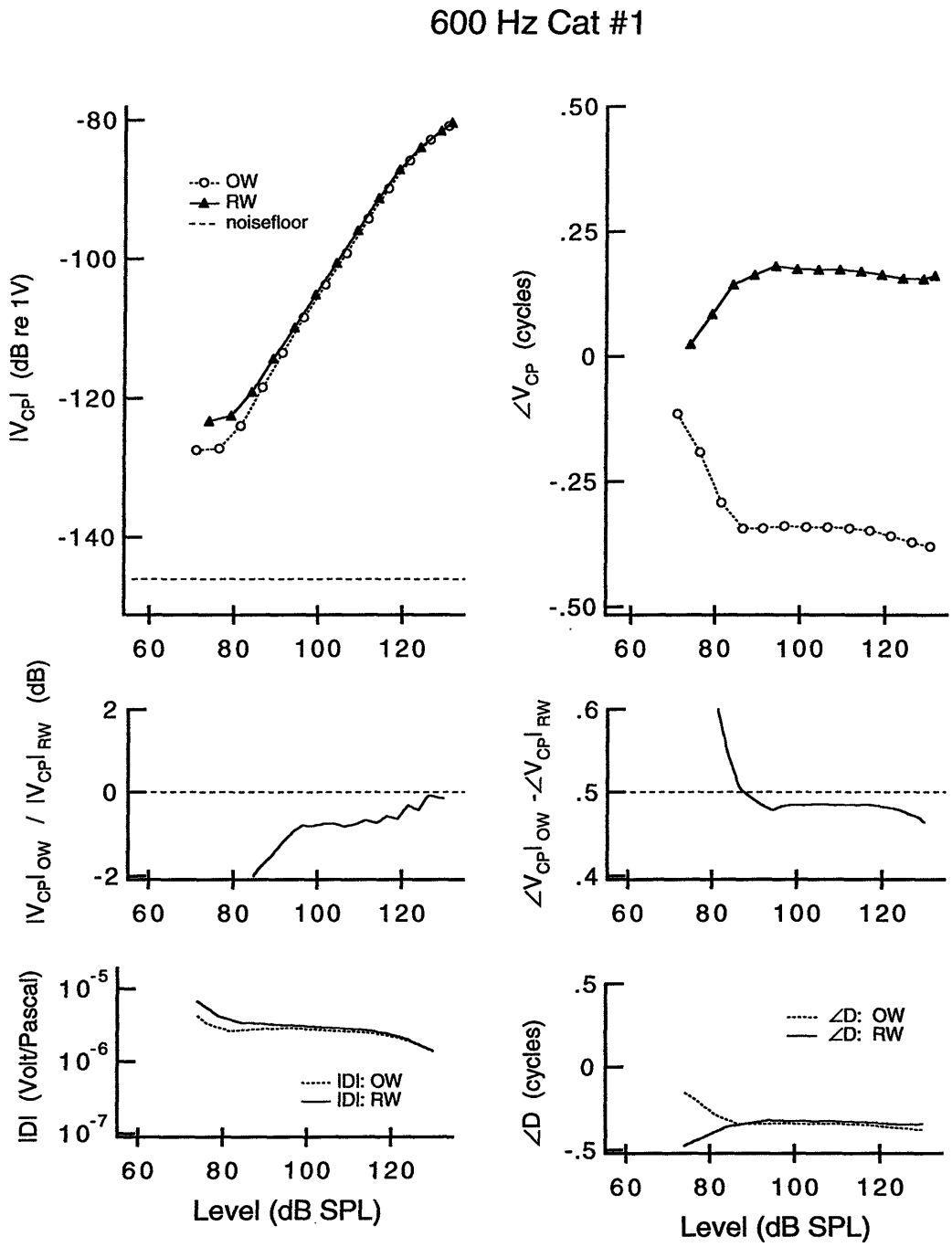

Figure B-20: TOP: Single-sided level-series measurements made on Cat #1 at 600 Hz. Either the oval or the round window was stimulated. MIDDLE: Ratio of the measurement made while the oval window was stimulated and the measurement made while the round window was stimulated. BOTTOM: Estimate of D (difference-mode gain) from the single-sided level-series measurements. In this estimation it is assumed that $|\underline{C}| << |\underline{D}|$.

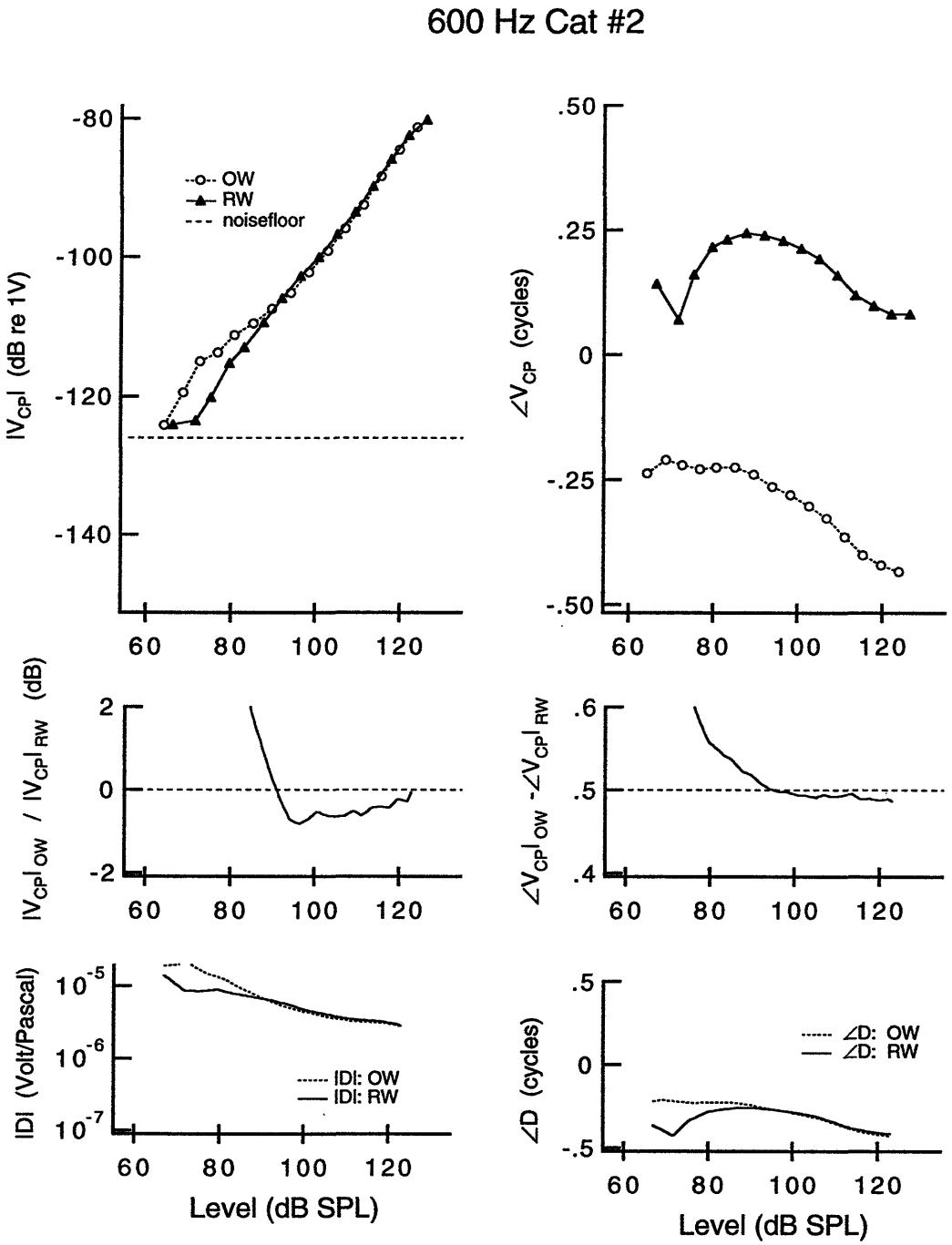

Figure B-21: TOP: Single-sided level-series measurements made on Cat #2 at 600 Hz. Either the oval or the round window was stimulated. MIDDLE: Ratio of the measurement made while the oval window was stimulated and the measurement made while the round window was stimulated. BOTTOM: Estimate of D (difference-mode gain) from the single-sided level-series measurements. In this estimation it is assumed that $|\underline{C}| << |\underline{D}|$.

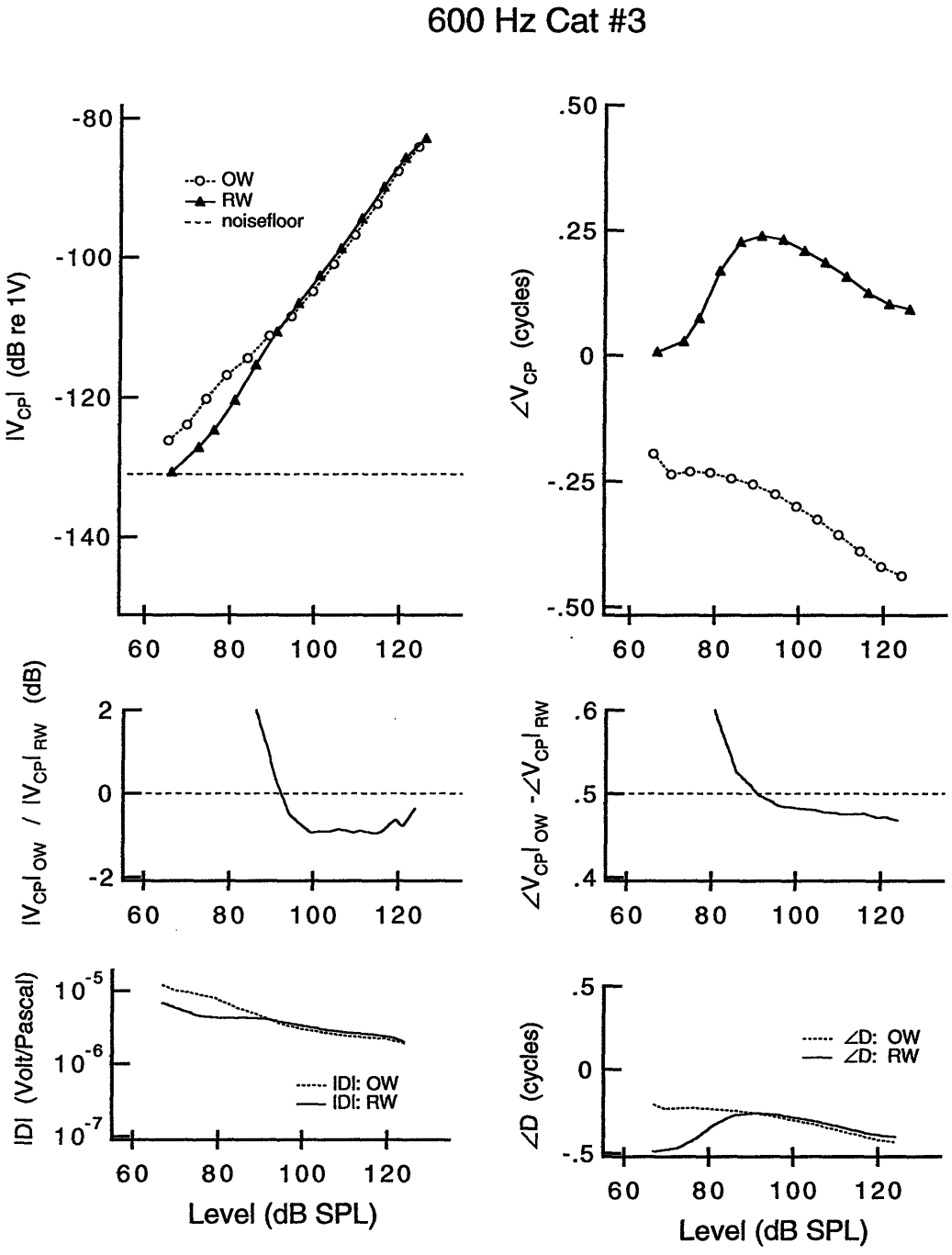

Figure B-22: TOP: Single-sided level-series measurements made on Cat #3 at 600 Hz. Either the oval or the round window was stimulated. MIDDLE: Ratio of the measurement made while the oval window was stimulated and the measurement made while the round window was stimulated. BOTTOM: Estimate of D (difference-mode gain) from the single-sided level-series measurements. In this estimation it is assumed that $|\underline{C}| << |\underline{D}|$.

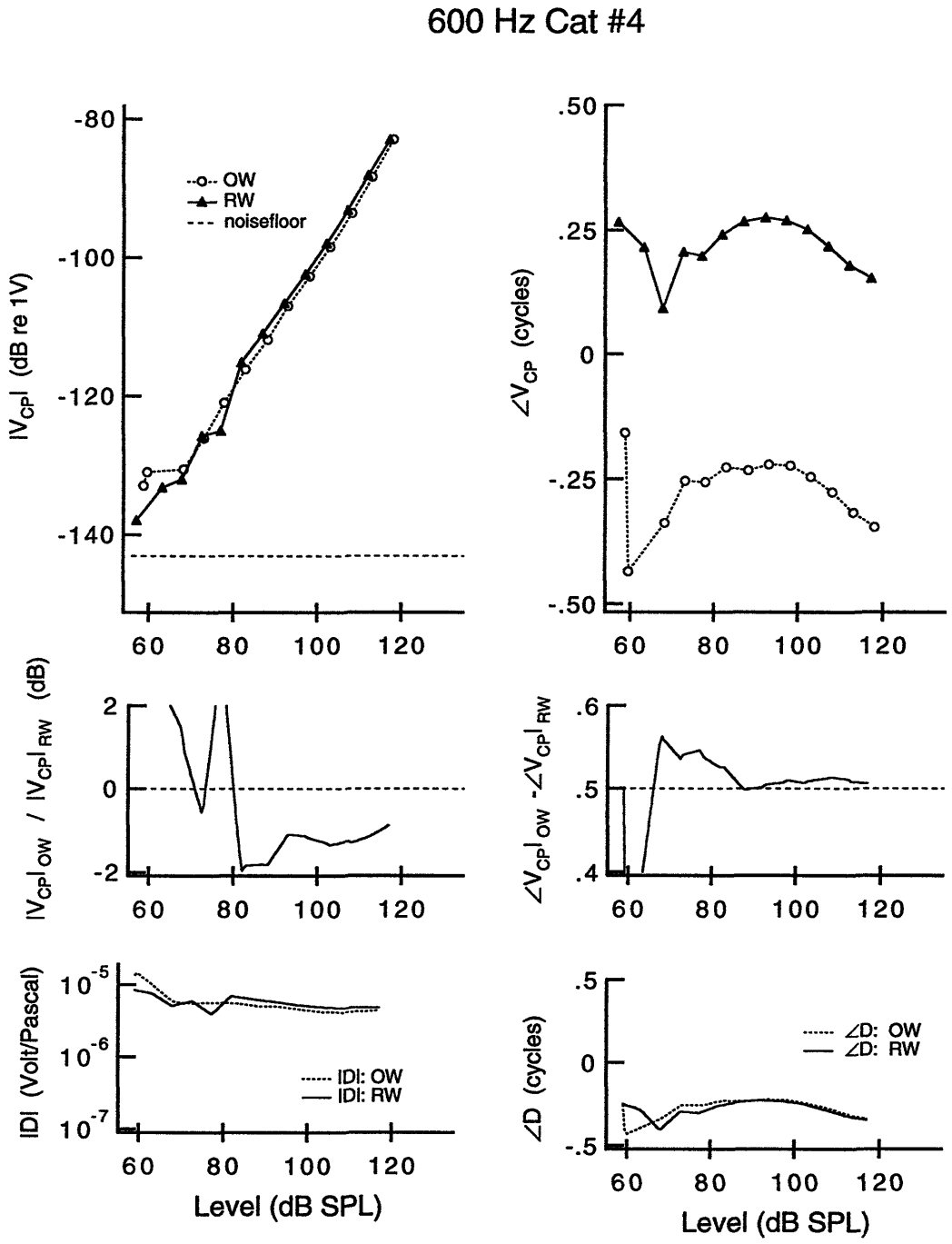

Figure B-23: TOP: Single-sided level-series measurements made on Cat #4 at 600 Hz. Either the oval or the round window was stimulated. MIDDLE: Ratio of the measurement made while the oval window was stimulated and the measurement made while the round window was stimulated. BOTTOM: Estimate of D (difference-mode gain) from the single-sided level-series measurements. In this estimation it is assumed that $|\underline{C}| << |\underline{D}|$.

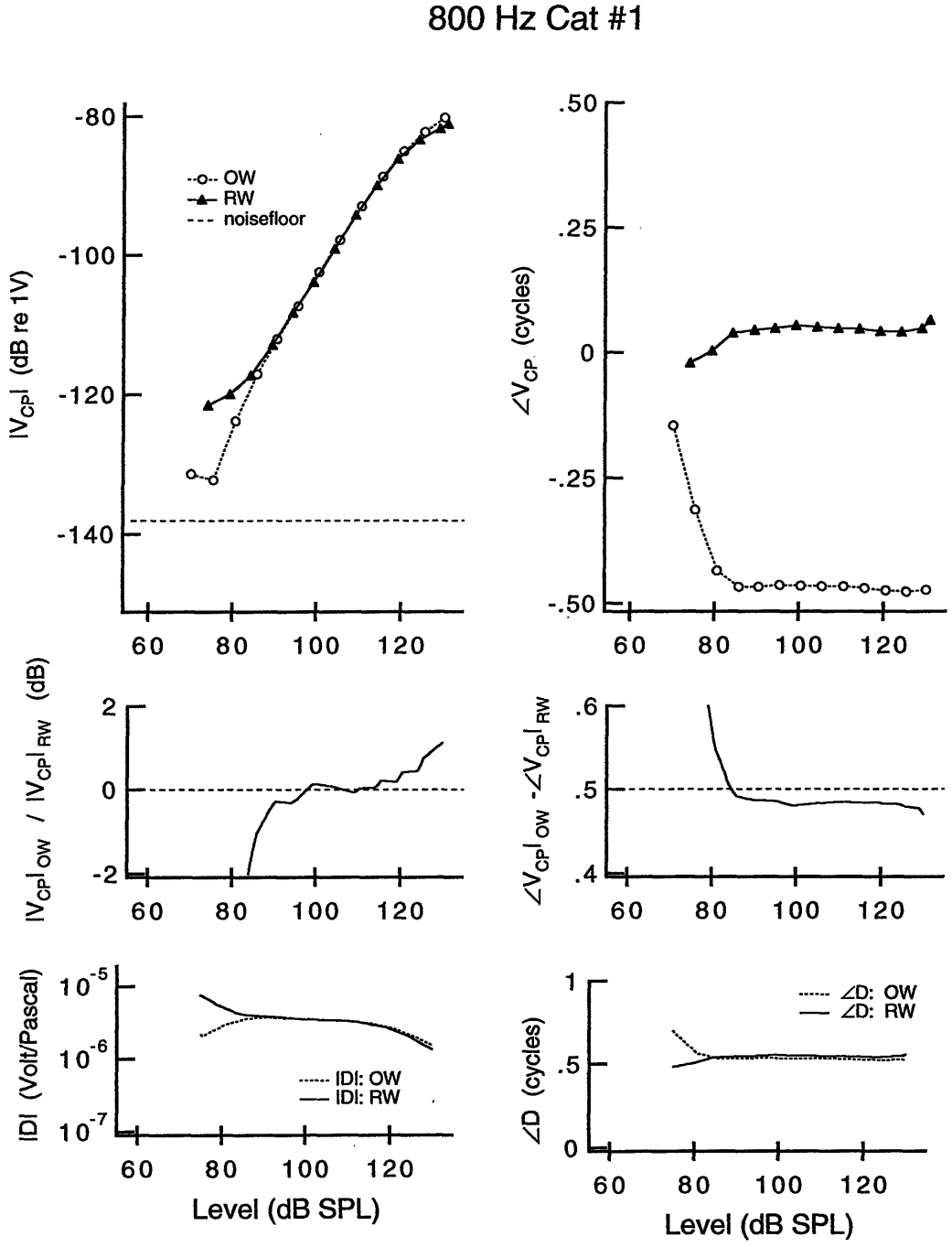

Figure B-24: TOP: Single-sided level-series measurements made on Cat #1 at 800 Hz. Either the oval or the round window was stimulated. MIDDLE: Ratio of the measurement made while the oval window was stimulated and the measurement made while the round window was stimulated. BOTTOM: Estimate of D (difference-mode gain) from the single-sided level-series measurements. In this estimation it is assumed that $|\underline{C}| << |\underline{D}|$.

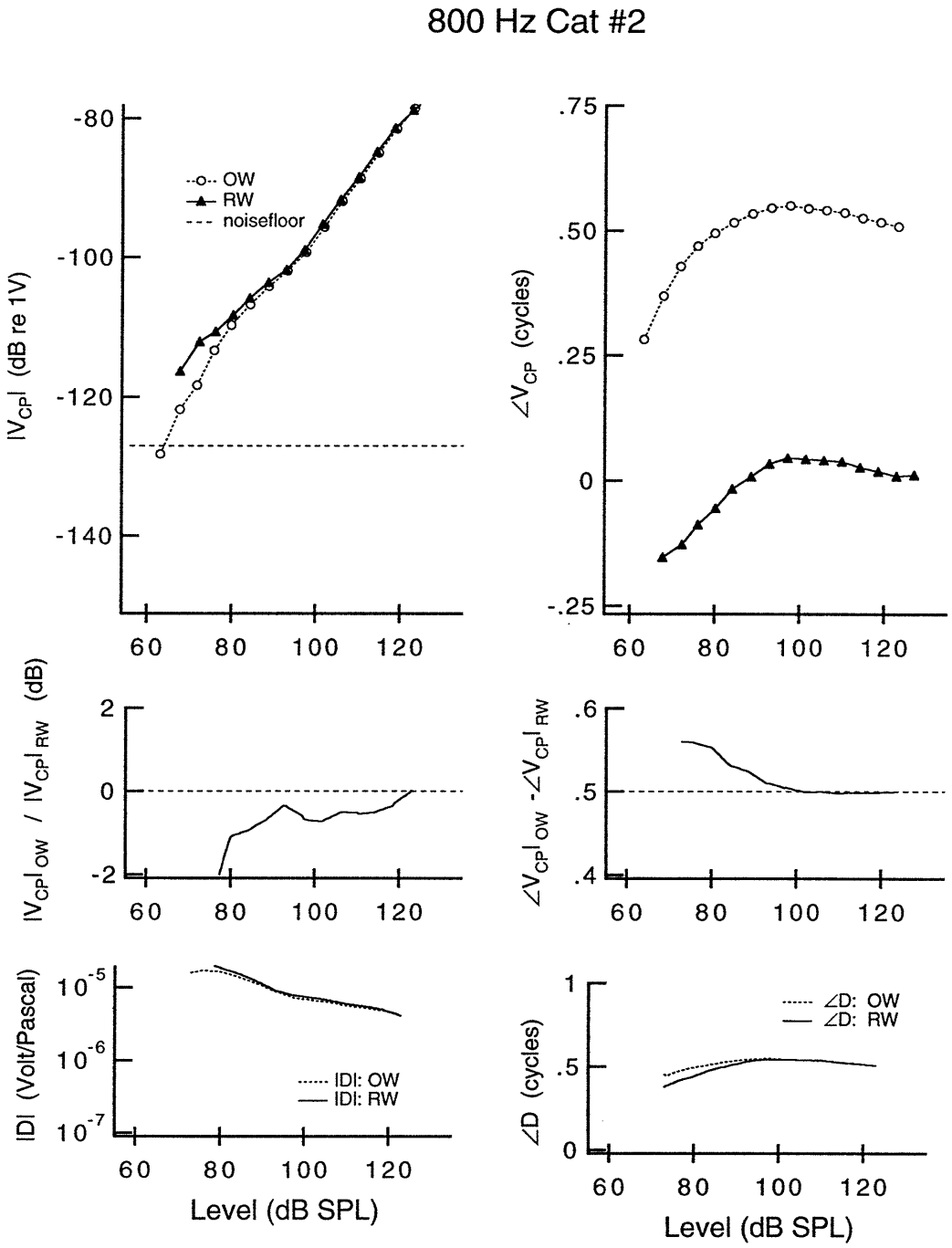

Figure B-25: TOP: Single-sided level-series measurements made on Cat #2 at 800 Hz. Either the oval or the round window was stimulated. MIDDLE: Ratio of the measurement made while the oval window was stimulated and the measurement made while the round window was stimulated. BOTTOM: Estimate of D (difference-mode gain) from the single-sided level-series measurements. In this estimation it is assumed that $|\underline{C}| << |\underline{D}|$.

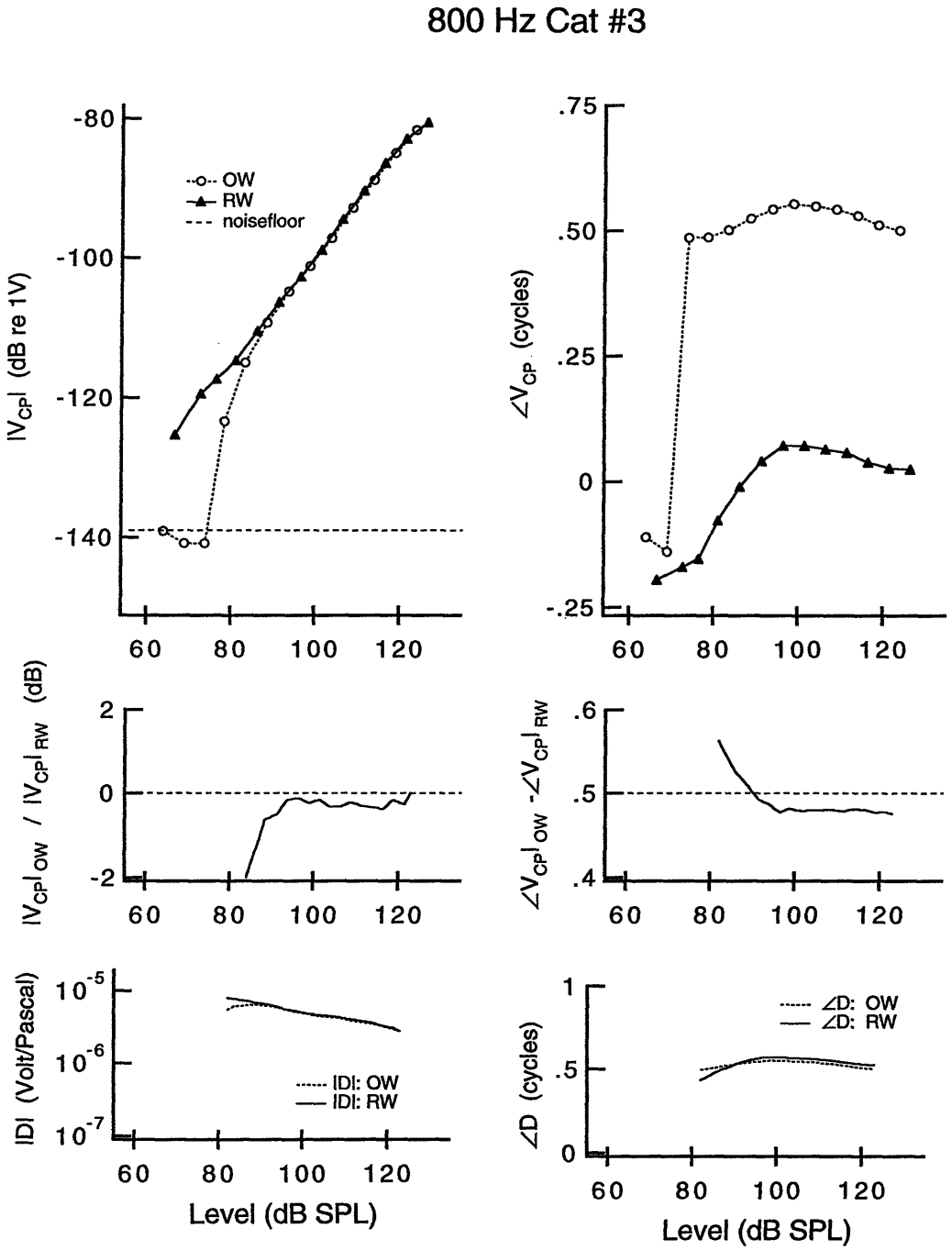

Figure B-26: TOP: Single-sided level-series measurements made on Cat #3 at 800 Hz. Either the oval or the round window was stimulated. MIDDLE: Ratio of the measurement made while the oval window was stimulated and the measurement made while the round window was stimulated. BOTTOM: Estimate of D (difference-mode gain) from the single-sided level-series measurements. In this estimation it is assumed that $|\underline{C}| << |\underline{D}|$.

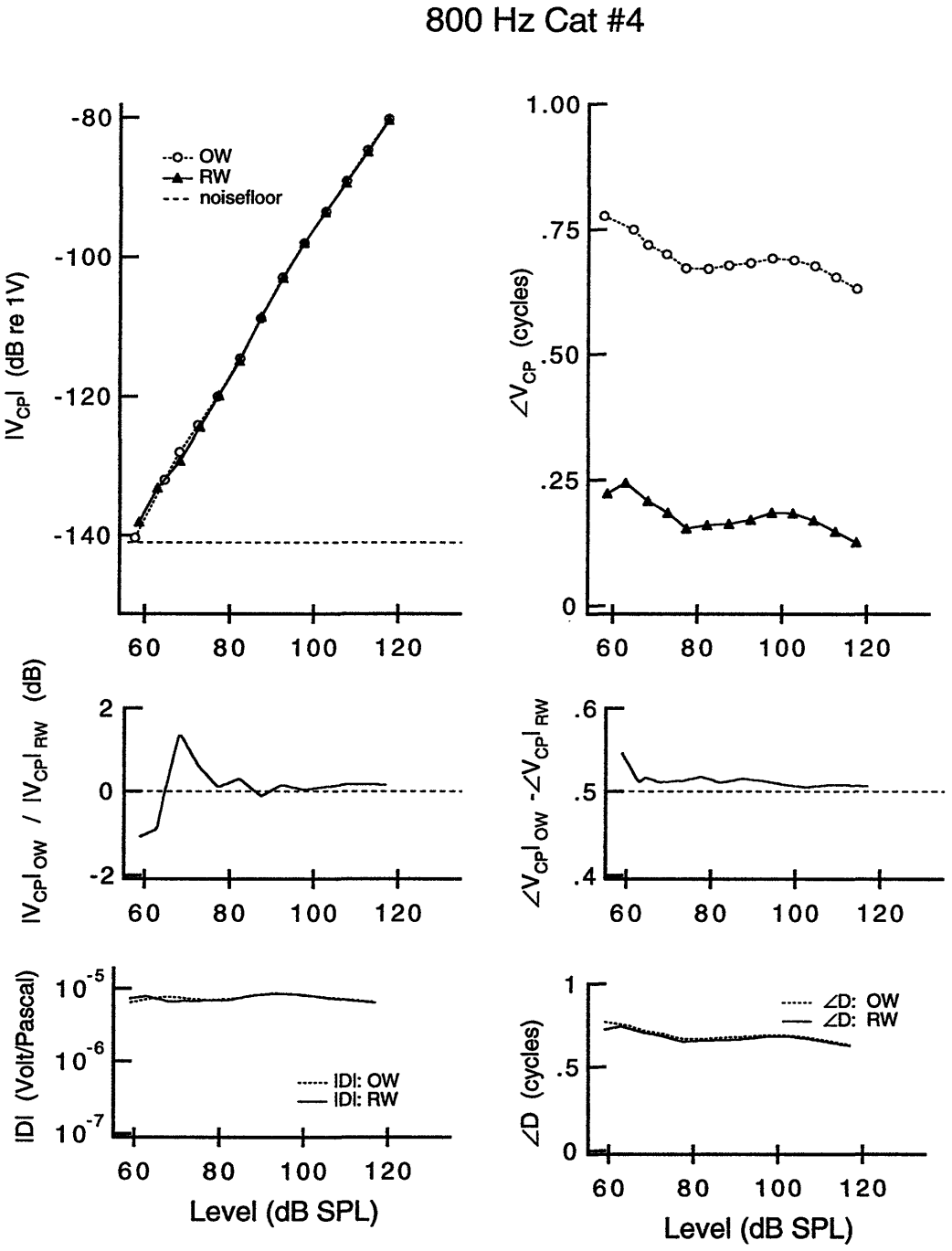

Figure B-27: TOP: Single-sided level-series measurements made on Cat #4 at 800 Hz. Either the oval or the round window was stimulated. MIDDLE: Ratio of the measurement made while the oval window was stimulated and the measurement made while the round window was stimulated. BOTTOM: Estimate of D (difference-mode gain) from the single-sided level-series measurements. In this estimation it is assumed that $|\underline{C}| << |\underline{D}|$.

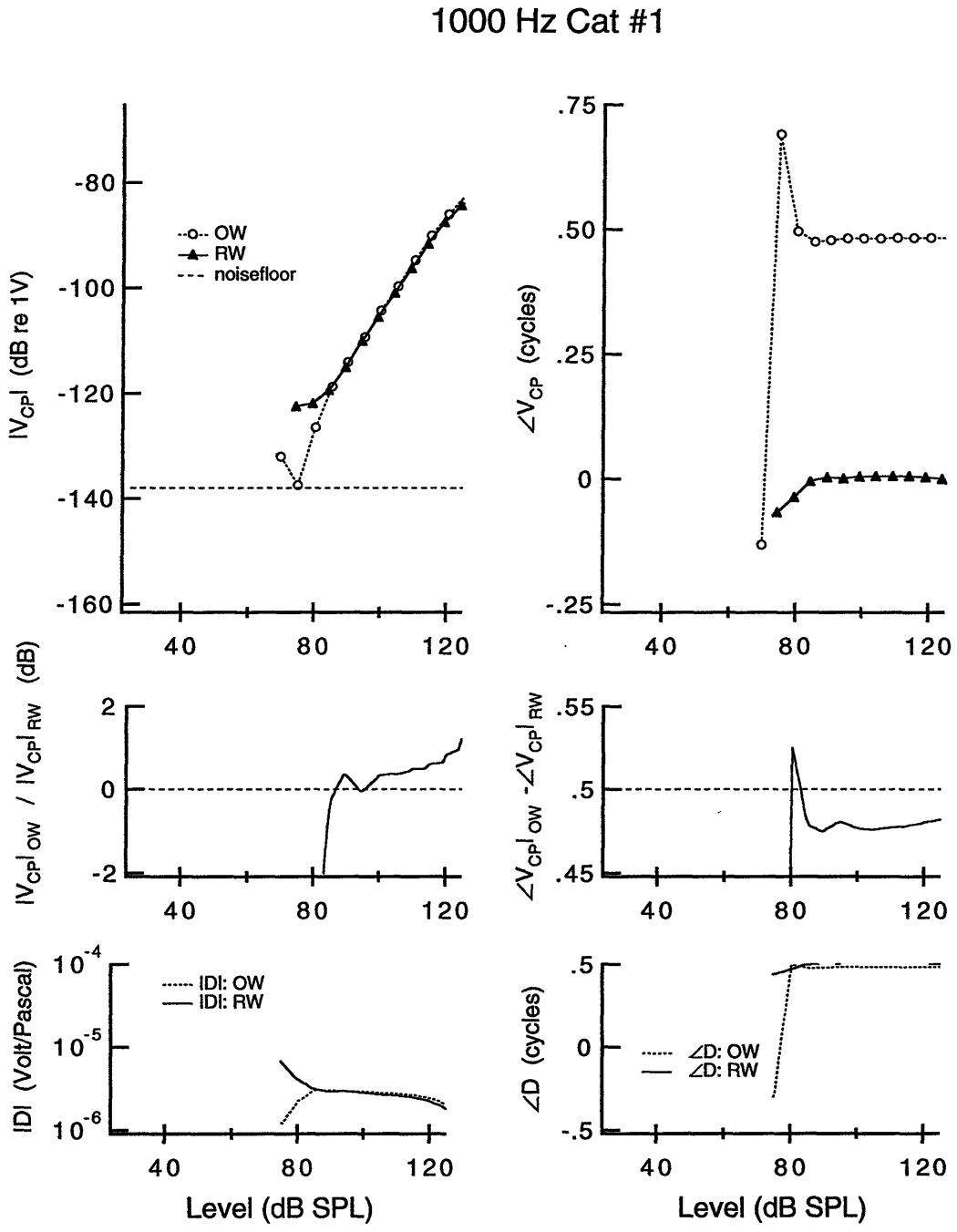

Figure B-28: TOP: Single-sided level-series measurements made on Cat #1 at 1000 Hz. Either the oval or the round window was stimulated. MIDDLE: Ratio of the measurement made while the oval window was stimulated and the measurement made while the round window was stimulated. BOTTOM: Estimate of D (difference-mode gain) from the single-sided level-series measurements. In this estimation it is assumed that $|\underline{C}| << |\underline{D}|$.

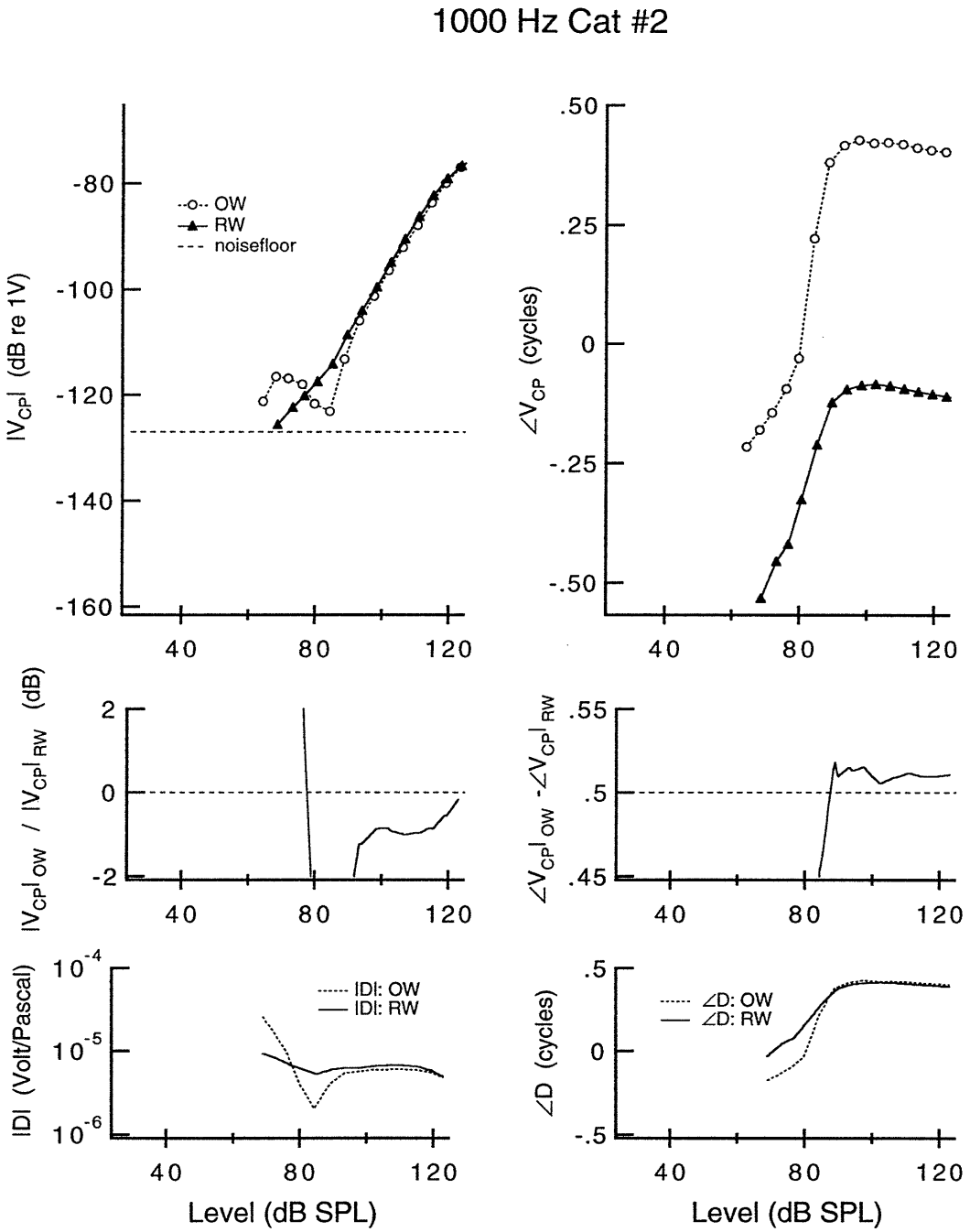

Figure B-29: TOP: Single-sided level-series measurements made on Cat #2 at 1000 Hz. Either the oval or the round window was stimulated. MIDDLE: Ratio of the measurement made while the oval window was stimulated and the measurement made while the round window was stimulated. BOTTOM: Estimate of D (difference-mode gain) from the single-sided level-series measurements. In this estimation it is assumed that $|\underline{C}| << |\underline{D}|$.

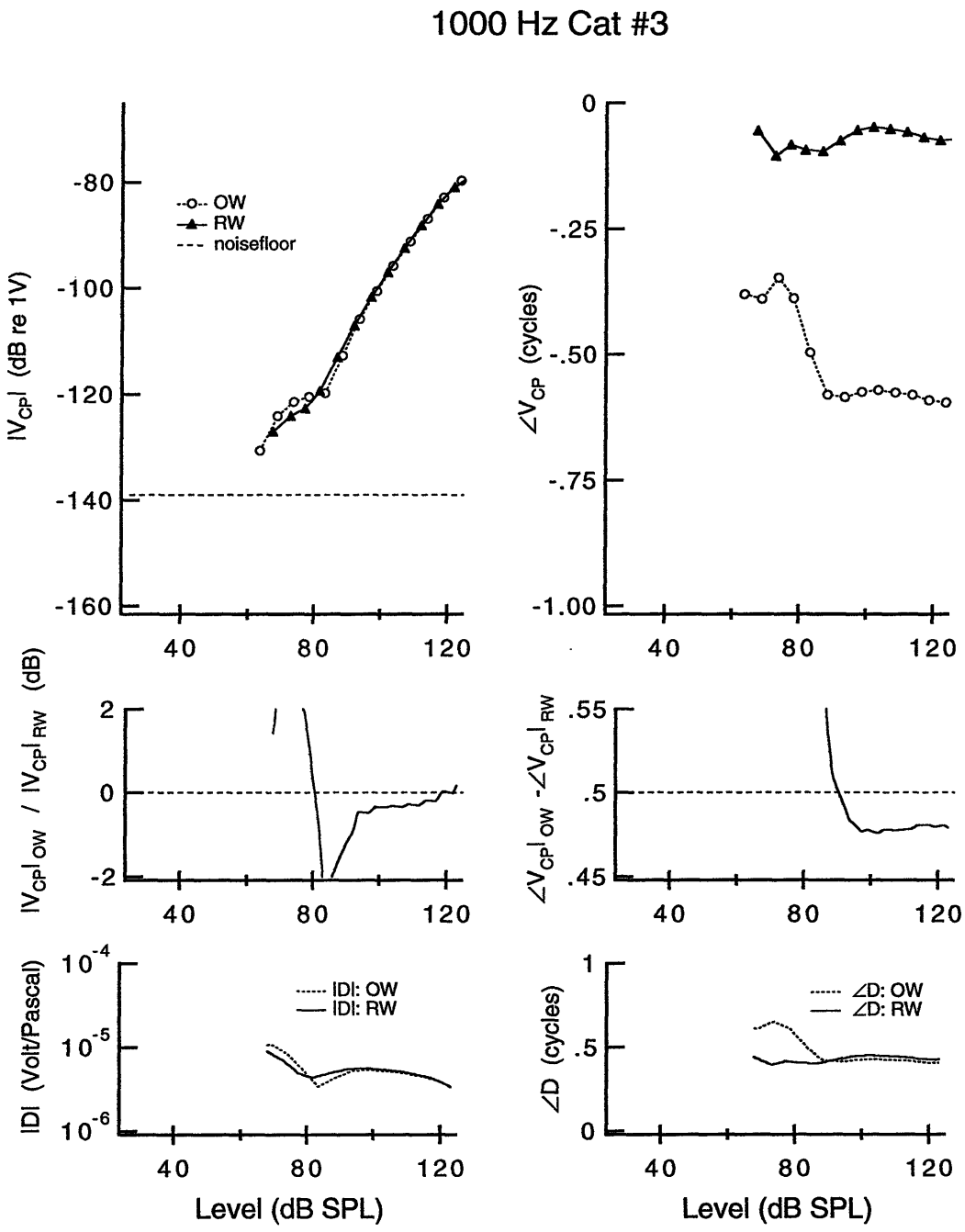

Figure B-30: TOP: Single-sided level-series measurements made on Cat #3 at 1000 Hz. Either the oval or the round window was stimulated. MIDDLE: Ratio of the measurement made while the oval window was stimulated and the measurement made while the round window was stimulated. BOTTOM: Estimate of D (difference-mode gain) from the single-sided level-series measurements. In this estimation it is assumed that $|\underline{C}| << |\underline{D}|$.

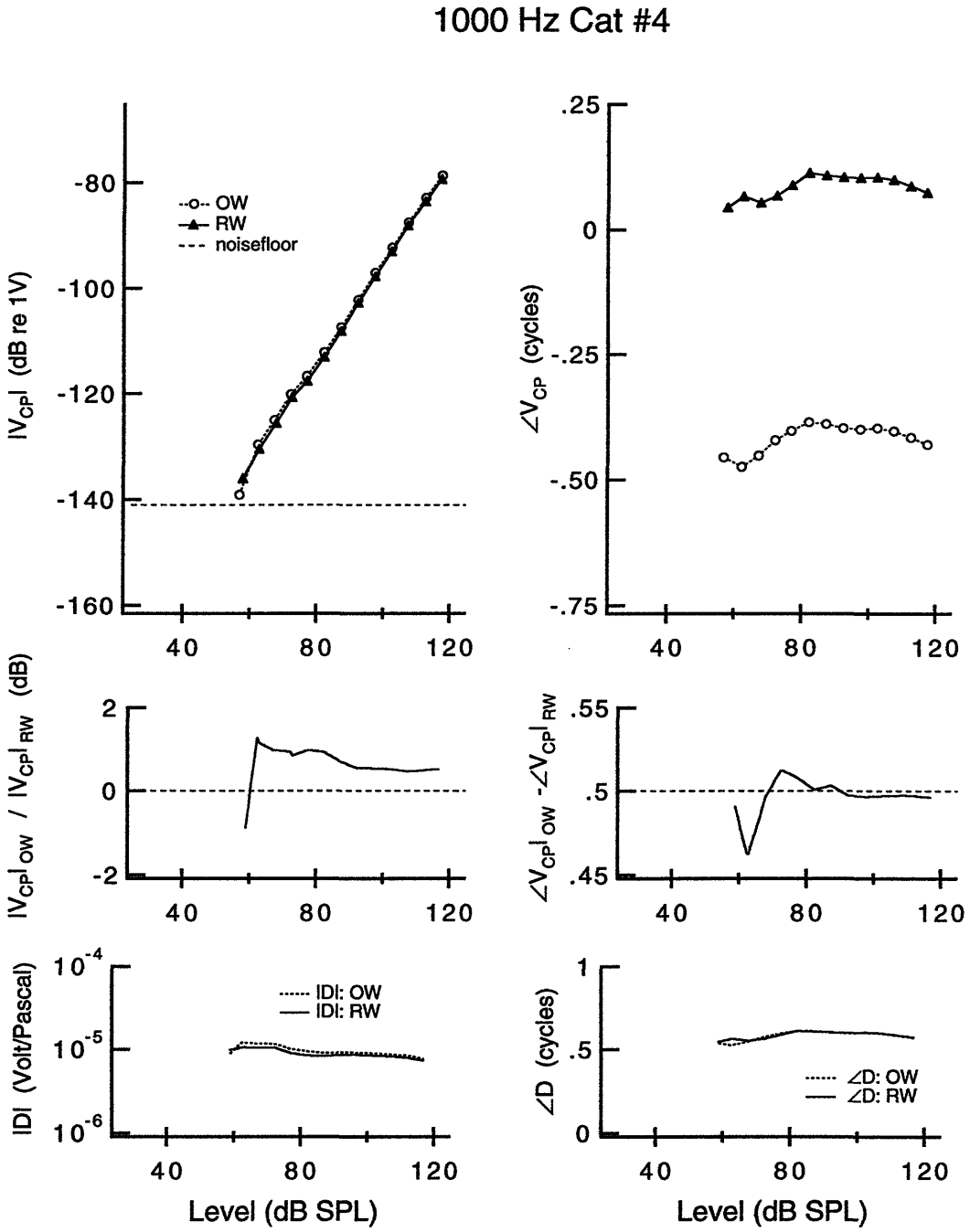

Figure B-31: TOP: Single-sided level-series measurements made on Cat #4 at 1000 Hz. Either the oval or the round window was stimulated. MIDDLE: Ratio of the measurement made while the oval window was stimulated and the measurement made while the round window was stimulated. BOTTOM: Estimate of D (difference-mode gain) from the single-sided level-series measurements. In this estimation it is assumed that $|\underline{C}| << |\underline{D}|$.

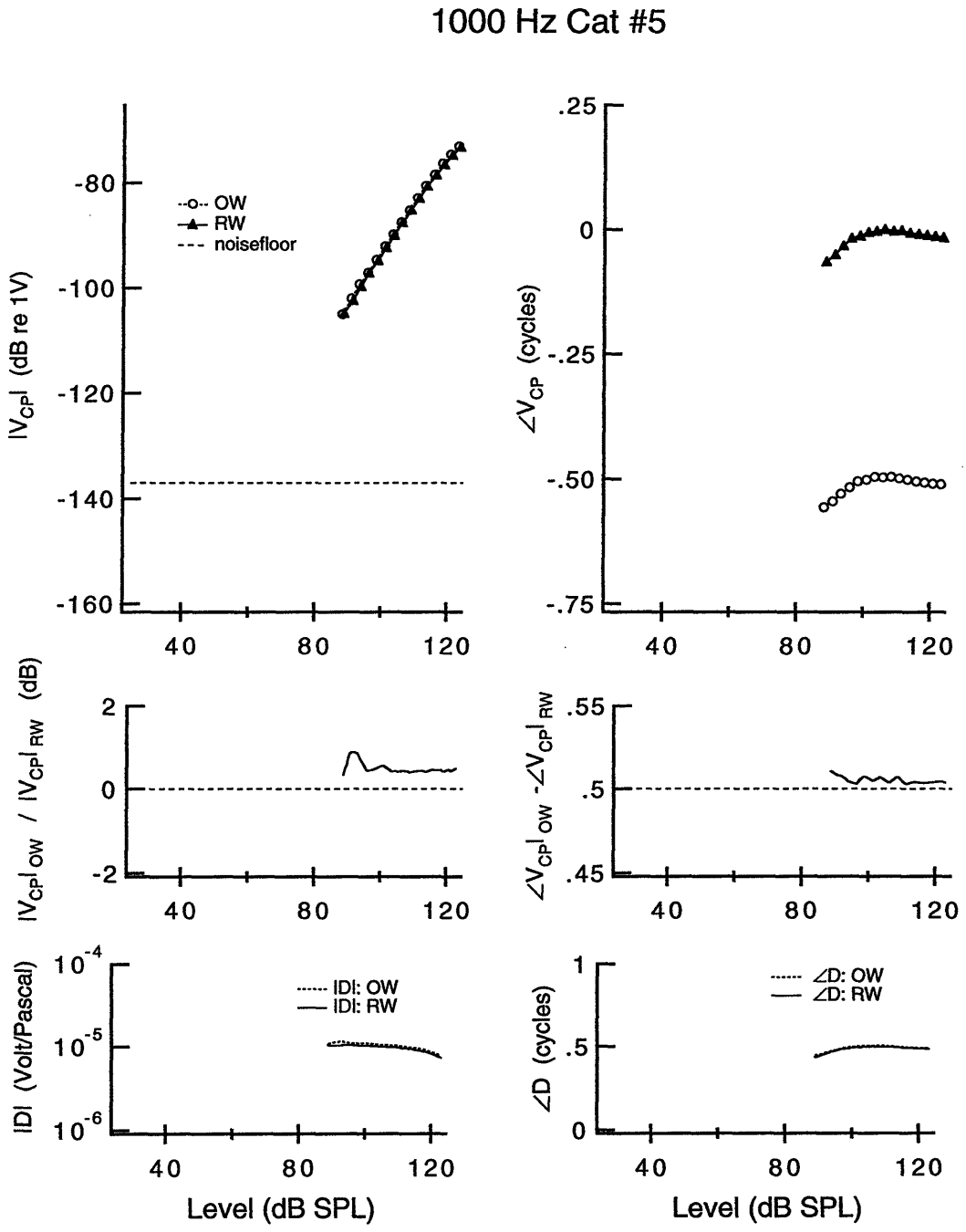

Figure B-32: TOP: Single-sided level-series measurements made on Cat #5 at 1000 Hz. Either the oval or the round window was stimulated. MIDDLE: Ratio of the measurement made while the oval window was stimulated and the measurement made while the round window was stimulated. BOTTOM: Estimate of D (difference-mode gain) from the single-sided level-series measurements. In this estimation it is assumed that $|\underline{C}| << |\underline{D}|$.

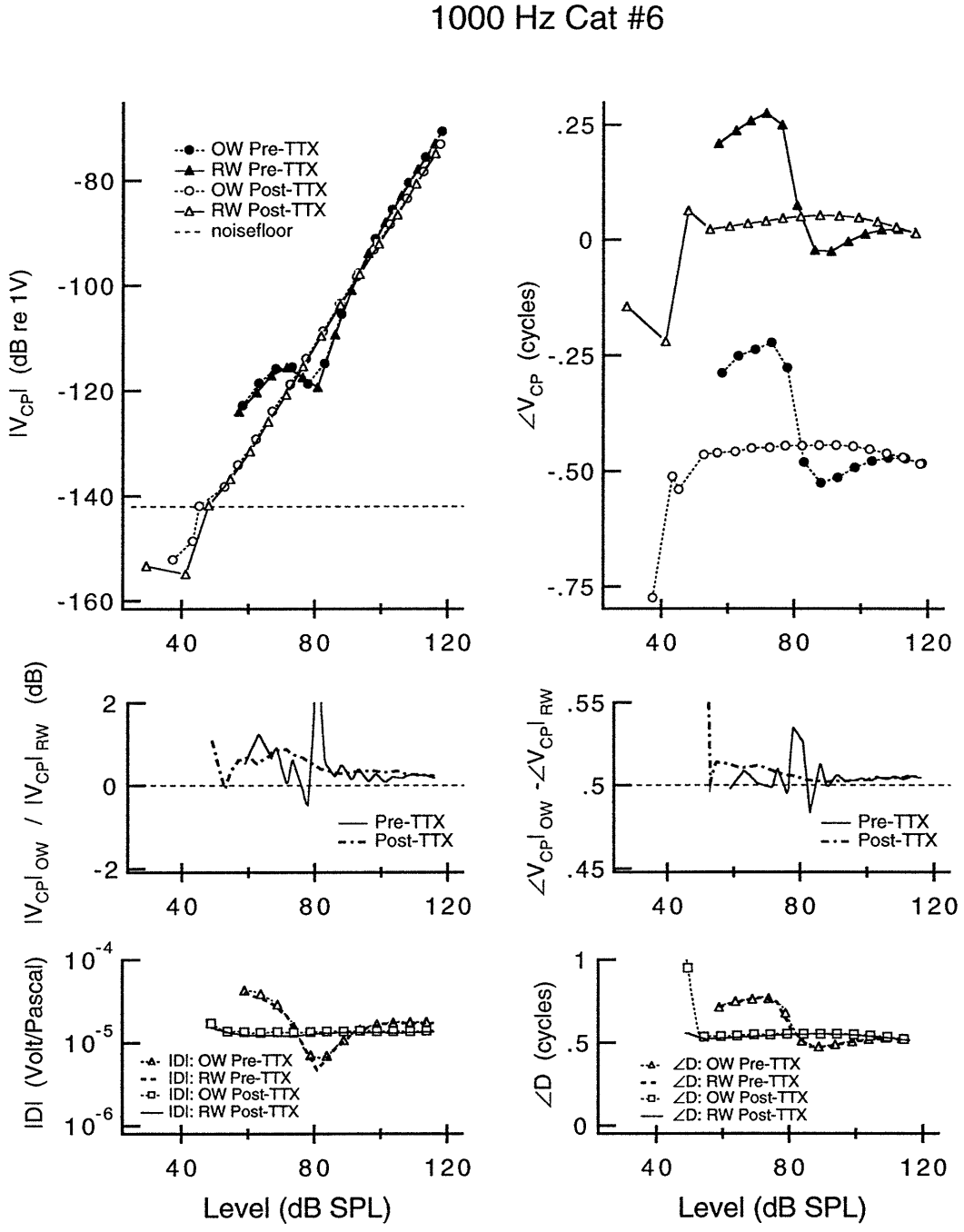

Figure B-33: TOP: Single-sided level-series measurements made on Cat #6 at 1000 Hz before and after the application of TTX. Either the oval or the round window was stimulated. MIDDLE: Ratio of the measurement made while the oval window was stimulated and the measurement made while the round window was stimulated. BOTTOM: Estimate of D (difference-mode gain) from the single-sided level-series measurements. In this estimation it is assumed that $|\underline{C}| << |\underline{D}|$.

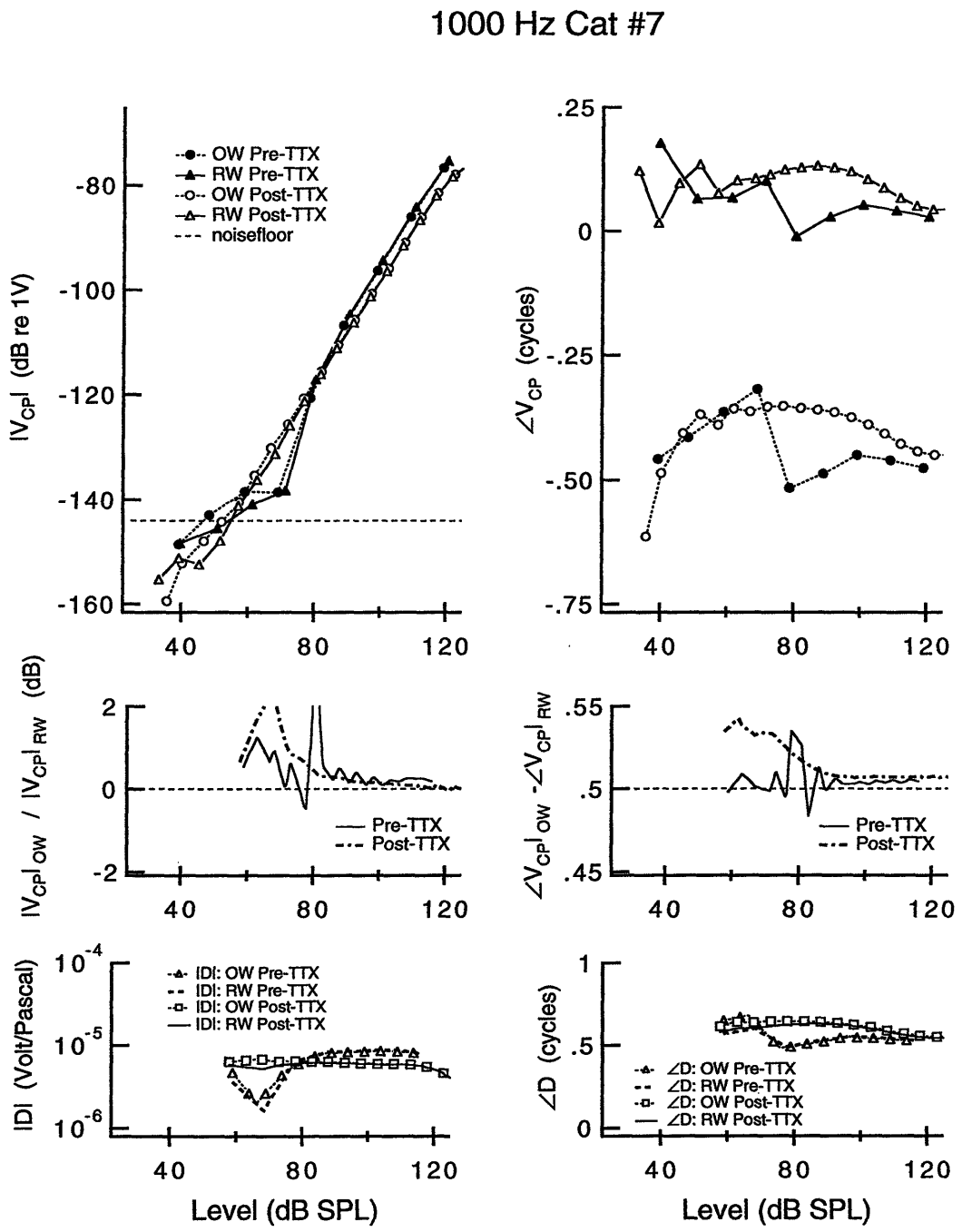

Figure B-34: TOP: Single-sided level-series measurements made on Cat #7 at 1000 Hz before and after the application of TTX. Either the oval or the round window was stimulated. MIDDLE: Ratio of the measurement made while the oval window was stimulated and the measurement made while the round window was stimulated. BOTTOM: Estimate of D (difference-mode gain) from the single-sided level-series measurements. In this estimation it is assumed that $|\underline{C}| << |\underline{D}|$.

Appendix C

Summary of results: Stimuli to both windows

Data from all simultaneous-stimuli measurements are contained within this appendix. There are differences in each of the experiments (Cats #1 to #7) which are further discussed in Appendix A; in general the results from Cats #1, #2, and #3 are not as accurate as the results from the later cats.

The figures in this appendix compare the cochlear-potential magnitude and angle measurements with model predictions. Each measurement set has three graphs associated with it; a cochlear-potential magnitude plot, a blow-up of the cochlear-potential magnitude plot around $\psi = 0$, and a cochlear-potential angle plot. Data points are represented with open circles and the model fits are drawn with solid (linear fit) and dashed (logarithmic fit) lines. The description "linear fit" refers to the model fit obtained from Equation 3.4 and the description "logarithmic fit" refers to the model fit obtained from Equation 3.14.

The figures in this appendix are organized in order of increasing frequency. Within

each frequency group the figures are arranged in chronological order of experiment by cat number. Measurement sets from a given cat at a given frequency are arranged in order of increasing sound-pressure level. Each measurement set has a label which describes the measurement frequency, cat number, and measurement order on the particular cat; for example, measurement set $1000a\_5$ refers to the first measurement set made on Cat #5 at 1000 Hz.

There are two tables for each frequency group within this appendix. The tables give model parameters for all measurement sets for the linear and logarithmic model fits.

Linear model parameters: 75 Hz										
Data set	dB SPL	CMRR	$\|D\|$	$\angle D$	$\|C\|$	$\angle C$	ρ_{MAG}	$\rho_{\angle}$	ψ_{MIN} Data	ψ_{MIN} Model
75a_4	124	24.52	1.95e-07	0.181	1.16e-08	-0.090	0.917	0.573	0.0035	0.0097
75b_4	120	30.83	2.04e-07	0.227	5.88e-09	-0.192	0.751	0.739	-0.0136	0.0027

Table C.1: Linear model parameters calculated from 75 Hz data.

Logarithmic model parameters: 75 Hz										
Data set	dB SPL	CMRR	$\|D\|$	$\angle D$	$\|C\|$	$\angle C$	ρ_{MAG}	$\rho_{\angle}$	ψ_{MIN} Data	ψ_{MIN} Model
75a_4	124	22.20	2.72e-07	0.321	2.11e-08	0.036	0.979	0.884	0.0035	0.0125
75b_4	120	28.12	3.04e-07	0.321	1.19e-08	0.462	0.915	0.873	-0.0136	-0.0046

Table C.2: Logarithmic model parameters calculated from 75 Hz data.

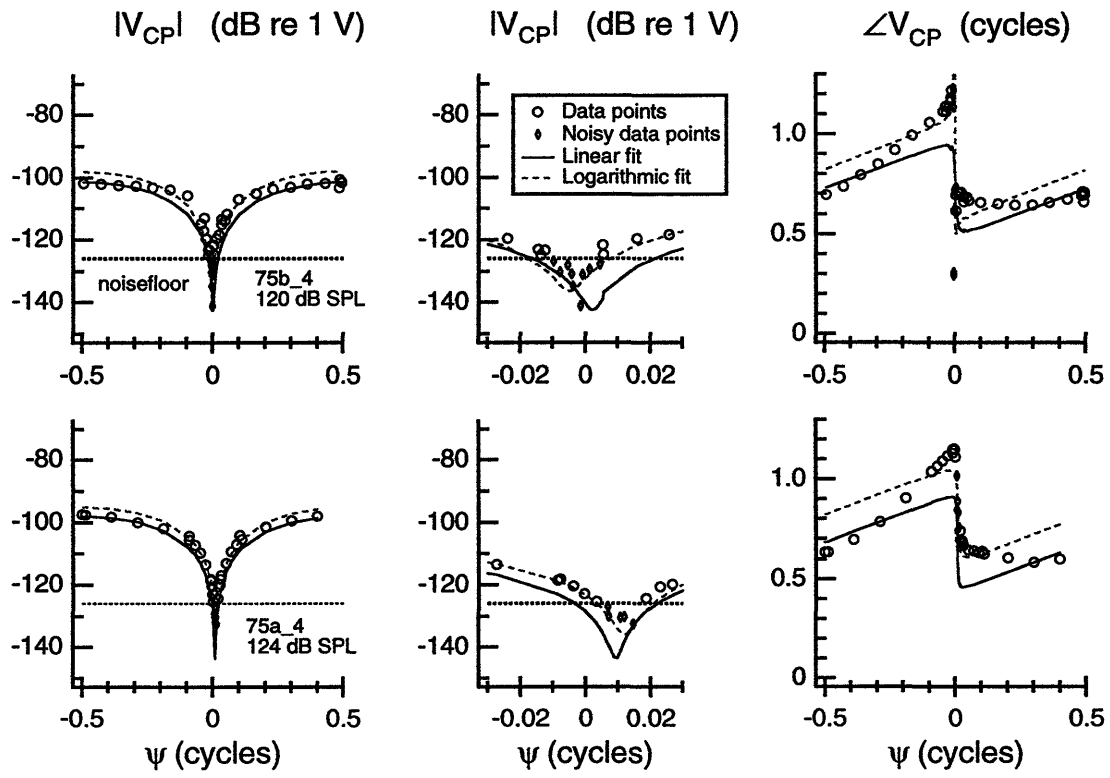

Figure C-1: Simultaneous-stimuli measurement sets and model fits at 75 Hz on Cat #4.

Linear model parameters:100 Hz										
Data set	dB SPL	CMRR	$\|D\|$	$\angle D$	$\|C\|$	$\angle C$	ρ_{MAG}	$\rho_{\angle}$	ψ_{MIN} Data	ψ_{MIN} Model
100a_4	121	26.96	3.97e-07	0.037	1.78e-08	0.480	0.989	0.766	-0.0047	-0.0024
100b_4	120	32.92	3.97e-07	0.033	8.96e-09	0.371	0.812	0.539	0.0024	-0.0037
100a_5	118	33.24	1.26e-06	-0.030	2.73e-08	-0.097	0.914	0.970	-0.0270	0.0018
100b_5	124	29.25	1.56e-06	-0.094	5.38e-08	0.474	0.960	0.974	-0.0088	0.0055
100c_5	120	21.56	7.29e-07	0.051	6.10e-08	0.271	0.843	0.968	-0.0014	-0.0134
100d_5	125	24.81	8.37e-07	-0.007	4.81e-08	0.347	0.982	0.924	-0.0002	-0.0075
100a_6	121	33.57	1.81e-06	-0.036	3.80e-08	0.421	0.978	0.770	0.0000	-0.0017
100b_6	126	20.06	1.12e-06	-0.077	1.11e-07	0.268	0.841	0.944	0.0038	-0.0133
100c_6	121	32.11	1.86e-06	-0.039	4.62e-08	0.297	0.965	0.915	-0.0004	-0.0033
100d_6	126	33.59	2.02e-06	-0.074	4.22e-08	0.447	0.967	0.980	0.0011	0.0001
100e_6	116	32.23	1.68e-06	-0.010	4.11e-08	0.232	0.972	0.707	-0.0027	-0.0028
100f_6	116	34.66	1.71e-06	-0.011	3.16e-08	-0.123	0.974	0.993	0.0007	0.0017
100g_6	100	34.25	1.56e-06	-0.042	3.03e-08	0.246	0.915	0.839	-0.0114	-0.0032
100h_6	110	32.26	1.81e-06	-0.008	4.41e-08	0.279	0.979	0.941	-0.0058	-0.0038
100i_6	121	47.71	1.85e-06	-0.036	7.60e-09	0.088	0.972	0.985	-0.0009	-0.0009
100a_7	119	30.71	1.01e-06	0.065	2.93e-08	0.206	0.985	0.972	-0.0196	-0.0035
100b_7	127	52.50	1.17e-06	-0.010	2.77e-09	0.271	0.975	0.907	0.0047	-0.0001
100c_7	102	27.60	6.72e-07	0.117	2.80e-08	-0.419	0.970	0.997	0.1580	-0.0018
100d_7	126	33.36	1.19e-06	-0.038	2.55e-08	0.152	0.985	0.905	0.0071	-0.0030
100e_7	118	23.24	1.23e-06	0.015	8.47e-08	0.051	0.985	0.954	-0.0110	-0.0113
100f_7	108	53.81	1.06e-06	0.118	2.16e-09	0.307	0.998	0.985	-0.0426	-0.0006
100g_7	98	41.34	1.03e-06	0.098	8.83e-09	-0.302	0.991	0.995	0.1341	0.0006

Table C.3: Linear model parameters calculated from 100 Hz data.

Logarithmic model parameters: 100 Hz										
Data set	dB SPL	CMRR	$\|D\|$	$\angle D$	$\|C\|$	$\angle C$	ρ_{MAG}	$\rho_{\angle}$	ψ_{MIN} Data	ψ_{MIN} Model
100a_4	121	4.94	2.67e-07	0.042	1.51e-07	-0.269	0.741	0.298	-0.0047	0.0827
100b_4	120	24.07	5.95e-07	0.037	3.72e-08	0.243	0.867	0.756	0.0024	-0.0094
100a_5	118	20.68	1.18e-06	-0.037	1.09e-07	-0.002	0.948	0.973	-0.0270	-0.0030
100b_5	124	45.06	1.39e-06	-0.090	7.78e-09	0.180	0.972	0.973	-0.0088	-0.0008
100c_5	120	12.23	6.88e-07	0.038	1.68e-07	0.180	0.946	0.972	-0.0014	-0.0303
100d_5	125	14.23	7.34e-07	-0.002	1.43e-07	0.172	0.947	0.967	-0.0002	-0.0275
100a_6	121	21.78	1.00e-06	-0.025	8.18e-08	0.158	0.893	0.720	0.0000	-0.0116
100b_6	126	24.78	9.70e-07	-0.086	5.60e-08	0.292	0.923	0.953	0.0038	-0.0064
100c_6	121	29.59	1.45e-06	-0.042	4.79e-08	0.296	0.974	0.927	-0.0004	-0.0052
100d_6	126	31.89	1.54e-06	-0.073	3.92e-08	0.449	0.980	0.980	0.0011	0.0001
100e_6	116	29.19	1.21e-06	-0.005	4.21e-08	0.210	0.975	0.653	-0.0027	-0.0057
100f_6	116	37.33	1.32e-06	-0.037	1.79e-08	-0.148	0.994	0.996	0.0007	0.0014
100g_6	100	26.87	1.31e-06	-0.049	5.94e-08	0.033	0.966	0.820	-0.0114	-0.0032
100h_6	110	32.19	1.65e-06	-0.007	4.07e-08	0.205	0.979	0.907	-0.0058	-0.0038
100i_6	121	48.34	1.38e-06	-0.044	5.27e-09	0.287	0.980	0.975	-0.0009	-0.0009
100a_7	119	32.14	9.05e-07	0.101	2.24e-08	0.212	0.992	0.983	-0.0196	-0.0025
100b_7	127	52.22	9.62e-07	-0.000	2.36e-09	0.436	0.984	0.923	0.0047	-0.0001
100c_7	102	27.60	6.72e-07	0.117	2.80e-08	-0.440	0.969	0.997	0.1580	-0.0019
100d_7	126	31.27	1.14e-06	-0.040	3.11e-08	0.068	0.990	0.903	0.0071	-0.0030
100e_7	118	27.79	1.12e-06	0.021	4.59e-08	0.058	0.989	0.962	-0.0110	-0.0113
100f_7	108	53.68	1.05e-06	0.117	2.17e-09	0.309	0.998	0.985	-0.0426	-0.0006
100g_7	98	26.93	1.02e-06	0.100	4.61e-08	-0.308	0.991	0.994	0.1341	0.0036

Table C.4: Logarithmic model parameters calculated from 100 Hz data.

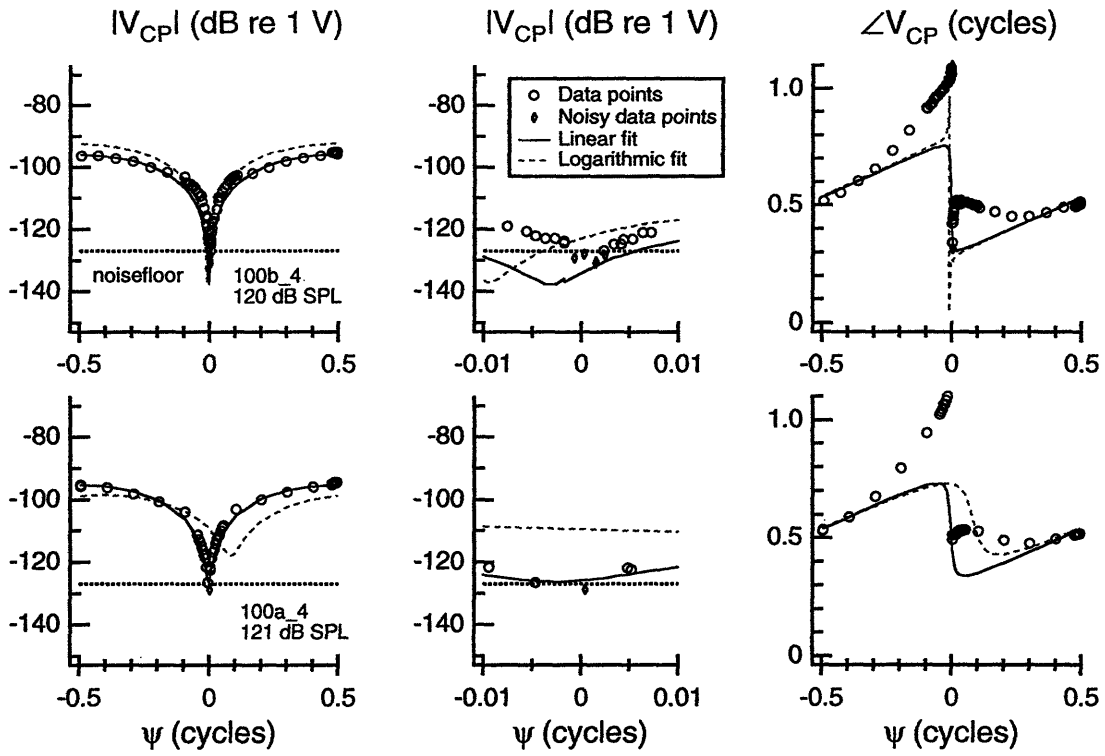

Figure C-2: Simultaneous-stimuli measurement sets and model fits at 100 Hz on Cat #4.

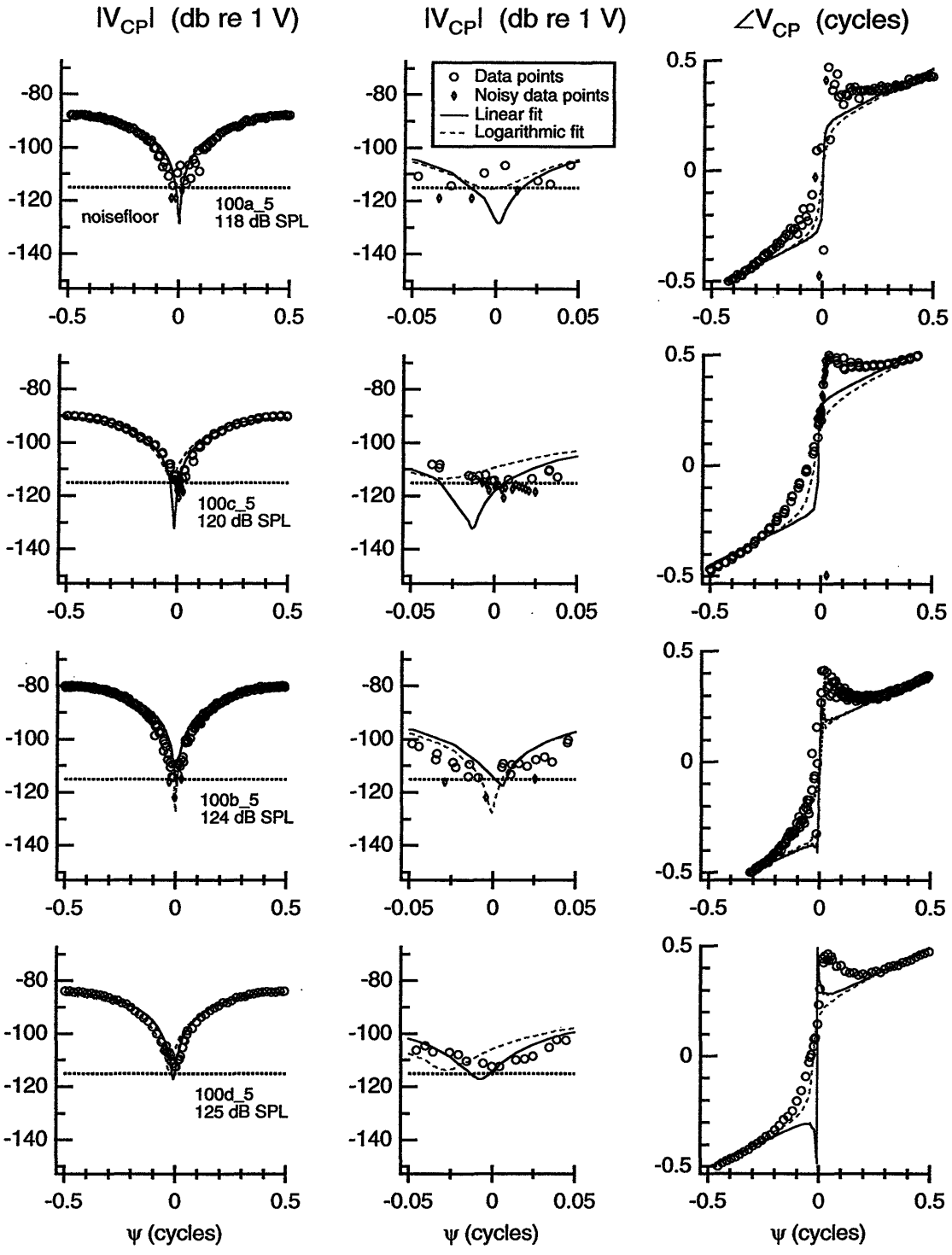

Figure C-3: Simultaneous-stimuli measurement sets and model fits at 100 Hz on Cat #5.

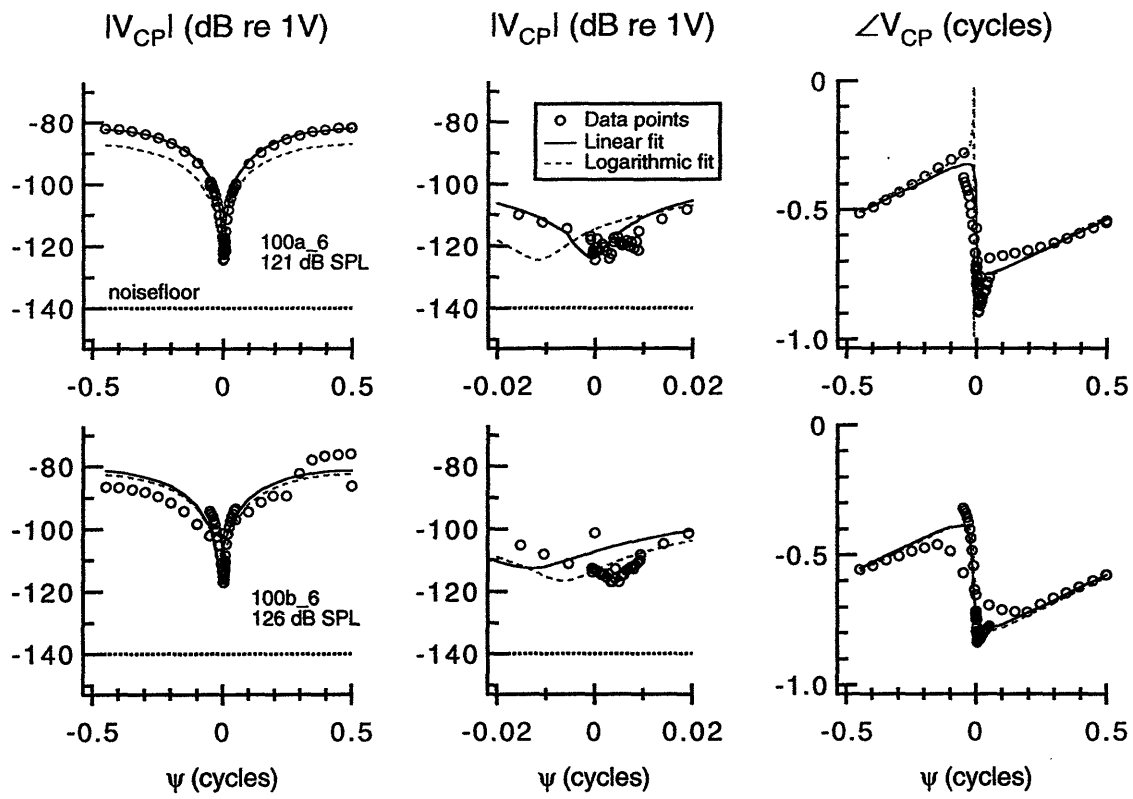

Figure C-4: Pre-TTX simultaneous-stimuli measurement sets and model fits at 100 Hz on Cat #6.

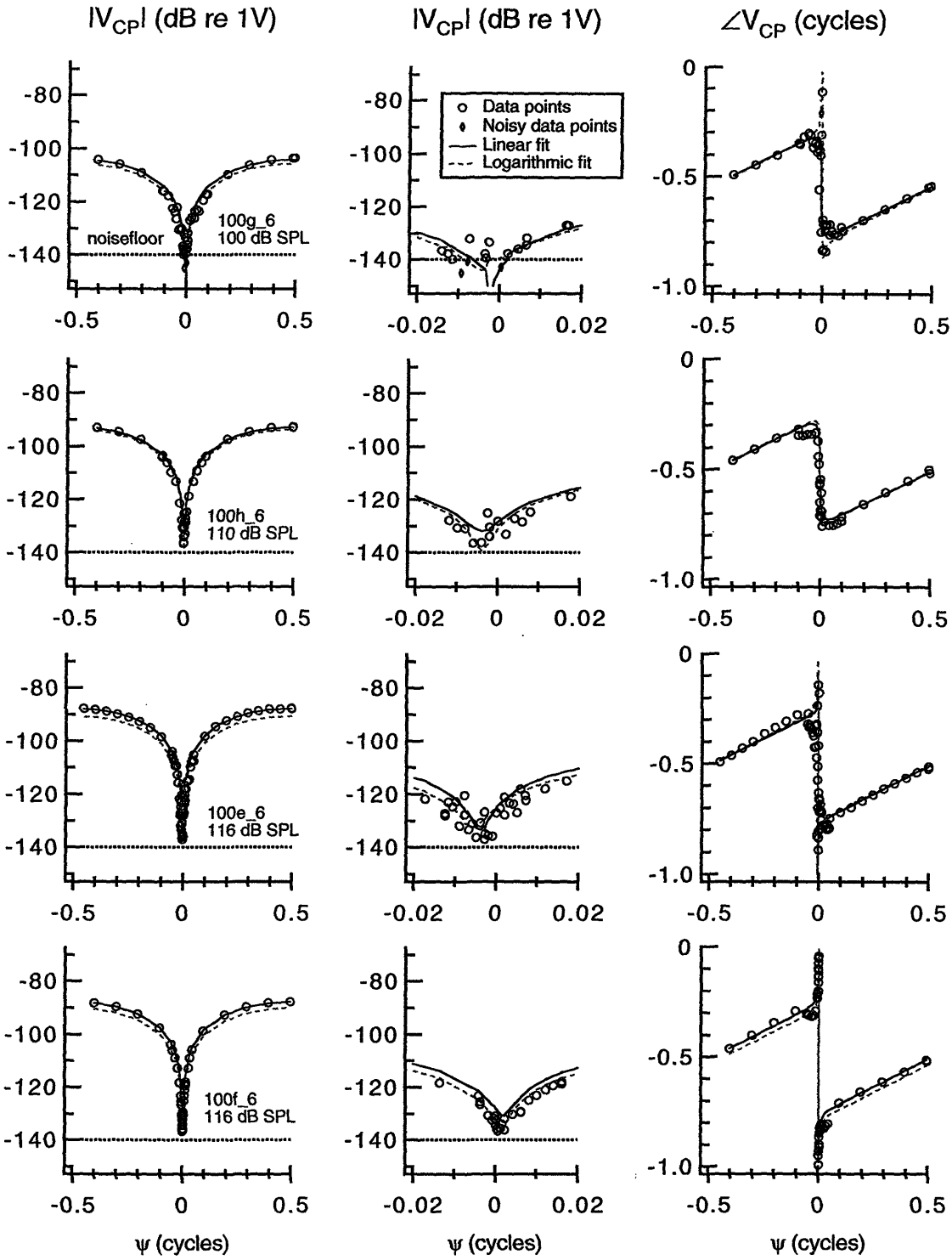

Figure C-5: Post-TTX simultaneous-stimuli measurement sets and model fits at 100 Hz on Cat #6.

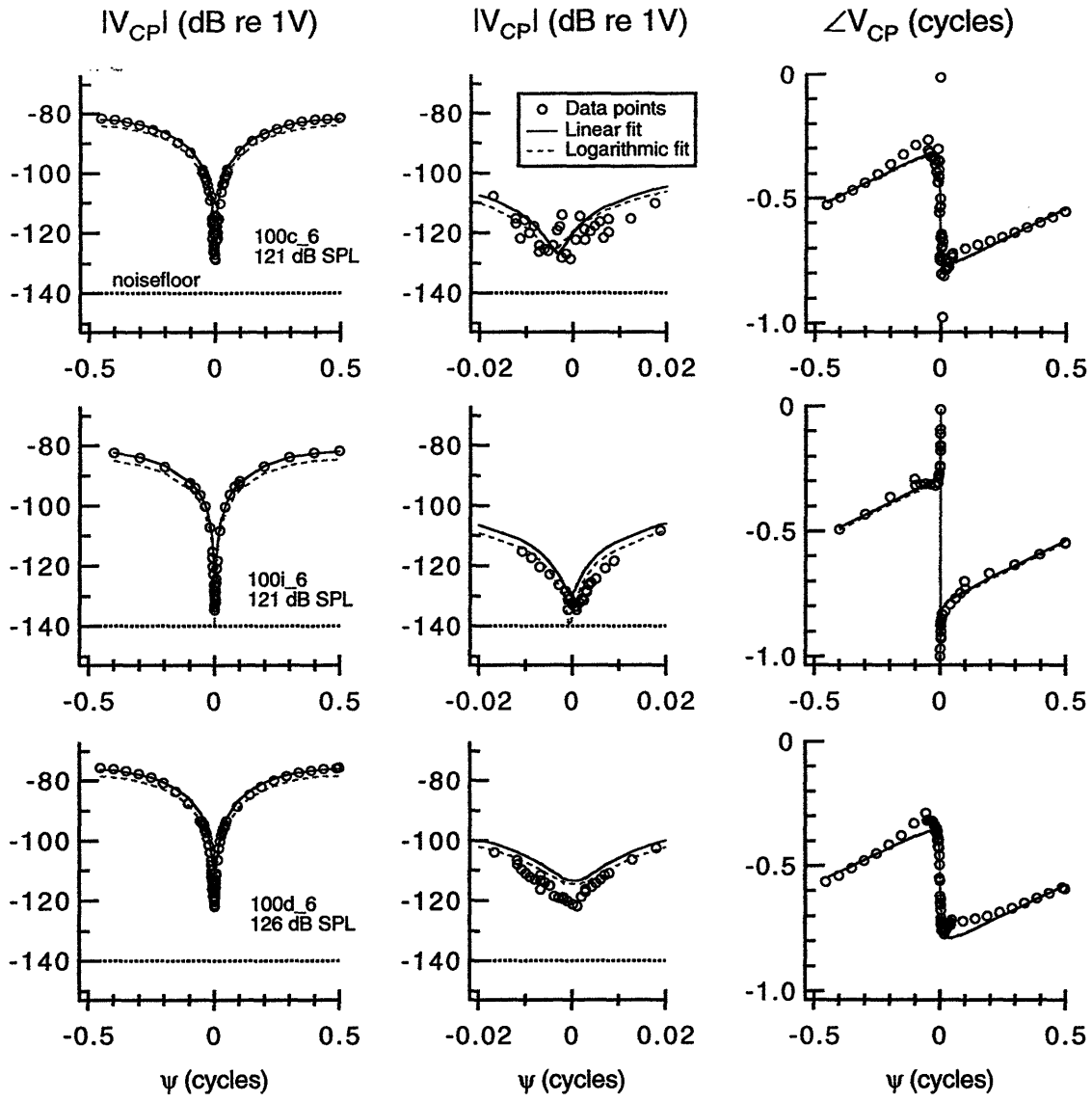

Figure C-6: Post-TTX simultaneous-stimuli measurement sets and model fits at 100 Hz on Cat #6.

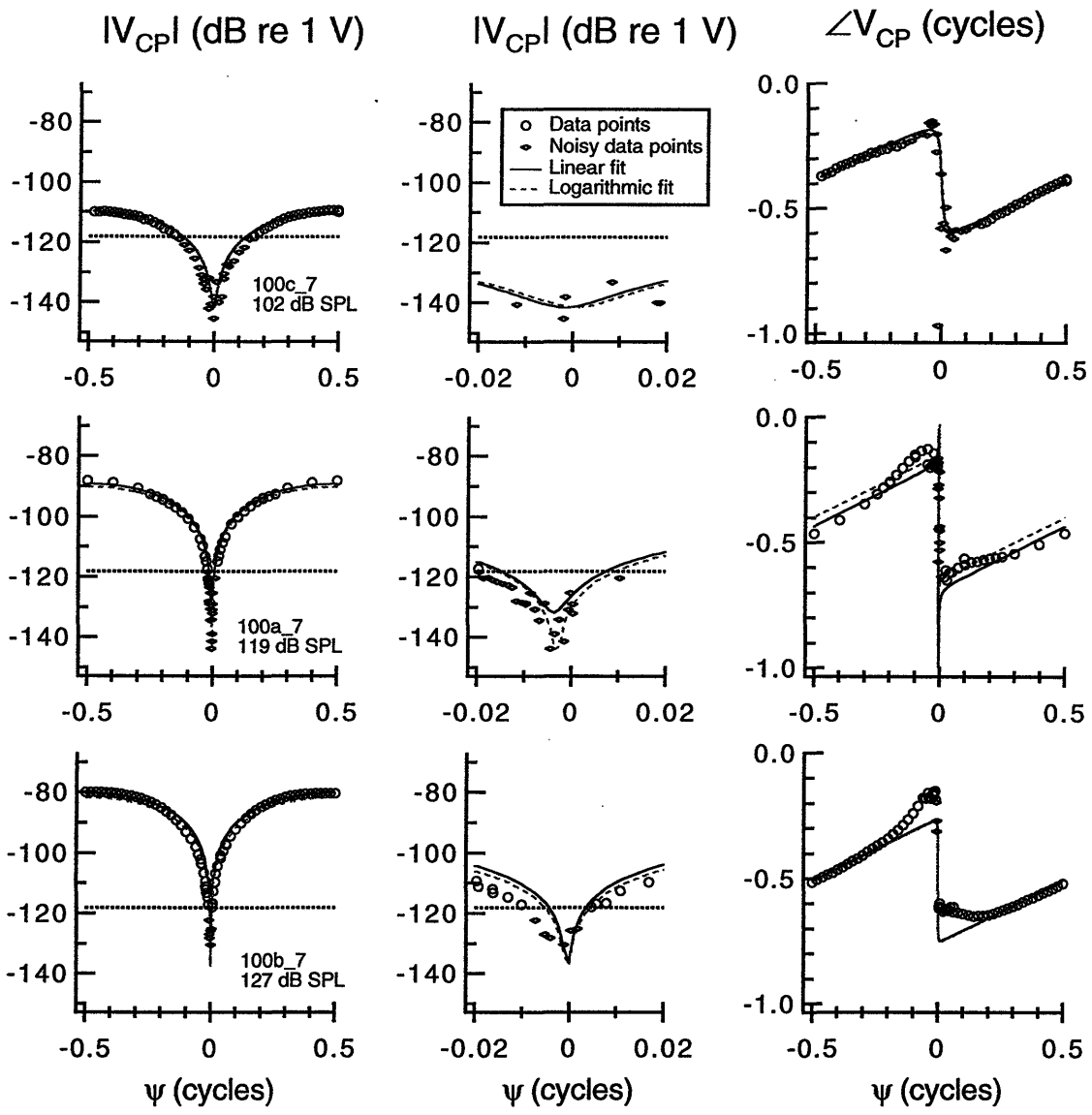

Figure C-7: Pre-TTX simultaneous-stimuli measurement sets and model fits at 100 Hz on Cat #7.

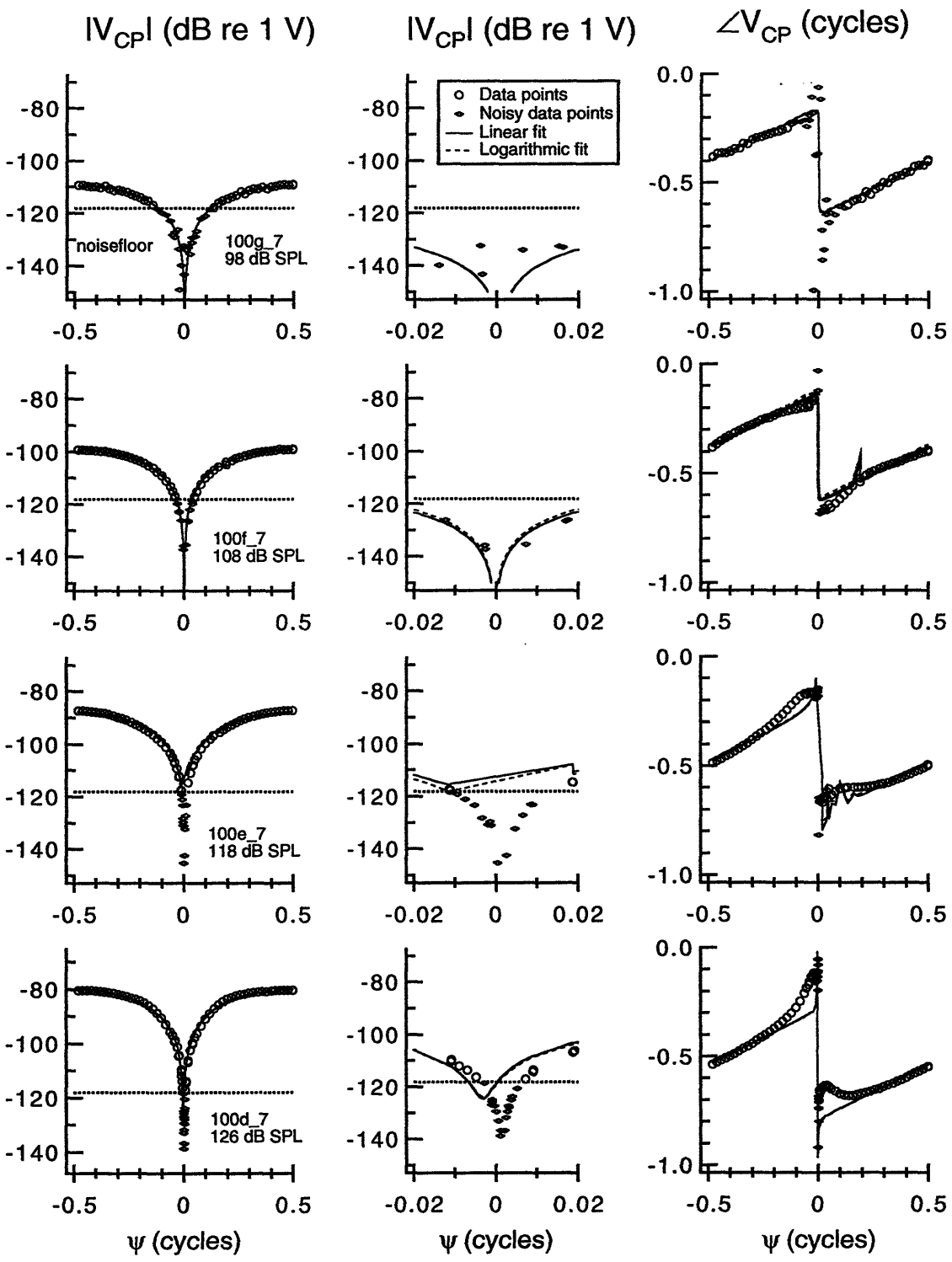

Figure C-8: Post-TTX simultaneous-stimuli measurement sets and model fits at 100 Hz on Cat #7.

Linear model parameters: 200 Hz										
Data set	dB SPL	CMRR	$\|D\|$	$\angle D$	$\|C\|$	$\angle C$	ρ_{MAG}	$\rho_{\angle}$	ψ_{MIN} Data	ψ_{MIN} Model
200a_1	124	8.46	3.49e-07	-0.113	1.32e-07	0.340	1.000	1.000	-0.0218	-0.0177
200b_1	125;122	8.55	3.48e-07	-0.114	1.30e-07	0.337	0.997	0.996	-0.0167	-0.0188

Table C.5: Linear model parameters calculated from 200 Hz data.

Logarithmic model parameters: 200 Hz										
Data set	dB SPL	CMRR	$\|D\|$	$\angle D$	$\|C\|$	$\angle C$	ρ_{MAG}	$\rho_{\angle}$	ψ_{MIN} Data	ψ_{MIN} Model
200a_1	124	8.44	3.51e-07	-0.111	1.33e-07	0.341	1.000	1.000	-0.0218	-0.0187
200b_1	125;122	8.50	3.41e-07	-0.115	1.28e-07	0.330	0.985	0.961	-0.0167	-0.0198

Table C.6: Logarithmic model parameters calculated from 200 Hz data.

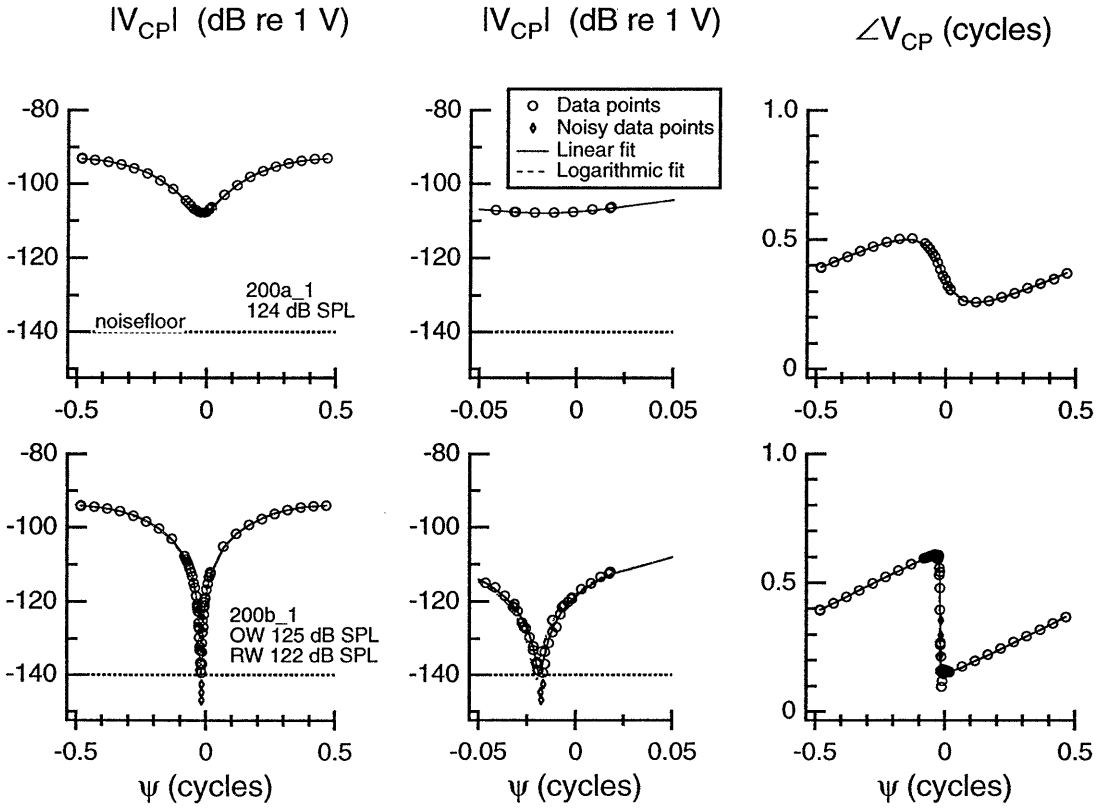

Figure C-9: Simultaneous-stimuli measurement sets and model fits at 200 Hz on Cat #1.

Linear model parameters: 250 Hz										
Data set	dB SPL	CMRR	$\|D\|$	$\angle D$	$\|C\|$	$\angle C$	ρ_{MAG}	$\rho_{/}$	ψ_{MIN} Data	ψ_{MIN} Model
250a_4	108	30.73	2.11e-06	-0.009	6.13e-08	0.396	0.998	0.925	-0.0092	-0.0027

Table C.7: Linear model parameters calculated from 250 Hz data.

Logarithmic model parameters: 250 Hz										
Data set	dB SPL	CMRR	$\|D\|$	$\angle D$	$\|C\|$	$\angle C$	ρ_{MAG}	$\rho_{/}$	ψ_{MIN} Data	ψ_{MIN} Model
250a_4	108	39.60	2.23e-06	-0.005	2.33e-08	0.415	0.997	0.941	-0.0092	-0.0012

Table C.8: Logarithmic model parameters calculated from 250 Hz data.

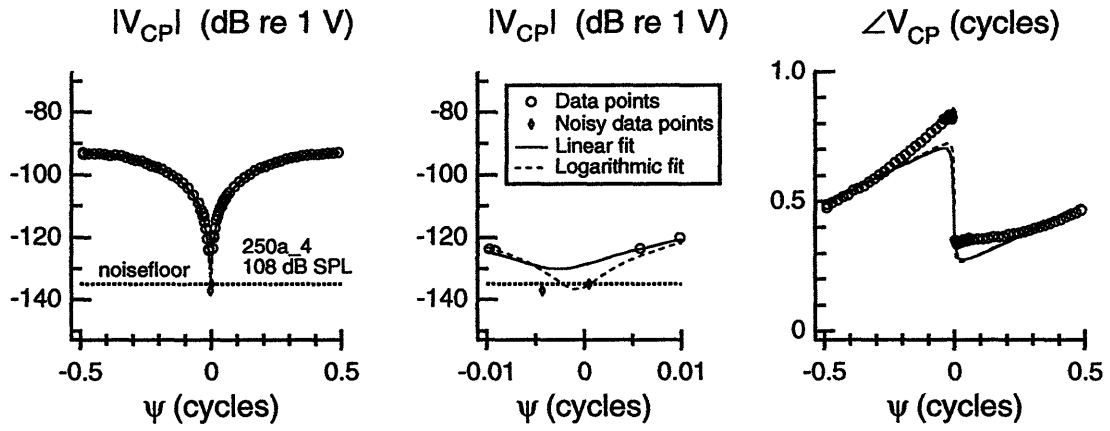

Figure C-10: Simultaneous-stimuli measurement set and model fits at 250 Hz on Cat #4.

Linear model parameters: 300 Hz										
Data set	dB SPL	CMRR	$\|D\|$	$\angle D$	$\|C\|$	$\angle C$	ρ_{MAG}	$\rho_{/}$	ψ_{MIN} Data	ψ_{MIN} Model
300a_5	100	24.36	6.20e-06	-0.093	3.75e-07	-0.433	0.922	0.769	0.0104	0.0078
300b_5	105	26.18	7.05e-06	-0.132	3.46e-07	0.453	0.950	0.564	0.0000	0.0036
300c_5	110	34.40	6.82e-06	-0.165	1.30e-07	0.248	0.990	0.499	-0.0018	-0.0011
300d_5	115	33.89	6.76e-06	-0.181	1.37e-07	0.291	0.890	0.512	-0.0040	-0.0011
300e_5	120	33.51	6.41e-06	-0.153	1.35e-07	0.212	0.936	0.847	-0.0047	-0.0029
300f_5	125	37.08	6.71e-06	-0.175	9.39e-08	0.303	0.959	0.865	-0.0024	-0.0002
300a_6	115	33.11	1.20e-05	-0.236	2.66e-07	0.270	0.980	0.982	0.0014	0.0003
300b_6	125	28.53	7.82e-06	-0.258	2.93e-07	0.177	0.979	0.960	-0.0003	-0.0021
300c_6	116	31.24	1.05e-05	-0.217	2.87e-07	0.336	0.988	0.964	-0.0007	0.0007
300d_6	120	35.58	9.92e-06	-0.231	1.65e-07	0.228	0.976	0.882	-0.0016	-0.0011
300e_6	126	34.83	7.35e-06	-0.237	1.33e-07	0.242	0.988	0.970	-0.0012	-0.0007
300f_6	120	39.62	9.59e-06	-0.224	1.00e-07	0.174	0.993	0.994	-0.0011	-0.0011
300g_6	110	42.89	9.50e-06	-0.202	6.81e-08	0.272	0.989	0.962	-0.0006	-0.0005
300h_6	100	49.11	8.14e-06	-0.209	2.85e-08	-0.029	0.984	0.879	-0.0001	-0.0008
300i_6	90	31.42	7.82e-06	-0.228	2.10e-07	0.228	0.981	0.969	0.0018	-0.0009
300a_7	121	31.78	4.80e-06	-0.221	1.24e-07	0.408	0.976	0.960	0.0015	0.0025
300b_7	101	39.41	4.21e-06	-0.159	4.51e-08	-0.492	0.995	0.990	0.0018	0.0015
300c_7	116	47.32	5.12e-06	-0.214	2.20e-08	0.403	0.985	0.874	0.0011	0.0002
300d_7	121	36.65	5.74e-06	-0.252	8.44e-08	-0.461	0.993	0.989	0.0029	0.0020
300e_7	111	35.27	6.86e-06	-0.228	1.18e-07	-0.431	0.992	0.993	0.0026	0.0021
300f_7	101	18.60	4.94e-06	-0.179	5.80e-07	-0.500	0.902	0.571	0.0046	0.0170
300g_7	90	32.38	3.33e-06	-0.147	8.01e-08	0.421	0.995	0.984	0.0034	0.0020

Table C.9: Linear model parameters calculated from 300 Hz data.

Logarithmic model parameters: 300 Hz										
Data set	dB SPL	CMRR	$\|D\|$	$\angle D$	$\|C\|$	$\angle C$	ρ_{MAG}	$\rho_{/}$	ψ_{MIN} Data	ψ_{MIN} Model
300a_5	100	25.18	6.35e-06	-0.082	3.50e-07	-0.488	0.961	0.785	0.0104	0.0048
300b_5	105	31.12	7.96e-06	-0.108	2.21e-07	0.458	0.946	0.656	0.0000	0.0010
300c_5	110	32.77	6.68e-06	-0.134	1.54e-07	0.156	0.919	0.722	-0.0018	-0.0038
300d_5	115	29.75	5.07e-06	-0.137	1.65e-07	0.082	0.985	0.817	-0.0040	-0.0052
300e_5	120	30.88	5.33e-06	-0.073	1.52e-07	0.253	0.993	0.938	-0.0047	-0.0042
300f_5	125	32.29	5.55e-06	-0.115	1.35e-07	0.315	0.990	0.942	-0.0024	-0.0009
300a_6	115	32.91	9.04e-06	-0.263	2.04e-07	0.263	0.992	0.972	0.0014	0.0000
300b_6	125	32.21	9.41e-06	-0.242	2.31e-07	0.257	0.991	0.994	-0.0003	-0.0003
300c_6	116	31.10	8.46e-06	-0.283	2.36e-07	0.264	0.995	0.920	-0.0007	0.0007
300d_6	120	35.73	8.00e-06	-0.227	1.31e-07	0.161	0.998	0.994	-0.0016	-0.0021
300e_6	126	39.64	7.86e-06	-0.219	8.19e-08	0.173	0.998	0.997	-0.0012	-0.0012
300f_6	120	39.23	8.49e-06	-0.215	9.28e-08	0.140	0.997	0.997	-0.0011	-0.0011
300g_6	110	43.87	6.08e-06	-0.160	3.89e-08	0.133	0.986	0.924	-0.0006	-0.0005
300h_6	100	41.11	7.51e-06	-0.220	6.61e-08	0.011	0.981	0.873	-0.0001	-0.0010
300i_6	90	29.10	7.88e-06	-0.257	2.76e-07	0.229	0.997	0.986	0.0018	-0.0005
300a_7	121	38.06	3.71e-06	-0.153	4.64e-08	0.315	0.980	0.917	0.0015	-0.0004
300b_7	101	39.73	3.66e-06	-0.141	3.78e-08	0.457	0.996	0.989	0.0018	0.0007
300c_7	116	38.87	4.44e-06	-0.183	5.06e-08	0.486	0.995	0.976	0.0011	0.0011
300d_7	121	34.78	5.49e-06	-0.225	1.00e-07	-0.465	0.998	0.994	0.0029	0.0025
300e_7	111	33.90	5.69e-06	-0.206	1.15e-07	-0.397	0.995	0.995	0.0026	0.0031
300f_7	101	22.04	5.86e-06	-0.197	4.64e-07	-0.496	0.923	0.715	0.0046	0.0119
300g_7	90	29.19	3.10e-06	-0.160	1.08e-07	0.240	0.987	0.960	0.0034	-0.0033

Table C.10: Logarithmic model parameters calculated from 300 Hz data.

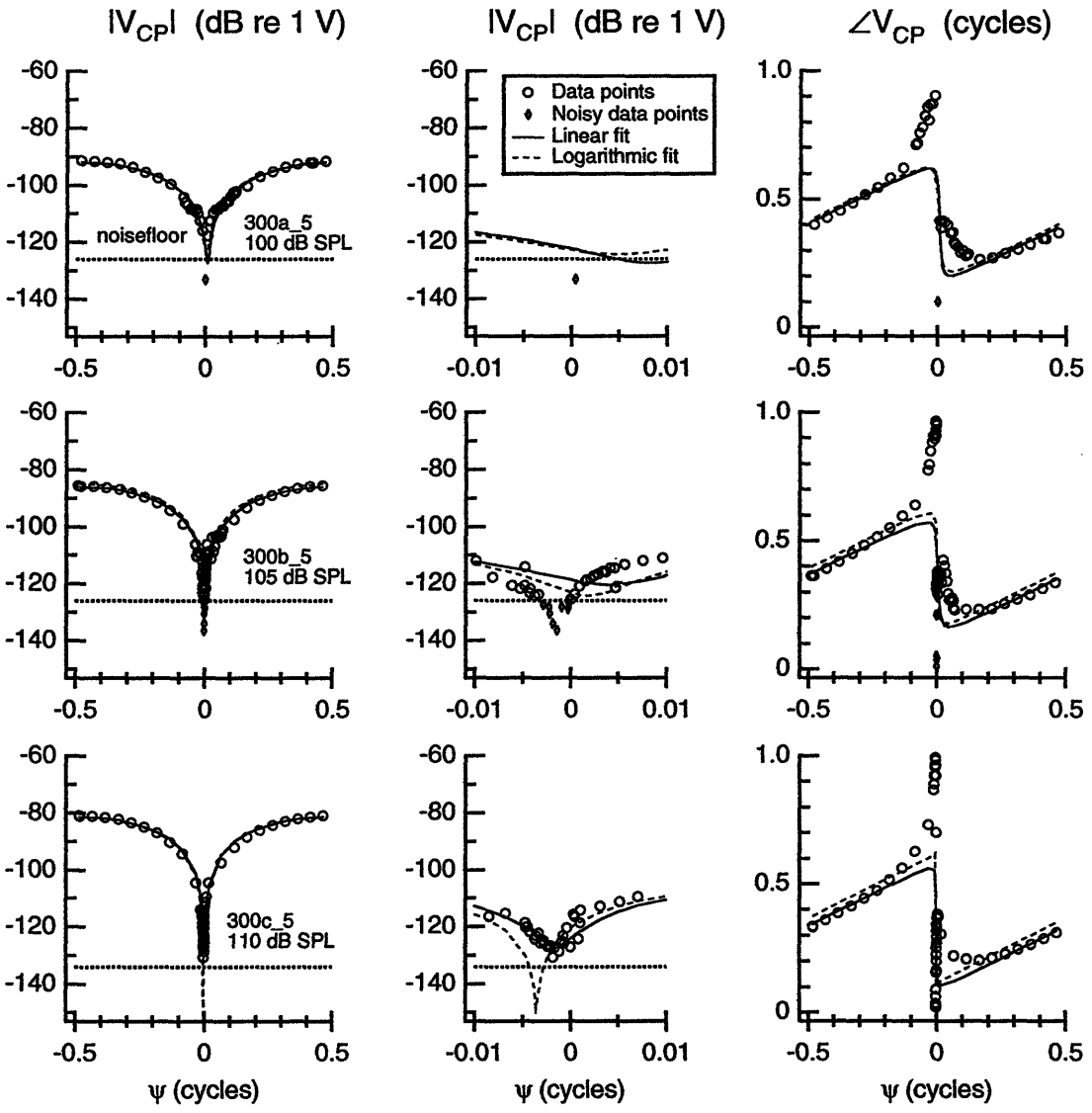

Figure C-11: Simultaneous-stimuli measurement sets and model fits at 300 Hz on Cat #5.

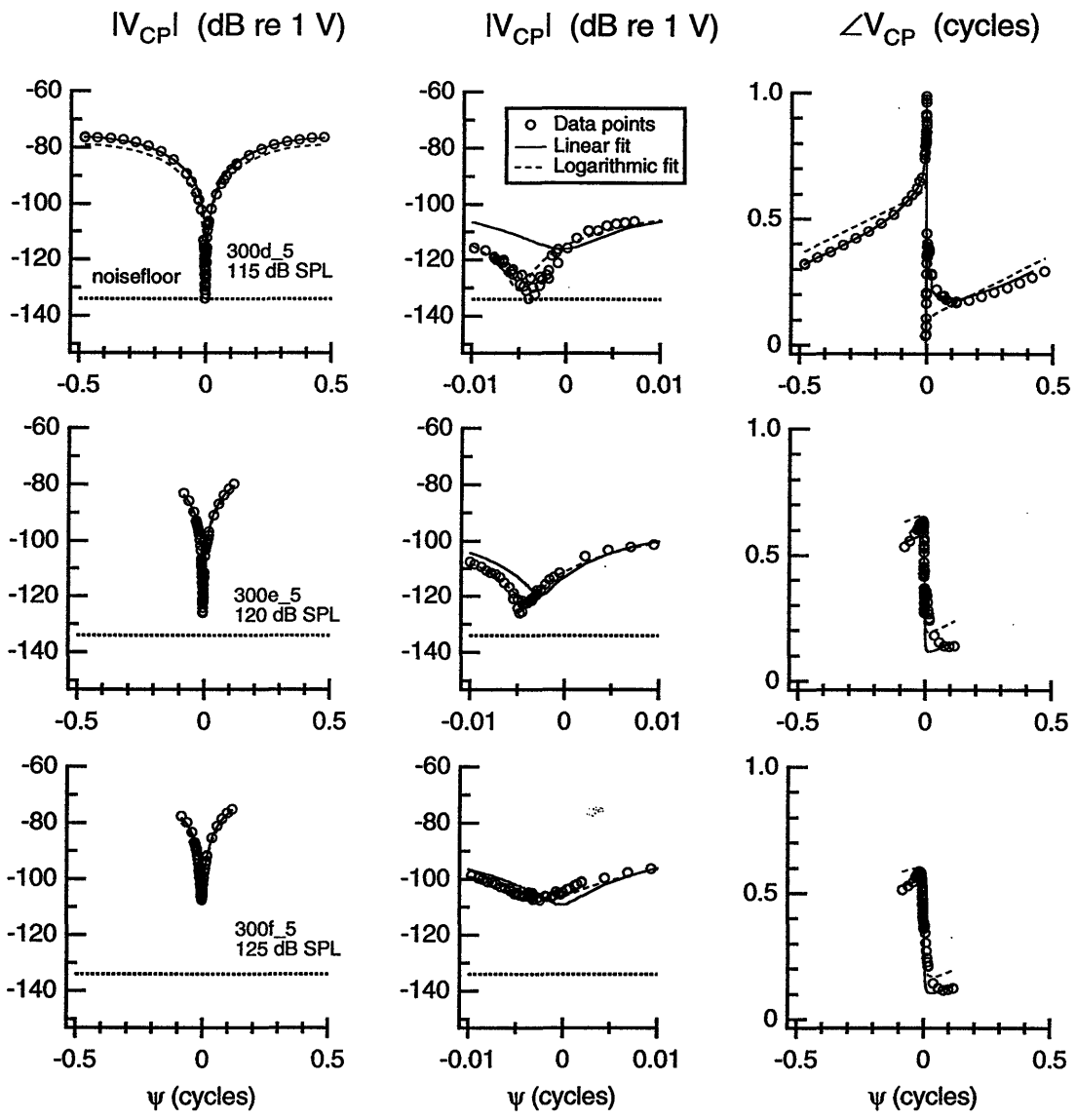

Figure C-12: Simultaneous-stimuli measurement sets and model fits at 300 Hz on Cat #5.

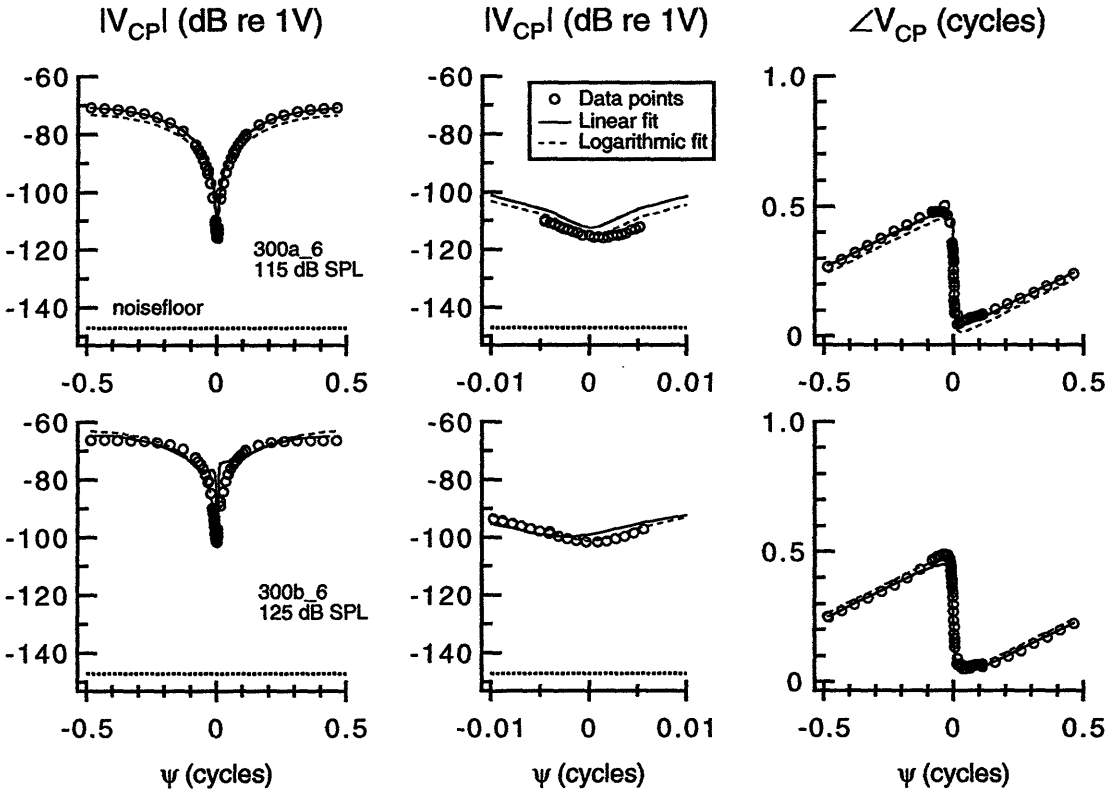

Figure C-13: Pre-TTX simultaneous-stimuli measurement sets and model fits at 300 Hz on Cat #6.

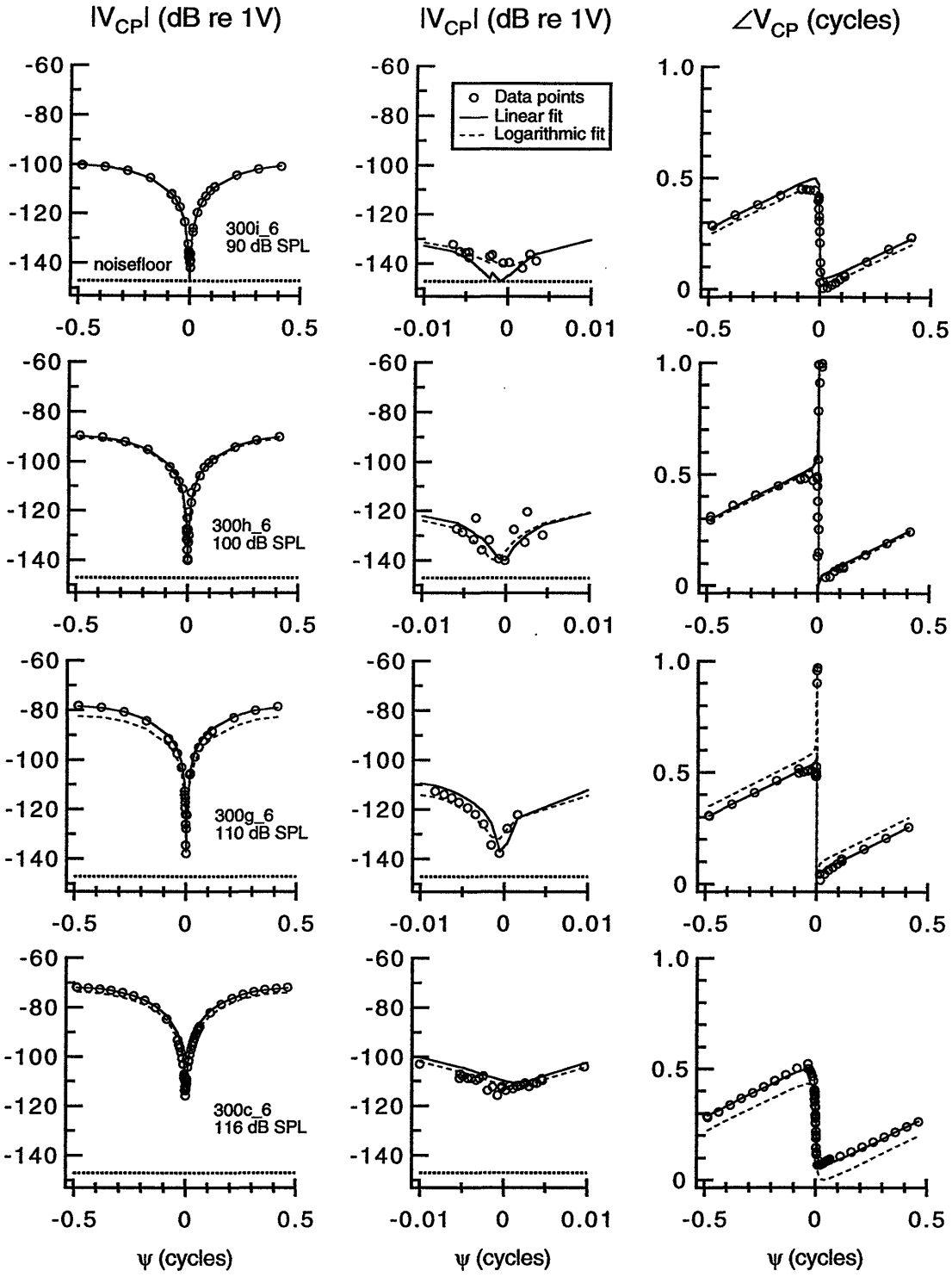

Figure C-14: Post-TTX simultaneous-stimuli measurement sets and model fits at 300 Hz on Cat #6.

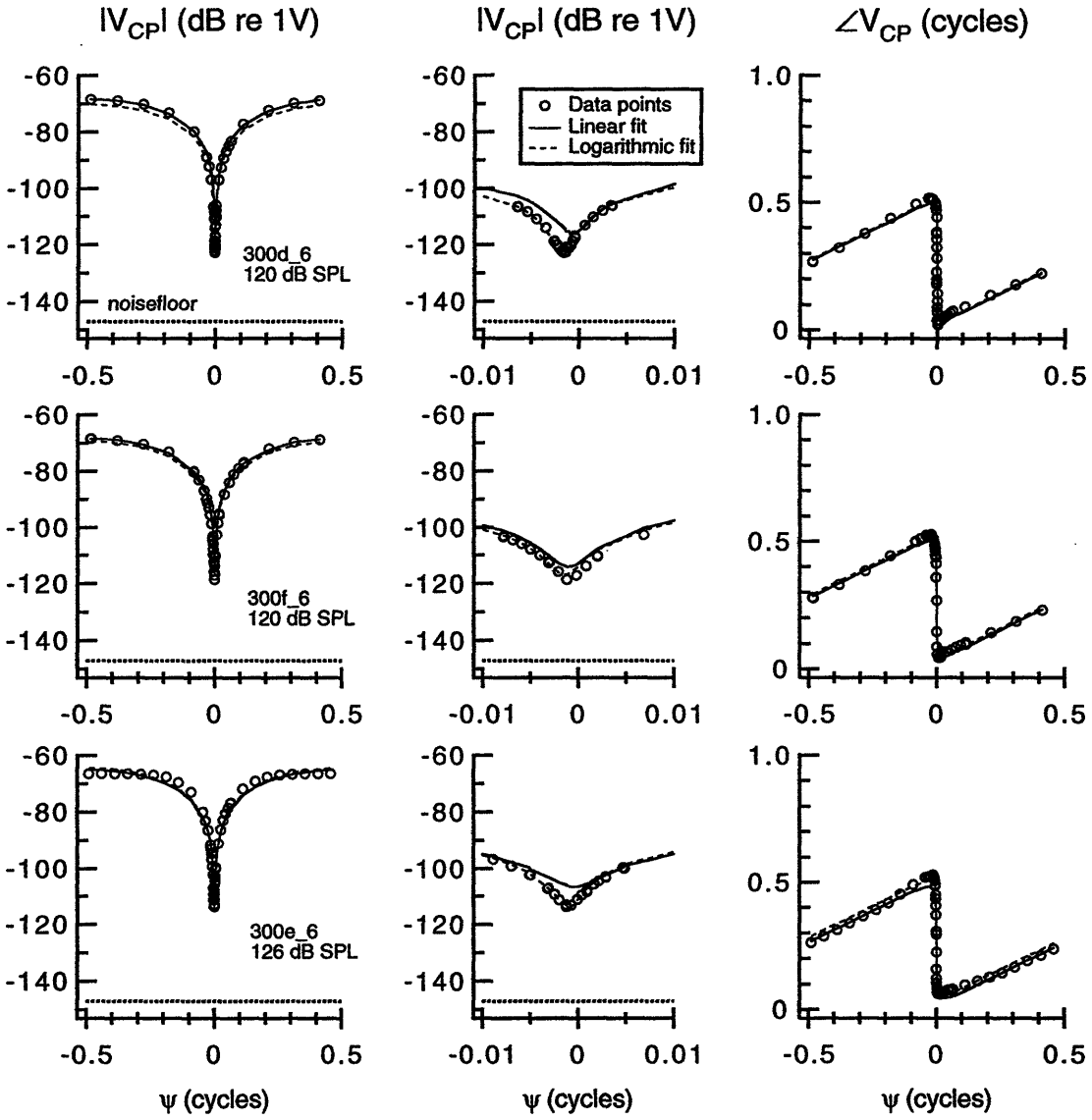

Figure C-15: Post-TTX simultaneous-stimuli measurement sets and model fits at 300 Hz on Cat #6.

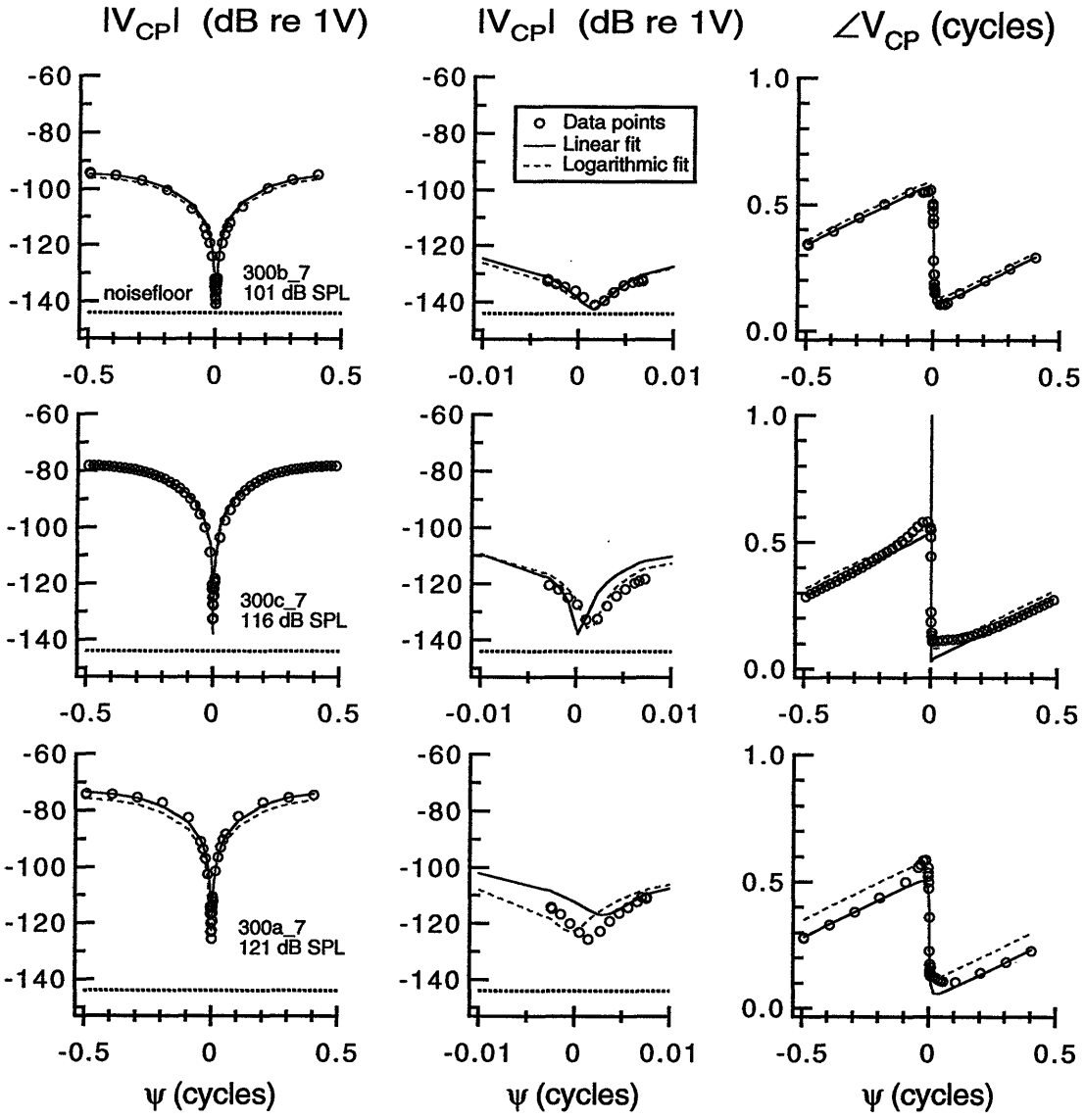

Figure C-16: Pre-TTX simultaneous-stimuli measurement sets and model fits at 300 Hz on Cat #7.

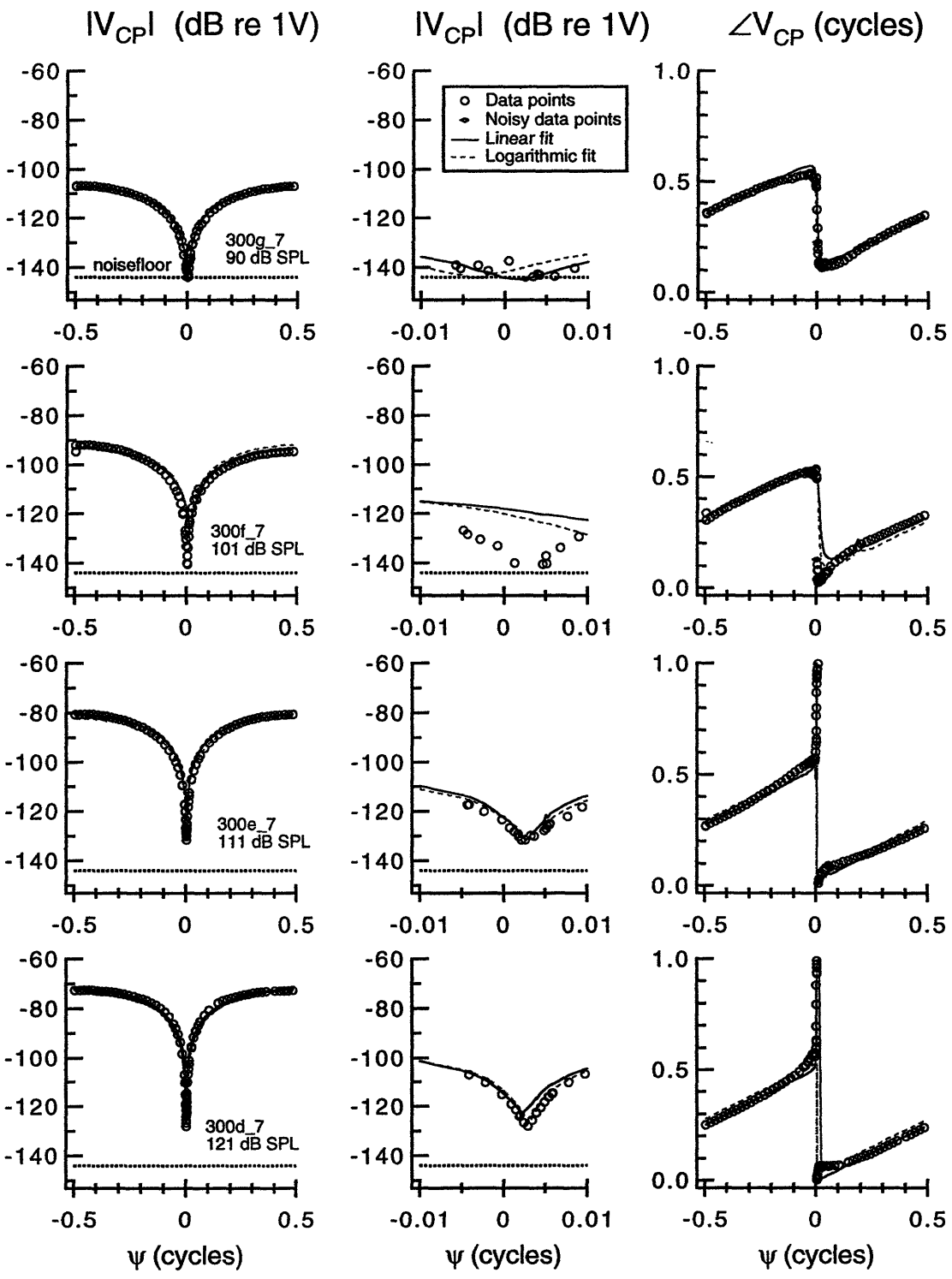

Figure C-17: Post-TTX simultaneous-stimuli measurement sets and model fits at 300 Hz on Cat #7.

Linear model parameters: 400 Hz										
Data set	dB SPL	CMRR	$\|D\|$	$\angle D$	$\|C\|$	$\angle C$	ρ_{MAG}	$\rho_{/}$	ψ_{MIN} Data	ψ_{MIN} Model
400a_1	110	13.21	1.25e-06	-0.227	2.74e-07	0.342	0.999	1.000	0.0159	0.0150
400b_1	110;108.5	13.49	1.24e-06	-0.231	2.62e-07	0.342	0.999	0.989	0.0155	0.0152
400a_2	114;113	19.37	9.42e-07	-0.018	1.01e-07	-0.493	0.846	0.807	-0.0034	0.0025
400a_3	112	23.15	1.26e-06	-0.189	8.79e-08	-0.472	0.983	0.966	0.0118	0.0109
400b_3	113	28.79	1.13e-06	-0.190	4.11e-08	-0.322	0.991	0.964	0.0042	0.0042
400c_3	115;114	34.58	1.08e-06	-0.195	2.01e-08	-0.338	0.993	0.997	0.0130	0.0027
400d_3	113;114	19.07	1.07e-06	-0.193	1.19e-07	-0.465	0.959	0.915	0.0156	0.0175
400e_3	113;114	23.74	1.08e-06	-0.188	7.00e-08	-0.403	0.970	0.917	0.0085	0.0105
400f_3	114	40.09	1.01e-06	-0.183	9.95e-09	-0.207	0.971	0.973	0.0029	-0.0001
400g_3	114	33.24	9.88e-07	-0.183	2.15e-08	-0.213	0.992	0.976	0.0019	0.0009

Table C.11: Linear model parameters calculated from 400 Hz data.

Logarithmic model parameters: 400 Hz										
Data set	dB SPL	CMRR	$\|D\|$	$\angle D$	$\|C\|$	$\angle C$	ρ_{MAG}	$\rho_{/}$	ψ_{MIN} Data	ψ_{MIN} Model
400a_1	110	13.23	1.28e-06	-0.227	2.79e-07	0.343	1.000	1.000	0.0159	0.0150
400b_1	110;108.5	13.40	1.28e-06	-0.228	2.73e-07	0.348	0.999	0.997	0.0155	0.0152
400a_2	114;113	25.50	1.28e-06	-0.019	6.77e-08	0.403	0.939	0.848	-0.0034	-0.0035
400a_3	112	23.51	1.32e-06	-0.174	8.80e-08	-0.444	0.990	0.974	0.0118	0.0109
400b_3	113	32.46	1.15e-06	-0.169	2.73e-08	-0.324	0.995	0.983	0.0042	0.0018
400c_3	115;114	32.03	1.11e-06	-0.176	2.78e-08	-0.448	0.995	0.999	0.0130	0.0042
400d_3	113;114	18.61	1.10e-06	-0.194	1.29e-07	-0.465	0.954	0.925	0.0156	0.0185
400e_3	113;114	23.58	1.11e-06	-0.164	7.35e-08	-0.403	0.993	0.976	0.0085	0.0105
400f_3	114	35.54	1.15e-06	-0.165	1.92e-08	-0.182	0.990	0.980	0.0029	0.0009
400g_3	114	34.08	1.11e-06	-0.166	2.20e-08	-0.174	0.995	0.985	0.0019	-0.0000

Table C.12: Logarithmic model parameters calculated from 400 Hz data.

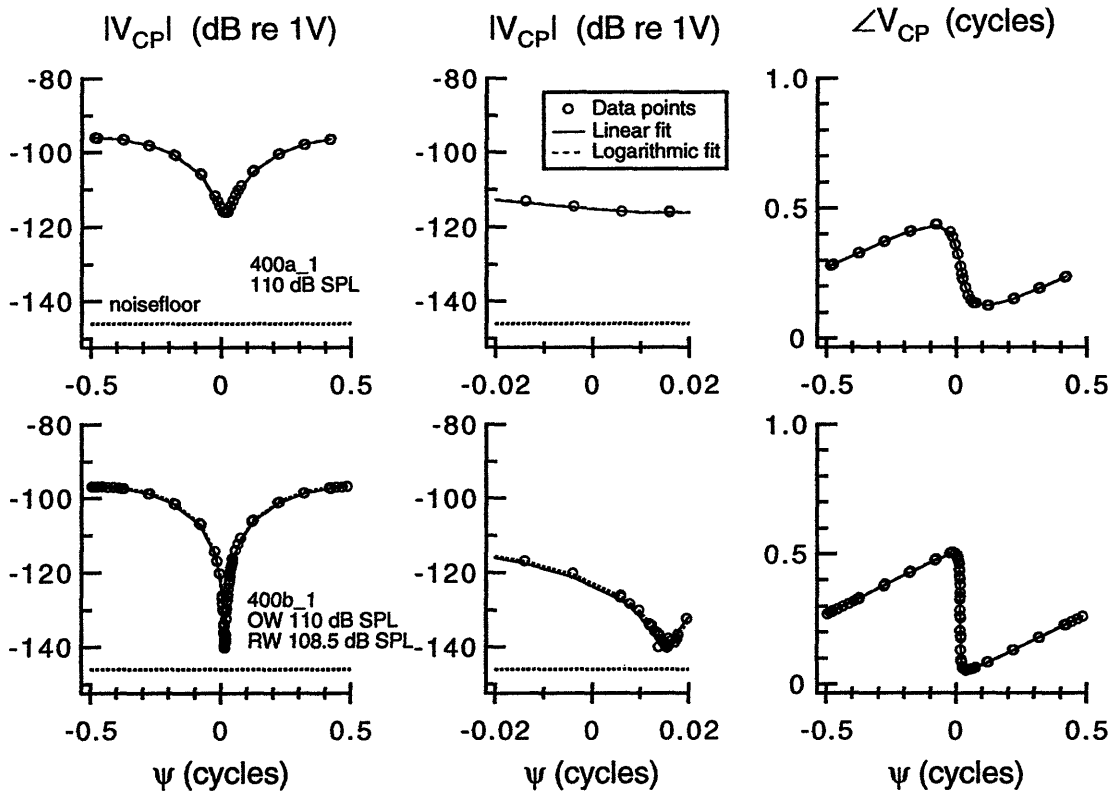

Figure C-18: Simultaneous-stimuli measurement sets and model fits at 400 Hz on Cat #1.

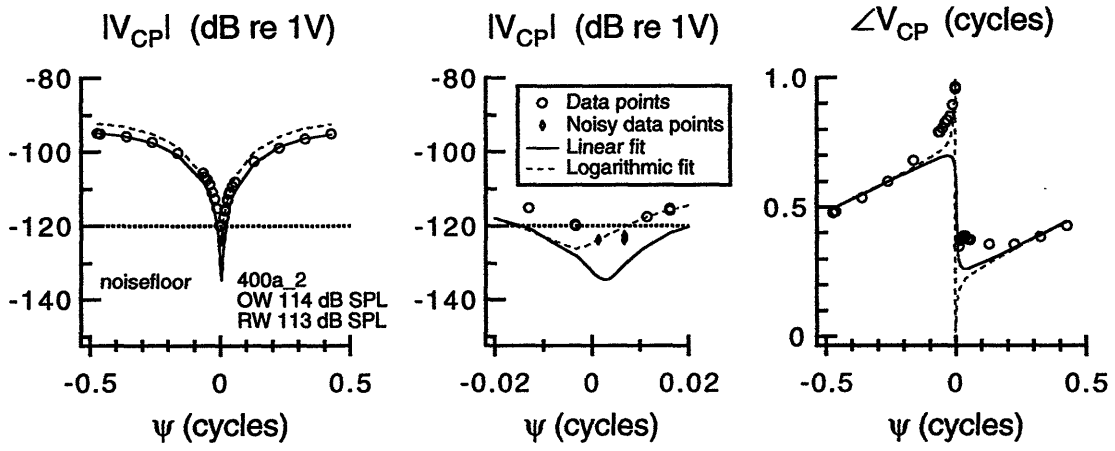

Figure C-19: Simultaneous-stimuli measurement set and model fits at 400 Hz on Cat #2.

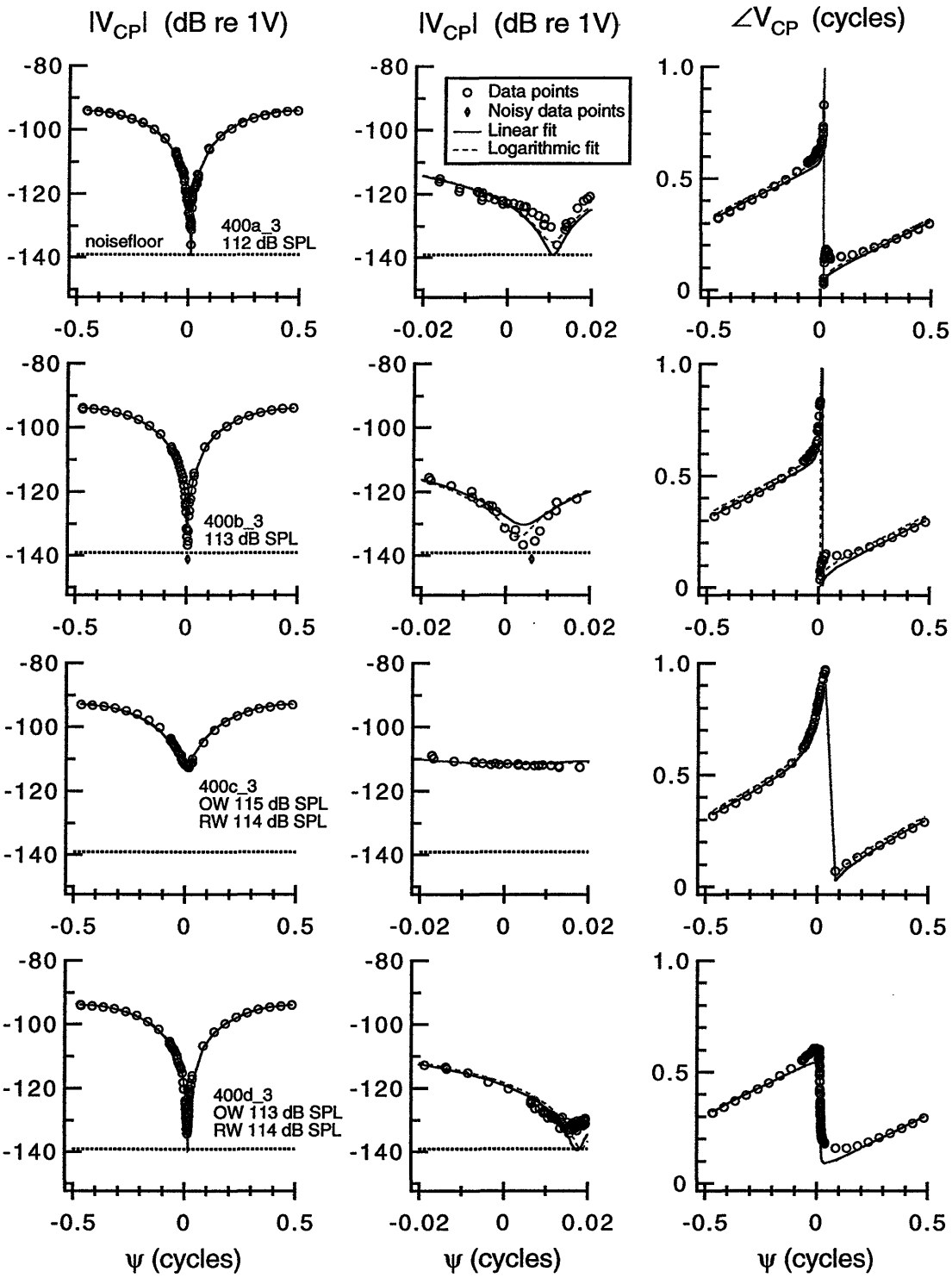

Figure C-20: Simultaneous-stimuli measurement sets and model fits at 400 Hz on Cat #3.

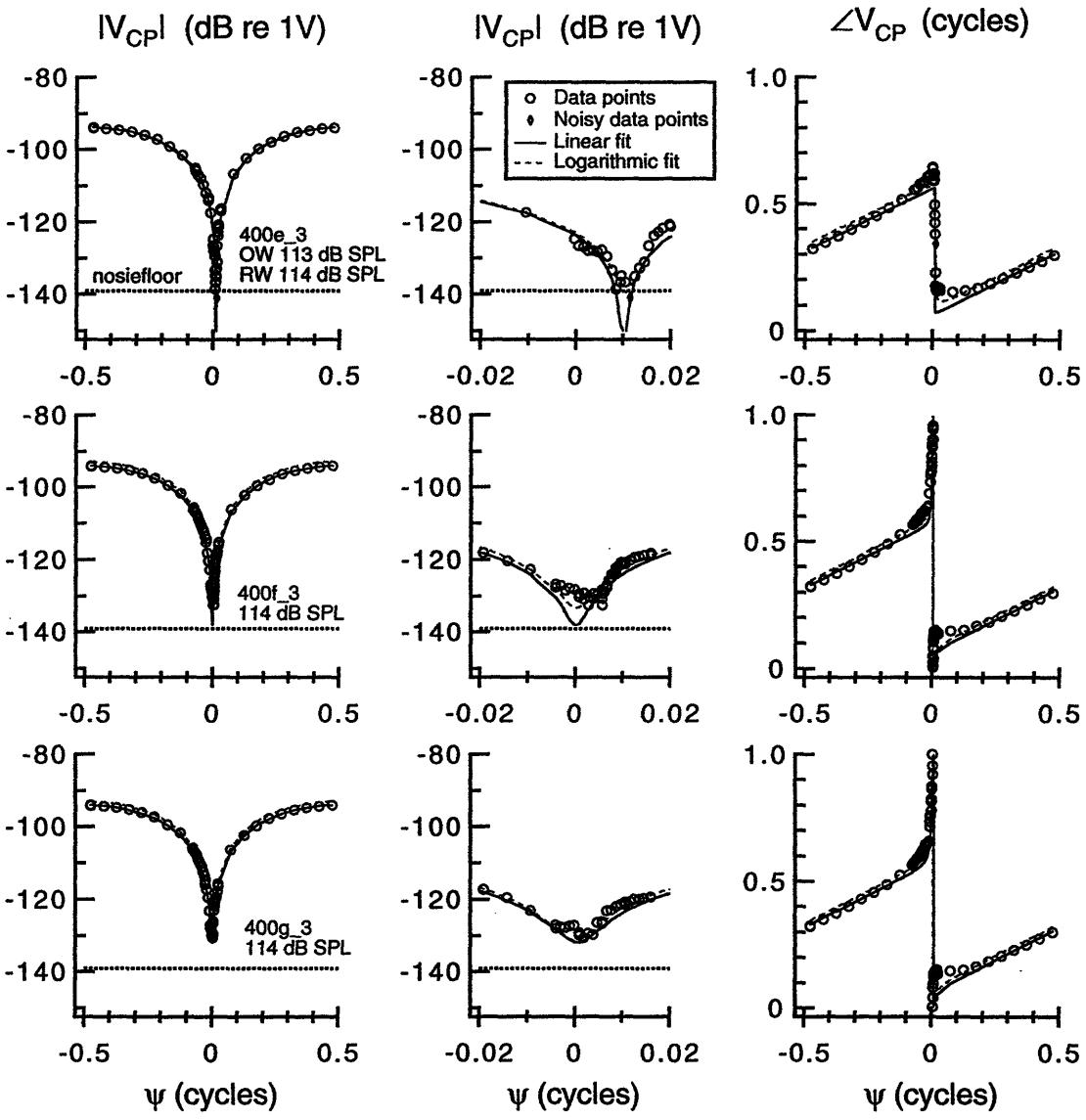

Figure C-21: Simultaneous-stimuli measurement sets and model fits at 400 Hz on Cat #3.

Linear model parameters: 500 Hz										
Data set	dB SPL	CMRR	$\|D\|$	$\angle D$	$\|C\|$	$\angle C$	ρ_{MAG}	$\rho_{\angle}$	ψ_{MIN} Data	ψ_{MIN} Model
500a_4	97	28.82	4.45e-06	-0.230	1.61e-07	0.353	0.992	0.958	0.0026	0.0025

Table C.13: Linear model parameters calculated 500 Hz data.

Logarithmic model parameters: 500 Hz										
Data set	dB SPL	CMRR	$\|D\|$	$\angle D$	$\|C\|$	$\angle C$	ρ_{MAG}	$\rho_{\angle}$	ψ_{MIN} Data	ψ_{MIN} Model
500a_4	97	29.00	4.19e-06	-0.187	1.49e-07	0.324	0.994	0.968	0.0026	0.0000

Table C.14: Logarithmic model parameters calculated from 500 Hz data.

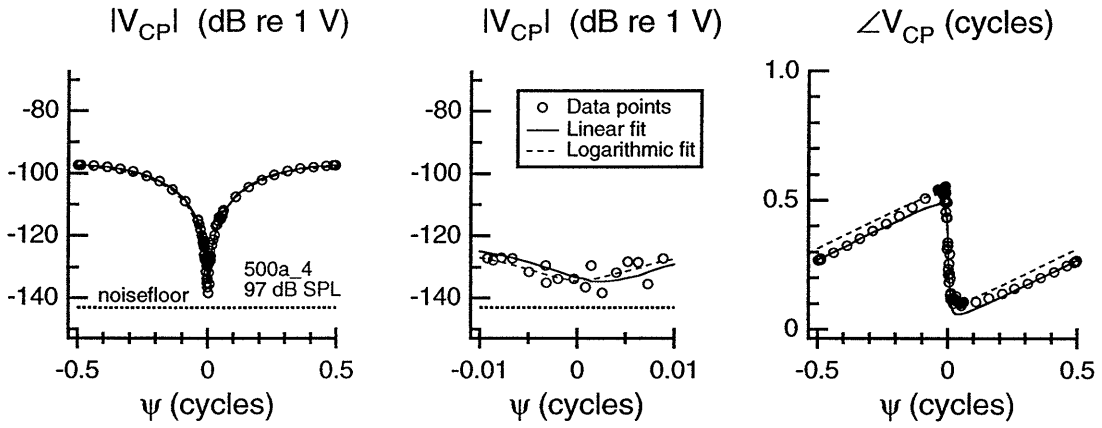

Figure C-22: Simultaneous-stimuli measurement set and model fits at 500 Hz on Cat #4.

Linear model parameters: 600 Hz										
Data set	dB SPL	CMRR	$\|D\|$	$\angle D$	$\|C\|$	$\angle C$	ρ_{MAG}	$\rho_{\angle}$	ψ_{MIN} Data	ψ_{MIN} Model
600a_1	106;105	15.37	2.60e-06	-0.331	4.43e-07	0.336	0.998	1.000	0.0196	0.0237
600b_1	113;112	15.22	2.40e-06	-0.344	4.16e-07	0.328	0.995	0.998	0.0246	0.0245
600c_1	100	14.72	2.67e-06	-0.330	4.91e-07	0.340	0.997	0.973	0.0224	0.0245

Table C.15: Linear model parameters calculated from 600 Hz data.

Logarithmic model parameters: 600 Hz										
Data set	dB SPL	CMRR	$\|D\|$	$\angle D$	$\|C\|$	$\angle C$	ρ_{MAG}	$\rho_{\angle}$	ψ_{MIN} Data	ψ_{MIN} Model
600a_1	106;105	15.20	2.74e-06	-0.329	4.77e-07	0.340	0.999	1.000	0.0196	0.0237
600b_1	113;112	15.27	2.83e-06	-0.348	4.87e-07	0.325	0.999	0.998	0.0246	0.0245
600c_1	100	15.11	2.70e-06	-0.324	4.74e-07	0.339	0.999	0.988	0.0224	0.0239

Table C.16: Logarithmic model parameters calculated from 600 Hz data.

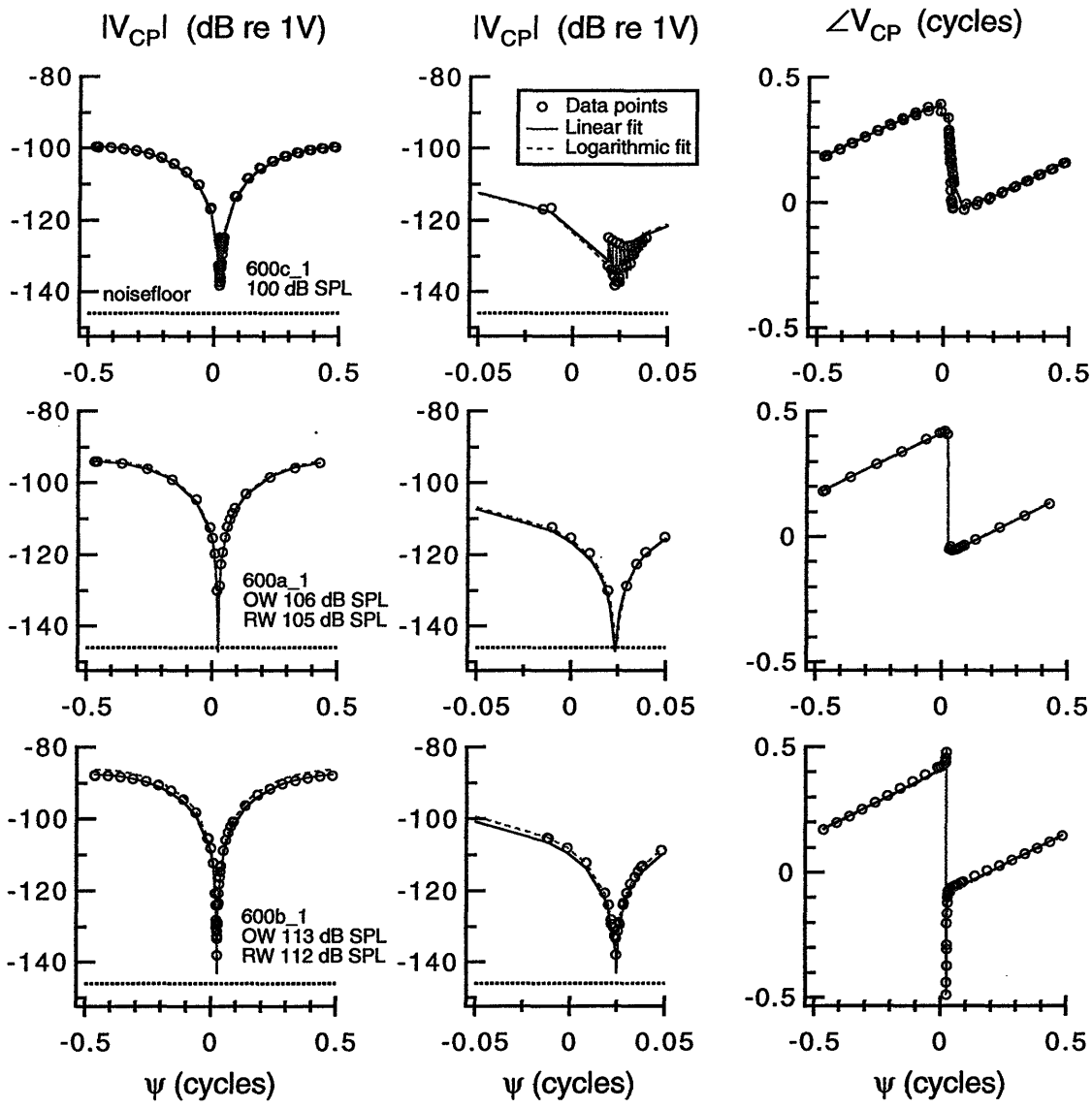

Figure C-23: Simultaneous-stimuli measurement sets and model fits at 600 Hz on Cat #1.

Linear model parameters: 800 Hz										
Data set	dB SPL	CMRR	$\|D\|$	$\angle D$	$\|C\|$	$\angle C$	ρ_{MAG}	$\rho_{\angle}$	ψ_{MIN} Data	ψ_{MIN} Model
800a_1	116	16.55	3.25e-06	-0.437	4.84e-07	0.260	0.999	1.000	0.0228	0.0227
800b_1	116	16.31	3.19e-06	-0.434	4.88e-07	0.271	0.998	0.999	0.0233	0.0232
800a_3	116	19.82	2.34e-06	-0.354	2.39e-07	0.387	0.968	0.947	0.0164	0.0159
800a_4	103	31.56	7.35e-06	-0.335	1.94e-07	0.446	0.995	0.991	0.0041	0.0041
800b_4	98	37.12	6.76e-06	-0.324	9.42e-08	-0.299	0.992	0.985	0.0006	0.0001

Table C.17: Linear model parameters calculated from 800 Hz data.

Logarithmic model parameters: 800 Hz										
Data set	dB SPL	CMRR	$\|D\|$	$\angle D$	$\|C\|$	$\angle C$	ρ_{MAG}	$\rho_{\angle}$	ψ_{MIN} Data	ψ_{MIN} Model
800a_1	116	16.54	3.40e-06	-0.436	5.06e-07	0.261	1.000	1.000	0.0228	0.0227
800b_1	116	16.32	3.41e-06	-0.432	5.20e-07	0.272	0.999	0.999	0.0233	0.0232
800a_3	116	19.58	3.19e-06	-0.348	3.35e-07	0.426	0.989	0.988	0.0164	0.0169
800a_4	103	31.74	7.40e-06	-0.330	1.91e-07	0.477	0.996	0.993	0.0041	0.0041
800b_4	98	33.94	5.87e-06	-0.342	1.18e-07	-0.324	0.991	0.992	0.0006	0.0001

Table C.18: Logarithmic model parameters calculated from 800 Hz data.

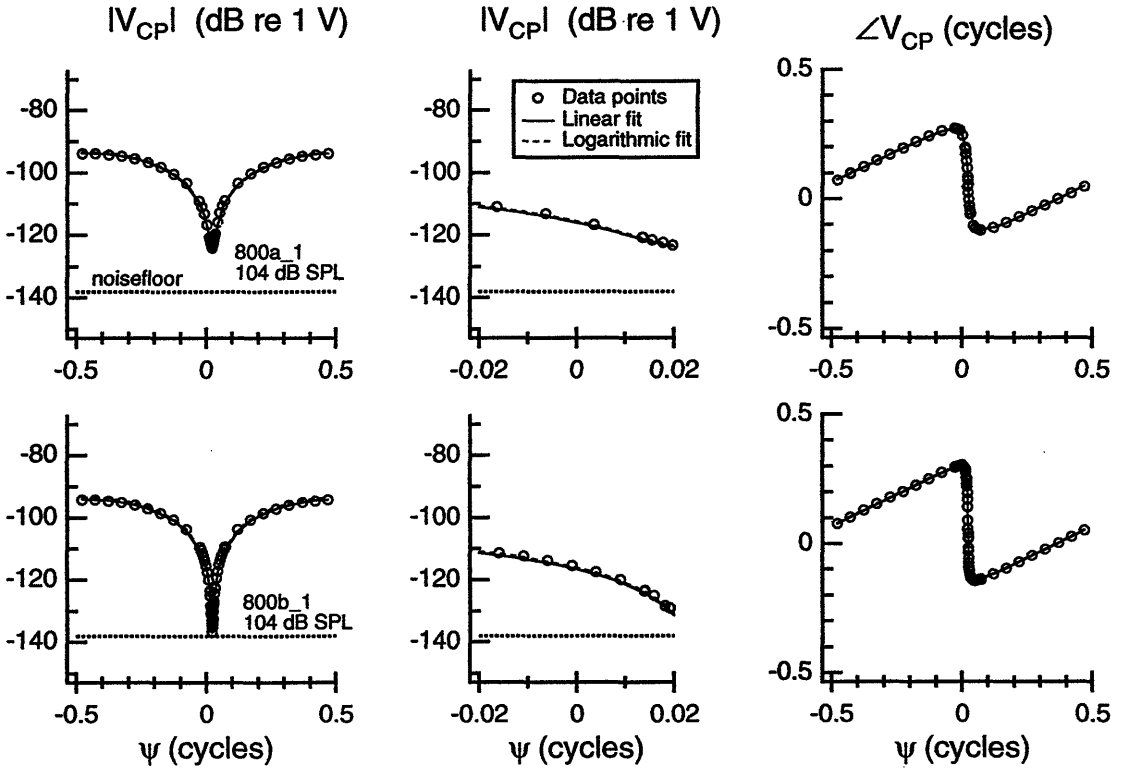

Figure C-24: Simultaneous-stimuli measurement sets and model fits at 800 Hz on Cat #1.

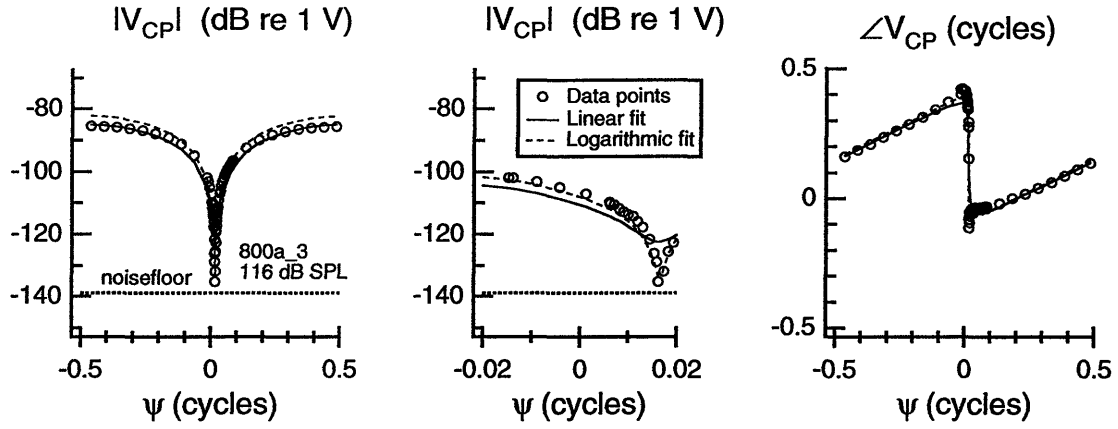

Figure C-25: Simultaneous-stimuli measurement set and model fits at 800 Hz on Cat #3.

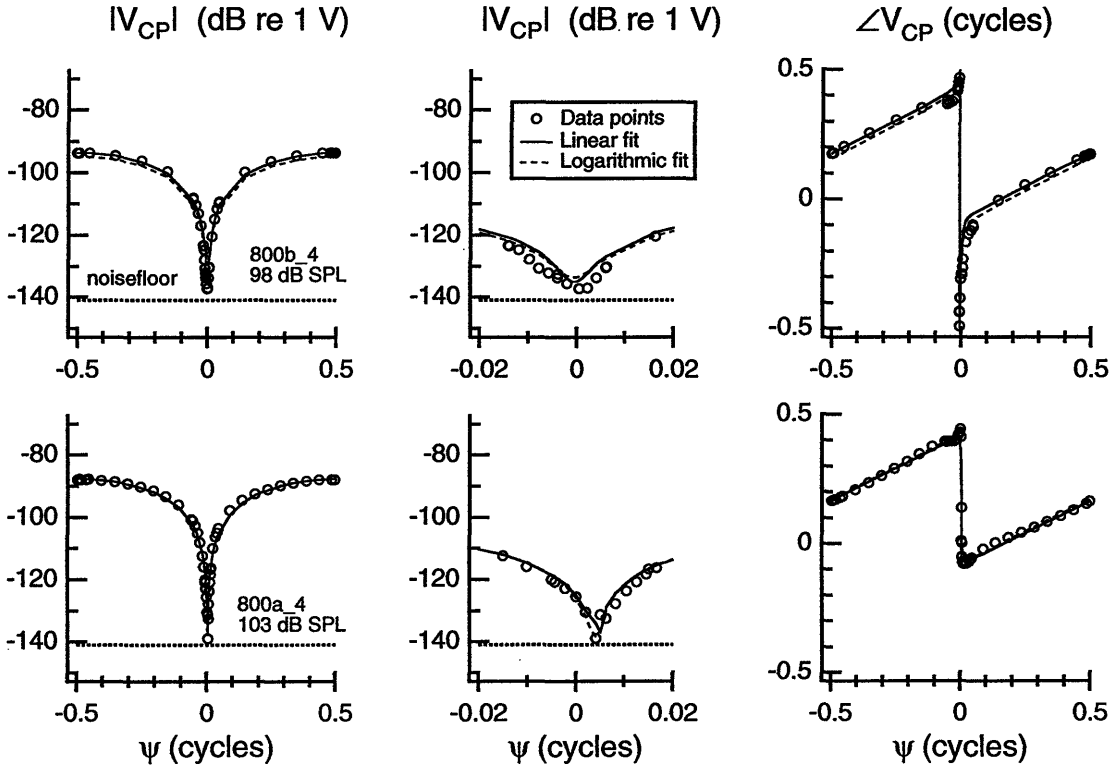

Figure C-26: Simultaneous-stimuli measurement sets and model fits at 800 Hz on Cat #4.

Linear model parameters: 1000 Hz										
Data set	dB SPL	CMRR	$\|D\|$	$\angle D$	$\|C\|$	$\angle C$	ρ_{MAG}	$\rho_{\angle}$	ψ_{MIN} Data	ψ_{MIN} Model
1000a_1	101	17.85	2.84e-06	-0.499	3.64e-07	0.264	0.999	1.000	0.0201	0.0204
1000b_1	100	17.77	2.90e-06	0.499	3.75e-07	0.272	0.998	0.999	0.0203	0.0204
1000a_2	101;99	13.36	5.63e-06	-0.383	1.21e-06	0.226	0.974	0.911	0.0018	0.0217
1000b_2	110;108	12.33	5.71e-06	-0.396	1.38e-06	0.184	0.986	0.988	0.0260	0.0187
1000c_2	111;108	12.43	5.58e-06	-0.395	1.33e-06	0.184	0.971	0.988	0.0260	0.0178
1000a_3	110	16.30	4.51e-06	-0.394	6.90e-07	0.488	0.986	0.994	0.0152	0.0162
1000b_3	110	16.42	4.43e-06	-0.395	6.70e-07	0.492	0.983	0.983	0.0139	0.0159
1000c_3	111	20.15	4.13e-06	-0.385	4.06e-07	0.478	0.993	0.976	0.0096	0.0120
1000d_3	111	20.49	4.11e-06	-0.387	3.88e-07	0.493	0.950	0.932	0.0093	0.0094
1000e_3	111	18.61	4.06e-06	-0.388	4.76e-07	0.316	0.990	0.939	0.0185	0.0170
1000f_3	111	16.88	3.90e-06	-0.393	5.59e-07	0.291	0.995	0.941	0.0210	0.0210
1000g_3	112	21.81	3.73e-06	-0.390	3.03e-07	0.259	0.987	0.978	0.0127	0.0098
1000h_3	111	15.68	3.94e-06	-0.372	6.48e-07	-0.157	0.980	0.942	-0.0278	-0.0258
1000i_3	111	46.08	3.89e-06	-0.383	1.93e-08	0.032	0.989	0.987	-0.0016	-0.0006
1000j_3	112	23.64	3.78e-06	-0.390	2.48e-07	0.289	0.965	0.940	0.0078	0.0098
1000k_3	112	17.37	3.83e-06	-0.397	5.18e-07	0.281	0.998	0.965	0.0198	0.0193
1000l_3	109;113	12.21	3.35e-06	-0.404	8.22e-07	0.272	0.996	0.996	0.0283	0.0353
1000m_3	113	15.23	3.14e-06	-0.406	5.44e-07	0.281	0.986	0.986	0.0231	0.0252
1000n_3	102	14.88	3.64e-06	-0.388	6.56e-07	0.308	0.986	0.981	0.0335	0.0272
1000a_4	106	31.23	7.96e-06	-0.421	2.19e-07	0.244	1.000	0.996	0.0022	0.0036
1000b_4	98	32.97	8.29e-06	-0.406	1.86e-07	0.303	0.998	0.997	0.0029	0.0029
1000c_4	106	33.64	7.36e-06	-0.426	1.53e-07	0.066	1.000	0.998	0.0002	-0.0007
1000d_4	106	28.80	7.43e-06	-0.421	2.70e-07	0.096	0.999	0.996	-0.0013	-0.0015
1000e_4	106	44.01	7.18e-06	-0.421	4.53e-08	0.345	0.999	0.992	0.0023	0.0013
1000f_4	98	44.63	7.42e-06	-0.407	4.35e-08	0.400	0.998	0.993	-0.0010	0.0010
1000g_4	106	44.95	6.99e-06	-0.419	3.95e-08	0.196	0.999	0.994	-0.0001	0.0009
1000a_5	103	25.45	1.71e-05	-0.435	9.11e-07	0.394	0.974	0.832	0.0104	0.0071
1000b_5	102.5;102.5	31.81	1.77e-05	-0.427	4.53e-07	0.450	0.965	0.842	0.0104	0.0015
1000c_5	103.2;101.9	24.68	1.78e-05	-0.426	1.04e-06	0.347	0.989	0.992	0.0030	0.0089
1000d_5	103.7;101.2	29.62	1.76e-05	-0.424	5.80e-07	0.376	0.997	0.999	-0.0050	0.0050
1000e_5	104.4;100.5	29.43	1.77e-05	-0.425	5.96e-07	0.398	0.999	1.000	0.0025	0.0049
1000f_5	103.0;102.3	27.07	1.77e-05	-0.425	7.83e-07	0.366	0.988	0.974	0.0043	0.0067
1000g_5	105	26.83	1.76e-05	-0.428	8.00e-07	0.474	0.928	0.874	0.0067	0.0017
1000h_5	110	25.94	1.68e-05	-0.431	8.47e-07	0.430	0.982	0.961	0.0018	0.0066
1000i_5	115	25.21	1.71e-05	-0.425	9.37e-07	0.433	0.961	0.964	0.0045	0.0063
1000j_5	100	29.02	1.70e-05	-0.433	6.00e-07	0.298	0.878	0.385	0.0108	0.0060
1000k_5	95	33.94	1.63e-05	-0.452	3.27e-07	0.335	0.728	0.602	0.0137	0.0033
1000l_5	110	25.65	1.17e-05	-0.510	6.11e-07	-0.294	0.939	0.781	-0.0083	-0.0083
1000m_5	105	25.77	1.22e-05	-0.504	6.26e-07	-0.283	0.985	0.628	-0.0099	-0.0089
1000n_5	100	23.30	1.21e-05	-0.502	8.31e-07	-0.237	0.958	0.751	-0.0092	-0.0112
1000p_5	95	29.04	1.24e-05	-0.515	4.38e-07	-0.306	0.953	0.778	0.0006	-0.0056
1000q_5	90	21.86	1.22e-05	-0.535	9.86e-07	-0.205	0.925	0.635	0.0067	-0.0113
1000r_5	115	26.70	9.34e-06	-0.513	4.32e-07	-0.352	0.991	0.996	-0.0085	-0.0087
1000s_5	120	22.65	6.65e-06	-0.513	4.90e-07	-0.453	0.969	0.995	-0.0028	-0.0031
1000a_6	104	36.78	1.70e-05	-0.475	2.47e-07	0.227	0.960	0.837	0.0068	0.0022
1000b_6	114	34.17	1.63e-05	-0.485	3.19e-07	-0.260	0.968	0.859	-0.0025	-0.0035
1000c_6	104	28.06	1.45e-05	-0.466	5.72e-07	-0.317	0.999	0.999	-0.0024	-0.0077
1000d_6	113	30.97	1.46e-05	-0.483	4.12e-07	0.007	0.991	0.986	-0.0015	-0.0005
1000e_6	98	37.10	1.39e-05	-0.451	1.94e-07	0.044	1.000	0.999	-0.0010	-0.0015
1000f_6	98	33.82	1.36e-05	-0.456	2.76e-07	-0.144	0.999	0.999	-0.0034	-0.0034
1000g_6	110	32.45	1.43e-05	-0.477	3.40e-07	-0.157	1.000	0.601	-0.0041	-0.0036
1000h_6	100	32.33	1.39e-05	-0.458	3.36e-07	-0.267	0.969	0.935	-0.0037	-0.0040
1000i_6	90	33.81	1.40e-05	-0.449	2.85e-07	-0.175	0.999	0.993	-0.0039	-0.0033
1000j_6	80	21.43	1.40e-05	-0.449	1.19e-06	-0.003	0.997	0.999	-0.0236	-0.0041
1000k_6	120	29.09	1.22e-05	-0.497	4.30e-07	-0.255	0.985	0.991	-0.0049	-0.0058
1000a_7	119	31.96	1.06e-05	-0.459	2.67e-07	0.129	0.979	0.923	0.0034	0.0024
1000b_7	99	33.25	1.31e-05	-0.433	2.86e-07	0.318	0.979	0.896	0.0020	0.0030
1000c_7	109	34.67	5.65e-06	-0.431	1.04e-07	0.147	0.996	0.973	0.0005	0.0018
1000d_7	99	35.04	5.64e-06	-0.393	9.98e-08	0.220	0.997	0.989	0.0001	0.0011
1000e_7	89	35.15	5.81e-06	-0.370	1.02e-07	0.096	1.000	0.998	0.0007	-0.0007
1000f_7	119	37.49	4.24e-06	-0.452	5.66e-08	0.063	0.972	0.850	0.0004	0.0001

Table C.19: Linear model parameters calculated from 1000 Hz data.

Logarithmic model parameters: 1000 Hz										
Data set	dB SPL	CMRR	$\|D\|$	$\angle D$	$\|C\|$	$\angle C$	ρ_{MAG}	$\rho_{\angle}$	ψ_{MIN} Data	ψ_{MIN} Model
1000a_1	101	18.02	2.98e-06	-0.499	3.74e-07	0.263	1.000	1.000	0.0201	0.0194
1000b_1	100	18.16	3.06e-06	0.499	3.79e-07	0.271	0.999	1.000	0.0203	0.0192
1000a_2	101;99	16.77	4.54e-06	-0.381	6.58e-07	0.155	0.968	0.889	0.0018	0.0046
1000b_2	110;108	13.01	5.48e-06	-0.381	1.23e-06	0.207	0.996	0.997	0.0260	0.0187
1000c_2	111;108	13.16	5.15e-06	-0.382	1.13e-06	0.209	0.992	0.997	0.0260	0.0188
1000a_3	110	16.53	5.20e-06	-0.385	7.75e-07	-0.488	0.997	0.999	0.0152	0.0143
1000b_3	110	16.27	5.04e-06	-0.390	7.73e-07	-0.489	0.998	0.996	0.0139	0.0138
1000c_3	111	20.62	4.70e-06	-0.380	4.38e-07	-0.497	0.998	0.999	0.0096	0.0096
1000d_3	111	20.47	4.49e-06	-0.378	4.25e-07	-0.485	0.998	0.999	0.0093	0.0089
1000e_3	111	18.32	4.64e-06	-0.377	5.63e-07	0.350	0.997	0.998	0.0185	0.0187
1000f_3	111	17.19	4.37e-06	-0.379	6.04e-07	0.312	0.997	0.995	0.0210	0.0210
1000g_3	112	21.15	4.10e-06	-0.378	3.59e-07	0.275	0.995	0.989	0.0127	0.0117
1000h_3	111	15.46	4.25e-06	-0.353	7.16e-07	-0.128	0.997	0.988	-0.0278	-0.0268
1000i_3	111	43.54	4.42e-06	-0.364	2.94e-08	0.125	0.995	0.994	-0.0016	-0.0006
1000j_3	112	23.45	4.12e-06	-0.360	2.77e-07	0.295	0.997	0.977	0.0078	0.0088
1000k_3	112	17.13	4.07e-06	-0.379	5.66e-07	0.302	0.998	0.980	0.0198	0.0203
1000l_3	109;113	12.66	3.45e-06	-0.400	8.03e-07	0.280	0.997	0.997	0.0283	0.0333
1000m_3	113	15.25	3.56e-06	-0.382	6.16e-07	0.298	0.997	0.993	0.0231	0.0252
1000n_3	102	14.07	3.65e-06	-0.373	7.22e-07	0.312	0.996	0.991	0.0335	0.0292
1000a_4	106	32.12	8.11e-06	-0.416	2.01e-07	0.241	1.000	0.998	0.0022	0.0036
1000b_4	98	33.29	8.48e-06	-0.407	1.84e-07	0.280	0.999	0.998	0.0029	0.0029
1000c_4	106	33.45	7.55e-06	-0.418	1.61e-07	0.060	1.000	0.999	0.0002	-0.0007
1000d_4	106	28.99	7.49e-06	-0.412	2.66e-07	0.105	0.999	0.999	-0.0013	-0.0015
1000e_4	106	44.22	7.10e-06	-0.408	4.37e-08	0.319	1.000	0.996	0.0023	0.0013
1000f_4	98	45.13	7.21e-06	-0.400	3.99e-08	0.432	0.999	0.994	-0.0010	0.0007
1000g_4	106	47.31	6.90e-06	-0.406	2.97e-08	0.188	1.000	0.996	-0.0001	0.0001
1000a_5	103	26.09	1.54e-05	0.462	7.65e-07	0.208	0.991	0.943	0.0104	0.0084
1000b_5	102.5;102.5	33.55	1.48e-05	0.479	3.10e-07	0.478	0.958	0.673	0.0104	-0.0004
1000c_5	103.2;101.9	26.21	1.75e-05	-0.474	8.57e-07	0.274	0.994	0.992	0.0030	0.0076
1000d_5	103.7;101.2	27.42	1.76e-05	-0.431	7.47e-07	0.335	0.996	1.000	-0.0050	0.0065
1000e_5	104.4;100.5	30.56	1.78e-05	-0.427	5.27e-07	0.366	0.999	1.000	0.0025	0.0049
1000f_5	103.0;102.3	22.88	1.72e-05	-0.461	1.23e-06	0.273	0.978	0.995	0.0043	0.0118
1000g_5	105	27.53	1.36e-05	0.495	5.73e-07	0.267	0.982	0.959	0.0067	0.0066
1000h_5	110	26.59	1.67e-05	-0.479	7.82e-07	0.364	0.986	0.982	0.0018	0.0066
1000i_5	115	24.69	1.67e-05	-0.458	9.71e-07	0.399	0.948	0.990	0.0045	0.0063
1000j_5	100	23.68	1.46e-05	0.400	9.55e-07	0.100	0.984	0.702	0.0108	0.0098
1000k_5	95	21.44	1.40e-05	0.348	1.19e-06	-0.476	0.584	0.530	0.0137	-0.0123
1000l_5	110	25.51	1.38e-05	0.455	7.34e-07	-0.290	0.995	0.979	-0.0083	-0.0081
1000m_5	105	23.41	1.37e-05	0.433	9.26e-07	-0.279	0.995	0.957	-0.0099	-0.0109
1000n_5	100	22.14	1.42e-05	0.427	1.11e-06	-0.284	0.993	0.921	-0.0092	-0.0120
1000p_5	95	39.82	1.44e-05	0.368	1.47e-07	0.469	0.949	0.851	0.0006	-0.0012
1000q_5	90	16.83	1.07e-05	0.428	1.54e-06	-0.229	0.942	0.876	0.0067	-0.0196
1000r_5	115	27.58	1.08e-05	0.479	4.53e-07	-0.345	0.995	0.997	-0.0085	-0.0046
1000s_5	120	24.92	8.60e-06	0.490	4.88e-07	-0.407	0.982	0.999	-0.0028	-0.0031
1000a_6	104	30.34	1.25e-05	-0.491	3.82e-07	0.192	0.983	0.925	0.0068	0.0042
1000b_6	114	38.00	1.26e-05	-0.472	1.59e-07	-0.184	0.981	0.946	-0.0025	-0.0020
1000c_6	104	28.91	1.44e-05	-0.451	5.16e-07	-0.292	1.000	0.999	-0.0024	-0.0028
1000d_6	113	34.35	1.44e-05	-0.463	2.75e-07	-0.016	1.000	0.995	-0.0015	-0.0012
1000e_6	98	36.94	1.35e-05	-0.447	1.91e-07	0.043	1.000	0.999	-0.0010	-0.0015
1000f_6	98	33.56	1.31e-05	-0.452	2.75e-07	-0.137	1.000	1.000	-0.0034	-0.0034
1000g_6	110	32.48	1.14e-05	-0.375	2.72e-07	-0.166	0.993	0.985	-0.0041	-0.0041
1000h_6	100	32.74	1.55e-05	-0.464	3.58e-07	-0.308	0.999	0.999	-0.0037	-0.0032
1000i_6	90	33.40	1.37e-05	-0.451	2.93e-07	-0.182	0.999	0.996	-0.0039	-0.0033
1000j_6	80	20.69	1.34e-05	-0.452	1.24e-06	-0.021	0.998	1.000	-0.0236	-0.0061
1000k_6	120	30.11	1.32e-05	-0.464	4.13e-07	-0.250	1.000	0.999	-0.0049	-0.0051
1000a_7	119	32.10	1.19e-05	-0.451	2.96e-07	0.211	0.999	0.994	0.0034	0.0033
1000b_7	99	30.77	9.48e-06	-0.431	2.74e-07	0.278	0.981	0.976	0.0020	0.0040
1000c_7	109	35.50	5.77e-06	-0.399	9.68e-08	0.128	1.000	0.985	0.0005	0.0002
1000d_7	99	37.79	5.68e-06	-0.374	7.33e-08	0.187	1.000	0.997	0.0001	0.0010
1000e_7	89	35.29	5.77e-06	-0.367	9.94e-08	0.090	1.000	0.998	0.0007	-0.0007
1000f_7	119	43.93	5.13e-06	-0.406	3.27e-08	0.378	0.998	0.979	0.0004	0.0001

Table C.20: Logarithmic model parameters calculated from 1000 Hz data.

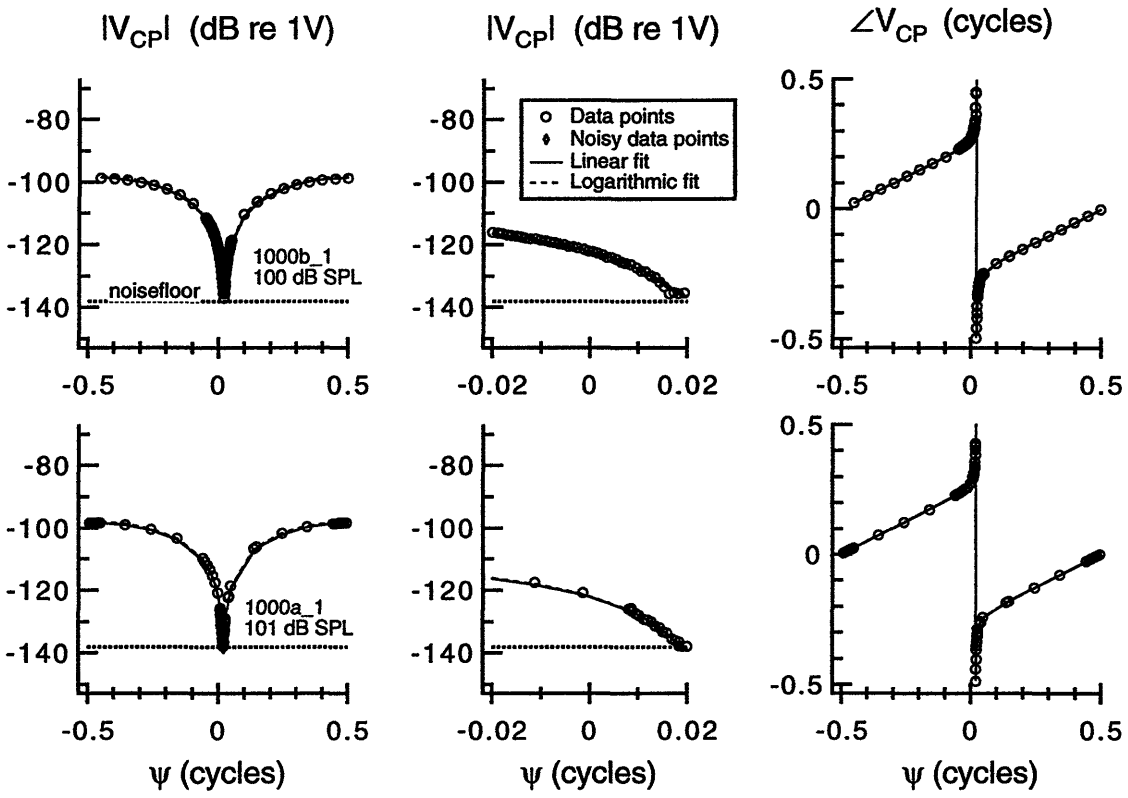

Figure C-27: Simultaneous-stimuli measurement sets and model fits at 1000 Hz on Cat #1.

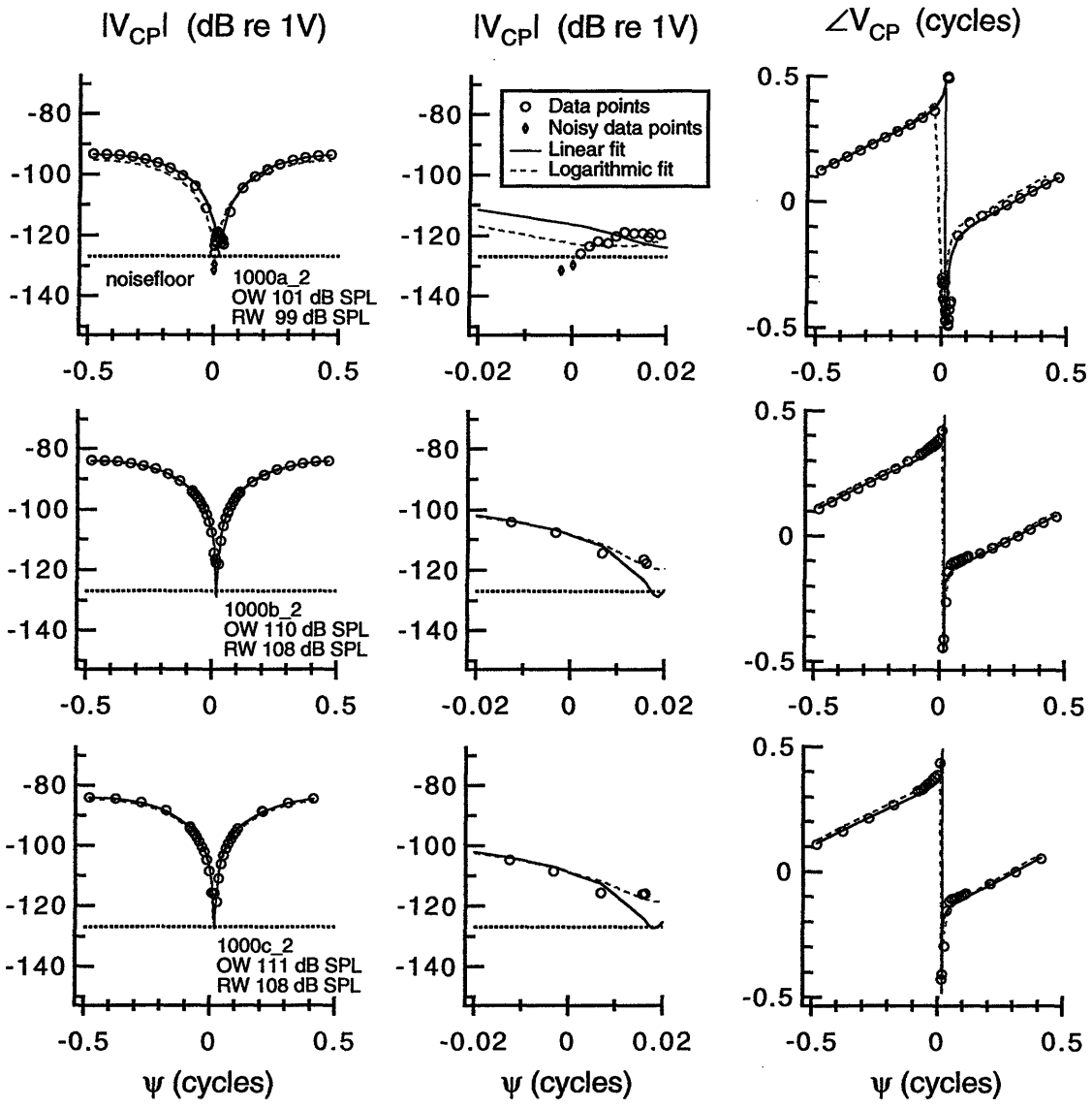

Figure C-28: Simultaneous-stimuli measurement sets and model fits at 1000 Hz on Cat #2.

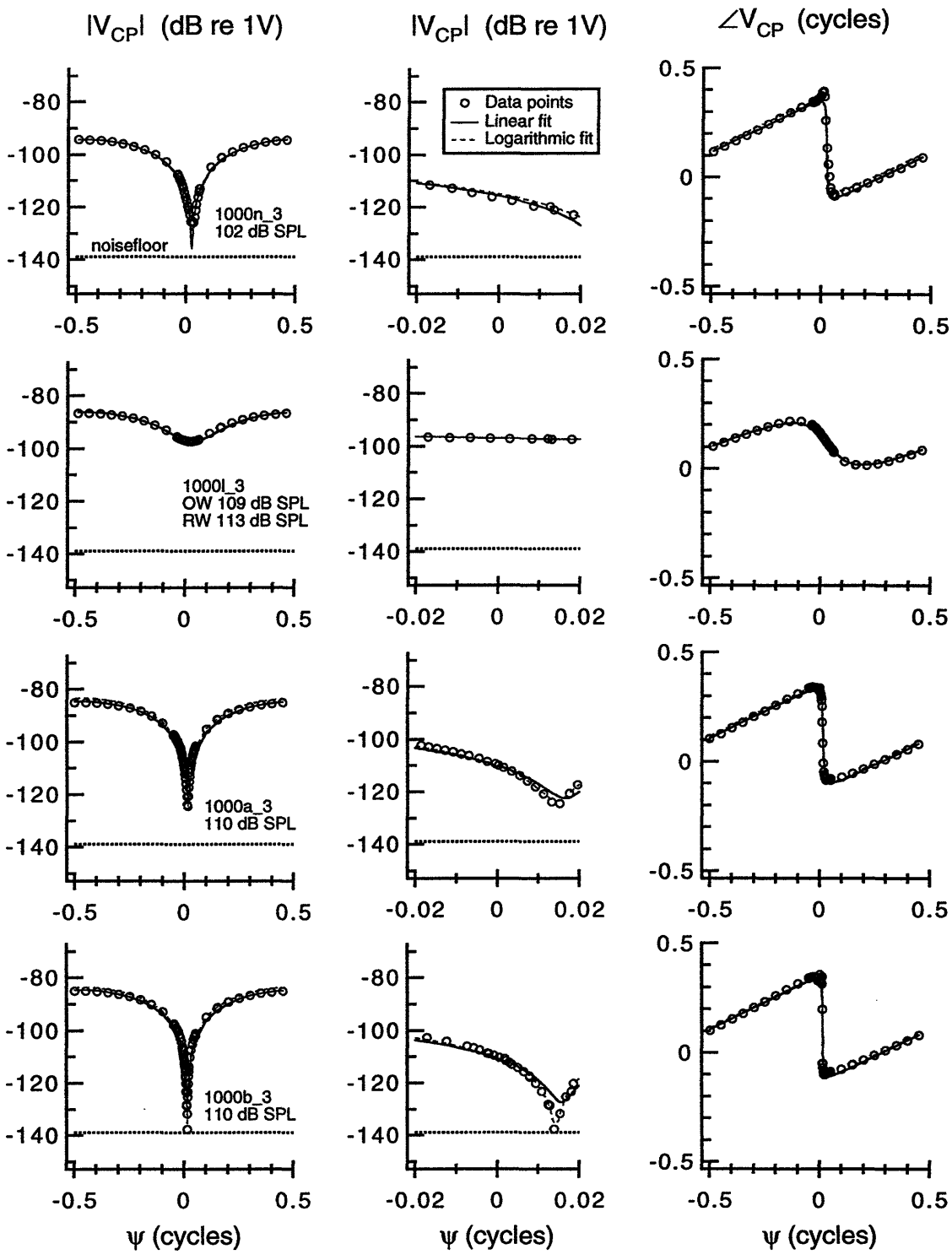

Figure C-29: Simultaneous-stimuli measurement sets and model fits at 1000 Hz on Cat #3.

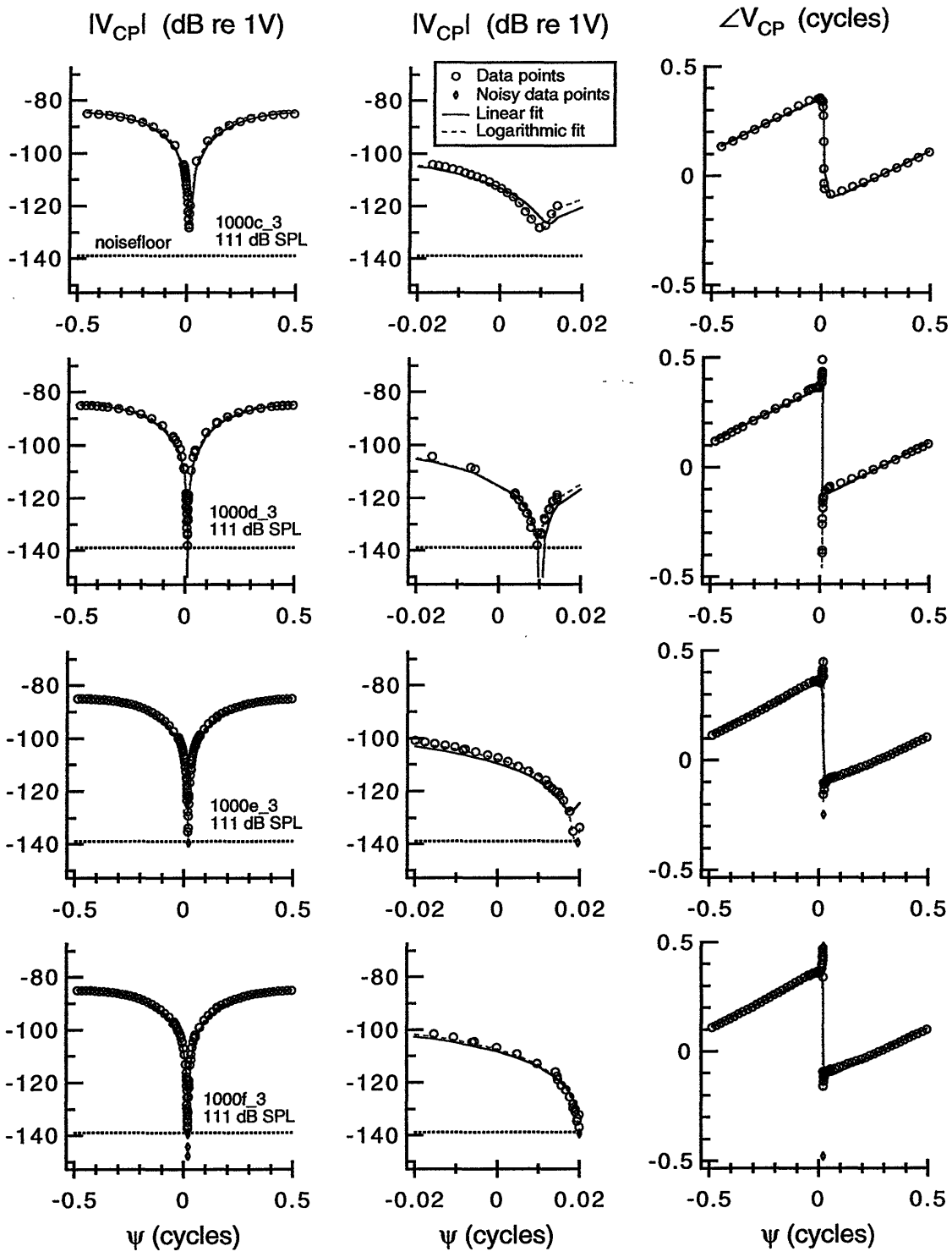

Figure C-30: Simultaneous-stimuli measurement sets and model fits at 1000 Hz on Cat #3.

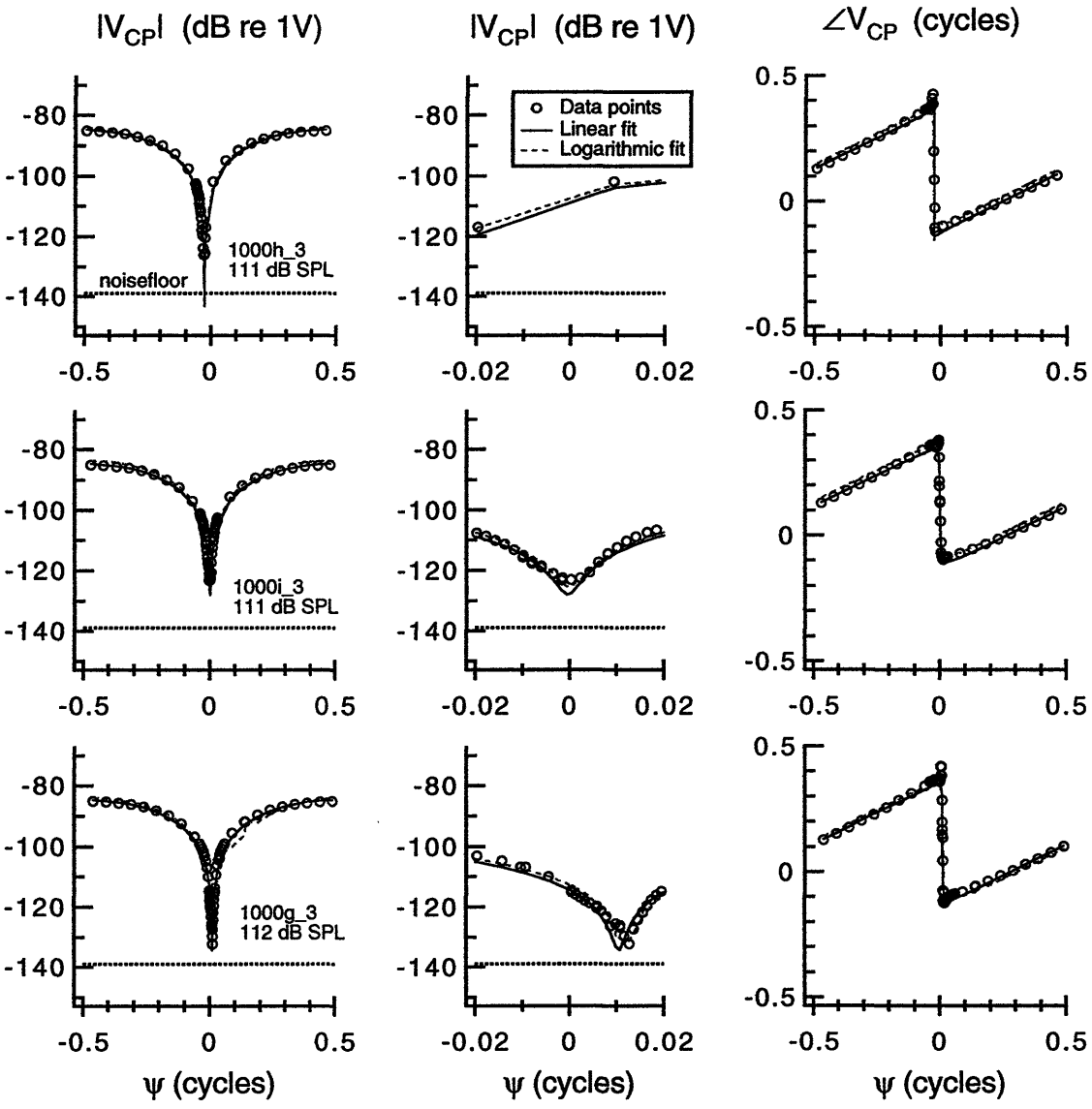

Figure C-31: Simultaneous-stimuli measurement sets and model fits at 1000 Hz on Cat #3.

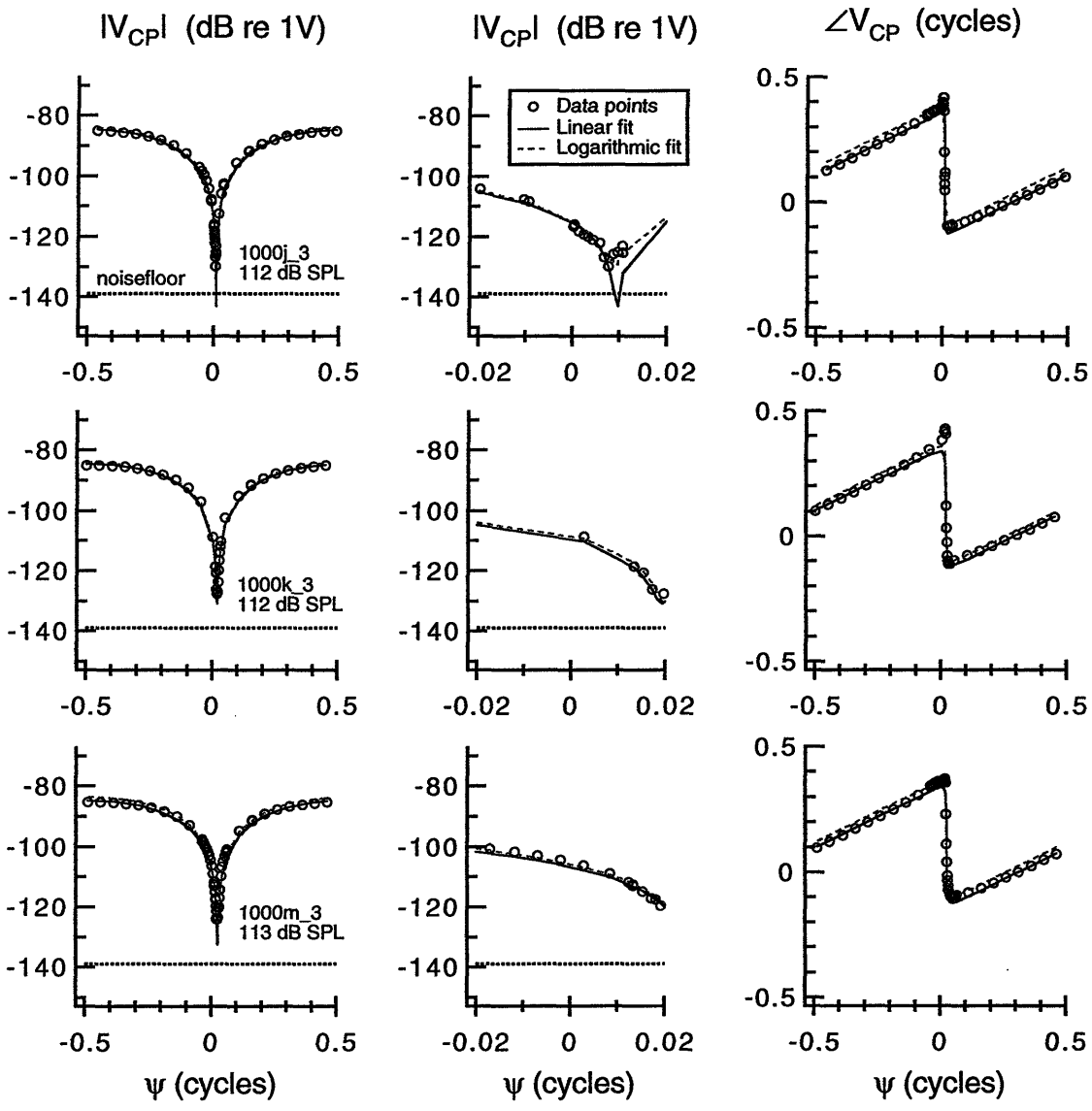

Figure C-32: Simultaneous-stimuli measurement sets and model fits at 1000 Hz on Cat #3.

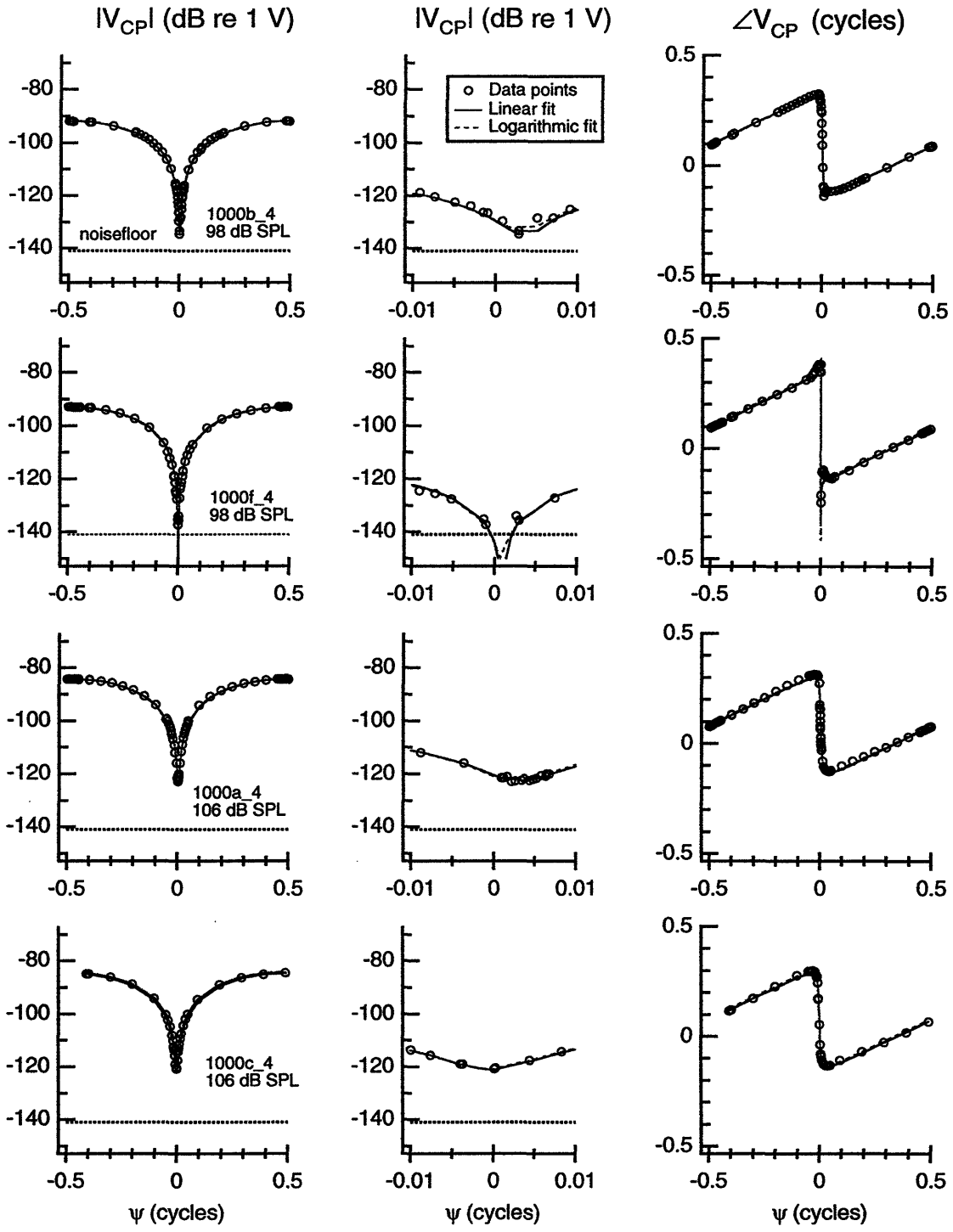

Figure C-33: Simultaneous-stimuli measurement sets and model fits at 1000 Hz on Cat #4.

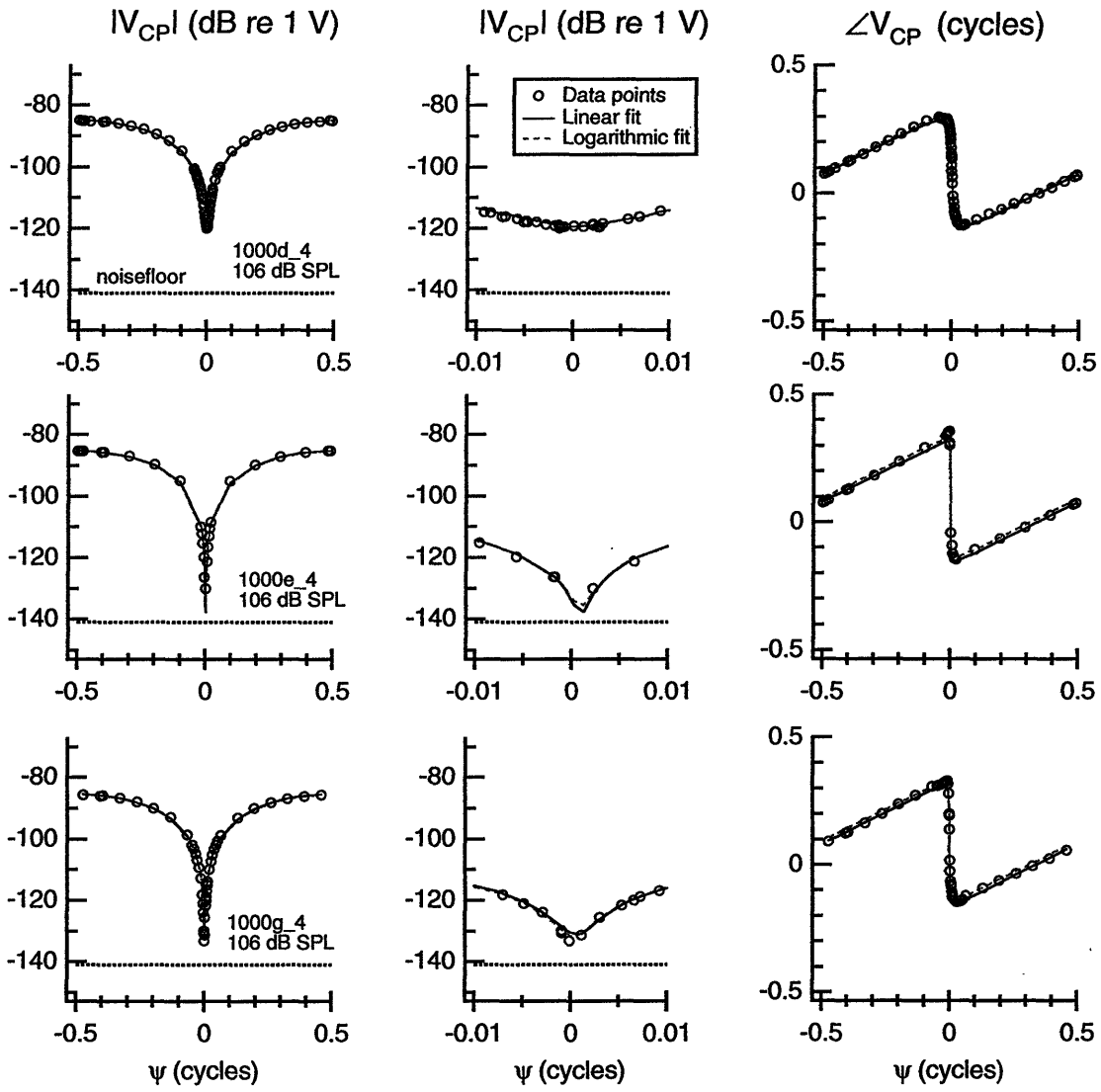

Figure C-34: Simultaneous-stimuli measurement sets and model fits at 1000 Hz on Cat #4.

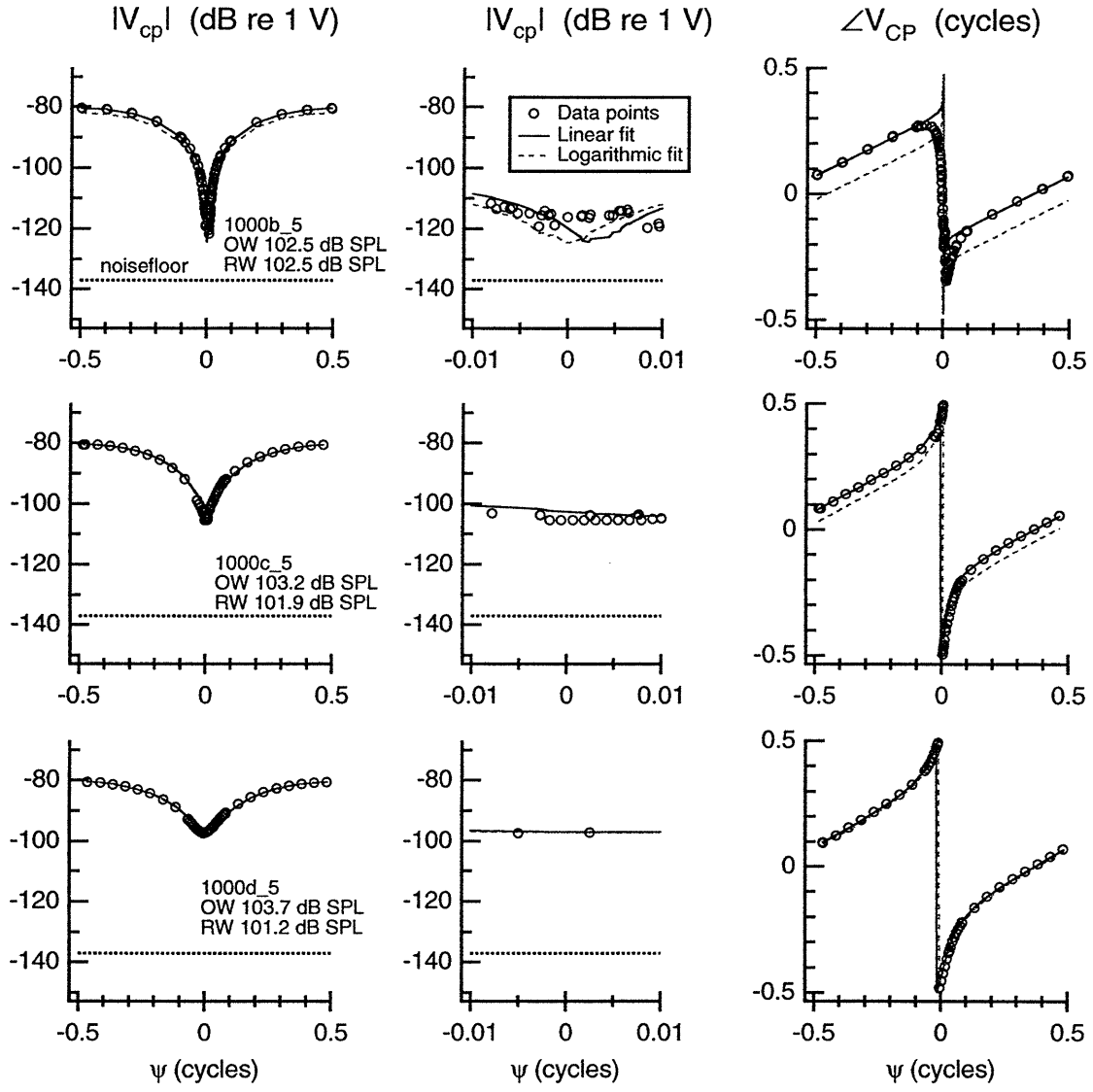

Figure C-35: Simultaneous-stimuli measurement sets and model fits at 1000 Hz on Cat #5. The sum of the magnitudes of $|P_{OW}|$ and $|P_{RW}|$ was held constant: $|P_{OW}| + |P_{RW}| = 5.3\ Pascals$.

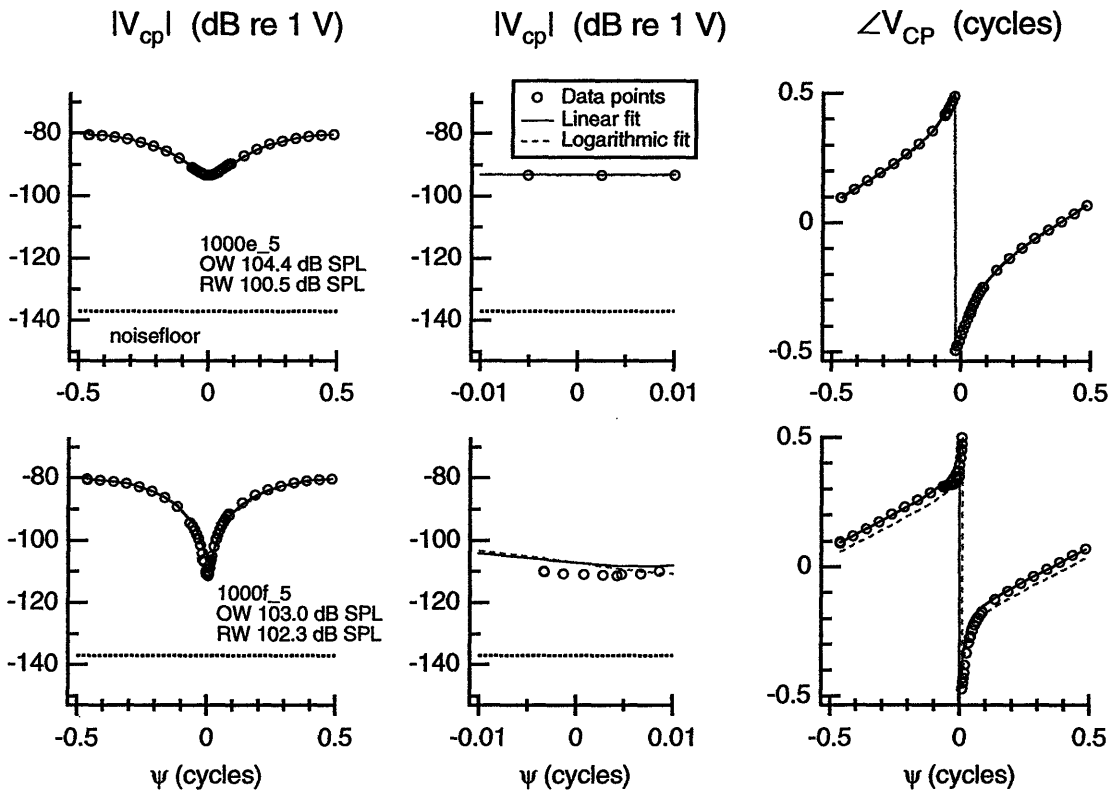

Figure C-36: Simultaneous-stimuli measurement sets and model fits at 1000 Hz on Cat #5. The sum of the magnitudes of $|P_{OW}|$ and $|P_{RW}|$ was held constant: $|P_{OW}| + |P_{RW}| = 5.3\ Pascals$.

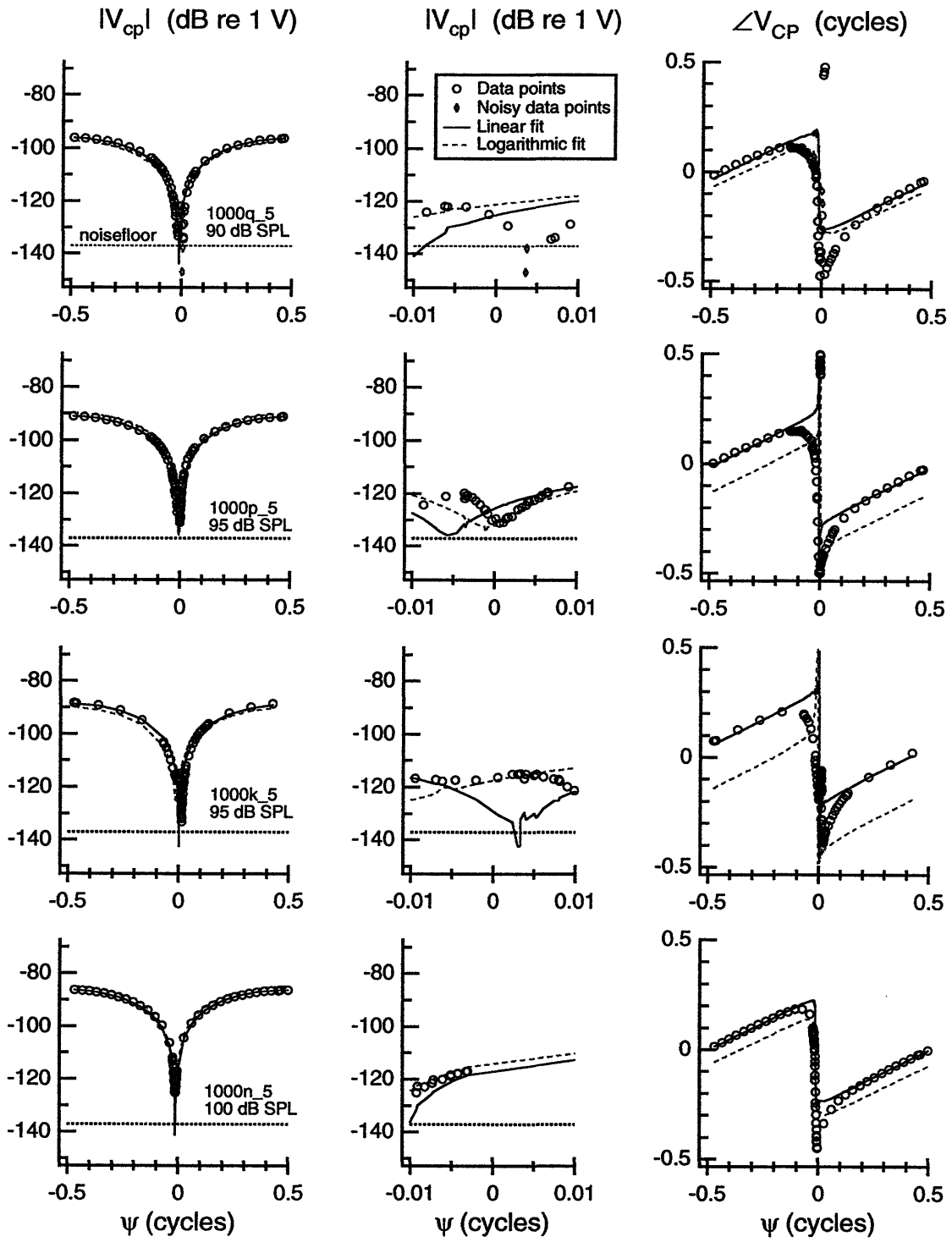

Figure C-37: Simultaneous-stimuli measurement sets and model fits at 1000 Hz on Cat #5.

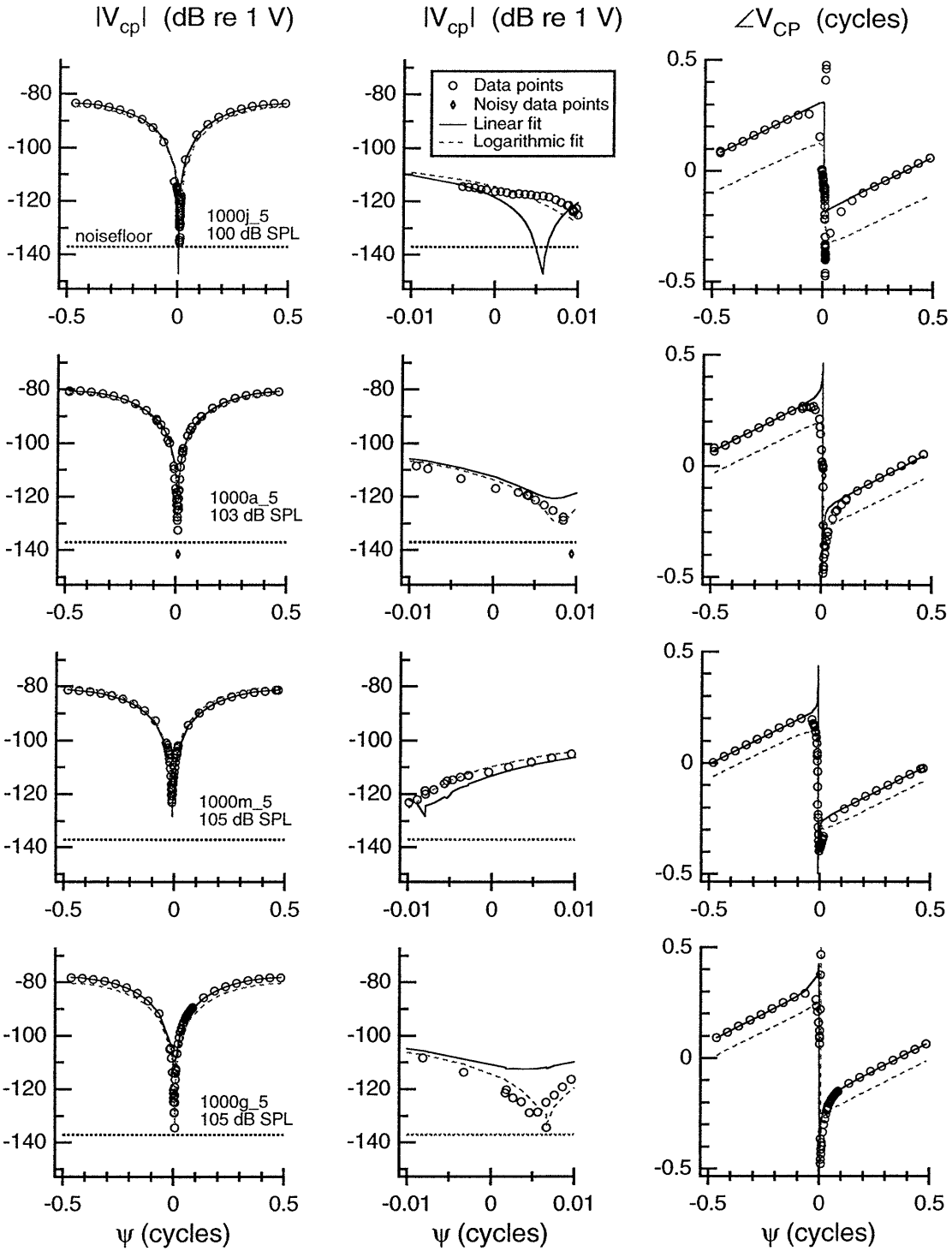

Figure C-38: Simultaneous-stimuli measurement sets and model fits at 1000 Hz on Cat #5.

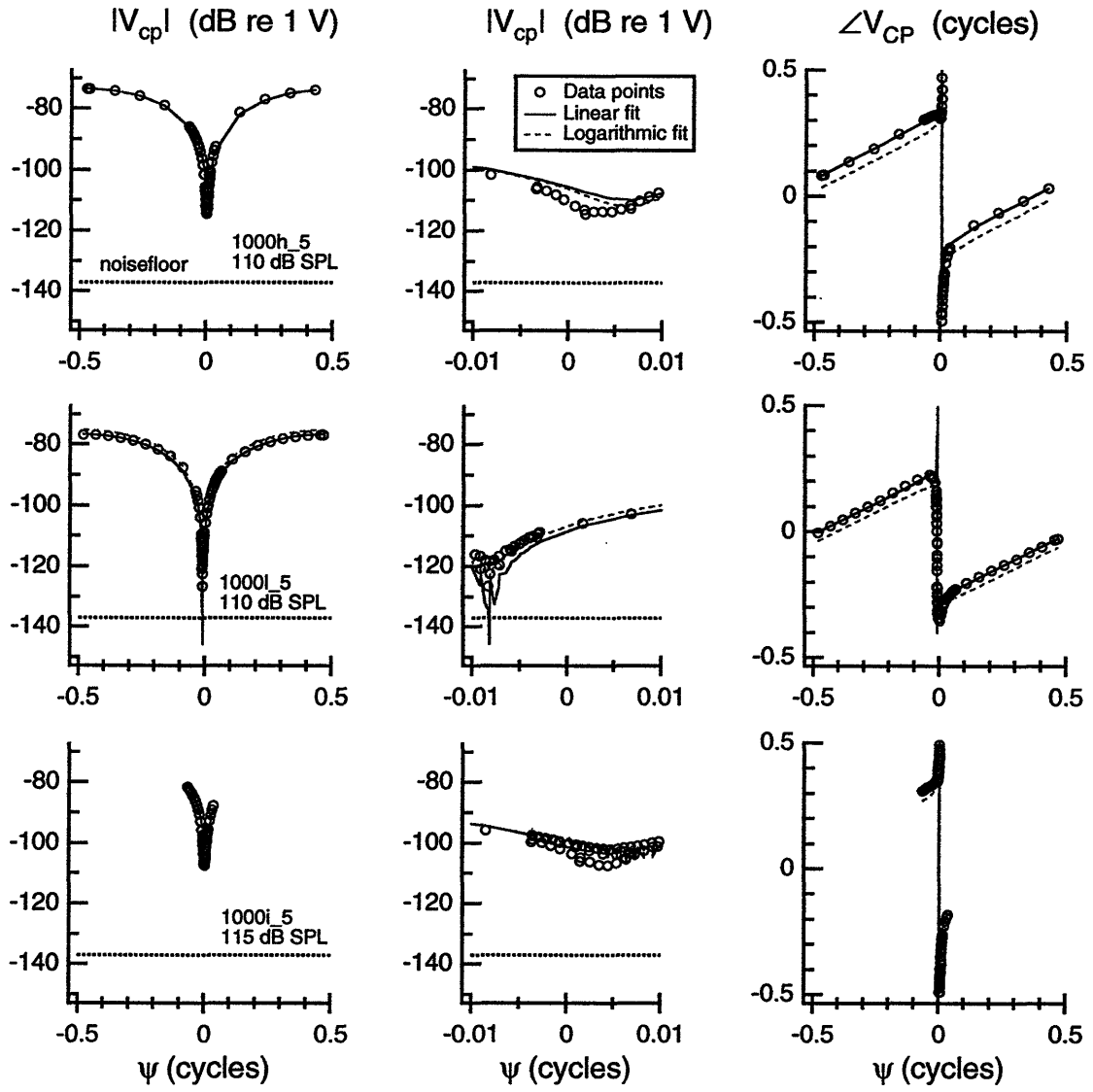

Figure C-39: Simultaneous-stimuli measurement sets and model fits at 1000 Hz on Cat #5.

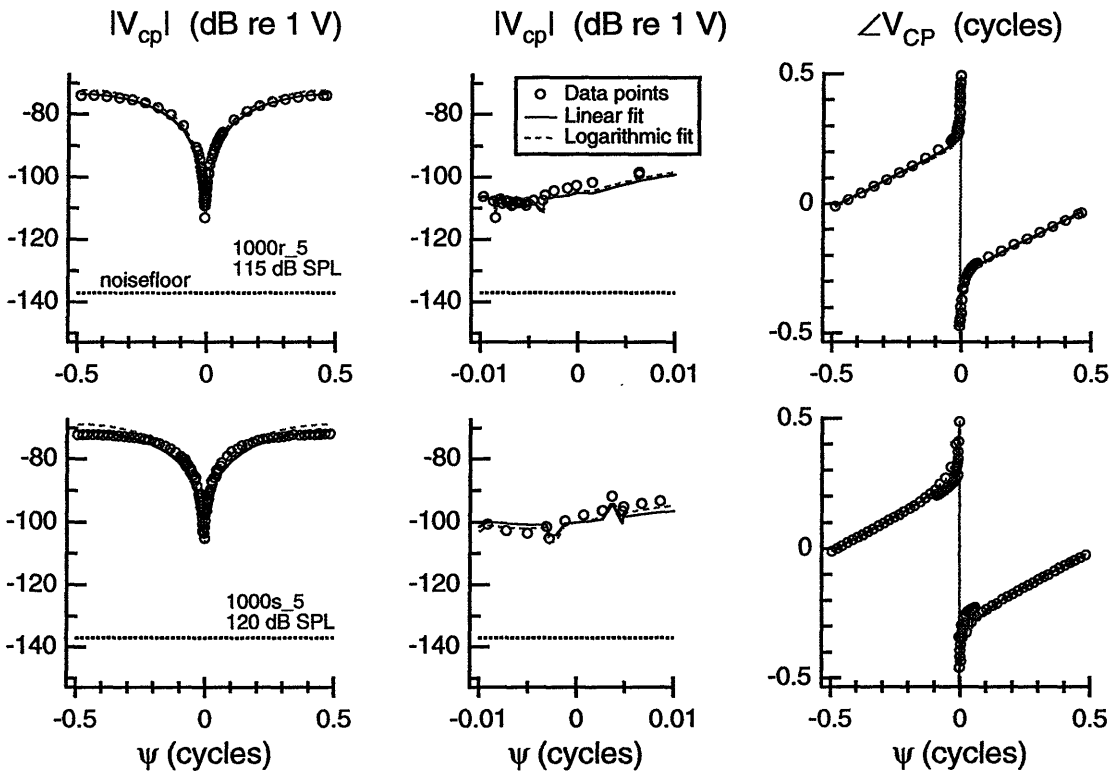

Figure C-40: Simultaneous-stimuli measurement sets and model fits at 1000 Hz on Cat #5.

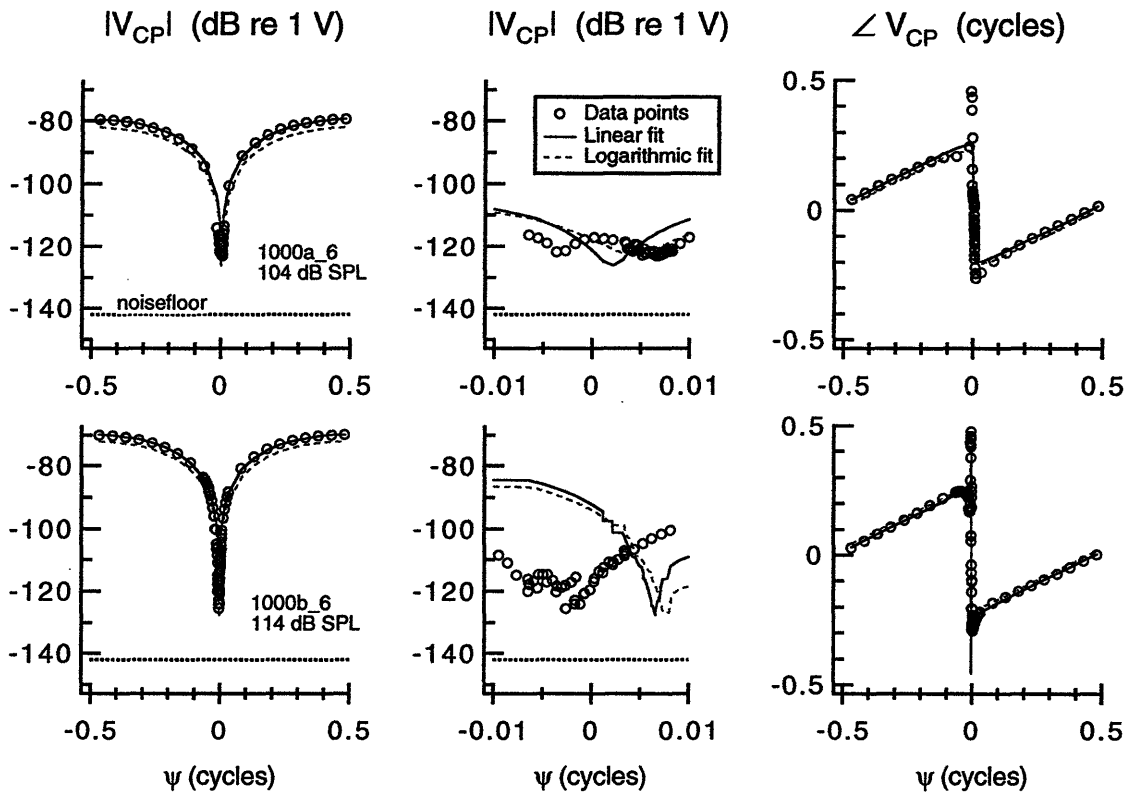

Figure C-41: Pre-TTX simultaneous-stimuli measurement sets and model fits at 1000 Hz on Cat #6.

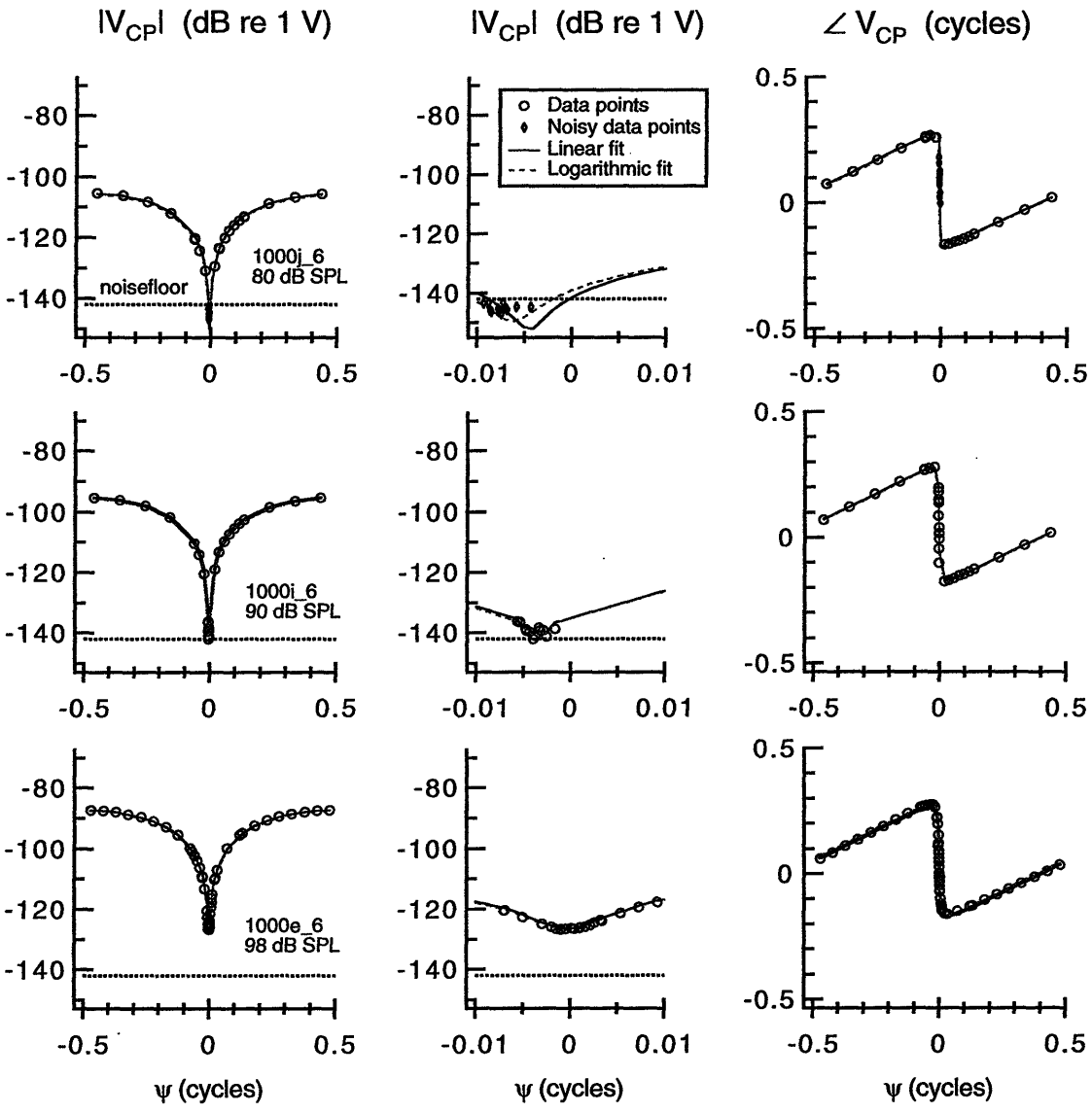

Figure C-42: Post-TTX simultaneous-stimuli measurement sets and model fits at 1000 Hz on Cat #6.

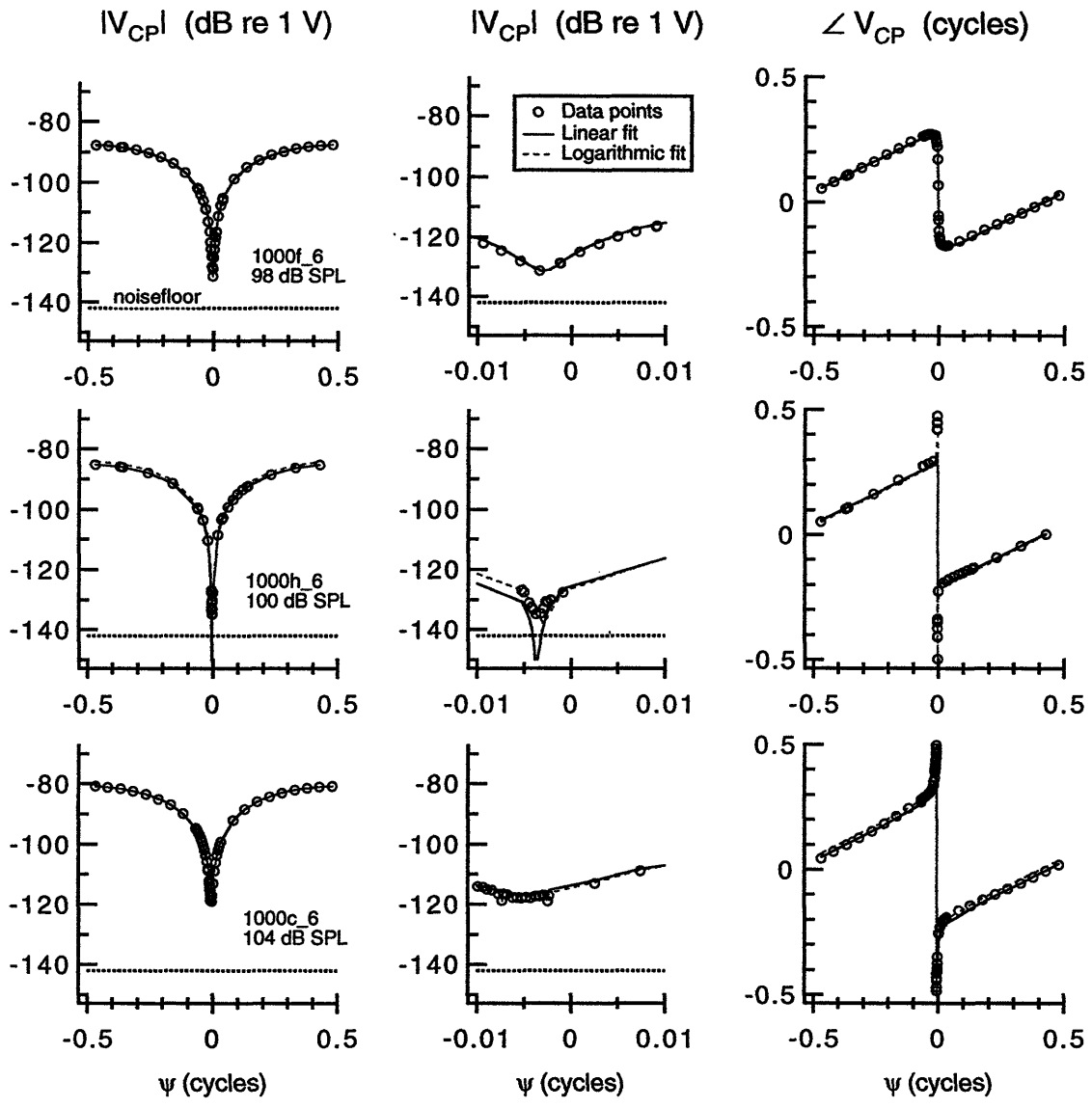

Figure C-43: Post-TTX simultaneous-stimuli measurement sets and model fits at 1000 Hz on Cat #6.

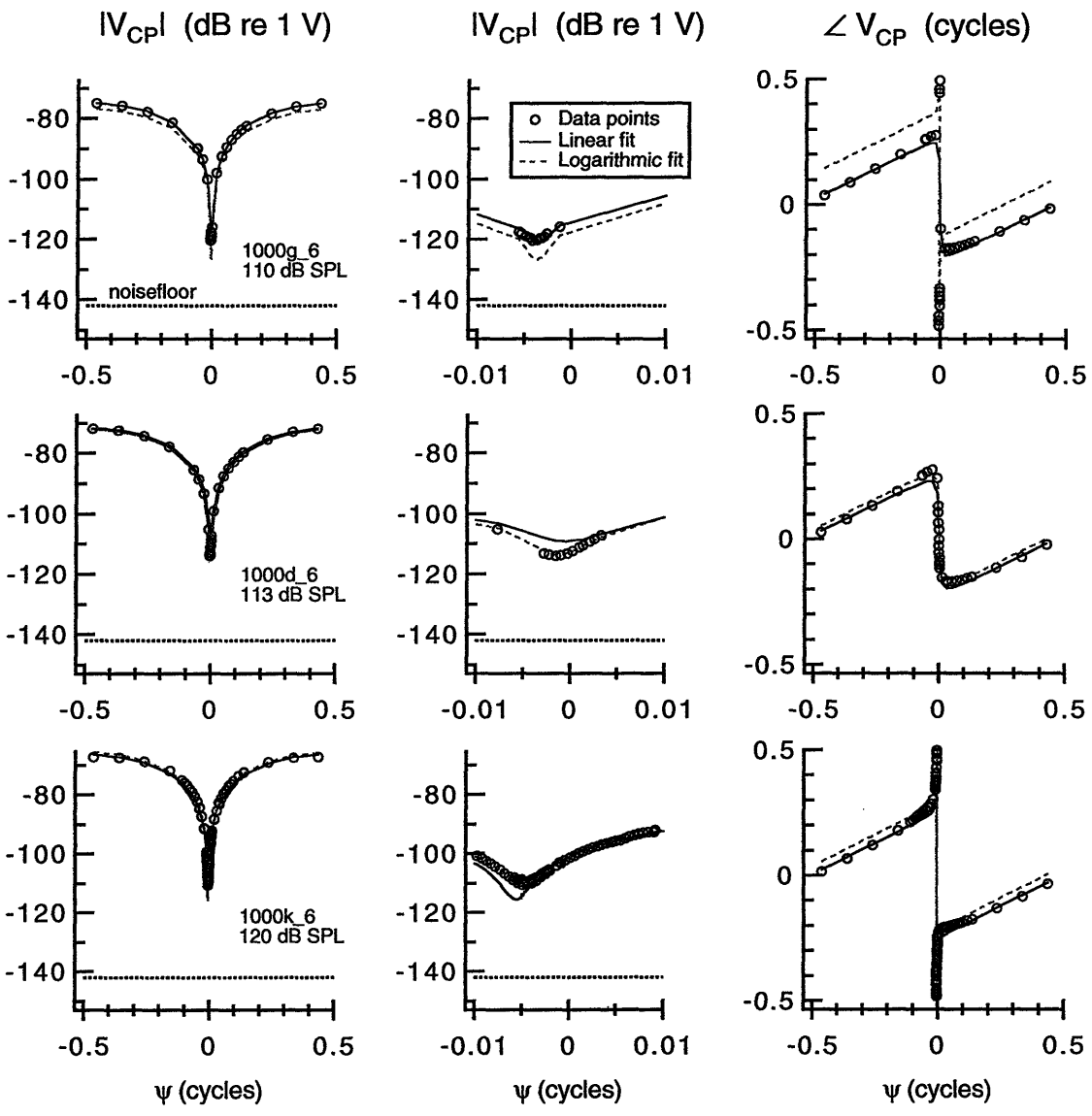

Figure C-44: Post-TTX simultaneous-stimuli measurement sets and model fits at 1000 Hz on Cat #6.

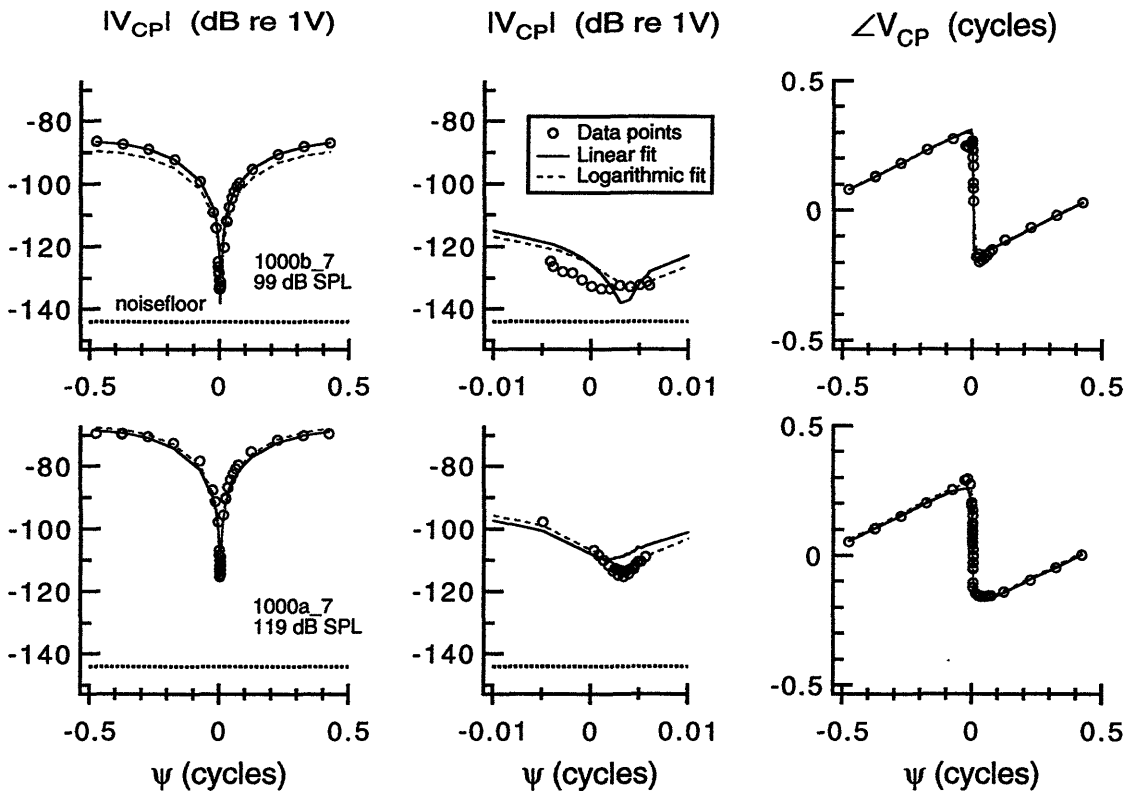

Figure C-45: Pre-TTX simultaneous-stimuli measurement sets and model fits at 1000 Hz on Cat #7.

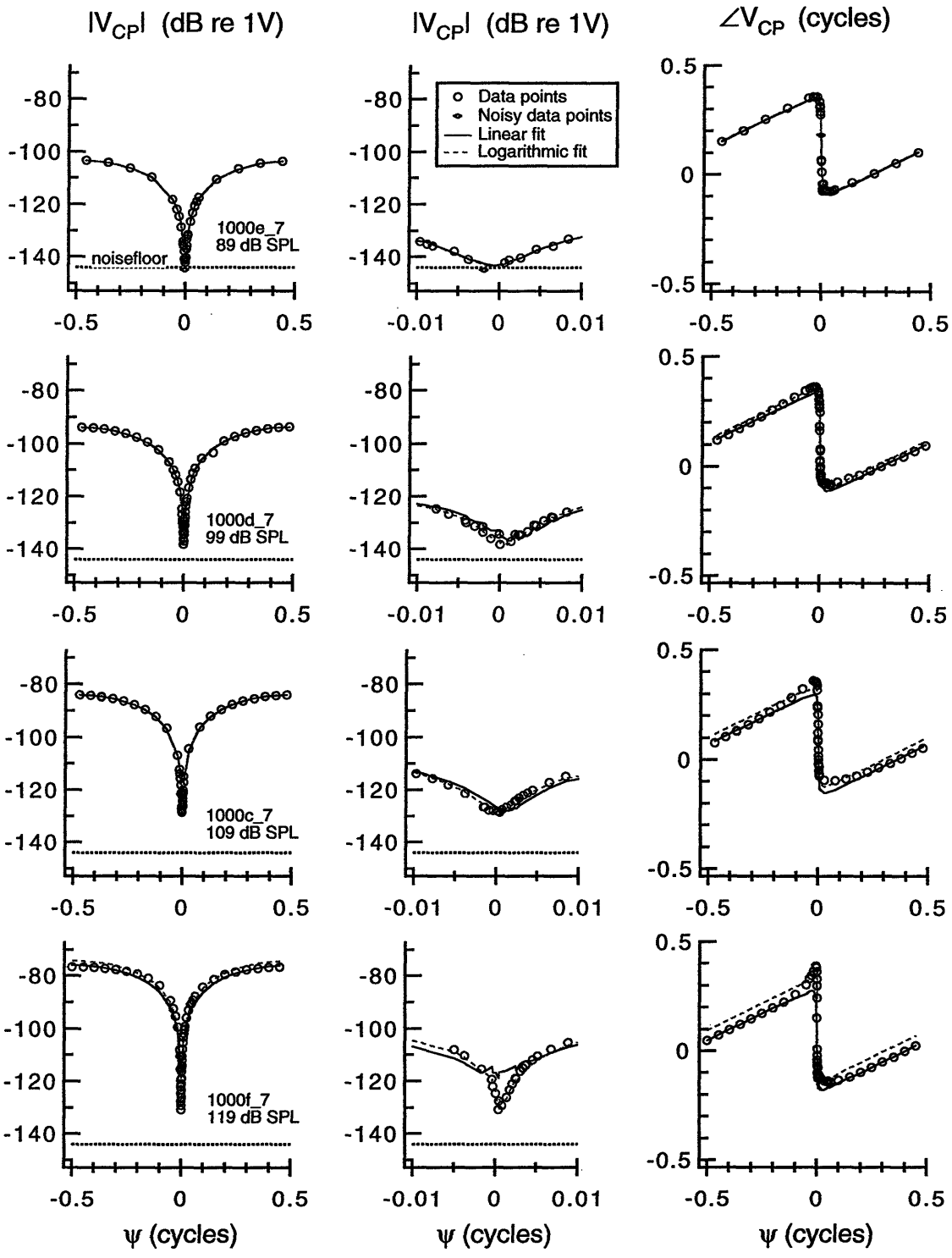

Figure C-46: Post-TTX simultaneous-stimuli measurement sets and model fits at 1000 Hz on Cat #7.

Bibliography

Allen, J. B. (1985). "Cochlear modeling," *IEEE ASSP* **2**(1):3–29.

Békésy, G. v. (1936a). "Zur Physik des Mittelohres und über das Hören bei fehlerhaftem Trommelfell," *Akust. Zeits* **1**:13–23 (pp. 104–115 in Békésy, 1960).

Békésy, G. v. (1936b). "Über die Hörschwelle und Fühlgrenze langsamer sinusförmiger Luftdruckschwandungen," *Ann. Physik* **26**:554–566 (pp. 257–267 in Békésy, 1960).

Békésy, G. v. (1960). *Experiments in Hearing.* McGraw-Hill, New York. Edited by E. G. Wever.

Dolan, D. F., Xi, L., and Nuttall, A. L. (1989). "Characterization of an EPSP-like potential recorded remotely from the round window," *J. Acoust. Soc. Am.* **86**(6):2167–2171.

Gotay-Rodriquez, V. M. and Schuknecht, H. F. (1977). "Experiences with type IV tympanomastoidectomy," *Laryngoscope* **87**:522–528.

Kaplan, M. S., Szaro, B. G., and Weiss, T. F. (1983). "Components of the cochlear electric responses in the alligator lizard," *Hearing Research* **12**:323–351.

Lee, K. and Schuknecht, H. F. (1971). "Results of tympanoplasty and mastoidectomy at the Massachusetts Eye and Ear Infirmary," *Laryngoscope* **81**:529–543.

Merchant, S. N., Rosowski, J. J., and Ravicz, M. E. (1995). "Middle-ear mechanics of type IV and type V tympanoplasty II. Clinical analysis and surgical implications,"*Am. J. Otolarngol.* in press.

Nash, J. (1979). *Compact Numerical Methods for Computers: linear algebra and function minimisation*, chapter 14, pages 141–152. John Wiley & Sons, New York.

Peake, W., Rosowski, J. J., and Lynch, T. J. (1992). "Middle-ear transmission: Acoustic versus ossicular coupling in cat and human," *Hearing Research* **57**:245–268.

Pickles, J. O. (1988). *An Introduction to the Physiology of Hearing.* Academic Press, 2 edition.

Press, W. H., Teukolsky, S. A., Vetterling, W. T., and Flannery, B. P. (1992). *Numerical Recipes in C.* Cambridge University Press.

Rosowski, J. J., Merchant, S. N., and Ravicz, M. E. (1995). "Middle-ear mechanics of type IV and type V tympanoplasty I. Model analysis and predictions," *Am. J. Otolarngol.* in press.

Shera, C. A. and Zweig, G. (1992). "An empirical bound on the compressibility of the cochlea," *J. Acoust. Soc. Am.* **92**(3):1382–1388.

Wever, E. G. and Lawrence, M. (1950). "The acoustic pathways to the cochlea," *J. Acoust. Soc. Am.* **22**(4):460–467.

Wever, E. G., Lawrence, M., and Smith, K. R. (1948). "The middle ear in sound conduction," *Archives of Otolaryngology* **48**:19–35.

Wullstein, H. (1956). "The restoration of the function of the middle ear, in chronic otitis media," *Ann. Otol. Rhinol. Laryngol.* **65**:1020–1041.

Zwislocki, J. (1965). "Analysis of some auditory characteristics," in Luce, R. D., Bush, R. R., and Galanter, E., editors, *Handbook of Mathematical Psychology*, volume 3, chapter 15, pages 1–97. John Wiley & Sons, New York.